AD_____

Award Number: W81XWH-04-2-0022

TITLE: Development of a Multileaf Collimator for Proton Therapy

PRINCIPAL INVESTIGATOR: Zelig Tochner, MD

CONTRACTING ORGANIZATION: Trustees of the University of Pennsylvania,
                                 Philadelphia PA 19104-6205

REPORT DATE: November 2012

TYPE OF REPORT: Final

PREPARED FOR: U.S. Army Medical Research and Materiel Command
                      Fort Detrick, Maryland 21702-5012

DISTRIBUTION STATEMENT:

   ☒ Approved for public release; distribution unlimited

   ☐ Distribution limited to U.S. Government agencies only;
      report contains proprietary information

The views, opinions and/or findings contained in this report are those of the author(s) and should not be construed as an official Department of the Army position, policy or decision unless so designated by other documentation.

REPORT DOCUMENTATION PAGE

Form Approved
OMB No. 0704-0188

Public reporting burden for this collection of information is estimated to average 1 hour per response, including the time for reviewing instructions, searching existing data sources, gathering and maintaining the data needed, and completing and reviewing this collection of information. Send comments regarding this burden estimate or any other aspect of this collection of information, including suggestions for reducing this burden to Department of Defense, Washington Headquarters Services, Directorate for Information Operations and Reports (0704-0188), 1215 Jefferson Davis Highway, Suite 1204, Arlington, VA 22202-4302. Respondents should be aware that notwithstanding any other provision of law, no person shall be subject to any penalty for failing to comply with a collection of information if it does not display a currently valid OMB control number. **PLEASE DO NOT RETURN YOUR FORM TO THE ABOVE ADDRESS.**

1. REPORT DATE *(DD-MM-YYYY)* November 2012	2. REPORT TYPE Final	3. DATES COVERED *(From - To)* 17 May 2004 – 31 October 2012

4. TITLE AND SUBTITLE	5a. CONTRACT NUMBER
Development of a Multileaf Collimator for Proton Radiotherapy (Phase 1) Development of Scanned Beam system for proton Radiotherapy (Phase 2) Image Guided, adaptive and efficient use of proton Therapy (Phase 3)	
	5b. GRANT NUMBER W81XWH-04-2-0022

6. AUTHOR(S)	5d. PROJECT NUMBER
Chris Ainsley PhD, Maura Kirk MS, Derek Dolney PhD, James McDonough PhD, Zelig Tochner MD, Neha Vapiwala MD	
	5e. TASK NUMBER
	5f. WORK UNIT NUMBER

7. PERFORMING ORGANIZATION NAME(S) AND ADDRESS(ES) Trustees of the University of Pennsylvania Philadelphia PA 19104-6205	8. PERFORMING ORGANIZATION REPORT NUMBER

9. SPONSORING / MONITORING AGENCY NAME(S) AND ADDRESS(ES) U.S. Army Medical Research and Materiel Command Fort Detrick, Maryland 21702-5012	10. SPONSOR/MONITOR'S ACRONYM(S)
	11. SPONSOR/MONITOR'S REPORT NUMBER(S)

12. DISTRIBUTION / AVAILABILITY STATEMENT

Approved for public release; distribution unlimited

13. SUPPLEMENTARY NOTES

14. ABSTRACT
This final report describes the work that was done during the past eight years of work on the award. The main focus during the initial 5 years of the project was to develop – design and construct- FDA approved multileaf collimator (MLC) to be used clinically in the proton therapy center at UPENN. During these years a work on Phase 2 and 3 of the projects started and once the proton center opened in January of 2010 phase 2 and 3 moved to the center stage and the work focused on the development of scanned beam technology for proton therapy and the development of adaptive, image guided, telemedicine and techniques for quality and efficient proton therapy.
This research project is a joint collaborative effort between the University of Pennsylvania (HUP) and the Walter Reed Army Medical Center (WRAMC), currently in Bethesda Maryland, and is part of a larger project to build a state-of-the-art proton radiotherapy facility in Philadelphia and development of telemedicine for proton radiotherapy for the US military.

15. SUBJECT TERMS
Radiation Oncology, Proton Therapy, Image-Guided Radiotherapy, PET

16. SECURITY CLASSIFICATION OF:			17. LIMITATION OF ABSTRACT	18. NUMBER OF PAGES	19a. NAME OF RESPONSIBLE PERSON USAMRMC
a. REPORT U	b. ABSTRACT U	c. THIS PAGE U	UU	154	19b. TELEPHONE NUMBER *(include area code)*

Standard Form 298 (Rev. 8-98)
Prescribed by ANSI Std. Z39.18

Table of Contents

Appendix I (List of personnel receiving pay from the research effort and publications)

The overall goal of this multi-year research project in collaboration with the Walter Reed Army Medical Center is to develop the necessary technology to make the proton facility that is being constructed in Philadelphia the most advanced proton radiotherapy center. The first technology (Phase I) is the development of a multileaf collimator (MLC) for proton therapy and investigates the issues that must be resolved to use MLC in proton therapy. The second technology (Phase II) under study is the optimization of the spot scanning delivery technique including the effects of organ motion. The third technology (Phase III) is the development of several components that are essential for quality and efficient delivery of proton therapy. The technologies in this award are cone beam CT for proton therapy for image-guided, adaptive radiotherapy, telemedicine for primarily military use with potential use in the civian world and the development of a decision- making algorithm to maximize the efficiency of the facility. Phase III is done in collaboration with the Walter Reed Army Medical Center and part of the work that was done with this group focused on telemedicine which is a major goal for the military. Much of Phase III of the award was done during the second half of the life of the award and some of the projects are continuing in some forms in Phase IV, V, and VI of this grant. The reports here including some work which is done in these phases. This report summarizes the progress during the eight years of the project in the relevant areas.

<u>Body</u>

Phase I. Development of a Multileaf Collimator for Proton Radiotherapy

The path from the design, through the manufacture and on to the testing and deployment of the proton multileaf collimator (MLC) system that we developed in collaboration with Varian Medical Systems and Ion Beam Applications S.A. (IBA) has been charted extensively in quarterly reports spanning from 2006 to 2010. The device was cleared by the FDA in late 2009 and has since been installed on universal nozzles on four of our proton gantries. The first of these has now been in routine clinical use for over a two-and-a-half years. In this final report, we refresh the reader on the need for a proton MLC and then highlight some of the key steps and findings along the way from the drawing board to its clinical implementation.

I.1. Motivation

Transverse beam collimation in double-scattered and uniform-scanned proton therapy is achieved conventionally through the use of a combination of snouts and patient-specific brass apertures affixed to the distal end of the treatment nozzle (Figure I.1). While being effective in shielding the patient from high doses of radiation outside of the target region, this approach unfortunately has a detrimental effect on patient throughput and departmental workload. A separate aperture must be fabricated for each treatment port of each patient, leading to a financial cost in purchasing the raw materials, a time cost in the manufacturing process, and the requirement of storage space and clear identification. Furthermore, for a patient requiring multiple treatment ports, the therapist must enter the treatment room to change apertures—a time-consuming process and one that also requires the repetitive lifting of heavy loads (up to ~25 kg for the heaviest apertures).

The deficiencies of apertures can be overcome through the use of an MLC (Figure I.2). This solution has, of course, been adopted by x-ray therapy for many years and, indeed, led to the advent of intensity-modulated radiation therapy (IMRT). However, because the physical interactions of protons and photons with matter are fundamentally different, it is not as straightforward a task as might first be thought to adapt a photon MLC for use in proton therapy. Photons, on the one hand, are massless, uncharged, indirectly-ionizing particles. Their fluence drops roughly exponentially with radiological depth in matter through interactions with atomic electrons. Consequently, some ever-decreasing fraction of photons will be transmitted through any collimating device as its shielding thickness is increased. The out-of-field shielding for photon beams is therefore designed to reduce this transmitted radiation to an acceptable level. Protons, on the other hand, are massive, charged, directly-ionizing particles. Their fluence drop with depth is instead due to inelastic nuclear collisions and is, in general, much slower than for photons (~1% per centimeter of water). Moreover, in contrast with photons, protons lose energy continuously via inelastic collisions with atomic electrons, and they thus possess a finite range beyond which their fluence falls rapidly to zero. In proton therapy it is therefore possible to reduce the out-of-field proton dose to zero by employing shielding collimators of adequate thickness. However, the inelastic nuclear collisions which protons undergo in high atomic number materials, such as those typically used in beam collimating devices, result in a secondary neutron dose that is potentially of much greater concern than the out-of-field dose in x-ray therapy.

To that end, we undertook extensive Monte Carlo computer simulation studies to guide the development of a suitable shielding design for a proton MLC and partnered with Varian and IBA to bring this to realization. Our objective was to design a solution that would replace the standard IBA system of snouts and apertures (Figure I.1) without requiring significant modifications to either the electronic and operational aspects of the tried-and-tested Varian Millennium photon MLC or to the IBA universal nozzle. The latter consideration placed stringent constraints on the size, shape and weight of the device, since it had to be designed to be able to translate from 10 cm to 55 cm upstream of isocenter, to rotate by ±95° about the beam axis, to split apart when retracted so as not to interfere with the delivery of pencil-beam scanning (PBS) across a 30 cm × 40 cm plane at isocenter, and to be less than ~267 kg in weight in order to cause no greater deflection of the nozzle under gravity as the gantry rotates than does their conventional snout and aperture system. Thus, is was necessary to strike a balance between (*i*) the clinical specifications (maximizing field size and leaf overtravel and minimizing degradation of the penumbra), which favor longer, less thick leaves, (*ii*) the shielding requirements (minimizing proton leakage dose, maintaining neutron

leakage to levels no worse than originate from conventional brass apertures, and avoiding appreciable activation), which favor thicker leaves, and (*iii*) the logistical constraints (size, shape and weight) which favor shorter leaves.

I.2. System design

Using the Geant4 (v9.1) toolkit, we constructed a model of the IBA beam delivery nozzle (Figure I.3), incorporating its most pertinent components. Primary protons were generated according to a phase-space derived from IBA beam data and their interactions in passing through the double-scattering system were simulated. Uniform scanning was modeled similarly, though with the scatterers removed from the beam-line and with the scan pattern designed to reflect a beam steered magnetically and uniformly across a plane perpendicular to its direction of propagation. The design of the MLC and its support structure (Figure I.4) followed an iterative process, aimed towards finding an acceptable balance between the clinical specifications, the shielding requirements and the logistical constraints. The highest-energy (*i.e.* most penetrating), maximally-modulated, largest field-size settings of the alternative modes were used to probe the evolving leaf-bank and support structure designs, leading us towards an optimal solution.

The shielding for the support structure was designed first. Simulations using a variety of different possible materials, shapes and sizes for the various shielding candidate components were performed, employing the aforementioned beam-line settings, until the point was reached where proton leakage around the outsides of the MLC leaves was reduced to an acceptable level (Figure I.5). The leaf banks were assumed to be infinitely shielded for proton leakage for this purpose. Next, the design of the leaves themselves was addressed. Early on it was decided that a tungsten-based alloy would be the material of choice for several reasons: first, because its high density would promote a compact design; second, because Varian has a wealth of experience in machining it to high tolerances; and third, because its activation when subjected to a therapeutic proton beam results in no long-lived radioisotopes. Via simulations, the leaves were then optimized for height, length and shape, for the number and depths of side and end steps, and for the chamfers that render the leaves more durable over time, with a satisfactory solution indicated by an intraleaf neutron leakage dose no worse than that obtained from brass apertures and an interleaf proton leakage comparable to the 1-2% photon leakage dose typical of MLCs employed with x-ray linacs (Figure I.6).

Our final design comprised 50 leaf pairs, with each leaf projecting to 0.5 cm at isocenter from a nominal MLC elevation. Each leaf, made of the tungsten-based alloy, is approximately 9 cm high (a little over twice the range in this material of the highest energy therapeutic proton beam) and 11 cm long and can overtravel the central axis by 1.5 cm (Figure I.7). Proton leakage through the gaps between adjacent leaves in the same bank was addressed by incorporating a 450 μm side-step running the half-height of each leaf; two one-third-height 300 μm steps were similarly introduced to the leaf ends to mitigate against proton leakage through closed leaf-pairs. As is illustrated in Figure I.7, the shielding part of the prototype leaf is based on three trapezoids (colored red, green and blue in the figure) of differing lengths stacked on top of one other and displaced with respect to each other perpendicularly to their long axes. For the leaves of one of the two banks, the blue length exceeds the green length, as the green length exceeds the blue length (the reverse applies for leaves in the other bank), by 300 μm—the size of each of the two leaf-end steps. To these are added the remaining parts of the 450 μm-wide side-steps (cyan and magenta) that protrude along the leaf-travel direction to the same extent as the central (green) trapezoid, and perpendicular to it to the same extent as the upper and lower trapezoids (red and blue). The upper and lower guides (yellow) and the leaf tails (red and blue) provide the necessary support for the leaf motion in practice, but serve little shielding purpose and could have been omitted from the simulation model. The leading edges of the leaf face are all smoothed off by 650 μm-wide, 150 μm–deep chamfers, which help to mitigate wear and tear.

Leaves were assembled into position in the manner shown in Figures I.8 and I.9. An ideal shielding trapezoid is defined as that which has a half-angle equal to 1/50th of the angle subtended by a 125 mm half-field length at 2330 mm SAD (0.0614°), and a base length equal to 1/25th of the length of that half-field projected to the reference plane 300 mm above isocenter (4.356 mm). The trapezoid so-defined is copied across the leaf bank with adjacent faces placed in contact, and the center of the distal face attached to a plane of uniform elevation. The leaf banks were then populated by laying identical prototype leaves (with the exception of the outermost moving leaves, for which the outer side-step of each is 700 μm wide compared to the 450 μm width elsewhere) over each of the ideal shielding trapezoidal templates, with the sloping leaf faces parallel to the sloping faces of these trapezoids. The fixed outboard leaves (cyan and magenta) were positioned similarly.

6

Figure I.10 compares the leakage dose into a water phantom resulting from the delivery of the same worst-case scenario proton fluence into the MLC with all leaf-pairs closed or into a 65 mm thick brass block (which the MLC was designed to replace) at the culmination of the design optimization process. From these, it is evident that the leakage dose is neutron-dominated in both cases, and that its maximum extent—on entrance to the phantom—is comparable. Moreover, as the leaf thickness extends to in excess of twice the range of the highest energy therapeutic proton beam, the leaves are largely self shielding, resulting in lower energy downstream neutrons, and hence a lower dose at depth, than is seen from the brass block.

I.3. System testing

Manufacturing and assembly of the first MLC system, according to our design, took place at Varian in late 2008 (Figure I.11), while delivery to the University of Pennsylvania and integration with the IBA nozzle in the first treatment room ensued in early 2009 (Figure I.12). Subsequently, the MLC was subjected to rigorous testing in the proton beam in order to interrogate the integrity of the shielding design formulated from our Monte Carlo simulation work. We performed comprehensive studies of proton leakage using, in turn, a uniform scanned beam of the highest energy and a double-scattered beam of the highest energy for which the maximum field-size can be achieved (akin to our simulation studies). Tests were conducted with the MLC fully extended (placing the distal leaf-face 10 cm upstream of isocenter) and fully retracted (placing it 55 cm upstream of isocenter) (Figure I.13). Measurements in the former condition sought leakage around the outsides of the support structure, since the assembly as a whole subtends the smallest solid angle in this case; measurements in the latter condition sought leakage through gaps within the support structure, since any gaps would then present the largest solid angle. We used a combination of Kodak XV film, Gafchromic film and IBA's MatrixX ion chamber array as detecting media to assess the leakage dose as a fraction of the mid-SOBP open-field dose for the same incident beam.

Unexpectedly, on first testing ~2% leakage dose was observed over considerable volumes in uniform scanning mode with the MLC fully extended. The regions concerned lay several centimeters outside the support structure walls (Figure I.14). The image of a wire indicated the likely presence of low energy x-rays, presumably generated in the upstream shielding material. However, the residual component from proton radiation was more concerning. The source of these protons was traced to bolt holes in the gear shield (Figure I.14). It transpired that the bolts only partially filled the holes that had been drilled out to accommodate them and, additionally, that a ring of material had also been removed from this shield to facilitate travel of the ball-bearings as the MLC rotates. In collaboration with Varian, we addressed this problem retrospectively by installing two 135°, 19 mm-thick, 42.5 mm-wide steel arcs (Figure I.15). Unfortunately, the problem was complicated by the fact that adding these arcs would have tipped the MLC over its maximum tolerable weight limit. Weight added here had to be compensated by weight subtracted elsewhere therefore. The implication of Varian's proposal to slough material from the interface plate (Figure I.15) was investigated, again by using our Monte Carlo model to assess the impact of this potential course of action on proton and neutron leakage dose distributions elsewhere. The proposal proved to be a sound one. Varian manufactured and installed the new plate in addition to the steel arcs, and further tests in the proton beam demonstrated that the solution was indeed successful.

I.4. System characteristics

During the acquisition of in-air profiles of square fields as part of the commissioning process of the treatment planning system, several artifacts of the leaf design were noted in the measurement data.

First, pronounced horns were observed along the leaf-travel direction at the field-edge (Figure I.16); their prominence was found to increase with beam energy. Measurements in water showed that these wash out rapidly with depth, however, and in clinical practice they would therefore be readily absorbed by a range-compensator. Nevertheless, we were able to reproduce the effect using our Monte Carlo model (Figure I.17). Furthermore, by replacing the MLC with a non-divergent brass aperture in our simulations, we discovered that the phenomenon then appears in both the inline and crossline directions. By tracking protons in the simulation that were identified as having interacted in the collimating devices, it became clear that the source of the horns was the in-scattering of protons from the field-defining aperture (Figure I.18). Of note, the extent of this effect is much reduced in our MLC for the direction perpendicular to leaf travel, where the leaf sides were designed to closely match the divergence of the beam, while along the leaf travel direction, the magnitude of the effect is comparable with that observed with the brass block (Figure I.17).

Second, the in-air penumbra resulting from the MLC was found to depend on the direction in which the scan was made, while the pattern of behavior differed according to whether a double scattering or uniform scanning beam was being delivered (Figure I.19). For double scattering beams the penumbrae resulting from the sides of the leaves are consistently larger than those from the leaf ends. For the worse of the two sides, the extent can be as large as 1-2 mm. This trend tracks with collimator rotation angle. For uniform scanning, however, the sensitivity to the MLC design is much reduced. The penumbra is more likely governed by the fact that the effective source size is roughly an order of magnitude smaller and that two scanning magnets are located at different positions along the beam direction. As would be expected geometrically, the magnet with the longer SAD, which scans in the crossline direction, gives rise to sharper penumbrae. Since the magnets do not rotate with the MLC, in uniform scanning the phenomenon is independent of the MLC rotation angle.
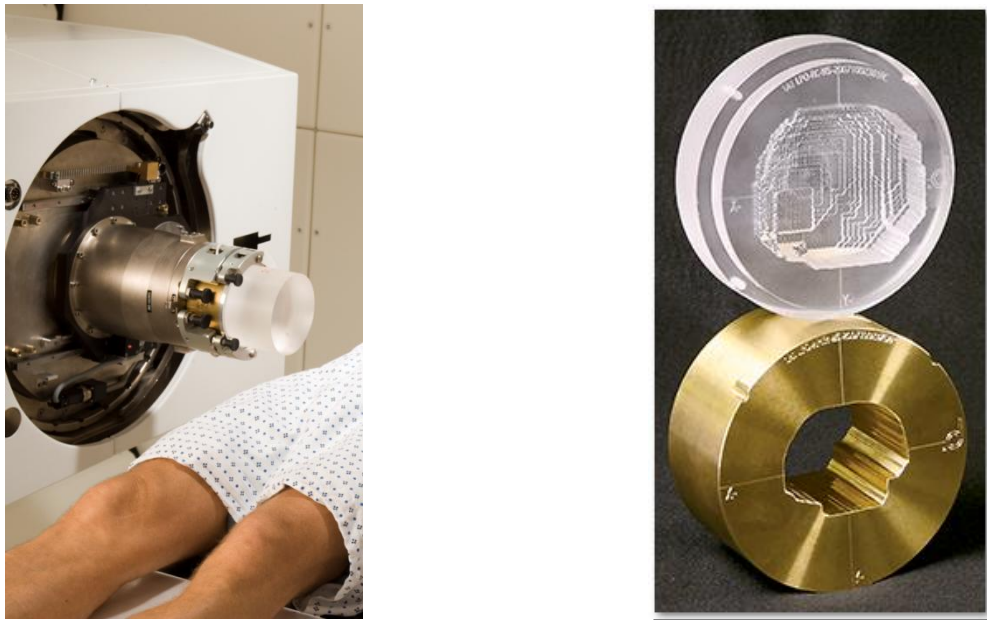
Figure I.1. The snout of a proton therapy treatment nozzle (*left*) on which are mounted the patient-field-specific brass aperture and Lucite (PMMA) range-compensator (*right*)
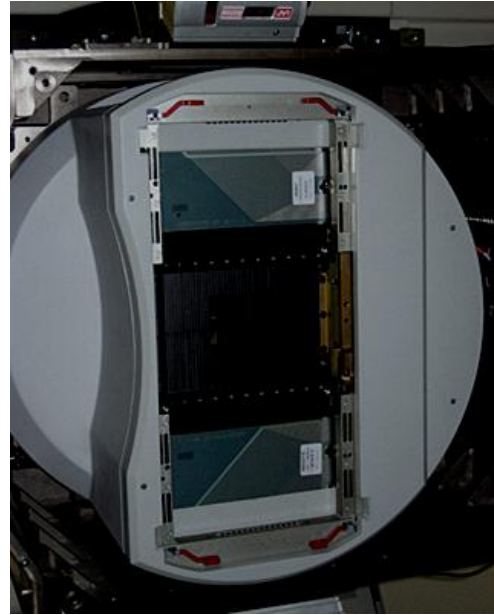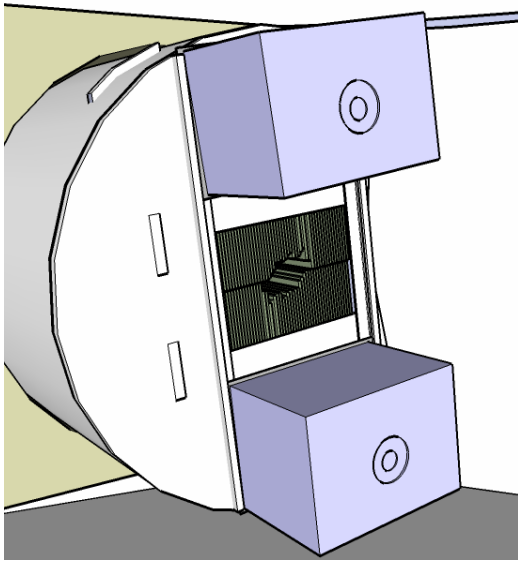
Figure I.2. Conceptual drawing of the multileaf collimator system with range-compensator exchanger fitted (*left*) and photo of the real thing (minus the range compensators) (*right*).
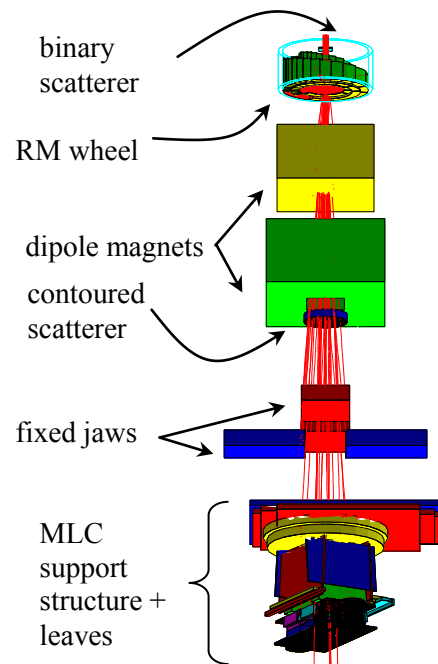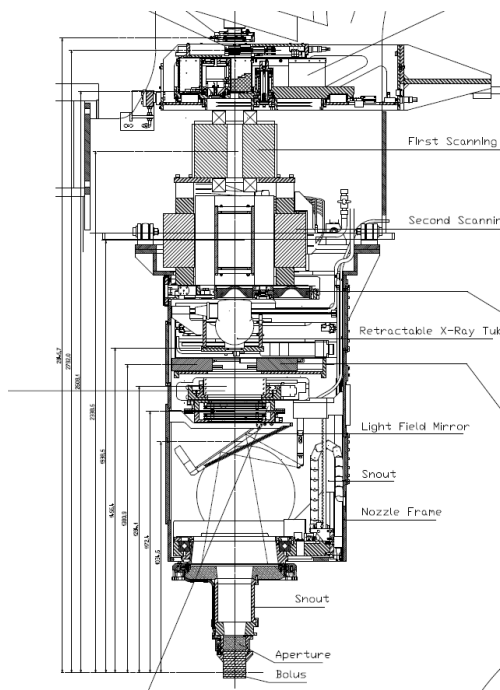

Figure I.3. Blueprint (*left*) and Monte Carlo simulation model (*right*) of the IBA universal nozzle.
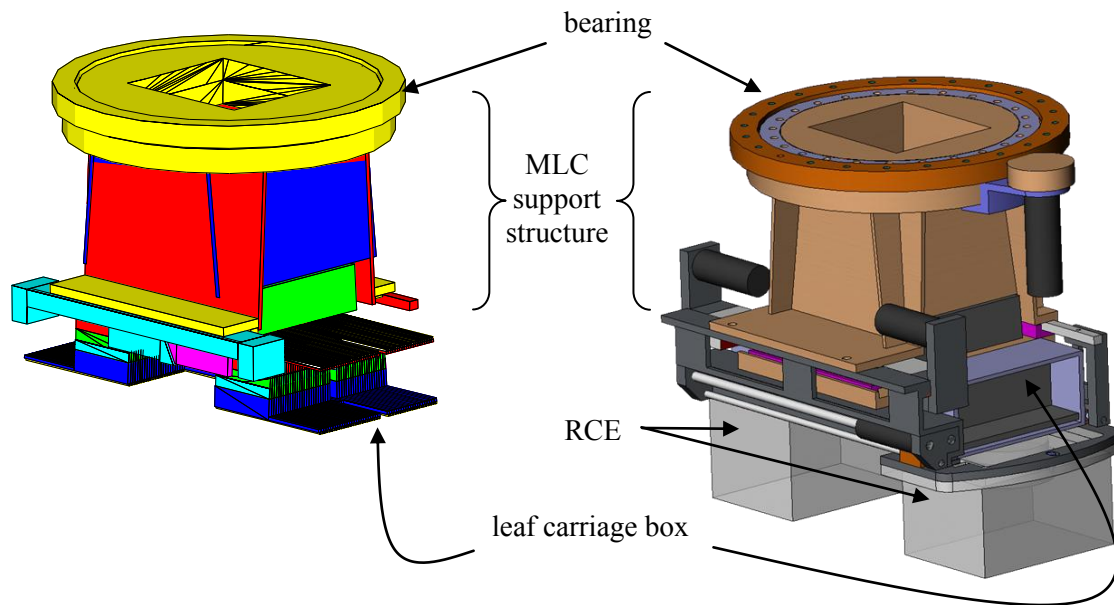
Figure I.4. Monte Carlo simulation model (*left*) and Varian CAD drawing (*right*) of the MLC support structure and leaf system. The system interfaces to the IBA nozzle via the rotatable bearing. The range-compensator exchanger (RCE) is also shown in the Varian illustration.
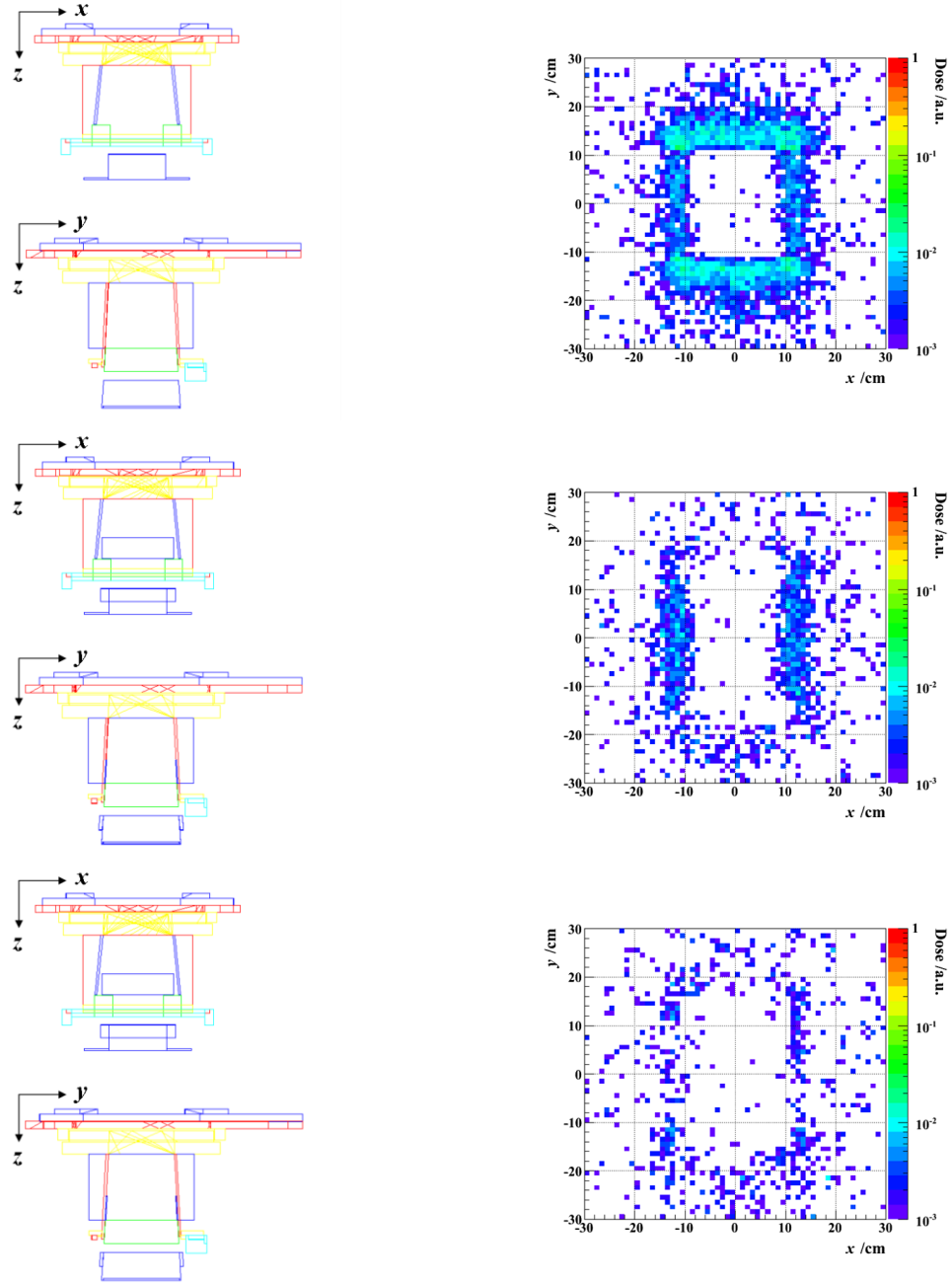
Figure I.5. Pairs of orthogonal cut-away sections of the MLC system (*left*) and the resulting entrance dose distribution attributable to leakage protons downstream of the closed-leaf system (*right*) at various stages of the iterative design process for the support structure: initial (*top*), intermediate (*middle*) and final (*bottom*) scenarios. Leakage doses are shown for the worst case combination of the highest energy and largest field-size and are normalized to the open-field mid-SOBP dose for the same proton fluence.
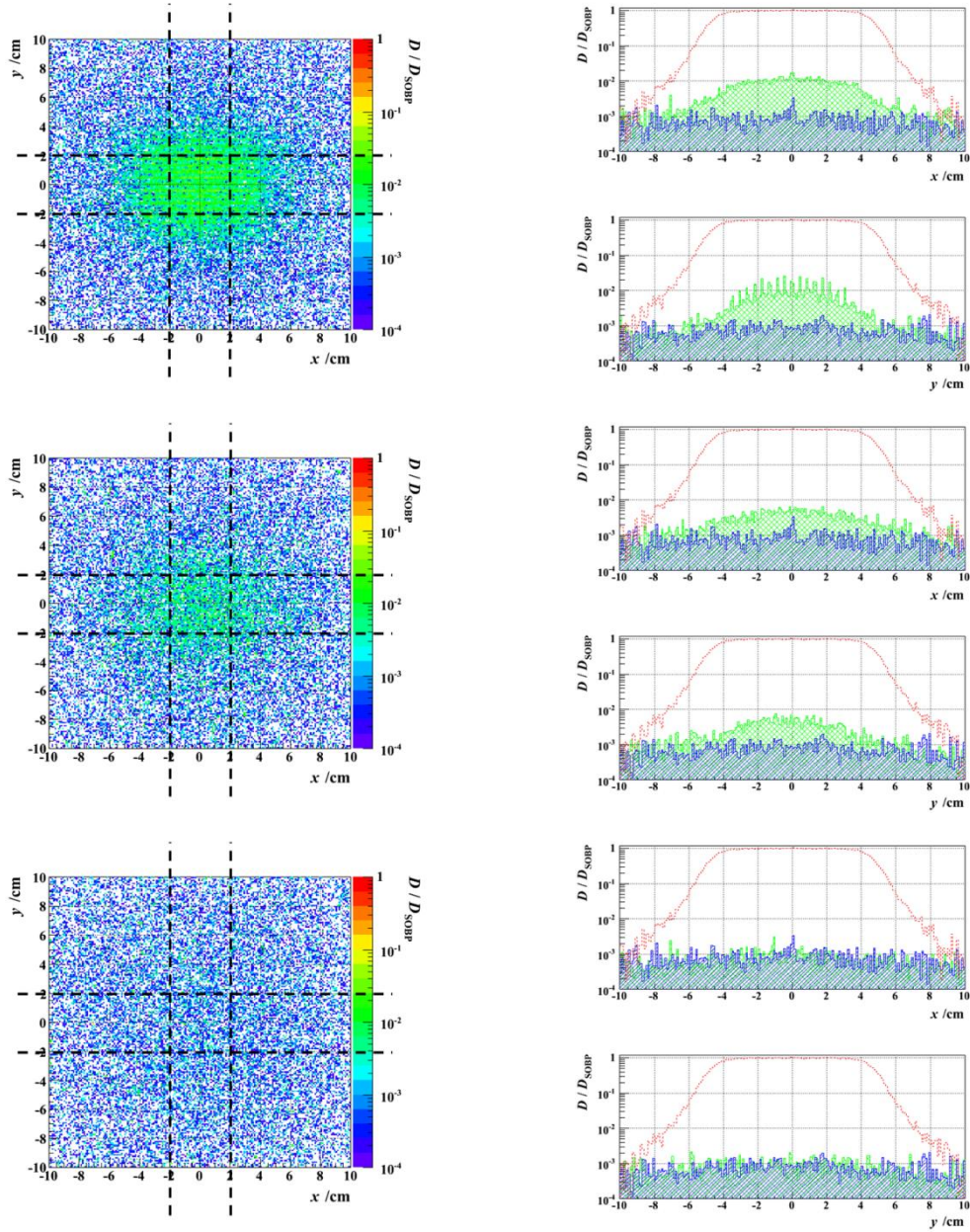
Figure I.6. 2D (*left*) and pairs of orthogonal 1D (*right*) entrance dose distributions (integrated through the band delimited by the dashed lines in the 2D distributions) from all sources of leakage downstream of the closed-leaf MLC system at various stages of the iterative design process for the leaves themselves: initial (*top*), intermediate (*middle*) and final (*bottom*) scenarios. Leakage doses are shown for the worst case of the highest energy and are normalized to the open-field mid-SOBP dose for the same proton fluence. In the 1D distributions interleaf leakage is colored green, intraleaf leakage is blue and open-field profiles are red.

~11 cm

~9 cm

~0.45 cm

0.15 mm × 0.65 mm chamfers

2 × 0.30 mm end steps

0.45 mm side steps

(note: dimensions exaggerated for clarity)

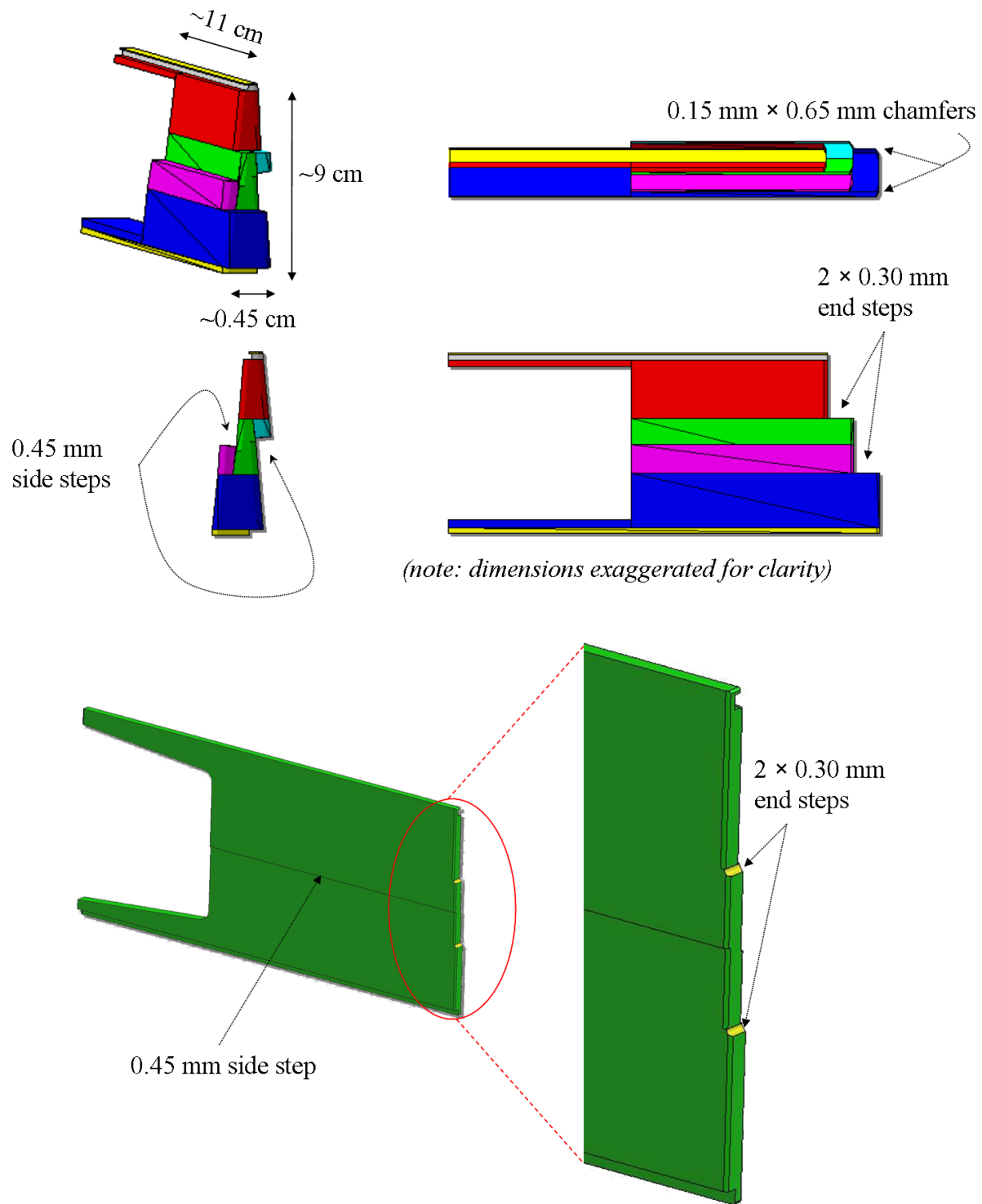2 × 0.30 mm end steps

0.45 mm side step

Figure I.7. Monte Carlo simulation model of a leaf shown in full 3D and in 2D projections (*top*), complete with the steps, chamfers and runners shown in the Varian CAD drawing (*bottom*).
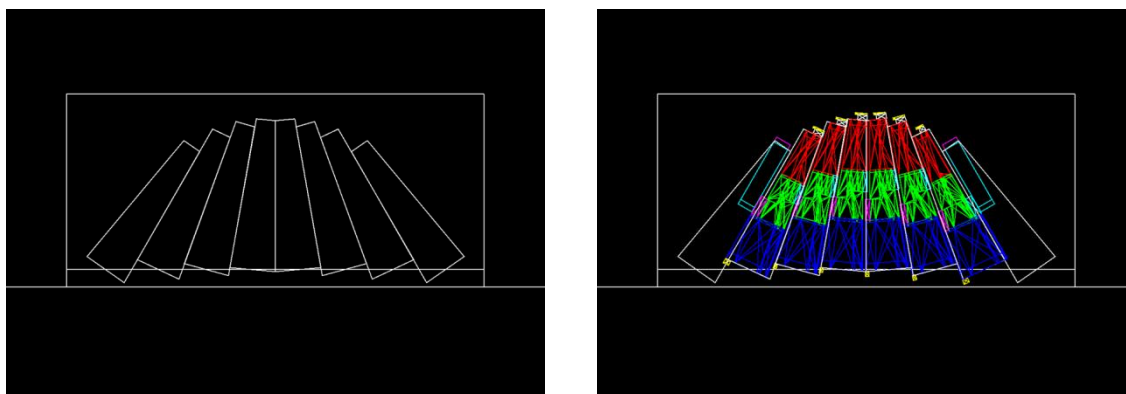
Figure I.8. Stacking of ideal trapezoids across the leaf bank (*left*) and placement of regular moving leaves (center four trapezoids), moving outboard leaves (second and seventh trapezoids) and fixed outboard leaves (first and last trapezoids) (*right*). Dimensions are exaggerated for clarity.
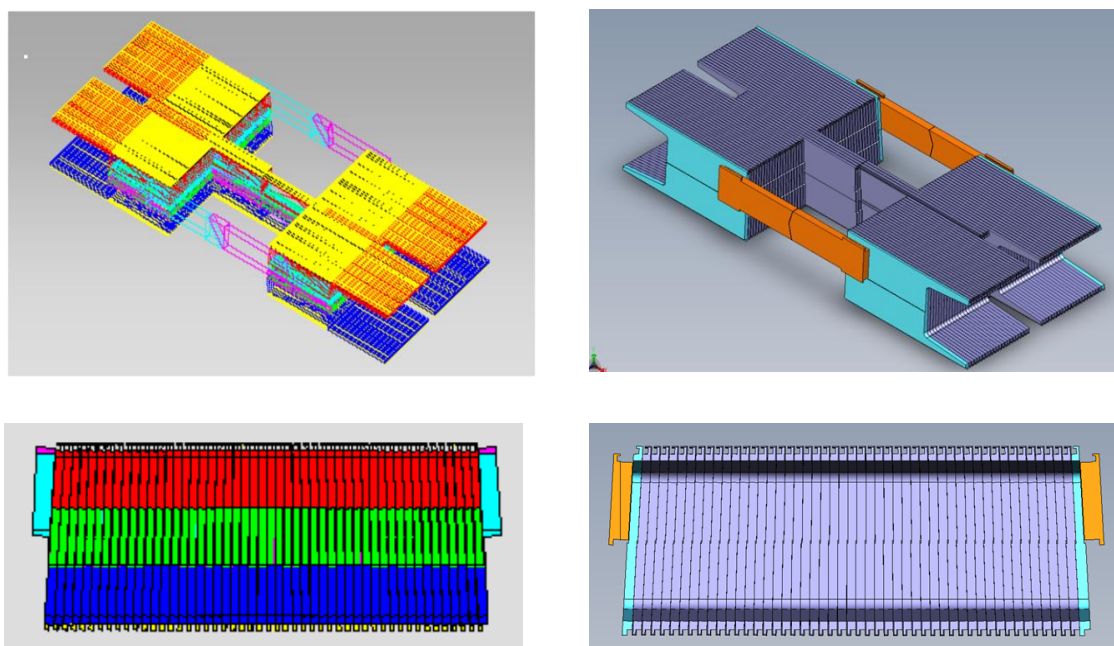

Figure I.9. Monte Carlo simulation model (*left*) and Varian CAD drawing (*right*) of the MLC leaf-banks in 3D (*top*) and from an elevation in which the leaves travel in-and-out of the plane of the paper (*bottom*). Dimensions are to scale.
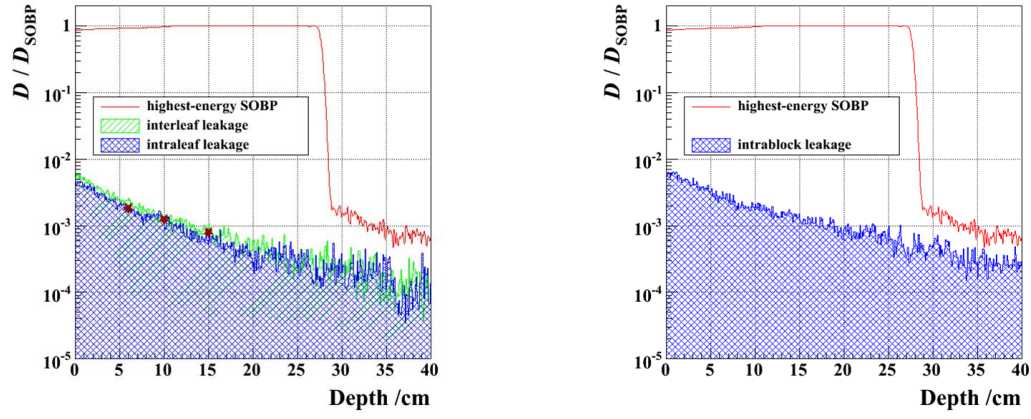
14

Figure I.10. Longitudinal leakage dose distributions in water from all sources of leakage downstream of the closed-leaf MLC system in the final design (*left*) and downstream of a brass block of typical thickness (*right*). Leakage doses are shown for the worst case of the highest energy and are normalized to the open-field mid-SOBP dose for the same proton fluence. Interleaf leakage is colored green, intraleaf leakage, blue and open-field depth-dose distributions, red. Measured data at several depths for the case of the MLC are indicated by the burgundy stars.

support structure

automatic bolus exchanger
(holds 2 compensators)

rotatable bearing

existing electronics

leaf carriage
box

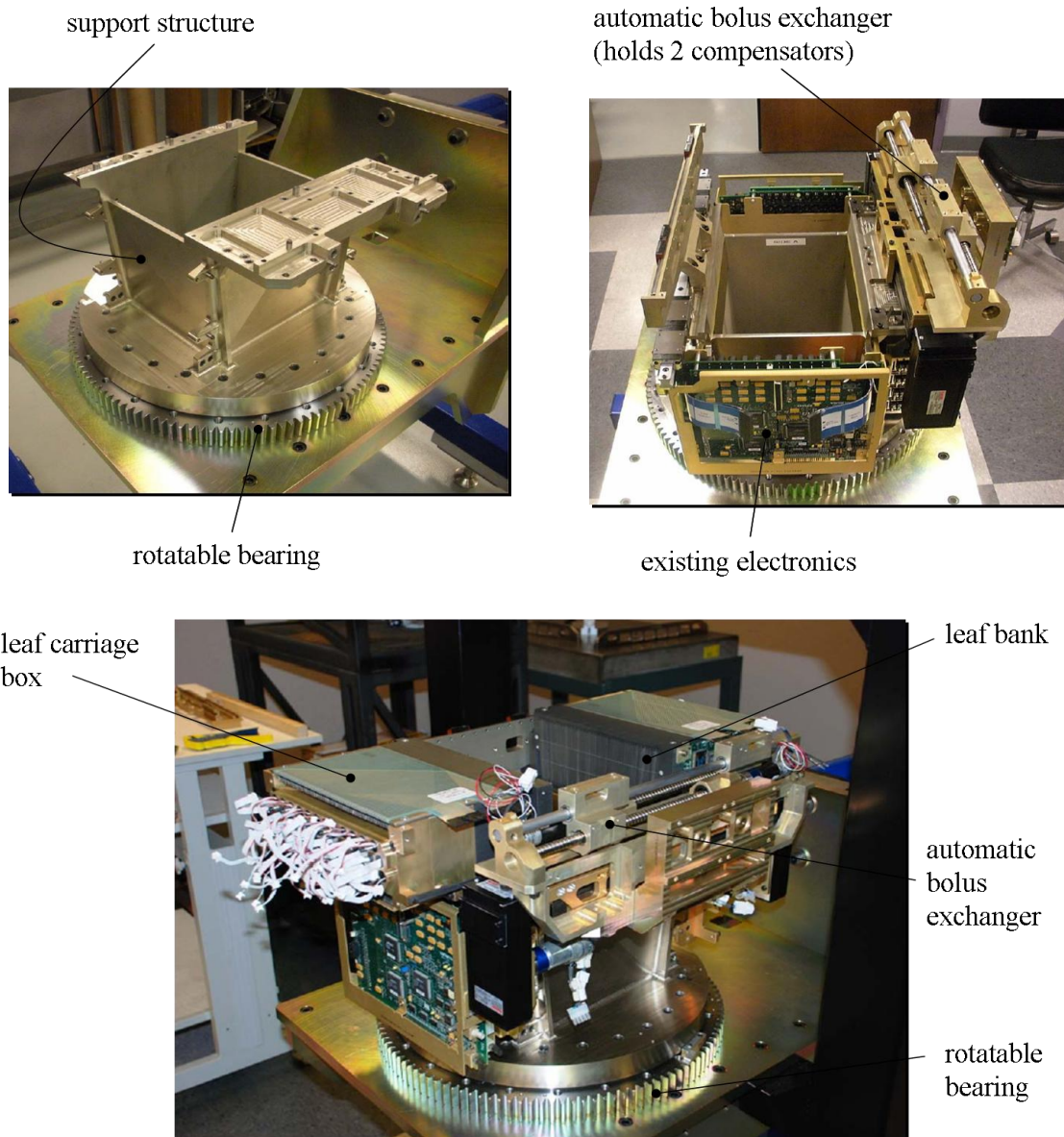leaf bank

automatic
bolus
exchanger

rotatable
bearing

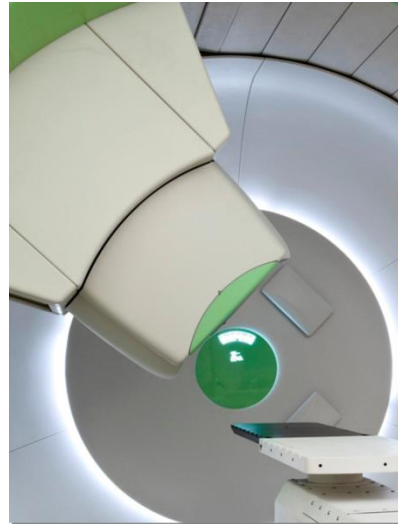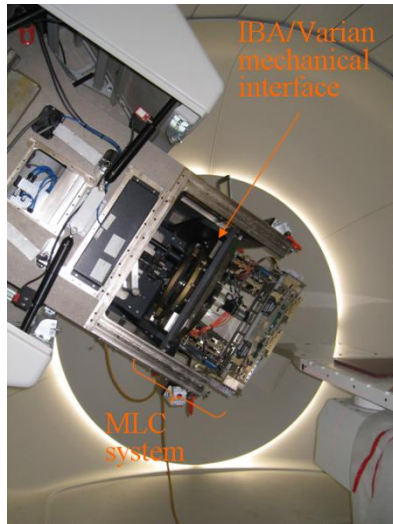Figure I.11. Photos of the MLC system in various stages of assembly.

16

Figure I.12. Photos of the MLC system mounted on the IBA nozzle prior (*left*) and subsequent (*right*) to adornment with beautifying covers.
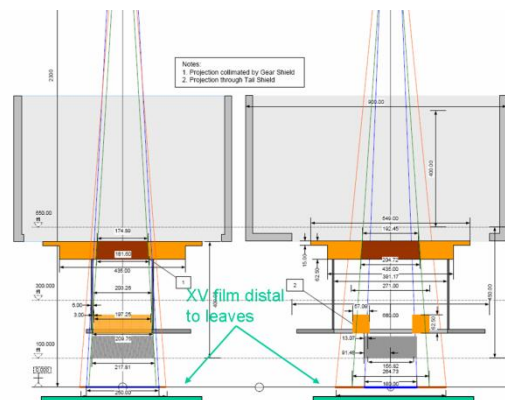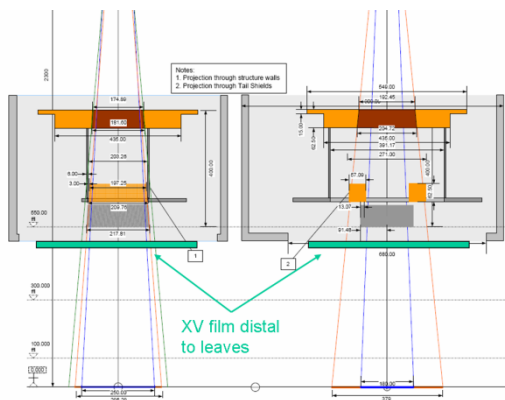
Figure I.13. Cut-away illustrations of the MLC system maximally (*left*) and minimally (*right*) retracted within the IBA nozzle, showing the locations of radiographic film used for leakage testing.
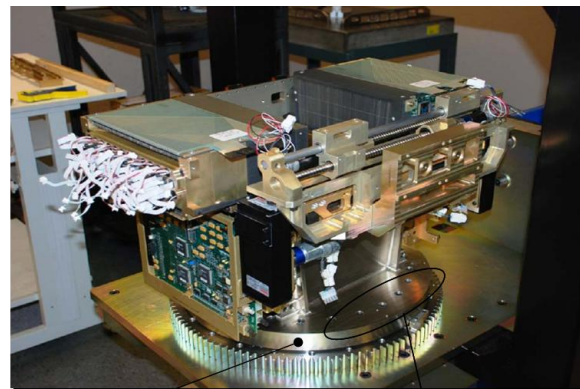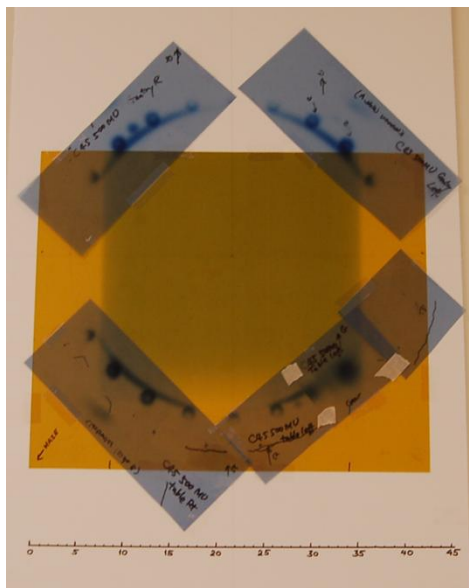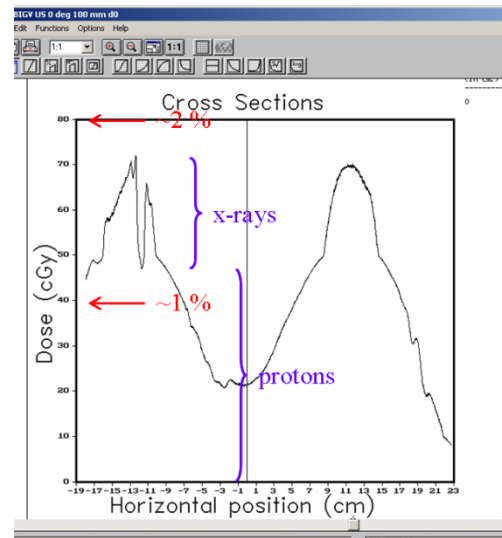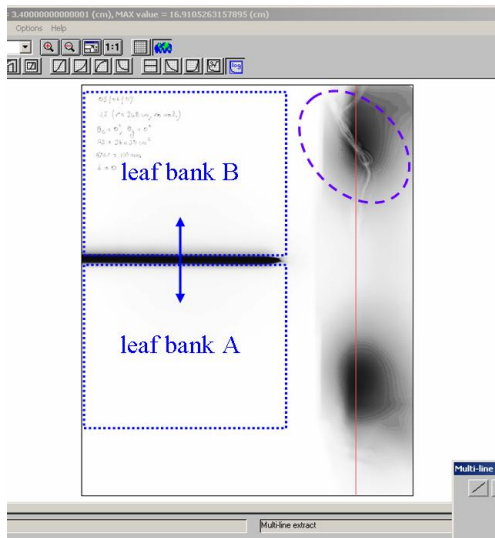
Figure I.14. Regions of clinically-significant leakage discovered on radiographic film downstream of the closed-leaf, minimally retracted MLC system, shown with respect to the positions of the leaf banks (*top left*), together with the dose profile along the vertical red line inscribed on that film (*top right*); and origins of the leakage traced via radiochromic film (*bottom left*) to inadequately-shielded bolt holes in the bearing (*bottom right*).
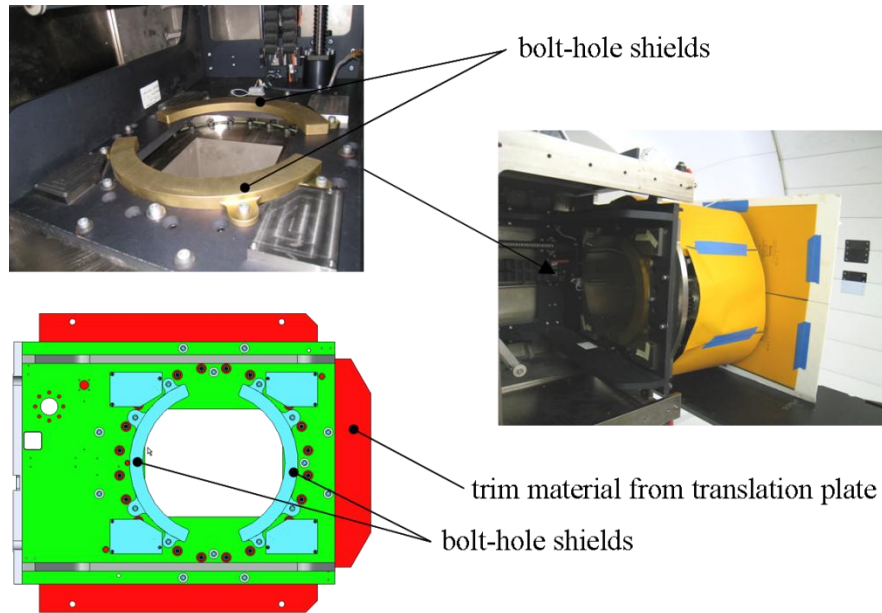
Figure I.15. Resolution of the bolt-hole leakage: bolt-hole shields added upstream of the Varian/IBA translation plate with the additional weight contributed offset by sloughing material from that plate.
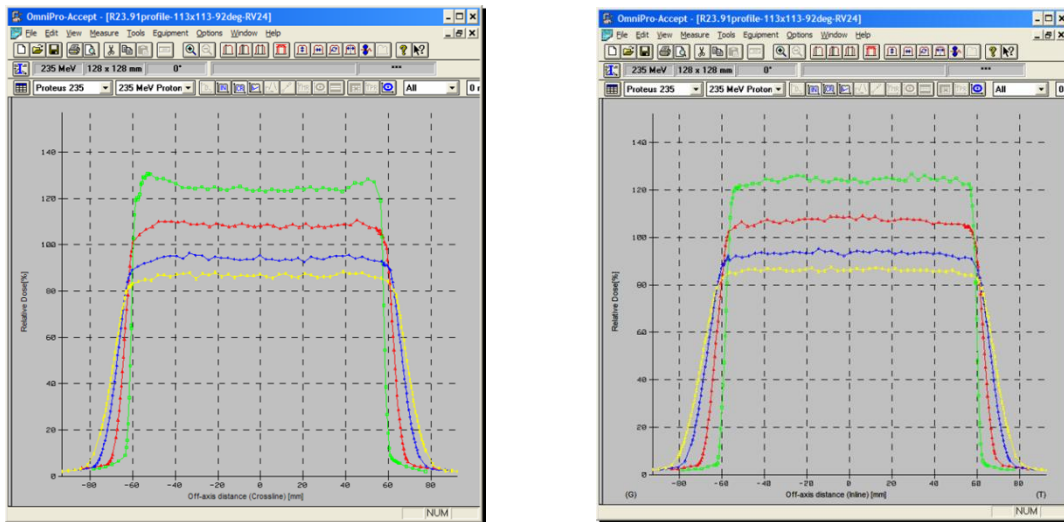
Figure I.16. Measured in-air crossline (*left*) and inline (*right*) transverse profiles at four locations downstream of a square aperture formed by the MLC leaves.
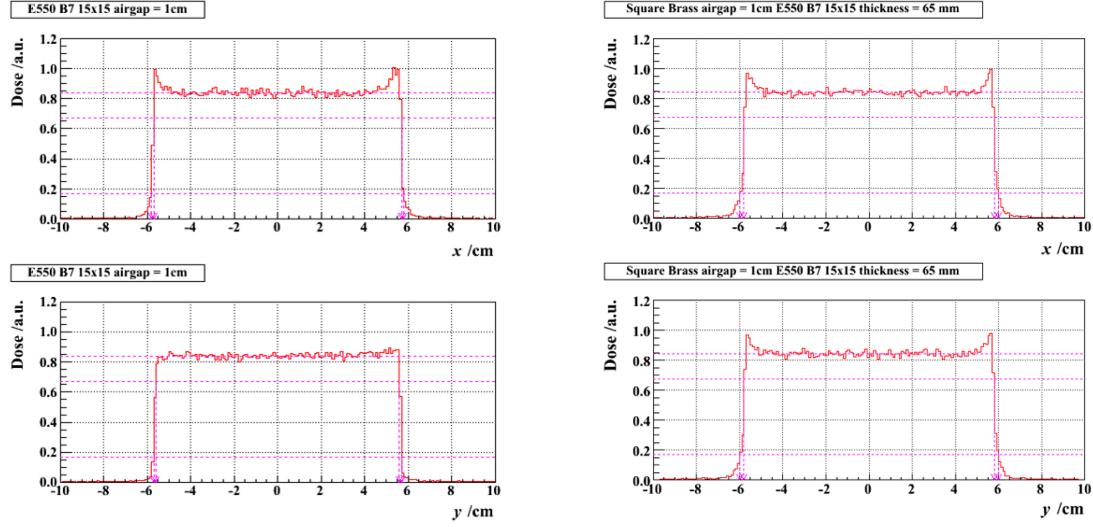
Figure I.17. Monte-Carlo-simulated in-air crossline (*top*) and inline (*bottom*) transverse profiles downstream of a square aperture formed by the MLC leaves (*left*) and by a brass aperture (*right*).
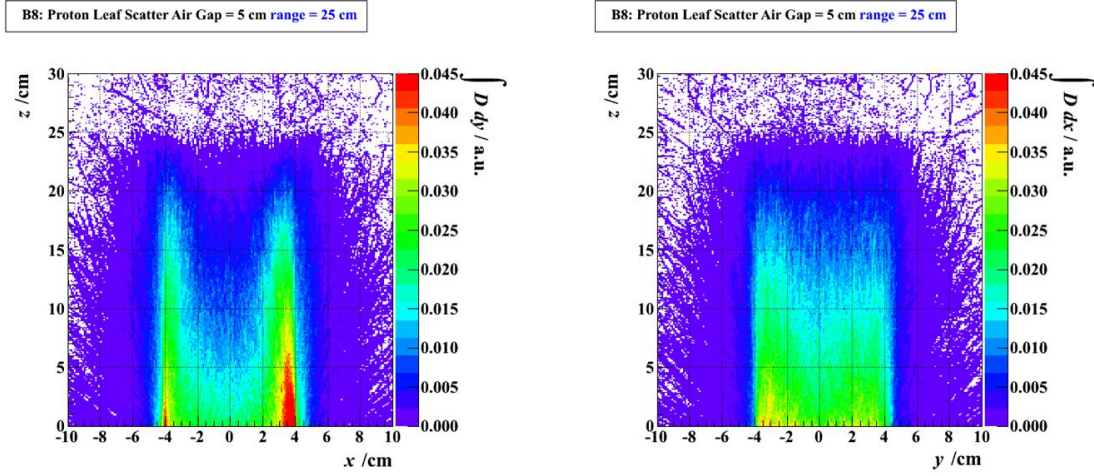
Figure I.18. Monte-Carlo-simulated dose distributions downstream of a square aperture formed by the MLC leaves due solely to protons flagged as having interacted in the leaves and scattered back into the field.
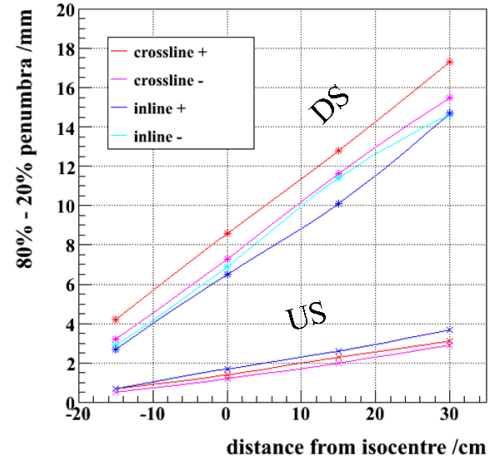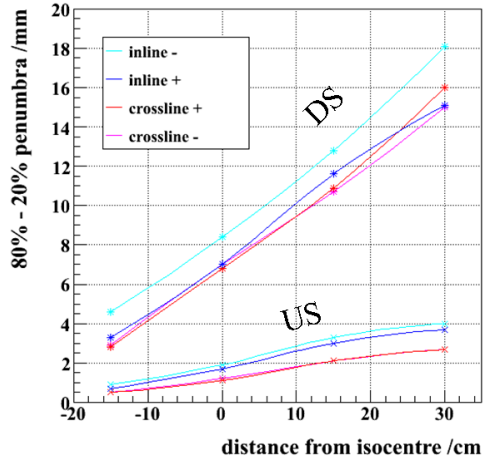
Figure I.19. Measured in-air penumbra across the four sides of a square field shaped by the MLC as a function of position along the beam direction for a double scattered and a uniform scanned field with an MLC rotation angle of 0° (*left*) and 90° (*right*).

Phase II: Development of a Scanned Proton Beam System for Proton Radiotherapy

Scan Optimization

Software code was developed by Josh Scheuermann and Mark Ingram to cover a PTV with PBS targets, to calculate dose kernels for each of those targets, and then to optimize the number of protons for each target in attempt to fulfill a given list of constraints. Two optimization algorithms were implemented: Cimmino and a standard gradient method. The Cimmino algorithm is a feasibility method suited to the radiation therapy inverse problem (Censor et al. 1988).

The Cimmino optimization for a single-field prostate plan with 1000 protons per spot takes about an hour to converge. It requires about 500 iterations, (each iteration involves projections onto all the constraint subspaces) for convergence. The convergence behavior is shown in the next figure.

Figure: Convergence of the Cimmino spot-weight optimization algorithm for the single-field IMPT prostate plans shown in previous figures. The optimization converges after about 500 iterations, which takes 3 hours.
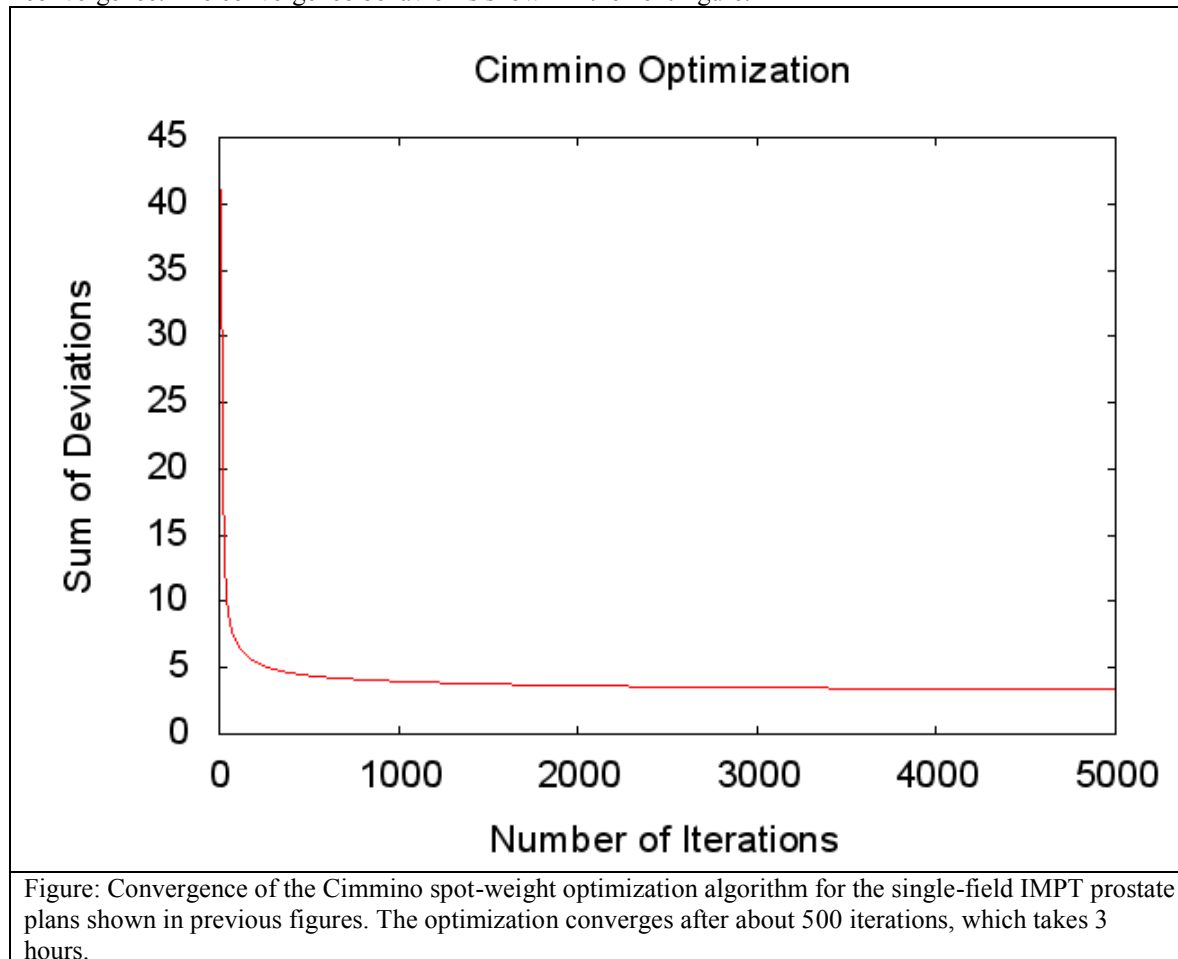
For the calculation of the dose kernels, Geant4 was used (Agostinelli et al. 2003). In Geant4, G4PhantomParameterisation is a relatively new class that provides an algorithm designed for fast navigation of particles through regular voxelized geometries. This is the fastest navigation algorithm available in Geant, and does not have a large extra memory requirement. Since CT datasets are voxelized structures, the G4PhantomParameterisation class is well suited to the task of constructing a patient geometry from a CT dataset. Previously our group had used G4SmartVoxel for navigation, which builds a 3D grid so that the location of voxels can be retrieved quickly, but requires a lot of memory (order N^3) for the grid. For a typical CT dataset, the old method required about 2 GB of memory. With G4PhantomParameterisation, the same geometry requires only 300 MB, with comparable execution times. The resulting dose kernels thus have resolution equal to that of the CT scanners: 1 mm x 1 mm x 3 mm.

A study was done to find a suitable number of protons per spot, and eventually a value of 1000 was selected. The plan shown in the next figure was optimized using kernels with 1000 protons per spot. Uniformity of dose to the PTV is now +/- 15%.
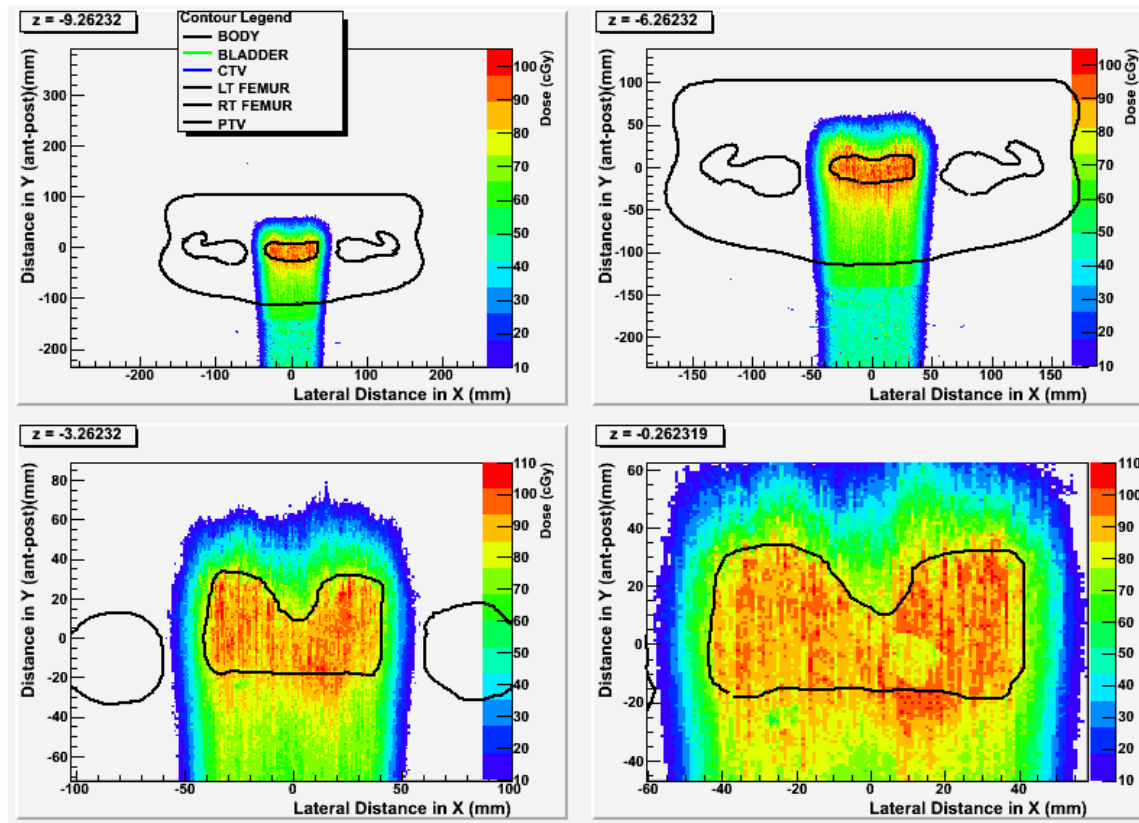
Besides the use of G4PhantomParameterisation, the CT to Geant4 geometry conversion was improved by increasing the density resolution. Instead of mapping the Hounsfield Units (HU) into density bins (of width 10 kg/m^3), we now define a unique density for each Hounsfield Unit. The density resolution is thus much higher, at the cost of a little over 10 minute overhead at the start of each simulation process to construct the table of materials, which typically contains over 3000 unique materials for a patient CT dataset. The material compositions are based on data from ICRU Report No. 46 (1992), as summarized in the table below. Large HU values (above ~1600), are difficult to map to a unique atomic composition, and should be chosen on a per patient basis given some knowledge about any implants they might have.

Material	H	C	N	O	Na	P	S	Cl	K	Fe	Mg	Ca
Air			0.7	0.3								
Lung, Inhale	0.103	0.105	0.031	0.749	0.002	0.002	0.003	0.002	0.003			
Lung, Exhale	0.103	0.105	0.031	0.749	0.002	0.002	0.003	0.002	0.003			
Adipose	0.114	0.598	0.007	0.278	0.001		0.001	0.001				
Breast	0.109	0.506	0.023	0.358	0.001	0.001	0.001	0.001				
Water	0.112			0.888								
Muscle	0.102	0.143	0.034	0.710	0.001	0.002	0.003	0.001	0.004			
Liver	0.102	0.139	0.030	0.716	0.002	0.003	0.003	0.002	0.003			
Trabecular Bone	0.085	0.404	0.058	0.367	0.001	0.034	0.002	0.002	0.001	0.001		0.044
Dense Bone	0.056	0.235	0.050	0.434	0.001	0.072	0.003	0.001	0.001		0.001	0.146

The calibration of CT Hounsfield unit to material type and density was improved early this past report year to allow a wider range of tissue densities: the number of density bins for the phantom materials was increased by a factor of 10. Additionally, a water equivalent CT calibration was implemented that can be used to investigate some of the shortcomings of Eclipse, which uses water equivalent materials everywhere for its dose calculations. Use of the water equivalent calibration helped to understand the origin of some dose inhomogeneities in the Cimmino spot weight optimization code, as described below, but we intend to implement a more suitable CT calibration like that developed by Paganetti et al. (2008), which only ne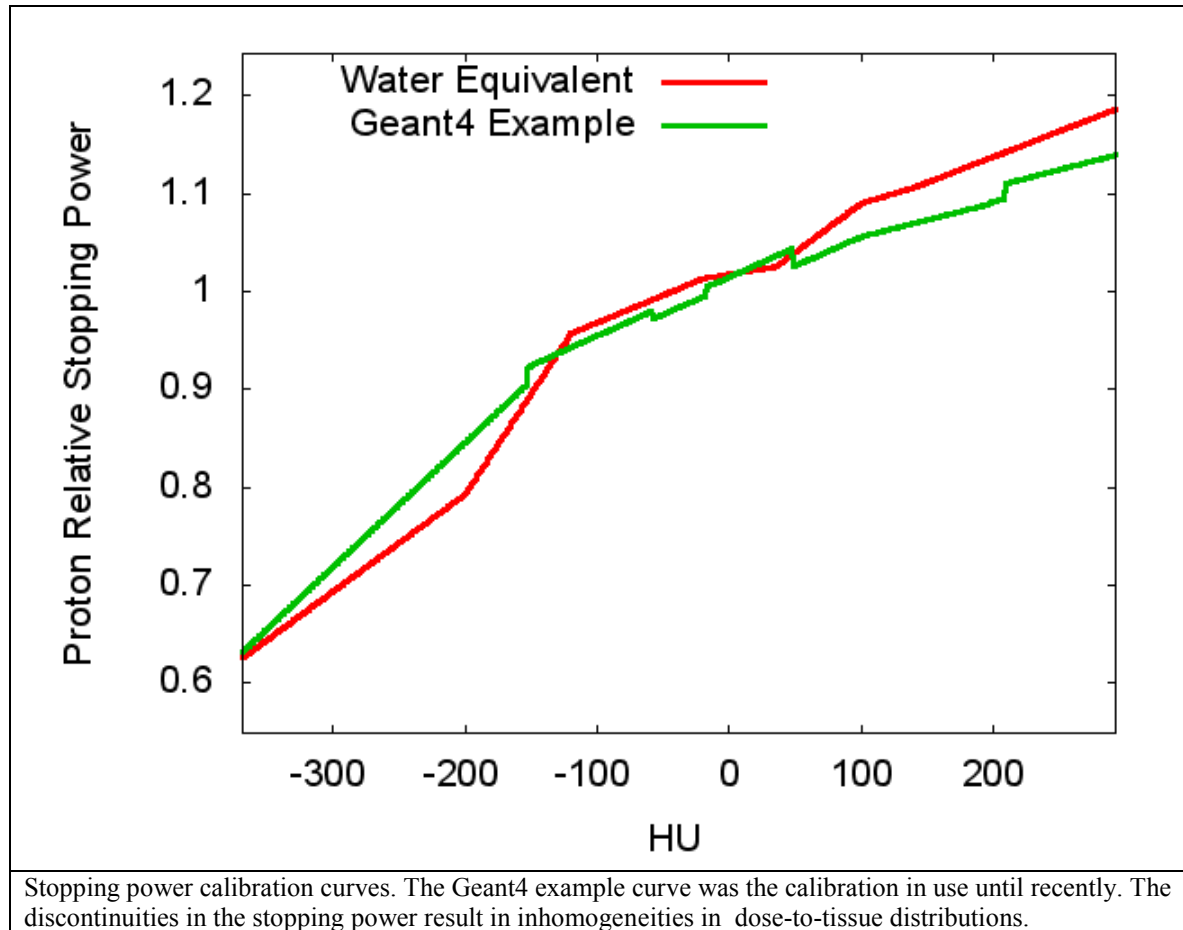eds to be adjusted to account for differences between CT scanner hardware and scanning protocol. The file format for Monte Carlo generated kernels files was changed. This permits full-resolution dose kernel data to be written to disk, facilitates parallel calculation of dose kernels, and allowed multi-field spot-weight optimization. The kernel generation code was underestimating the energy needed to reach targets in the patient phantom. This is presently worked around by adding energy layers distal to the PTV, and could be improved further as a student project, by working out a relationship between the particle range in the continuous slowing down approximation, and the depth of the Bragg Peak. Additional spots are also added around the target volume to ensure coverage. Improvements to the spot weight optimization code were necessary mostly to reduce the memory requirement in order to allow multi-field optimization. By improving memory management by our implementation of the Cimmino algorithm, we reduced the optimization time by a factor of 8. We also expanded the dose objective capabilities for the Cimmino optimization: the planner may now specify single-ended inequality constraints in addition to the double-ended inequalities from before. Single-ended constraints are useful to lower the patient integral dose, for example, by specifying that all tissues outside the treatment volume be below some threshold.

The next figure showns a more realistic two-field proton plan, optimized using the Cimmino implementation at Penn. This optimization gave a cold spot in the PTV, which appears yellow in the lower right dose slice of the next figure. The optimizer has turned up the intensity of spots to that region, resulting in a hot ring around the cold spot. It was determined that the Hounsfield unit values corresponding to the voxels in the cold spot are higher (greater than 50) than the rest of the PTV. The CT dataset was examined, and there is no anatomical feature corresponding to the cold spot. In this case, the cold spot is an unrealistic artifact resulting from the stopping power calibration.
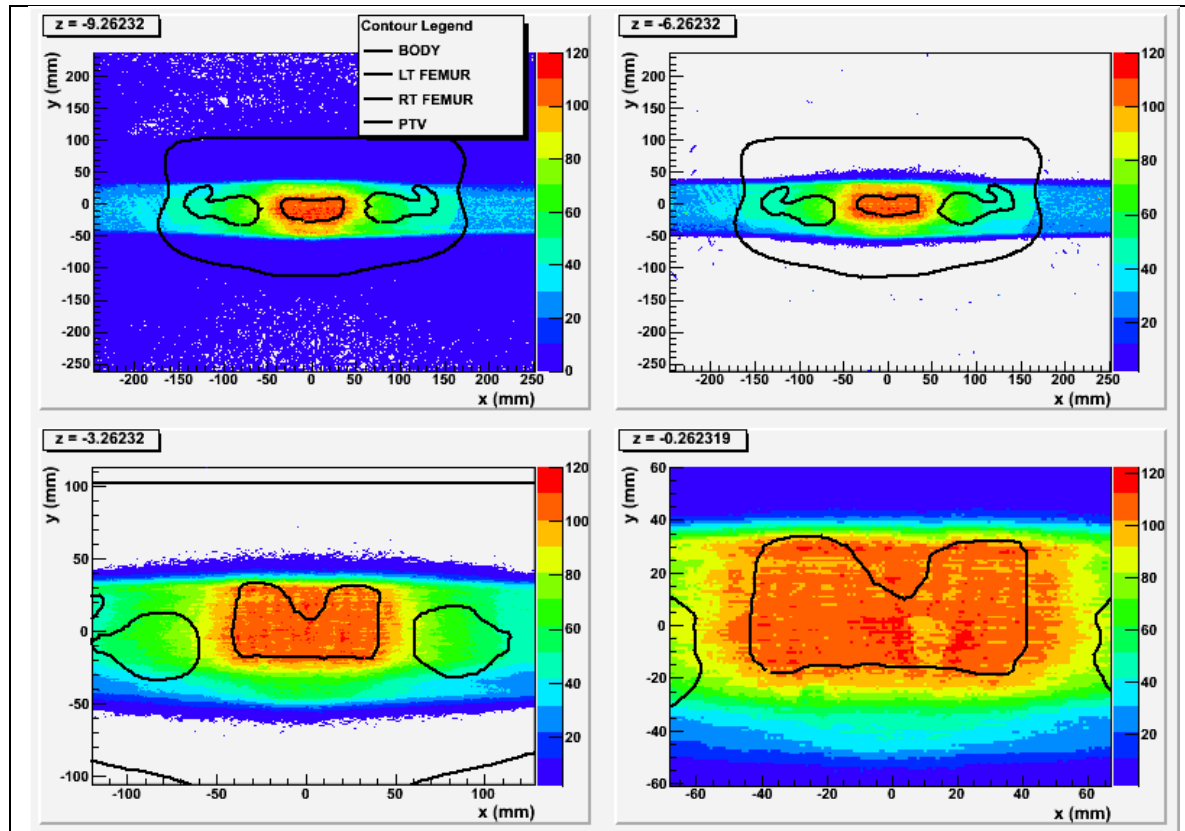
Two-field IMPT prostate plan. In the lower-right slice of the dose colorwash, a cold spot (yellow) can be seen in the PTV. The spot size is 1 cm FWHM at this depth. The intensity of spots near the cold spot have been increased by the optimization in order to bring the dose closer to prescription (100 Gy), resulting in a hot ring balanced by a cold center of dose. The center is cold because of a discontinuity in the HU-to-stopping-power calibration curve.

The stopping power calibration is plotted below. The calibration in use is the calibration contained in the Geant4 DICOM example code, but with a factor of ten higher density resolution. The full range of Hounsfield units is divided into 10 subranges, and a unique material composition is assigned to each subrange. The density also varies as a function of the Hounsfield unit, with a unique density for each HU value. When the proton stopping power that results from the Geant4 example calibration is plotted, it can be seen that there are discontinuities in the stopping power curve. The discontinuity at about HU = 50 is responsible for the cold spot in the figure above. The material in the cold spot has a lower stopping power than the surrounding tissue, so the dose deposited there is lower.

Stopping power calibration curves. The Geant4 example curve was the calibration in use until recently. The discontinuities in the stopping power result in inhomogeneities in dose-to-tissue distributions.

A water equivalent stopping power calibration was implemented, in part to verify that the cold spot would be resolved. The water equivalent calibration could also be used to determine the effect of ignoring material inhomogeneities in the patient, as is done by Eclipse. Using the water-equivalent calibration, we found improved dose homogeneity to the PTV, as shown in the next figure. The coverage to the PTV for the plan on the left is very good, with the entire PTV receiving >= 80 Gy as prescribed.
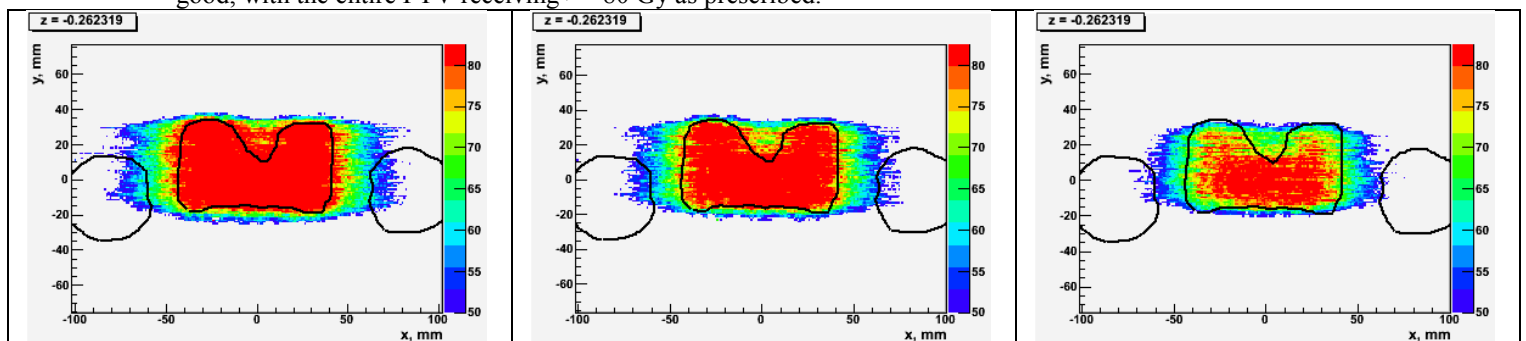
For a two-field IMPT prostate plan, effect of the priority parameter for dose constraints. Each optimization has PTV >= 80 Gy and other tissue <= 50 Gy objectives. On the left, the priority of the other tissue objective is 0.01 (relative to the PTV objective), in the middle the priority is 0.1, and on the right the priority is 1 (same priority as the PTV objective). The dose to the femoral heads can be reduced by increasing the priority of the body dose objective, at the cost of poorer PTV coverage: the dose to the periphery of the PTV on the left is the full prescription dose (80Gy), in the middle it is 75 Gy, and on the right only 65 Gy.

The other plans in the figure above show the effect of increasing the priority of a maximum dose objective for the tissue outside the PTV. An objective that dose outside the PTV be <= 50 Gy was included in the optimization, and the priority successively increased. The dose to femoral heads should typically be kept below 50 Gy. Increasing the

26

priority of the normal tissue objective lowers the dose to the femoral heads, at the cost of some of the PTV periphery does not receive the full prescription dose.

Maura Kirk wrote a C++ class to write dicom RT Dose files. That allowed dose scored on the voxelized patient CT geometry to be written to a dicom file that could then be opened by a dicom viewer. We used Velocity AI to open our dose files, calculate DVHs, and perform registrations and deformations. Velocity can open the dicom structure files, and plot the physician-drawn contours with the CT and dose data. An example is shown in the next figure, which is the prostate case above, optimized with Cimmino using Monte-Carlo calculated pencil beam kernels.
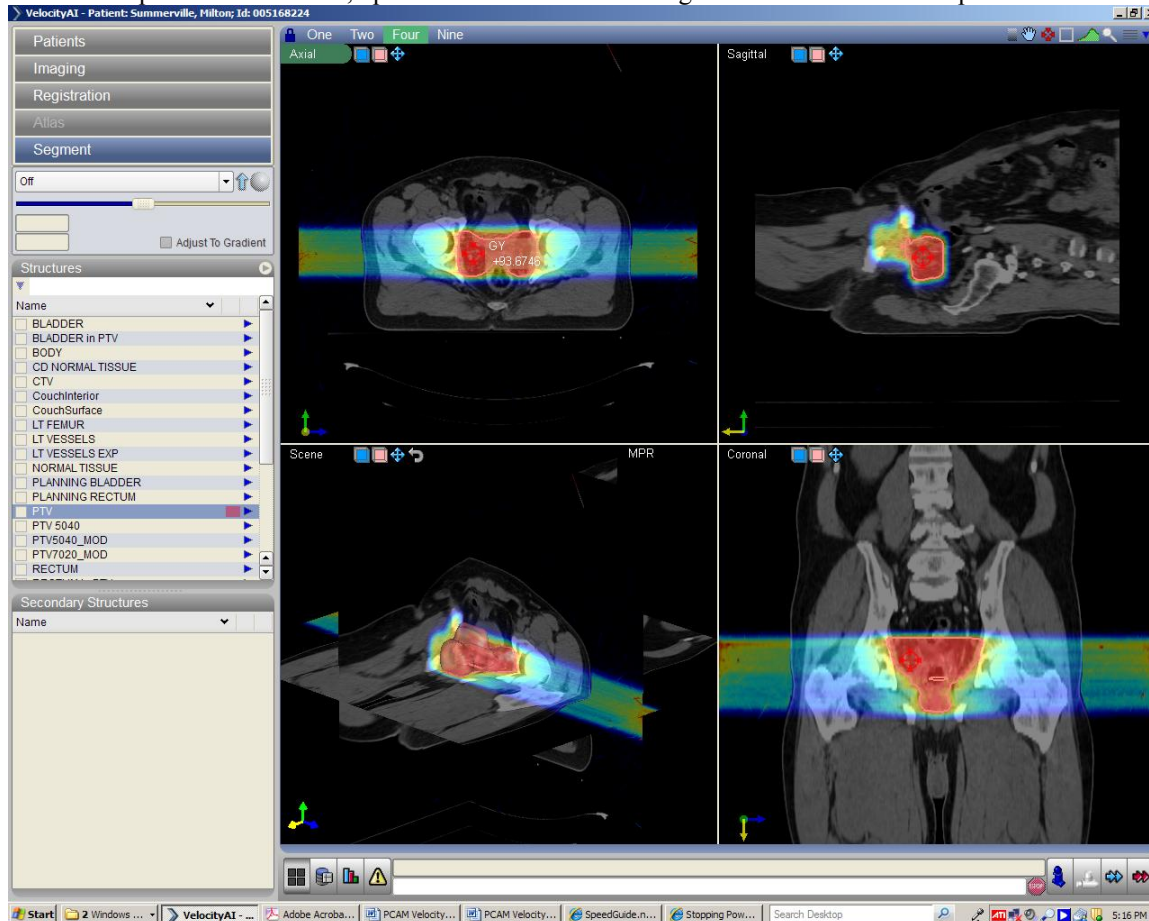
We were concerned with the ability to delivery sufficient proton dose at shallow depths due to the fact that the IBA system cannot deliver a beam to the nozzle with less than 4 cm range. We investigating the use of ridge filters and range shifters as a possible solution.

A student in the Master's of Medical Physics program, James Durgin, worked on simulations to determine the effect of range shifters and ridge filters on scanned pencil beams. One ridge filter design consisted of four stacked boxes. The widths of the boxes were adjusted individually to create a more uniform Spread-Out-Bragg-Peak (SOBP). By using a 100 MeV pencil beam passed through a PMMA ridge filter with dimensions found in the table below, a SOBP of 9mm is created within +/- 1% of the desired dose. This design also retains a steep distal dose falloff. The observed 80-20% distal falloff increases less than 0.5 mm when comparing the 100 MeV ridge filter SOBP to an unobstructed pencil beam.

Water Equivalent Material	Distance in Terms of Ridge Peak Spacing
1.1 cm	12%
0.825 cm	22%
0.55 cm	32%
0.275 cm	55%
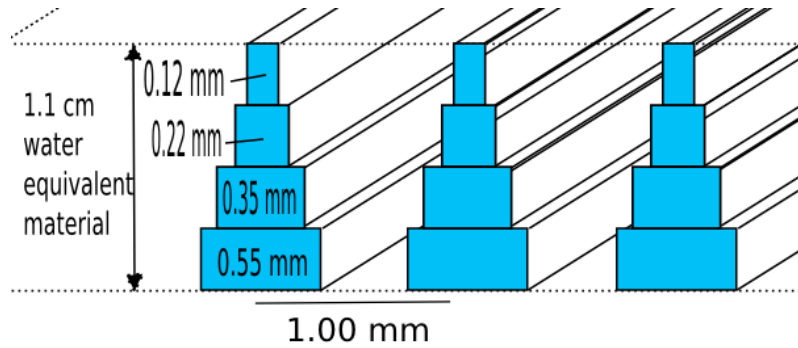
Figure: Ridges composed of stacked boxes.

The improved box design was tested using several materials, positions in beam nozzle, and beam energies. Since the filter is defined by water equivalent depth, PMMA, polyethylene, and aluminum all produced approximately the same SOBP. A similar SOBP was also observed when the proximal edge of the ridge filter was placed on the surface of a phantom or at 25, 37, and 50 cm from the isocenter at 10 cm depth. As beam energy increases, a significant change in the SOBP is observed. This change is greatest at high energies where it is unlikely the ridge filter will be used and is relatively small in the range that would be used to treat shallow tumor depths.
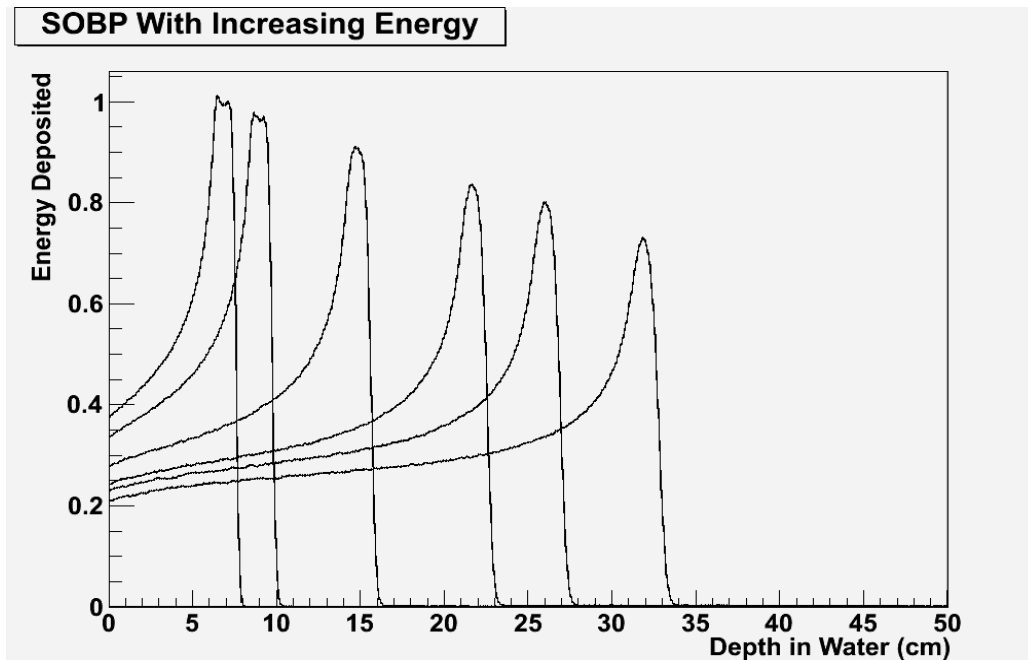
Figure: Changing SOBP with increasing energy for a 1.1 cm water equivalent ridge filter made of PMMA and placed 50 cm from isocenter. From left to right: 100, 115, 150, 185, 205, and 230 MeV.

The lateral penumbra for ridge filters composed of different materials, positions in beam nozzle, and thicknesses were also modeled. Increasing the distance from patient of the ridge filter significantly increased penumbra, as shown in the next several figures, as did increasing the overall thickness of the ridge filter. Because higher Z materials result in more lateral spreading of the beam, PMMA had a slightly degraded penumbra compared to polyethylene (< 0.5% larger), and aluminum gave a penumbra that was about 3% larger than PMMA.

28
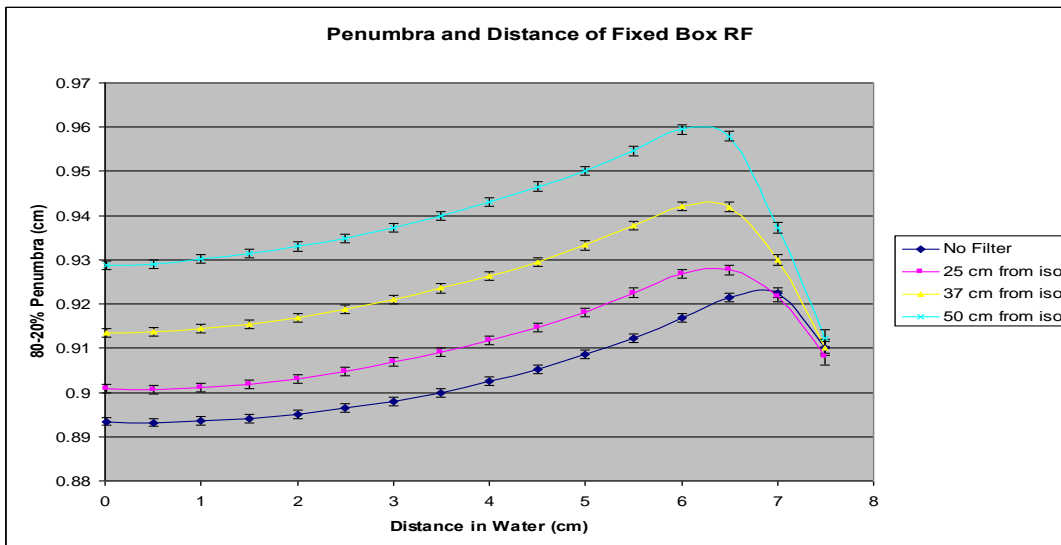
Figure:. Bottom to top: penumbra without RF and RF 25, 37, and 50 cm from isocenter.
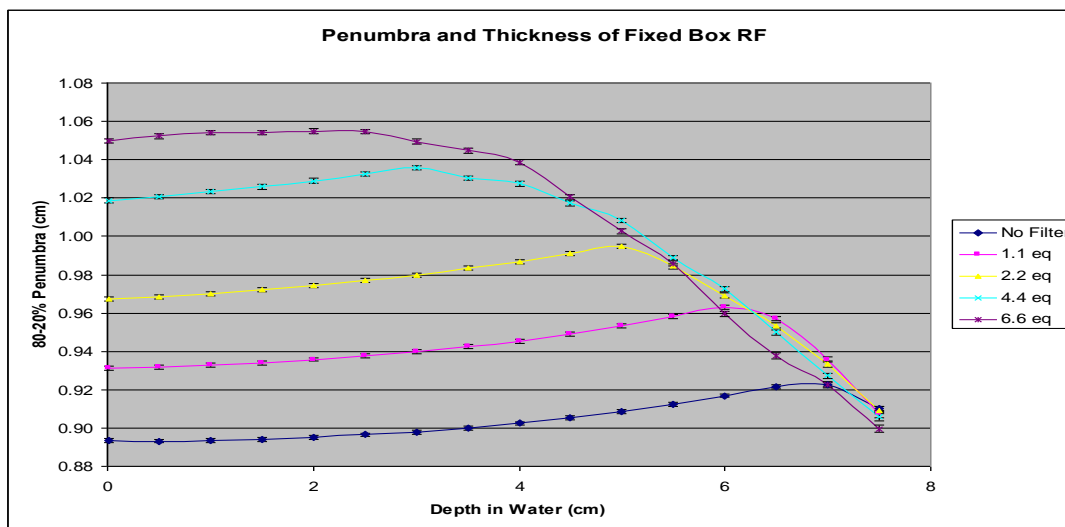
Figure: Bottom to top: penumbra without RF and RF of 1.1, 2.2, 4.4, and 6.6 cm water equivalent PMMA.
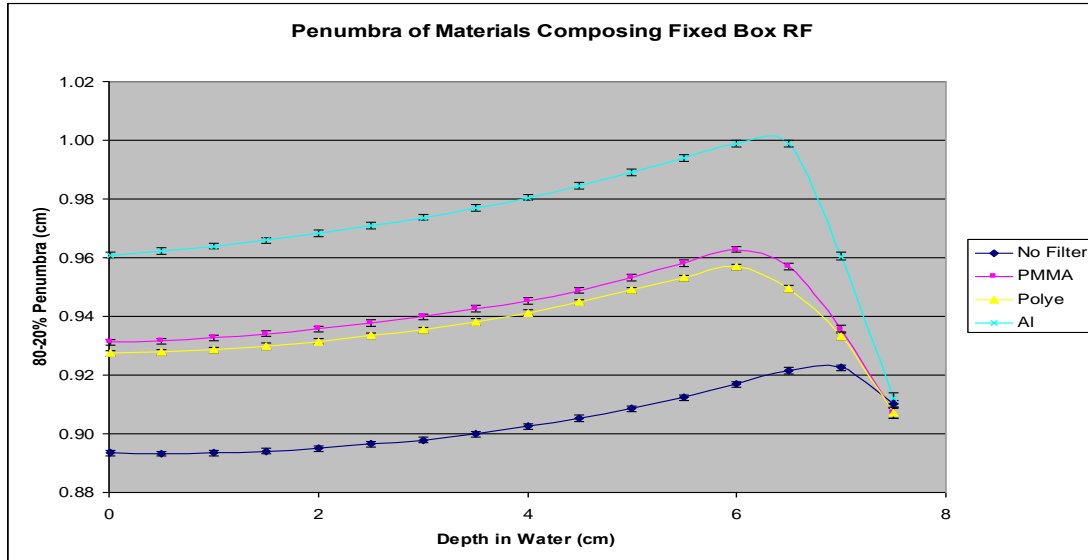
Figure: Bottom to top: penumbra without RF, for polythene, PMMA, and aluminum.

Ridge filters were also compared to range shifters of the same materials, positions, and thicknesses. Ridge filters had a consistently smaller 80-20% penumbra than range shifters. This difference is dramatic for aluminum and as distance and thickness increases.

James arrived at a design for a ridge filter that produces a flat spread out Bragg peak (SOBP) of about 8 mm width. The design is shown in the following figure.
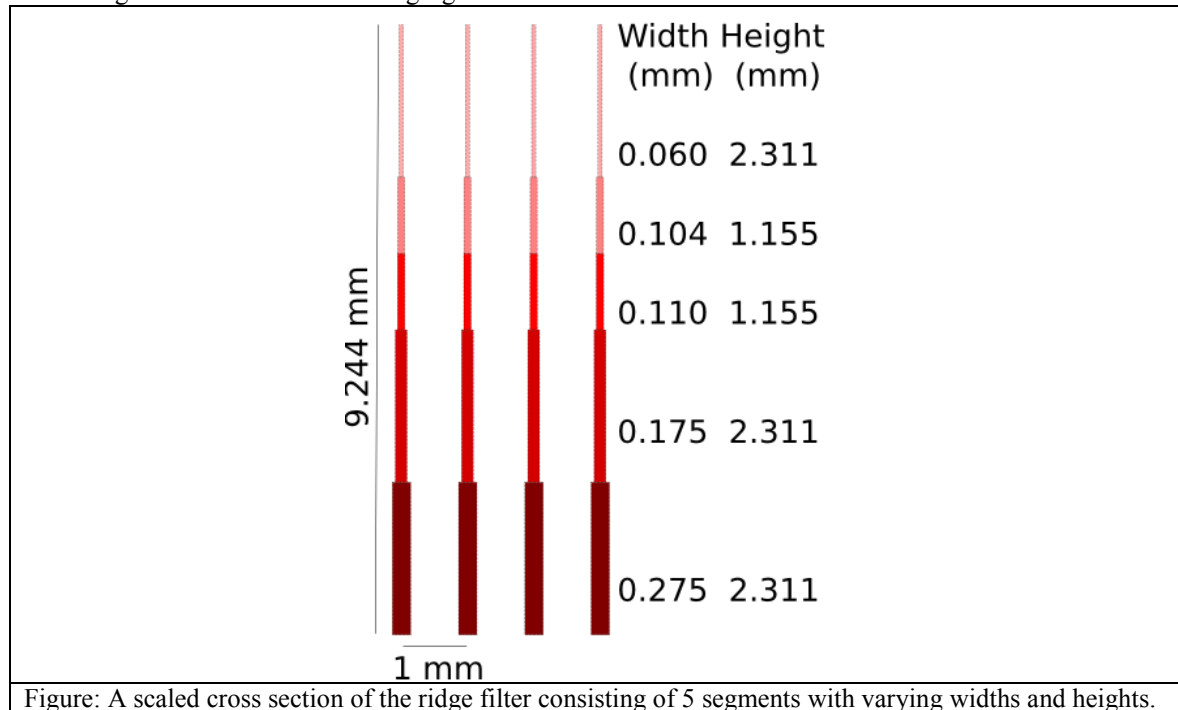
Figure: A scaled cross section of the ridge filter consisting of 5 segments with varying widths and heights.

That design would be difficult to machine, because of the ridges with thicknesses less than 100 um. It is really the ratio of the width of each ridge to the width of the entire pattern that is responsible for creating the flat SOBP. That is, the entire design can be scaled in the dimension of the filter widths, as long as the scale of the filter remains small compared to the size of the beam spot that strikes the ridge filter, to avoid having any shadow from ridge filter in the dose distribution. James looked at the dose profile for pencil beams delivered through the ridge filter design with the lateral dimensions scaled by a parameter s, labeled "RF Multiplication" in the following figure. With a scaling of

about 4 or larger, one can start to see a shadow left by the ridge filter in the beam profile. The factor of 4 is valid for a ridge filter mounted close to the patient. Because additional lateral scatter smears the shadow, James found that for a ridge filter mounted 50 cm from isocenter, a scaling factor of 6 produced a good profile. Thus, a ridge filter with smallest ridge dimension about 250 um could be used to produce an SOBP in our beam line, and can probably be machined on the milling machine that produces our compensators.

Maximum relative error calculated from a Gaussian fit of a lateral X profile. Each point has been calculated from 5 million events and blue line represents the average of multiple seeds. The maximum relative error of an unobstructed beam is represented by a ridge filter multiplier of 0.
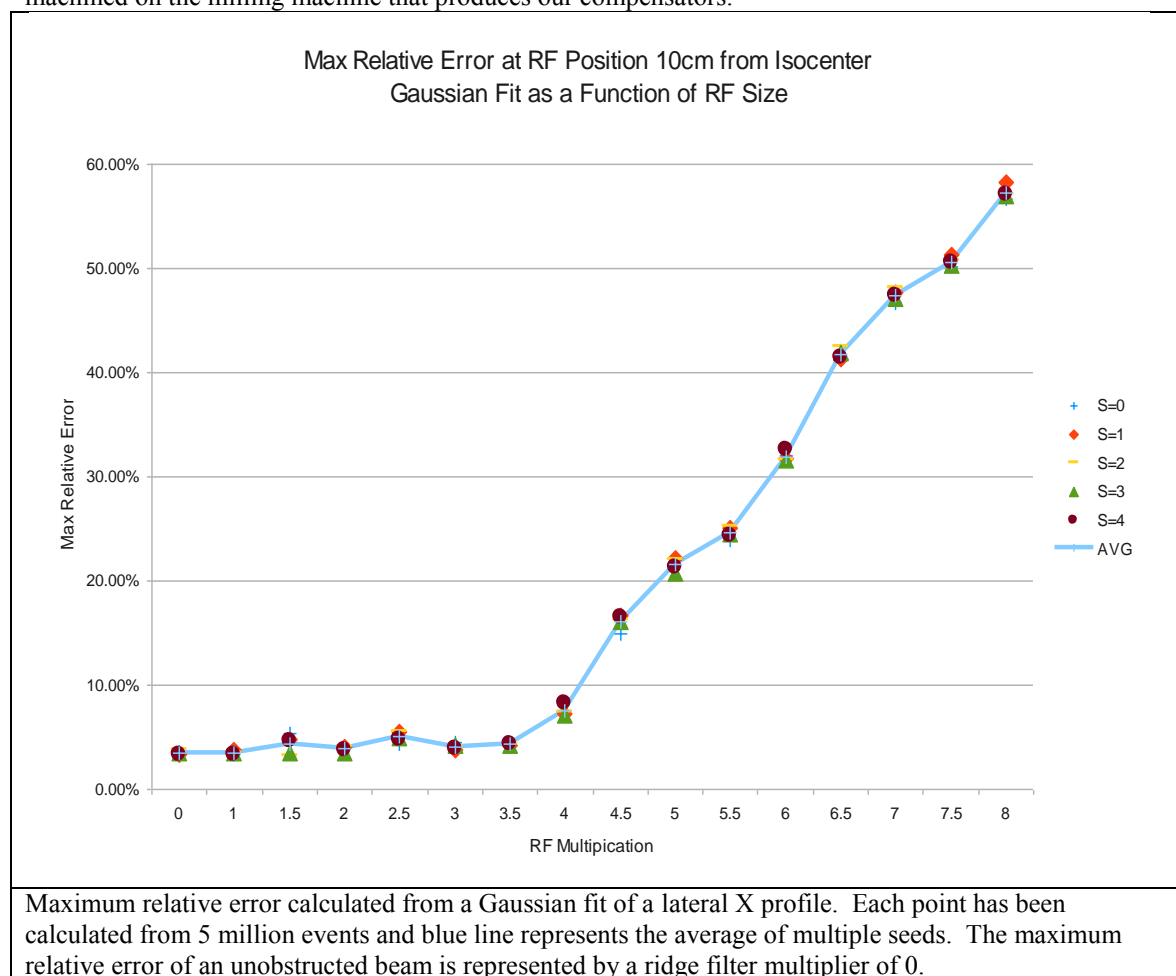
James Durgin also studied methods for treating shallow tumors with pencil beam scanning. He simulated range shifters for shallow depths, and investigated the effect of different materials and different mounting positions on the beam penumbra. James commissioned the Eclipse treatment planning system with simulated commissioning data, and studied plan cases with the beam modification devices. Test treatment plans were generated to determine coverage for a prostate and brain case. These test plans were used to determine the clinical impact of various configuration parameters including use of range shifters/ridge filters, lateral spot spacing, and energy layer spacing. Using energy layer spacing of twice range sigma, the parallel opposed beams for the prostate case each required 25 energy layers for the unobstructed beam. With the IBA ridge filter, this decreased to 21 energy layers. The ridge filter also introduced lateral scattering, which decreased the total number of spots from 4481 to 3687 and as a result reduced plan quality.

For a shallow brain case, a 7.5 cm water equivalent range shifter showed promise over an unobstructed beam. The use of the range shifter decreased energy layers by ~35% both per field and total energy layers per plan. In this particular case, the range shifter would have decreased treatment time by approximately 1.5 minutes per day of treatment assuming 3 seconds to switch between energy layers.

Development of Dosimetry Systems for Scanned Beams: Three-Dimensional Dosimetry for Proton Therapy using Micromegas Detectors

Derek Dolney, in collaboration with Professor Robert Hollebeek from the Physics Department at the University of Pennsylvania, has developed a gas chamber layer based on the Micromegas technology (Giomataris et al. 1996, Giomataris 1998, Giomataris et al. 2006, Giomataris 2006, Titov 2007). Micromegas was developed for high-energy physics experiments at CERN. There the conditions are similar since the CERN chambers also see extremely high particles rates. However, in proton therapy one is typically interested in integrated measures (dose) rather than counting individual pulses. Therefore, the readout electronics for the proton therapy adaptation will be somewhat different. Derek and Professor Hollebeek have succeeded in developing a working two-dimensional Micromegas layer and demonstrated that it provides better (2D) spatial and time resolution than any other device currently available for proton therapy beam measurements. A publication was submitted to a Special Issue titled "Detectors for Hadron Therapy: Operational Principles, Techniques, and Readout" of the journal Physics Research International. The manuscript is expected to be published in December and is attached as an Appendix to this report and will be referred to below as the "PRI manuscript". Derek will give an oral presentation of that work at the 2012 Nuclear Science Symposium, Medical Imaging Conference in Anaheim at the end of October.

The final goal of the proton dosimetry project is to develop a new device for proton dosimetry with resolution in all three spatial dimensions, with good time resolution, that can be used to characterize rapidly scanned proton pencil beams. A schematic is shown in the next figure. Multiple layers of the two-dimensional Micromegas will be stacked to provide full 3D dose resolution. In addition, the layer readout is fast, so that the device will in fact have fine time resolution. The device could be called a 4D dose monitor. Such a technology will be very valuable for room commissioning and QA, and for research projects involving advanced proton delivery techniques. Because proton therapy is just now becoming widespread, there is a lack of tools designed specifically for protons, but since proton
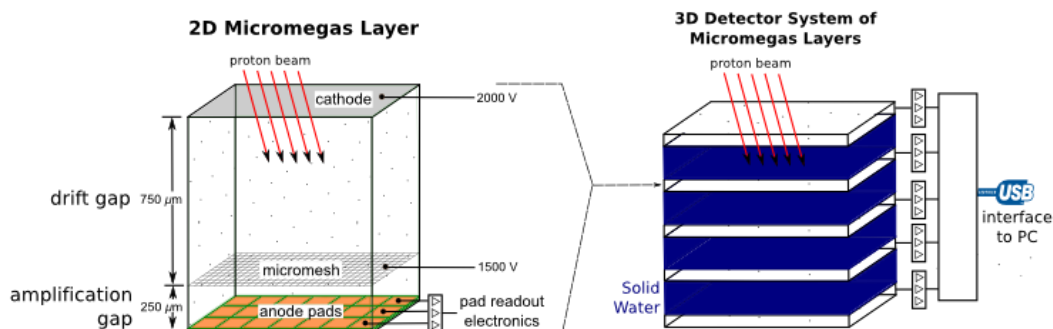
delivery equipment can modulate dose in full 3D, commissioning and QA hardware would ideally be 3D measuring devices. Currently in the clinic we use 2D technologies that were really developed for MV-scale photon therapy. This project aims to develop the 3D technology and thereby modernize the technology available for proton therapy beam measurements.

Here is summarized entire Micromegas development project. This is exciting research that will continue beyond the end of this award. Derek and Bob Hollebeek prepared and submitted an NIH R01 proposal using the preliminary data that was collected during the award period. That proposal will be reviewed in February or March.

Single Channel Prototypes

The conditions for a proton monitor are similar to those for inner vertex chambers at the CERN LHC since the CERN chambers see extremely high particle rates; therefore we have selected the initial gas for testing to be 70/30 Argon CO_2. This choice is based on having extremely low radiation ageing, fast drift velocity to clear the accumulated charge, no flammable components, short pulses, and good time and spatial resolution. These gases have been well studied and their properties are well known. The next figure for example shows the drift velocity at 0.75 kV/cm to be about 2 cm per microsecond. (Chang et al. 1992)
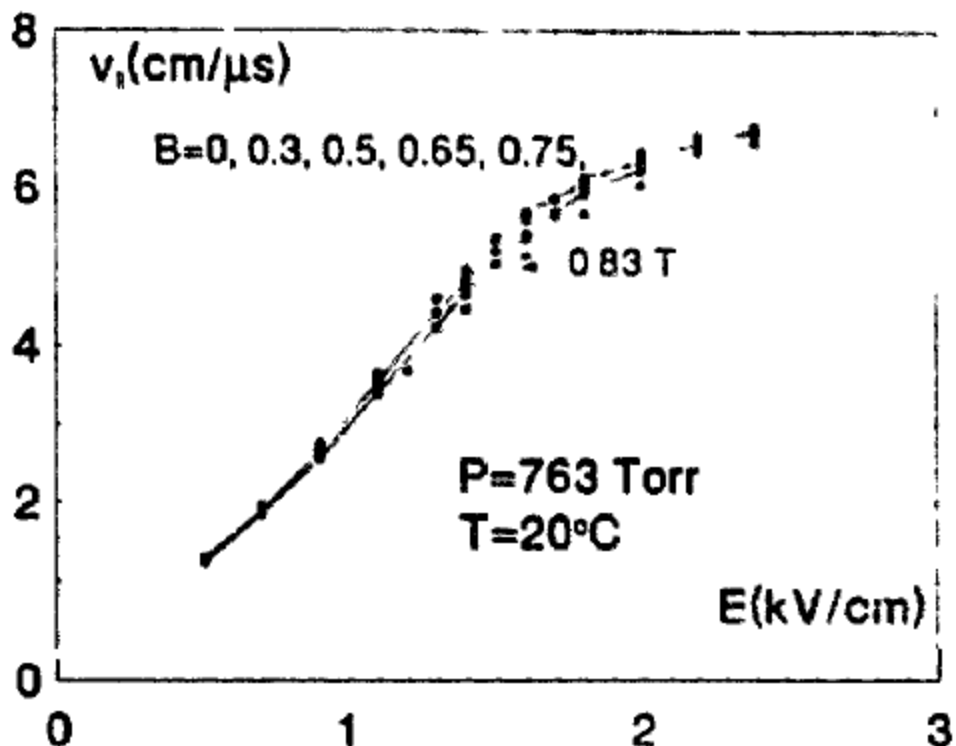
We completed the construction of a test system with gas supplies, high voltage systems, low noise preamps, oscilloscope, radiation sources, a pair of scintillators for using cosmic rays, calibration signals, and coincidence electronics for cosmic ray triggers. The test system also has a multi-channel analyzer and computer system for taking pulse spectra.

Chamber prototypes are constructed from modular planes and can be easily modified or combined together. The figure below shows a two gap prototype which was constructed from a pair of single gap systems

Operation in the proton and electron beams will require an adjustable gain in the gap of about 1 to 10. While gas gains of 10^4 to 10^5 are possible in these systems, since we are detecting relatively large currents rather than individual pulses, the required gain is much lower.

During Q1 2012, Derek and Bob Hollebeek studied various construction techniques for ionization and Micromegas chambers. Two designs were acheived that could be used to implement a wide gap (5mm) or small gap (1.67mm) ionization chamber using either a wire mesh stretched over a PVC frame or braised to a copper ring. They also developed a technique to produce a laminate of an insulating mesh and the wire mesh which could be used to produce chambers with a 250 micron gap. Example single-channel prototypes are shown in the next figures.

When under voltage, electrostatic forces eliminate any gap between the insulating mesh and the cathode surface. In the large gap chambers, the voltage on the wire mesh is positive and electrons drift toward the wires.

In a Micromegas hundred micron scale gap the mesh is at a negative voltage. Electrons drift toward the mesh due to a slightly higher drift potential then pass through the mesh and are amplified below it. This has numerous advantages for high rate environments since large numbers of positive ions are confined to the region below the mesh.

Measurements were performed with one of the single-gap Micromegas prototypes in proton room #2 using pencil-beam delivery. The detector was placed downstream of solid water. We hoped to measure a Bragg curve this way to demonstrate that the detector does not quench in the peak. The next figure shows the gain curve measured with prototype #2 in the proton Treatment Room #2. A single pencil beam of maximum energy (226.7 MeV) is delivered through the center of the prototype. The bias voltage is the potential of the top plate that defines the drift region. The mesh is held at 80% of the top plate (voltage divider). We achieve gains of 30 or so with this prototype. The bias voltage is limited by arcing inside the prototype. The amplification gap is defined by a 1.7 mm thick spacer ring of diameter 10 cm. At high voltage the mesh deflects towards the anode and eventually arcs. We are working on better ways to maintain uniform gaps of various thicknesses. One solution is to use a woven fiberglass or PVC screen. Bob has successfully laminated the screen to a copper cathode, but the gap is fixed to be the thickness of the screen (1 mm). We have assembled a thicker gap using nylon washers as spacers. The washers are also 1.7 mm gap, but in this case they are arranged in a grid. This prevents the mesh from deflecting across such a wide area and the performance is somewhat improved. Of course, the CERN parts are laminated with Kapton standoffs spaced every 5 mm between the mesh and cathode which maintain a uniform gap, but we need prototypes of different thicknesses to choose the gap dimensions first so we continue to try to develop in-house solutions.
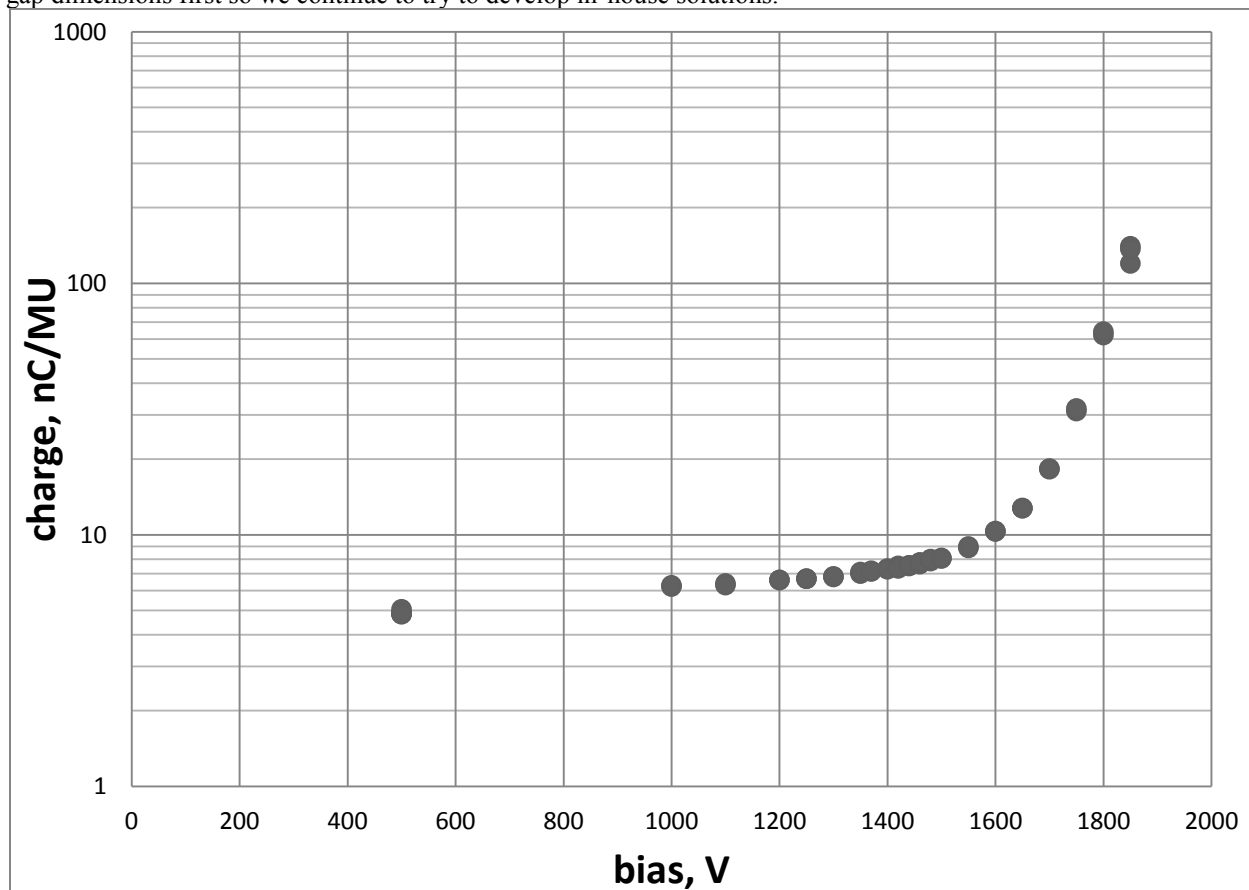
Computer Simulations of Micromegas Chambers

We are using computer simulations for guidance in making design choices for the Micromegas chambers. We have implemented the chamber geometry in Geant4 Monte Carlo simulation and can add Micromegas chambers to the existing IBA nozzle simulation code already developed at UPenn: the double-scattering and uniform-scanning

simulations including the MLC implemented by Chris Ainsley, and the pencil-beam delivery implemented by Derek Dolney. The next figure shows a Geant4 simulation of the chamber geometry and fields.
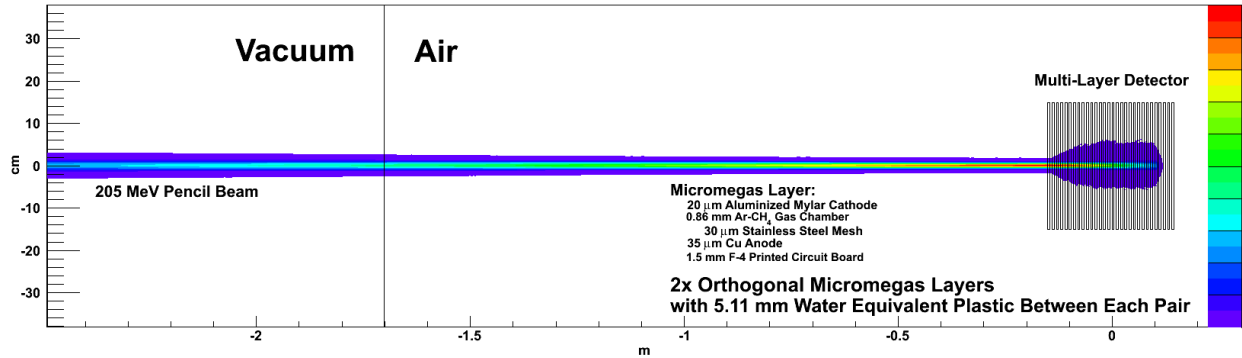
We are also using the Garfield software to simulate the electromagnetic field in the chamber. An example Garfield output is shown next.
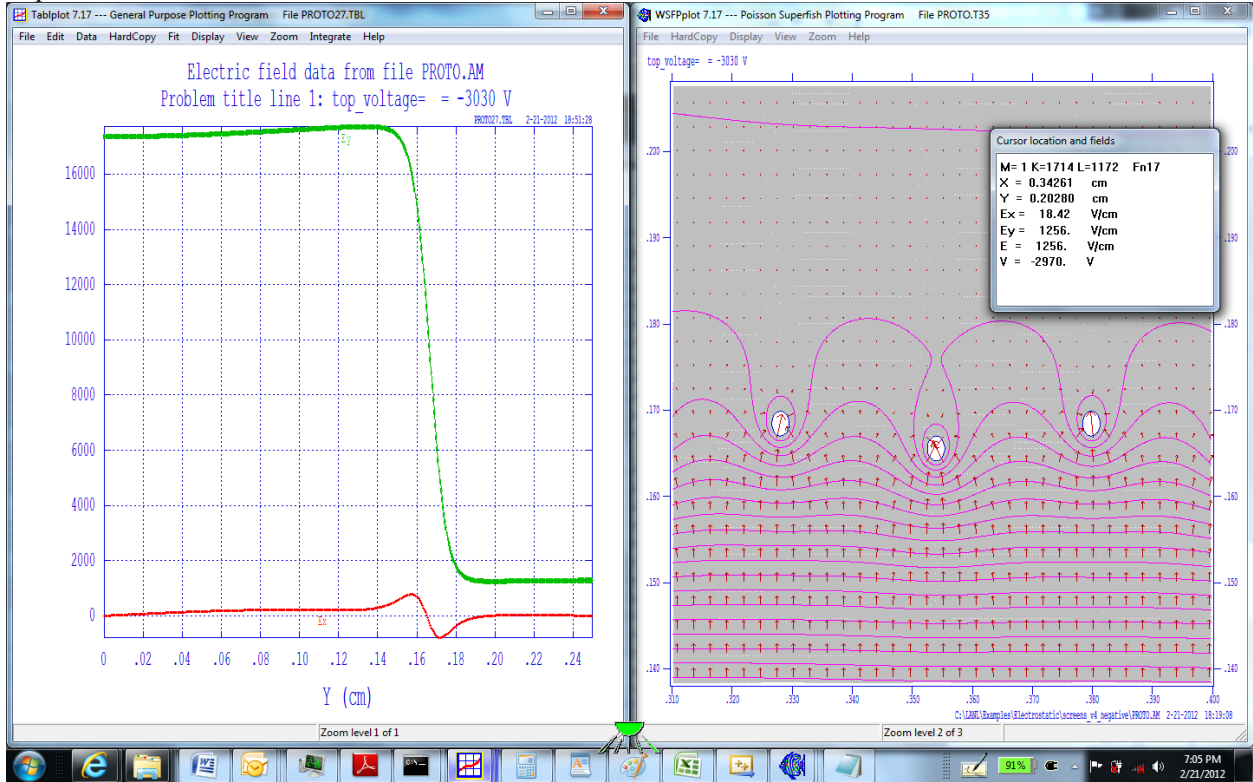
We are using these field simulations to guide our choices of operating potentials, gap thicknesses, and to help understand some of our measured results. We have not chosen materials for tissue-equivalence because it will depend on the final dimensions, mostly the gap size. Note in the plot on the right that the fields above the wire mesh are bent in such a way as to produce a focusing effect toward the hole for electrons travelling out of the upper drift region.

The focusing effective produced by operating with the mesh at negative potential relative to the collecting plate was understood to be important for stable operation at high beam currents. The next figure compares the field lines generated by the two polarities. In the case of the mesh held at negative potential relative to the collecting electrode, a high field region is created in the relatively narrow amplification gap between the mesh and the anode where gas gain occurs. The shape of the field near the mesh is such that it tends to focus electrons between the wires of the mesh as they move from the drift gap into the amplification region. Since the amplification occurs in the small gap region, positive ions can be cleared out more quickly. Alternatively, the configuration with the mesh held positive

36

relative to the electrodes is more like a multiwire proportional counter, with the electrons being collected at the mesh. Ionization gain occurs near the mesh wires where the field strength is very high, proportional to log (r_wire/r). Some gain is also realized in the amplification gap for primary ionization produced there, however primary electrons from the drift region do not generally cross the mesh plane and the number of primary ions produced is small. A drawback of this configuration at high current is that slowly drifting positive ions produced near the mesh wires tend to build up in the low field regions that can be seen around the mesh wires in the next figure. A buildup of positive ions near the mesh wires has the effect of increasing the effective wire diameter, r_wire, and so this type of chamber generally has less gain as beam current increases. We found by measurements in proton beams of the gain using the two polarities that the mesh held negative gives the ability to produce higher gains and that the gain is more stable with respect to variations in the beam current. There are also low field regions in the configuration with the mesh negative, but they tend to be located just above the mesh wires in the drift gap, where an accumulation of positive space charge may tend to defocus electrons drifting into the amplification region, however the gain of the device is observed to be more stable.
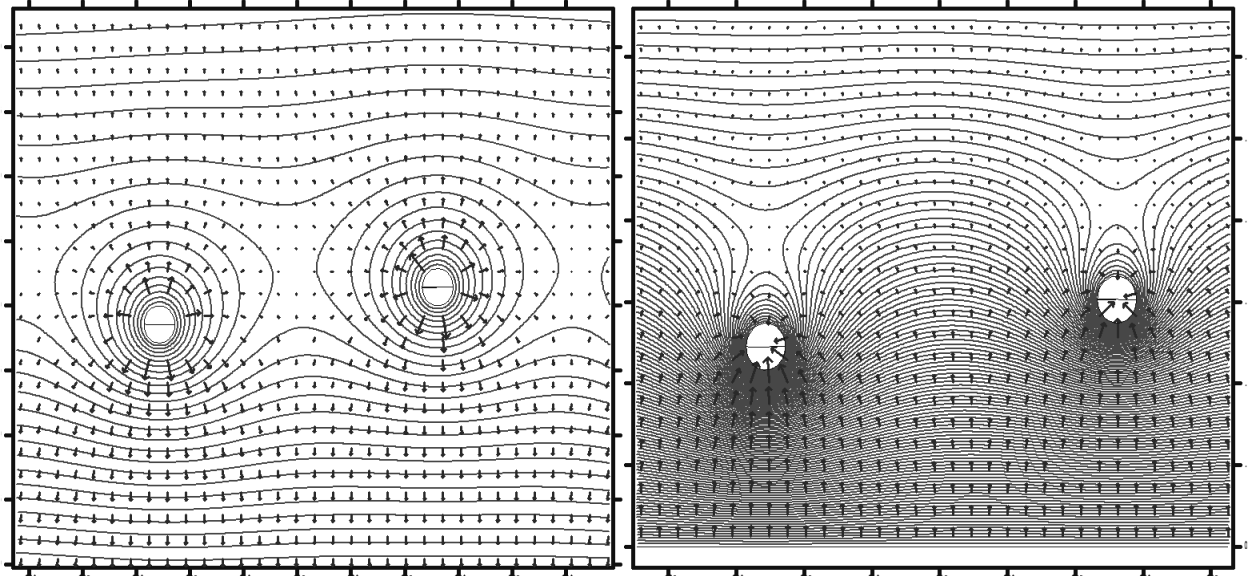
We have implemented the copper sheets, printed circuit layers, and gas in Geant4 simulations and can simulate the three modalities of proton delivery to the Micromegas geometry using the existing simulation code including the proton MLC. Some simulation results of SOBP and pristine Bragg peaks deliveries are compared with data measured by a Micromegas prototype in the following sections.

Multi Strip Prototype

To test the position resolution of these devices in electron and proton beams, we have constructed a prototype with a readout plane which is divided into 8 strips and a left and right guard region. The plane is divided in half so there is an upper and lower half making 20 channels total. The first 20 channel prototype was produced in Q1 2012 and is shown below.
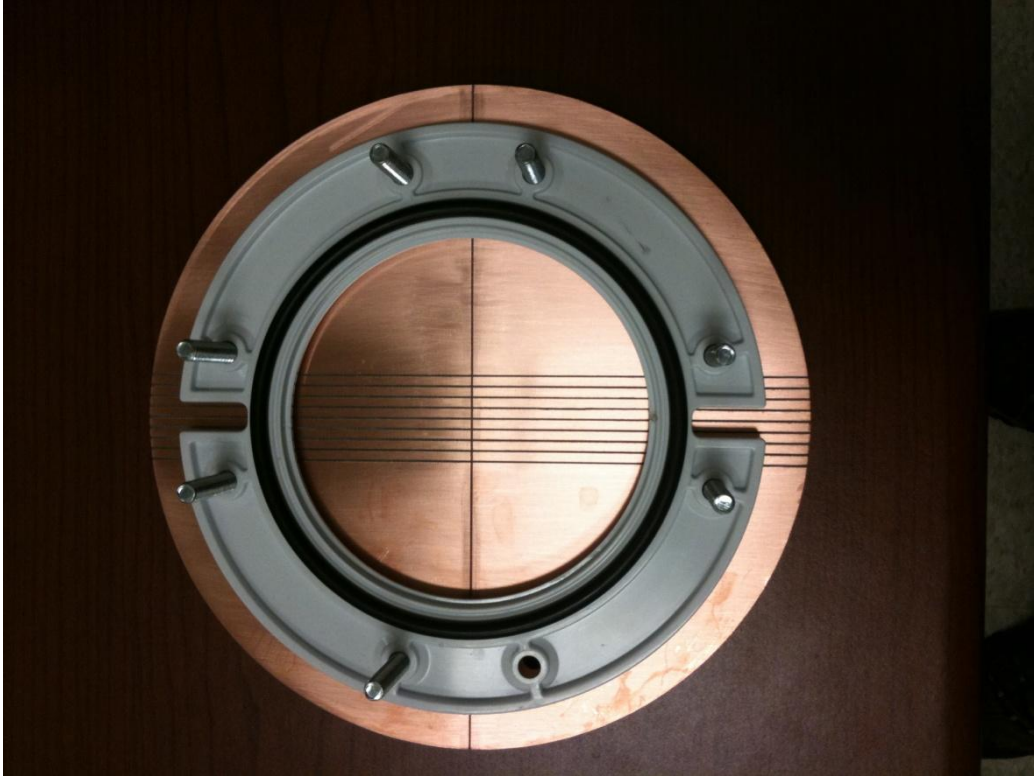
CERN Pilot Device

We have obtained from CERN a 5-channel pilot Micromegas device. During Q1 2012, we prepared the mechanical design for this first pilot Micromegas chamber produced at CERN using the BULK micromegas technique. The gap region is constructed from PEEK insulators and also provides gas inlets and outlets, gas seals, and provision for a spring connection to the mesh plane.

The next picture shows the pilot device assembled with the insulator ring visible. The cathode layer is divided into a central region and 4 surrounding regions for the beam test. The gap size is 300 microns. The mesh is supported above the cathode by the small support posts which can be seen distributed on the surface. The mesh HV feed is on

the right.
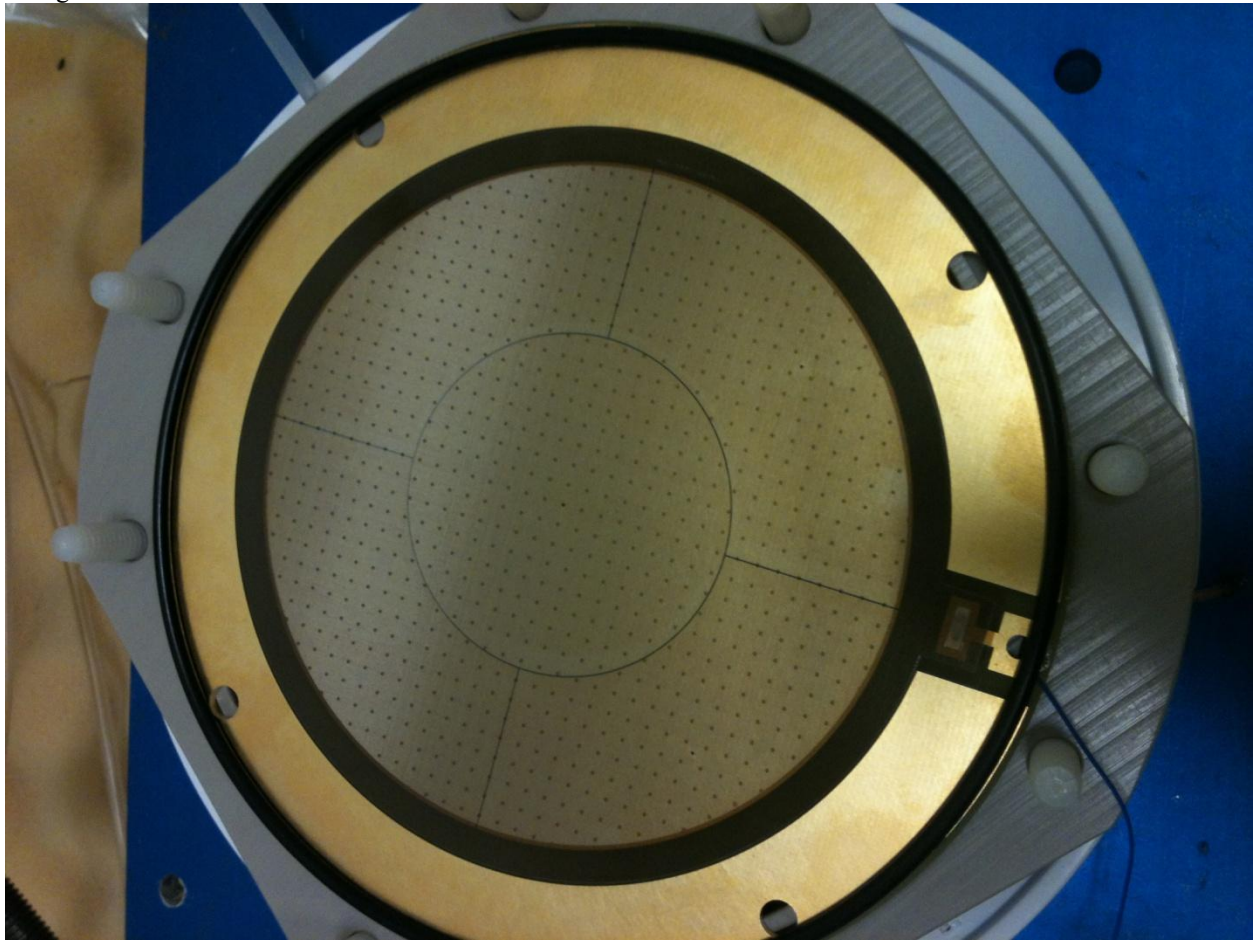
Next is a picture of the bottom side of the pilot where the 5 regions are connected to output cables leading to the preamps.
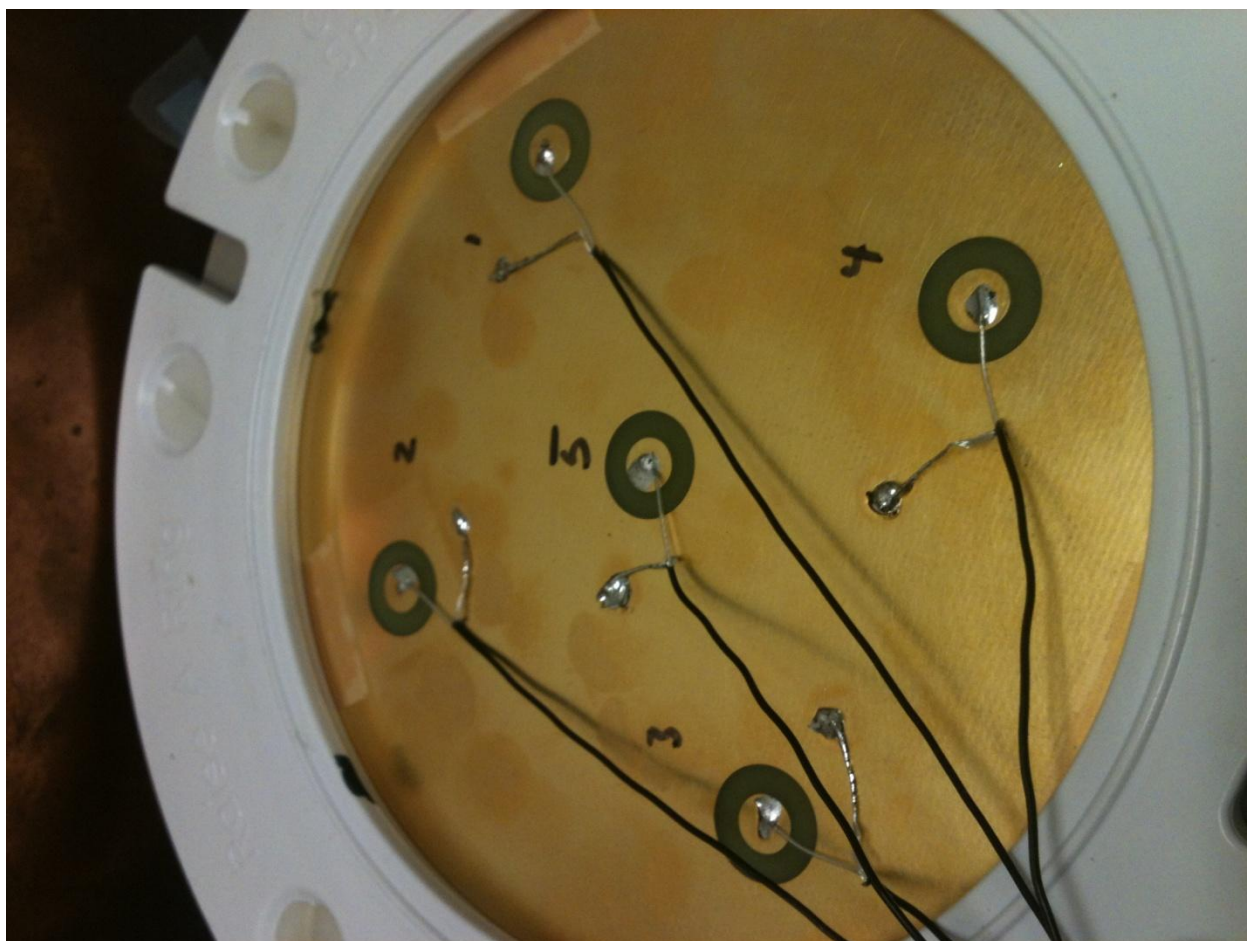
The pilot device has been tested in 70/30 Argon Co2 low gain gas using an Fe55 source which is embedded within the chamber. The pulse height spectrum of the 55 Fe calibration (Figure 6) can be used to correct for variations in the absolute gain due to changes in gas, voltage, temperature, or pressure since it measures the absolute gain. An example spectrum is shown in the next figure. The smaller peak is the Argon escape peak.
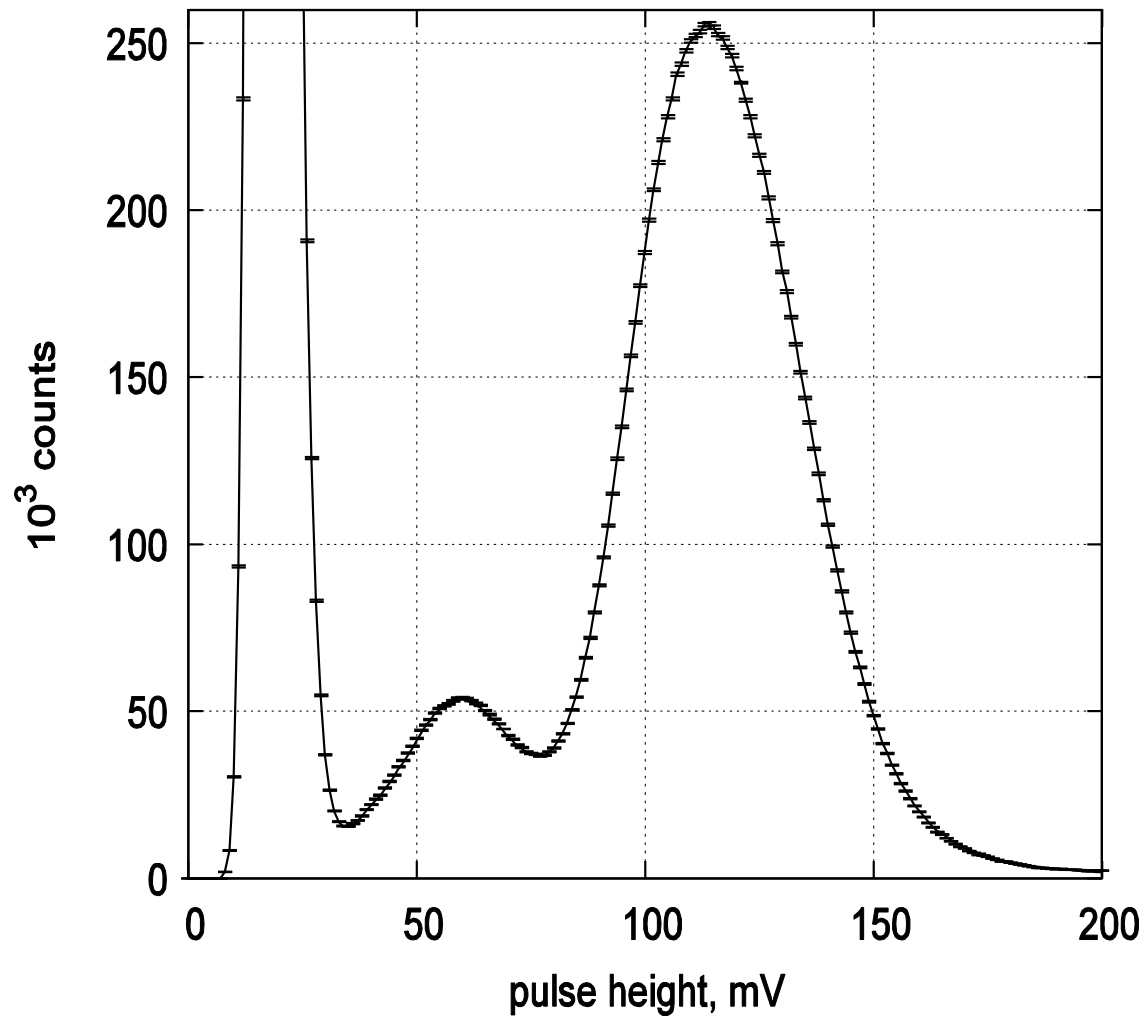
The Fe55 source provides an absolute calibration of the entire chain of electronics which includes the chamber gain, the preamp gain and the amplifier gain. The following figure shows a separate calibration of the preamp/amp using an injected charge pulse which allows us to extract the chamber gain. Below is the resulting calibration curve. The calibration was stable to less than ½% overnight without correcting for changes in atmospheric pressure.
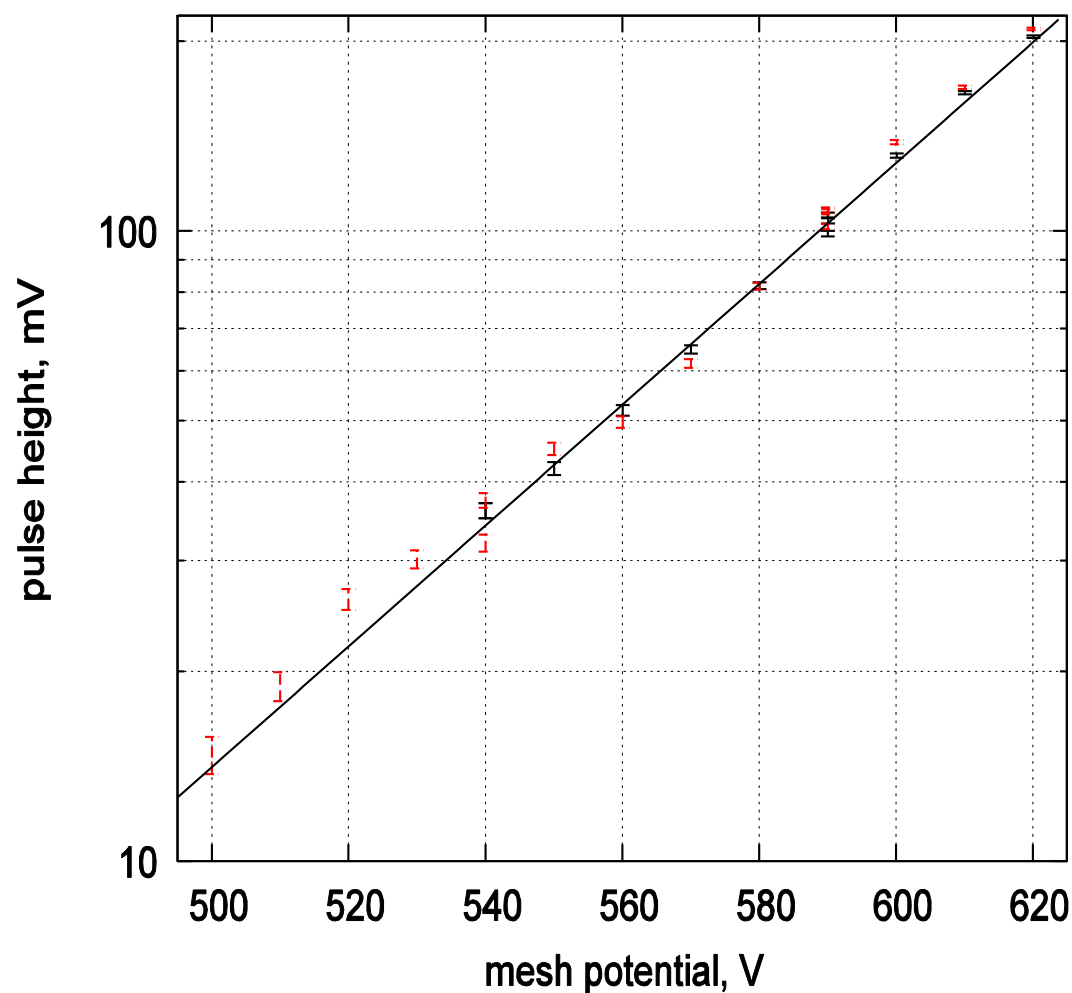
The next figure shows an individual pulse from the chamber: cosmic ray trigger (cyan), preamp output (green) and amplifier output (magenta)
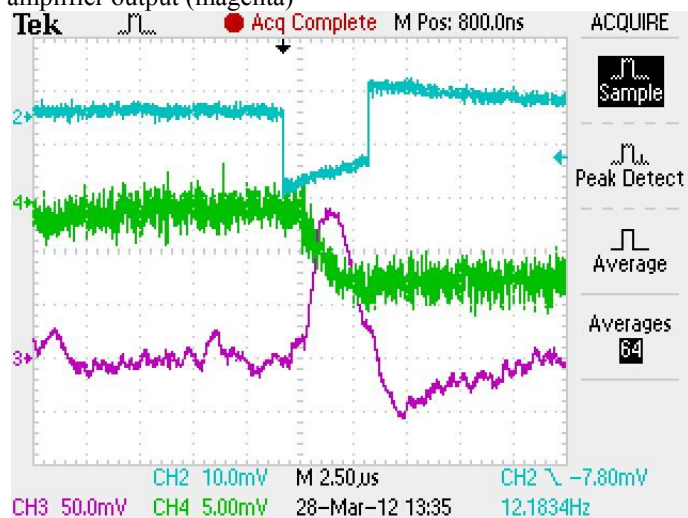
We have successfully measured the distal end of an SOBP with the Micromegas pilot device. Our experimental setup is shown in the next few photographs. First are the two chambers, to be irradiated from above. The top chamber is the multi-strip Micromegas prototype. The gap is large so that chamber has no gain, i.e. is running in ionization mode. The 5-channel Micromegas pilot device is inside the copper shielding box. Gas flows through both chambers and both are sharing the same high voltage feed.
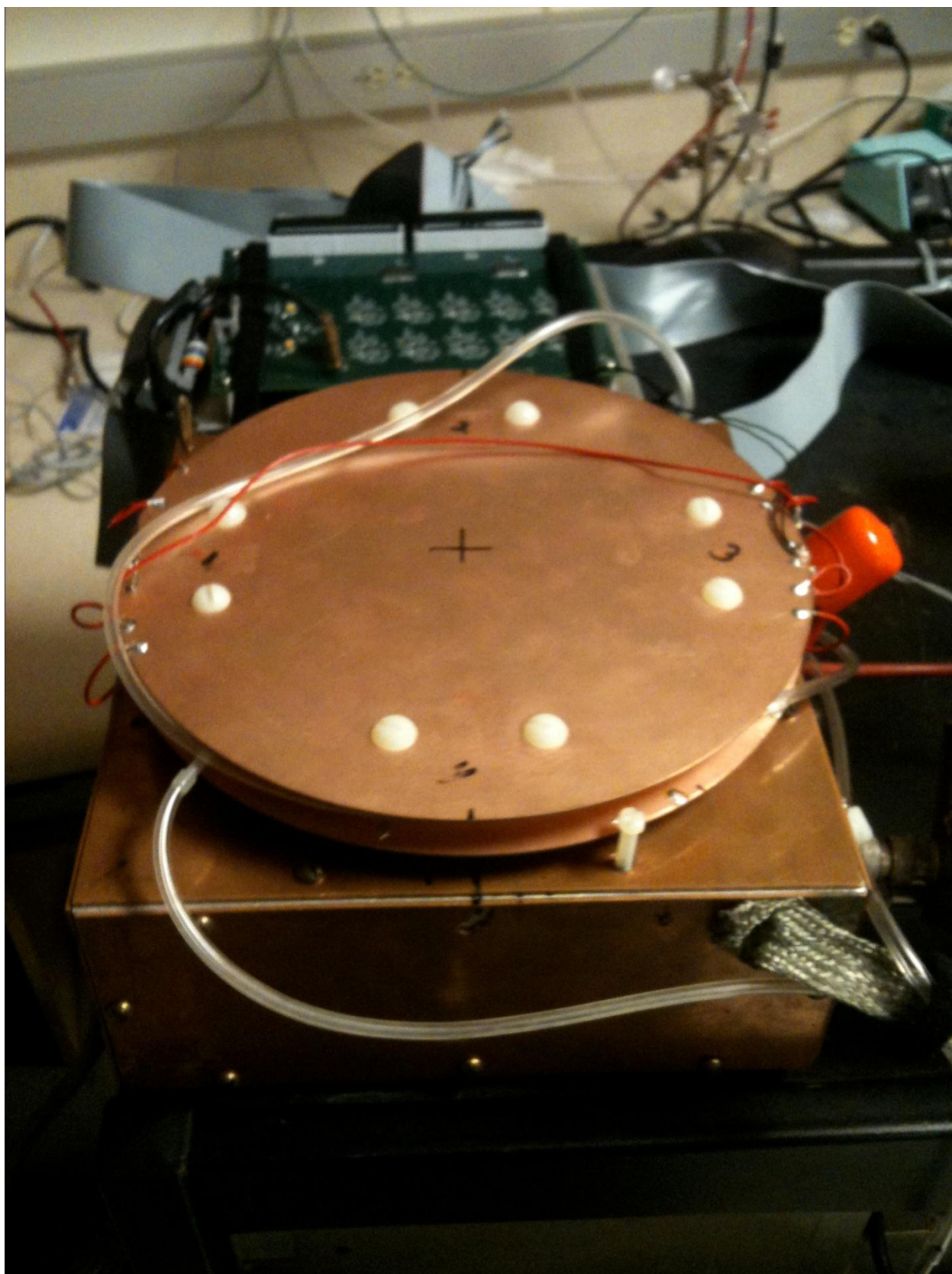
This is the experiment setup in the proton room. We are using the MLC to collimate to a very small 5 mm x 5 mm field in order to simulate the flux that the 5 mm x 5 mm voxels of the pixellated CERN prototype will see.

Below you can see the chambers centered just downstream of the MLC.

For the SOBP measurement, the couch was lowered, a tank made of lexan was placed on top of the chambers, downstream of the MLC, and filled with water, and an R17.5 M10 SOBP was delivered to the Micromegas chamber. A drain tube was used to flow water out of the tank continuously while the beam was on and data was collected. In this way, we hoped to collect an entire SOBP quickly without having to reenter the room and adjust water depth or solid water stack. The water tank worked well, but we did not have enough time to collect the entire SOBP yet. The tank starts full, so we got the distal falloff and some of the plateau of the R175M10. The next figure shows the data that we collected. You can see the tuning pulses, and some data where we checked that our gain settings were not saturating in the dose rate within the SOBP. Then the tank was filled and the beam restarted to gather the SOBP data.

R17.5M10 fragment

Tuning Pulses

Check Gain Settings

Beam Off to Fill Water Tank

Beam On and Water Draining

center channel ■
off axis channel ■
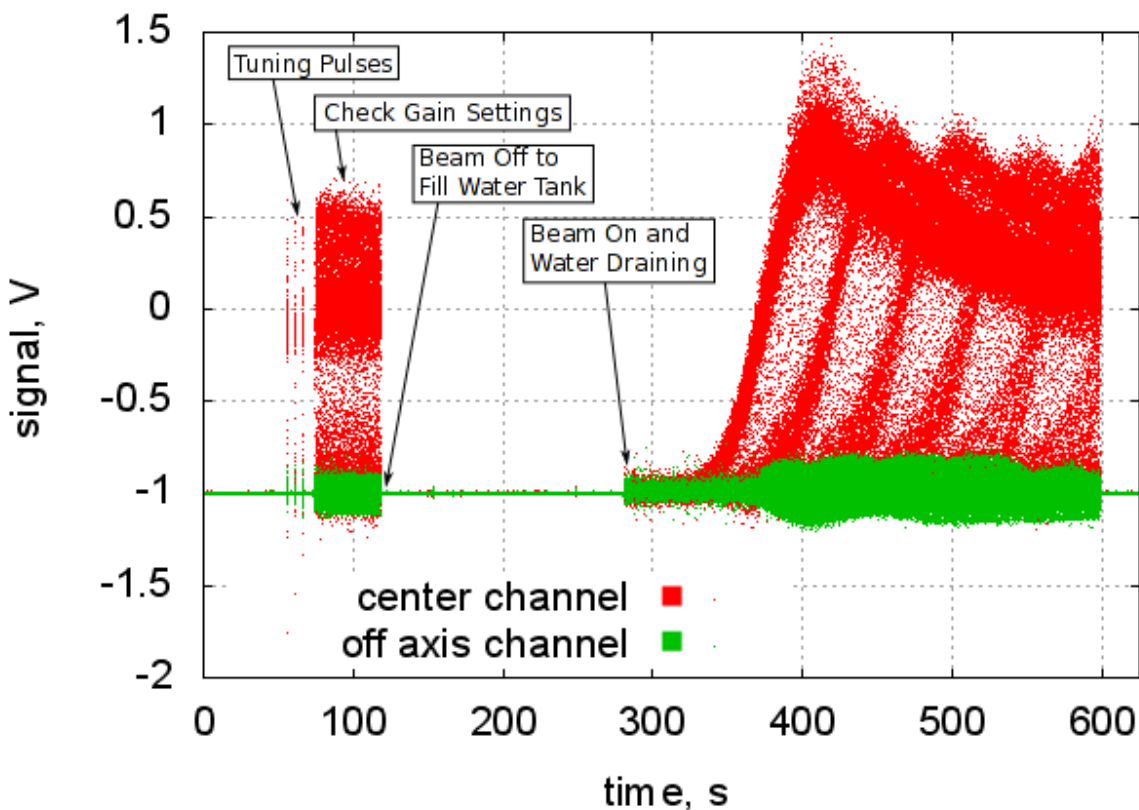
This is a double-scattering delivery, using a range modulator wheel. Each segment of the modulator wheel delivers a different pristine Bragg peak, and you can see the pristine peaks in the SOBP data. The dose at any given depth should be the sum of the dose of all the pristine peaks. We have performed the sum over each wheel rotation. That is shown as the black curve on the next plot. The depth was obtained by recording the water level as a function of time. By adding the water-equivalent thickness of the copper and printed circuit layers above the Micromegas pilot, we obtain a range measurement for this beam: 17.2 cm.

R17.5M10 fragment
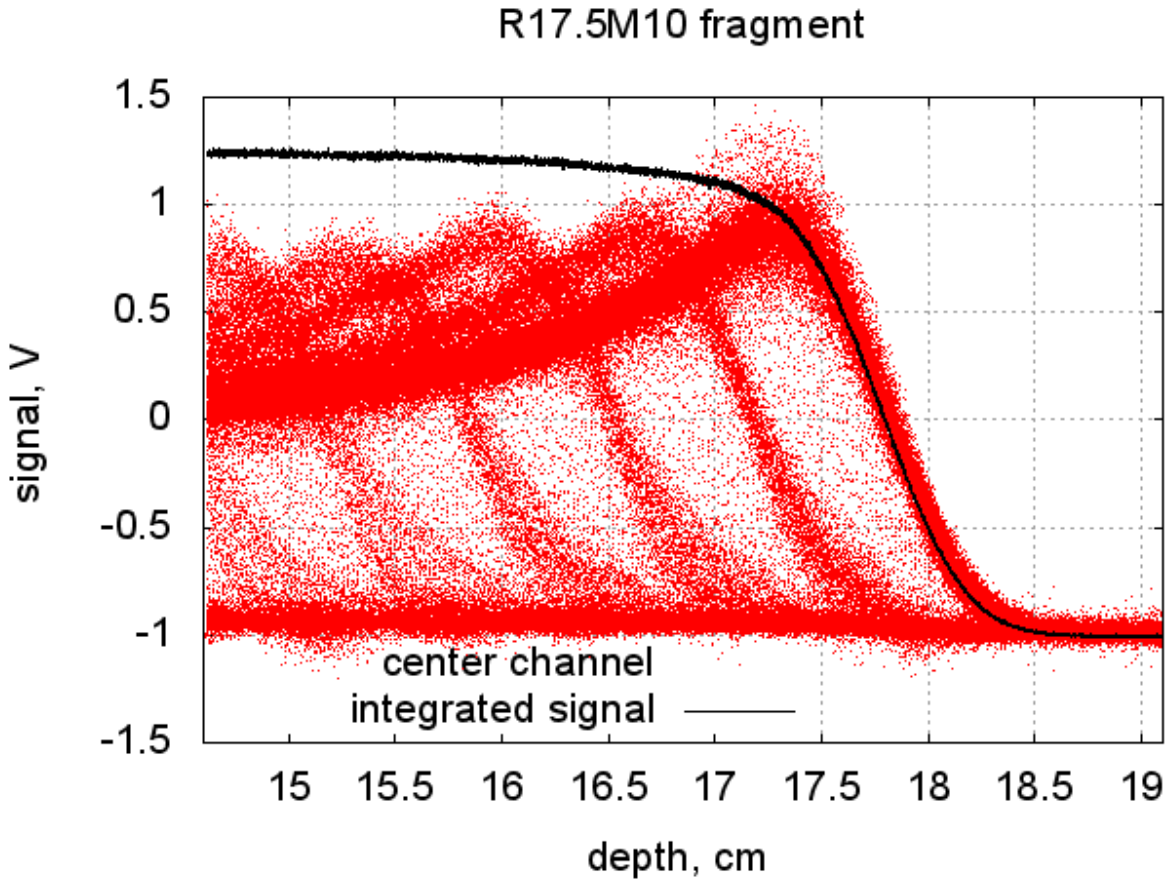
A more polished version of this figure appears in the PRI manuscript that is attached as an appendix, and two regions are zoomed to reveal the time structure of the beam delivery

It is very interesting and exciting that we can resolve the individual segments of the rotating modulator wheel. The water-equivalent thicknesses of the segments are needed to commission the treatment planning system. The Micromegas chamber, even a single layer used with a water tank, could be used to quickly measure that data. Those data have been measured in a very time consuming way in the past by stopping the wheel on each segment and delivering beam to an ion chamber. Some more discussion and figures appear in the PRI manuscript.

The SOBP measured with we measured with Geant4 simulation results. That is shown in the next figure. The simulated SOBP was normalized to 1 in mid-SOBP. The measured data was normalized to the simulated data at the shallow end of the measured data (approx 15 cm). We are not yet attempting absolute dosimetry with the chamber.

Relatively the agreement is good.
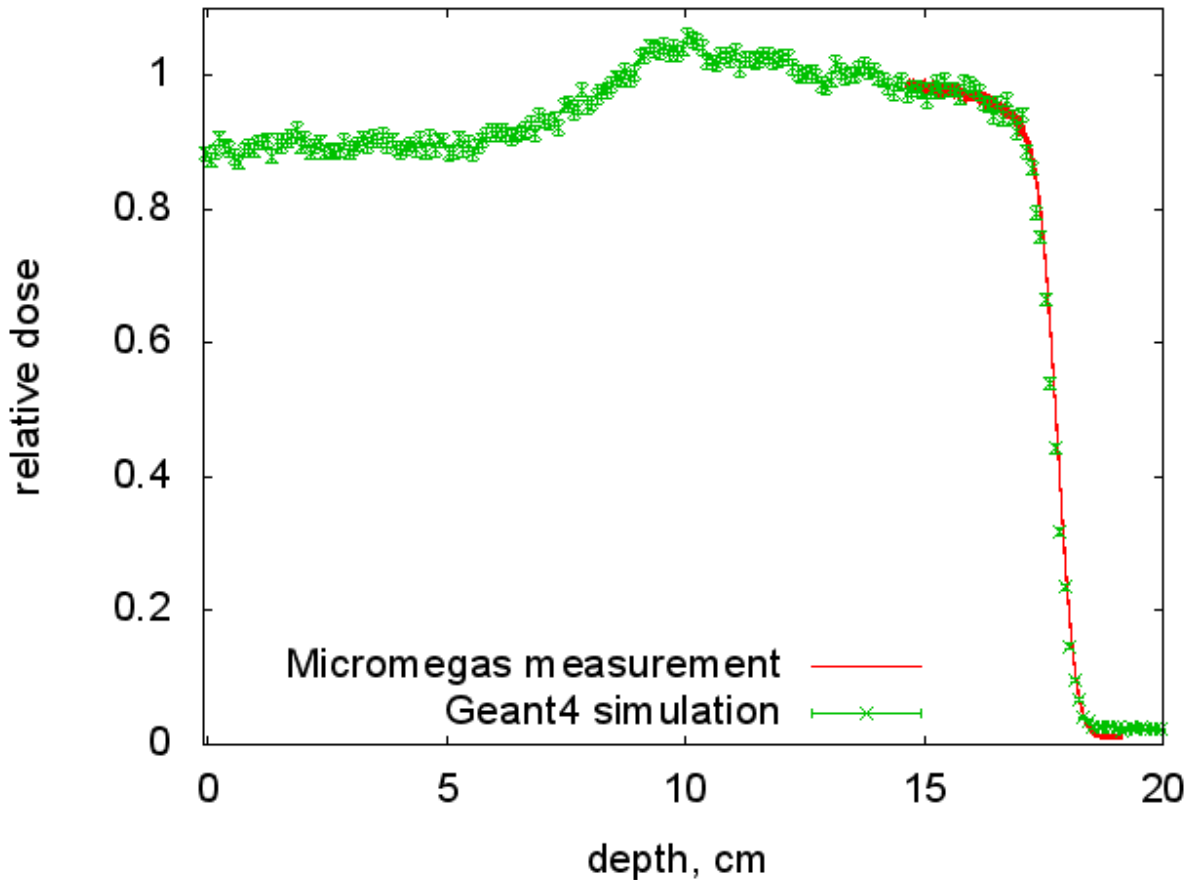
Another comparison of Geant4 simulation to Micromegas measurement for a pristine Bragg peak appears in the PRI manuscript. Overall the agreement is within 5%. There are some features in the measured data that are not reproduced by Geant simulations and we continue to work to understand the difference. Some possible explanations are described in the manuscript.

We measured with our Micromegas chamber, to high precision (0.002%), important aspects of the proton beam time structure: the frequency of the modulator wheel, and the beam scanning frequencies. Those details can be found in the PRI manuscript.

We did an experiment to set an upper limit on the spatial resolution that is achievable with our Micromegas design. We moved a small spot, 5 mm x 5mm, across the boundary between the center channel and one of the outer quadrant channels. Analysis of the data obtained indicates that the Micromegas design can produce a resolution better than 1.1 mm (1 sigma). This is better than any existing chamber-based technology for proton therapy. The measurement precision was limited by the couch positioning accuracy, and likely the chamber could reach even finer resolution. More details can be found in the PRI manuscript.

CERN Micromegas Board

In Q1, we completed the first design of a pad detector which will be mated to a drift region and a MicroMegas amplification plane. The pads are 5x5 mm. The eventual design will have a pad size between 5x5 and 3x3 mm. Position resolution for the 5x5 design will be approximately 1.4 mm or 0.86 for the 3x3 configuration.

The board layout consists of a 10cm array of pads and a four layer board to bring the pad signals out to the connectors. The figure below is a rendering of the PCB with each layer drawn in a different color. The Micromegas and drift planes sit on top of this PCB board.
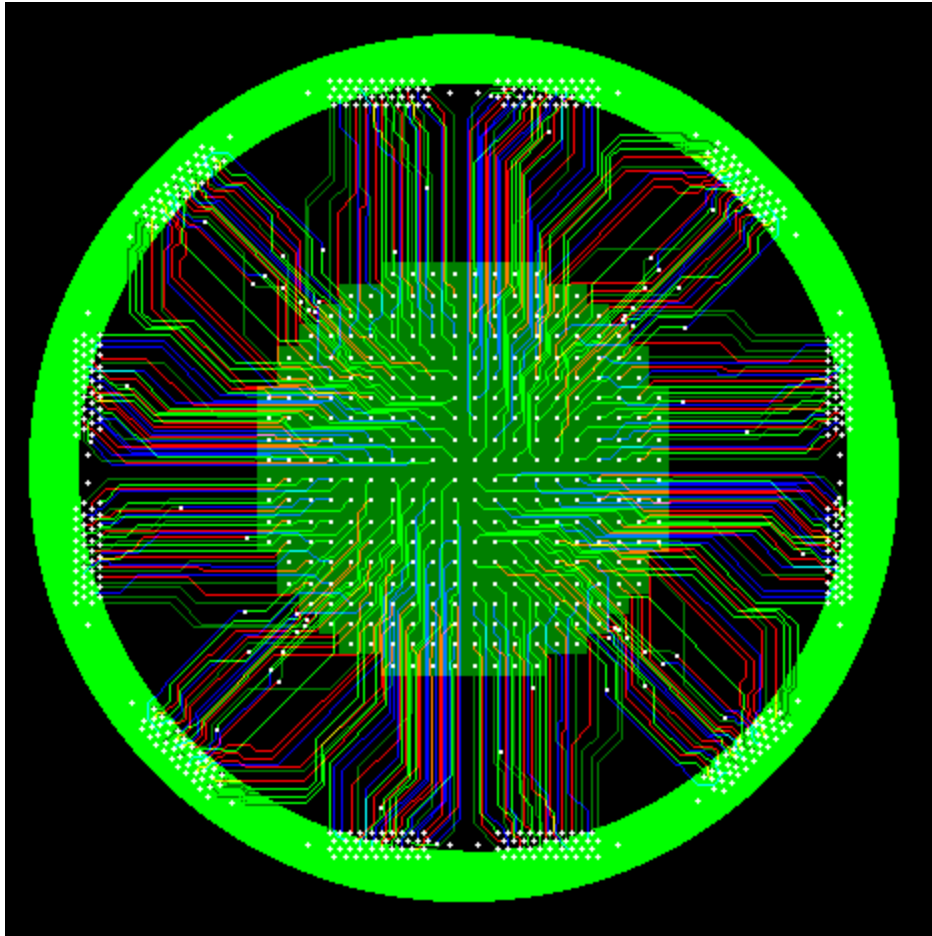
The second figure shows an expanded view of the pad structure on the top layer.
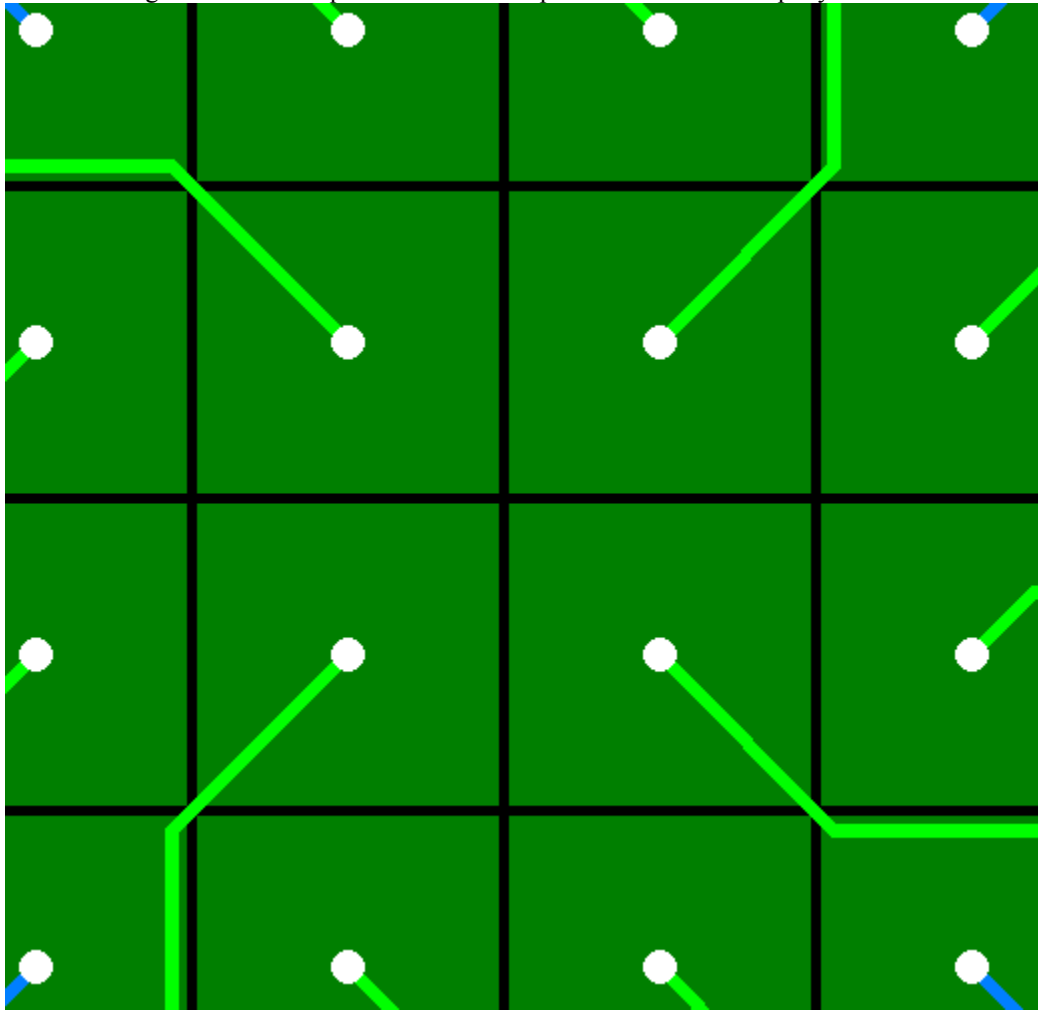
The pixellated Micromegas design was sent to CERN and was reviewed by the CERN electronics engineer who found some minor problems with the board design. There was a short circuit found and an o-ring was located on top of a high-voltage feed.

The initial problems were rectified and a first batch of pixellated Micromegas boards were produced. Two of the new layers are shown in the next photo.
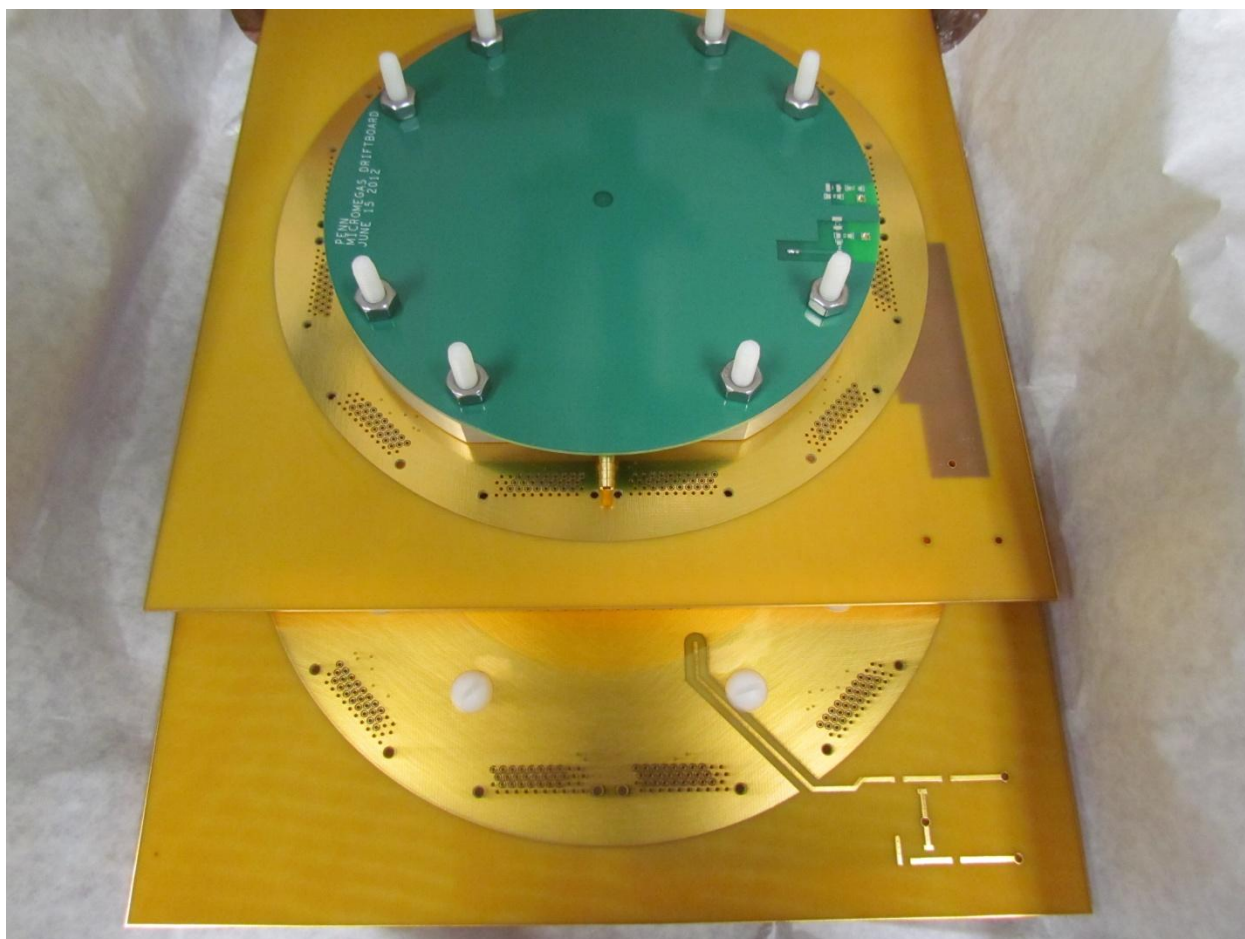
The figure shows two layers of a completed detector seen from the front and back sides.
The connectors for the signal outputs are shown in the next figure
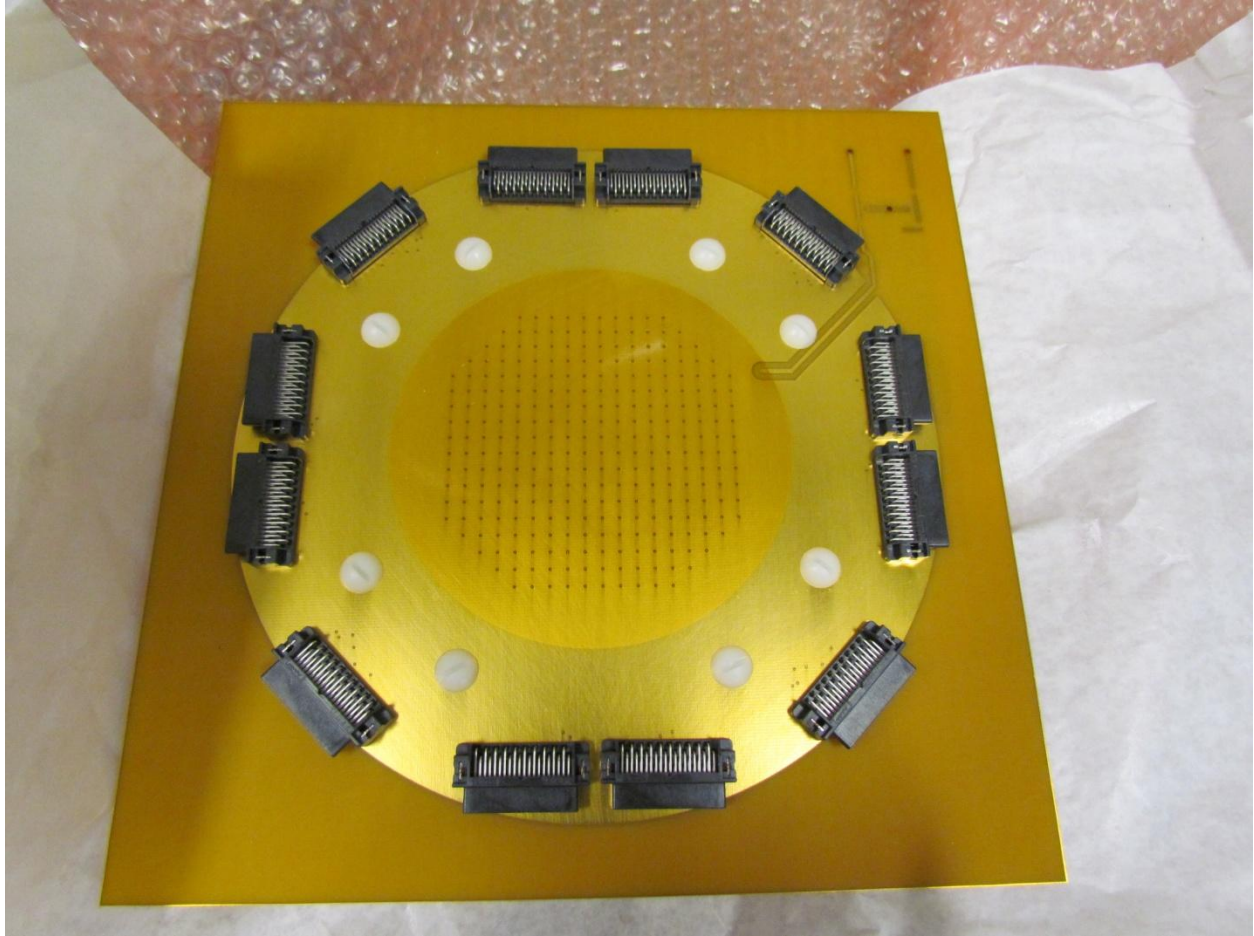
The following figure shows the interior of the chamber.
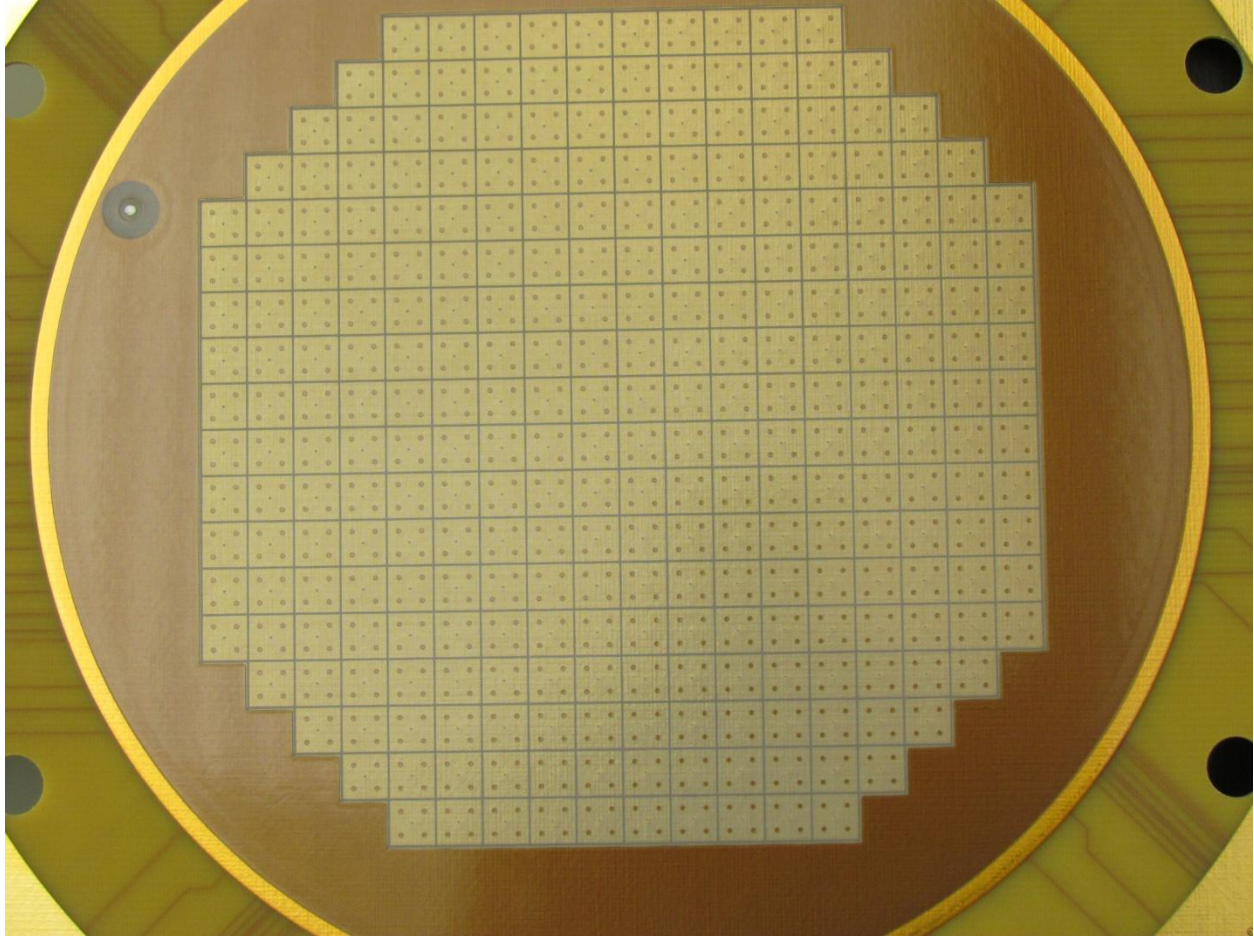
The small dots are the support pillars for the screen (which is too fine to see in the photograph).
These chambers are being tested with test electronics in the Physics Department. They will be irradiated in the proton beam at Roberts when beam time becomes available for research.

Amplifier Design

To readout the multiple channels of layer, we have designed a readout chain consisting of pre-amplifier boards, a readout DAQ, and have written some PC software to control the data acquisition.
 The preamp and readout for the strip detector and the pad detector are the same. The design was finished in Q1 and the first two boards have been assembled and will be tested in Q2.
The readout system uses a custom design proton monitor preamp board (designed at Penn) together with a commercially available readout (DI-720).
The DI-720 has 14- bit resolution and 150- 200kHz waveform recording capability. It communicates with a PC through an Ethernet link. Each device has 16 differential analog inputs . We require 10 differential inputs for the Proton Monitor in the strip layout. All channels support a measurement range of 1.25 to 10V full scale and gain factors of 1, 2, 4, and 8 are programmable per channel.
Two boards of the custom design 10 channel Proton Monitor Preamp Board have been produced and will be tested in Q2. The channels have a dual gain configuration which is controlled by outputs from the DI-720. The specifications are:
Hi- gain mode: 20mV/nA design. (16.6mV/nA measured in spice simulation.)
14bit ADC: 16384 counts
Vdc Range = 10V (+- 5V)
Least count (SPICE) = 10/16384 = 0.610mV/cnt
Resolution = 36.8 pA/cnt.
 Actual Gain may be higher due to differences in simulation of the switch and the real switch.
Lo- gain mode: 500mV/uA design. (488mV/uA measured in spice simulation)

14-bit ADC: 16384 counts
Vdc Range = 10V (+- 5V)
Least count (SPICE) = 10/16384 = 0.610mV/cnt
Resolution = 1.25nA/cnt

This dual gain system uses one op-amp with two feedback loops per channel, one permanently wired, and the other switched on by a logic level. The gain can be set individually using digital I/O bits available on the DI-720 A/D convertor board. This provides dual gains for each channel, that feed directly into the multiplexed A/D inputs, switches and buffers for additional digital I/O gain control. This system provided flexibility for adjusting the gain across the plane.

While lots of automatic techniques are possible, the simplest (therefore fastest) way to automatically adjust the gain would be to have a monitoring program look at the data as it's coming back and go to high gain if the output goes below 1/20 of the full scale range. The output would stay fixed unless it went above its 10X upper window limit ~1/10 of the coarse scale reading. This kind of switching could accommodate wide variations in dose across a treatment field.

A screenshot of the software that we have developed to provide a high-level user interface to control the DAQ and handle the multi-channel data from the DAQ is shown next. The software was developed mostly by a physics student, Gaurov Shukla. The software records multiple channels and also allows to switch the individual gains for the channels. A plot of 10 data channels is displayed on the computer screen in real time. The acquired data is written to a file that can be re-opened, manipulated off-line, and saved as comma-separated values for work in Excel, gnuplot, or elsewhere.
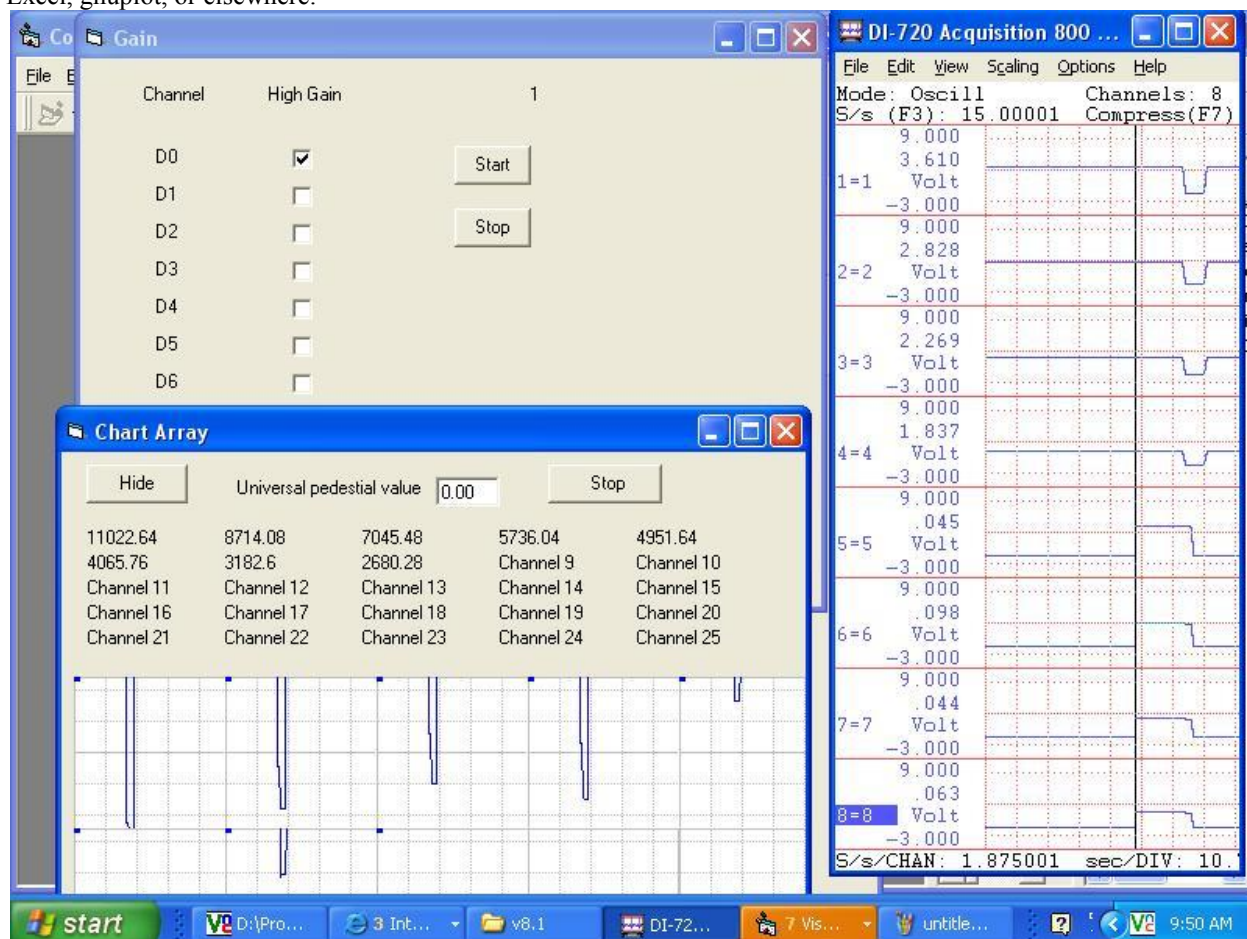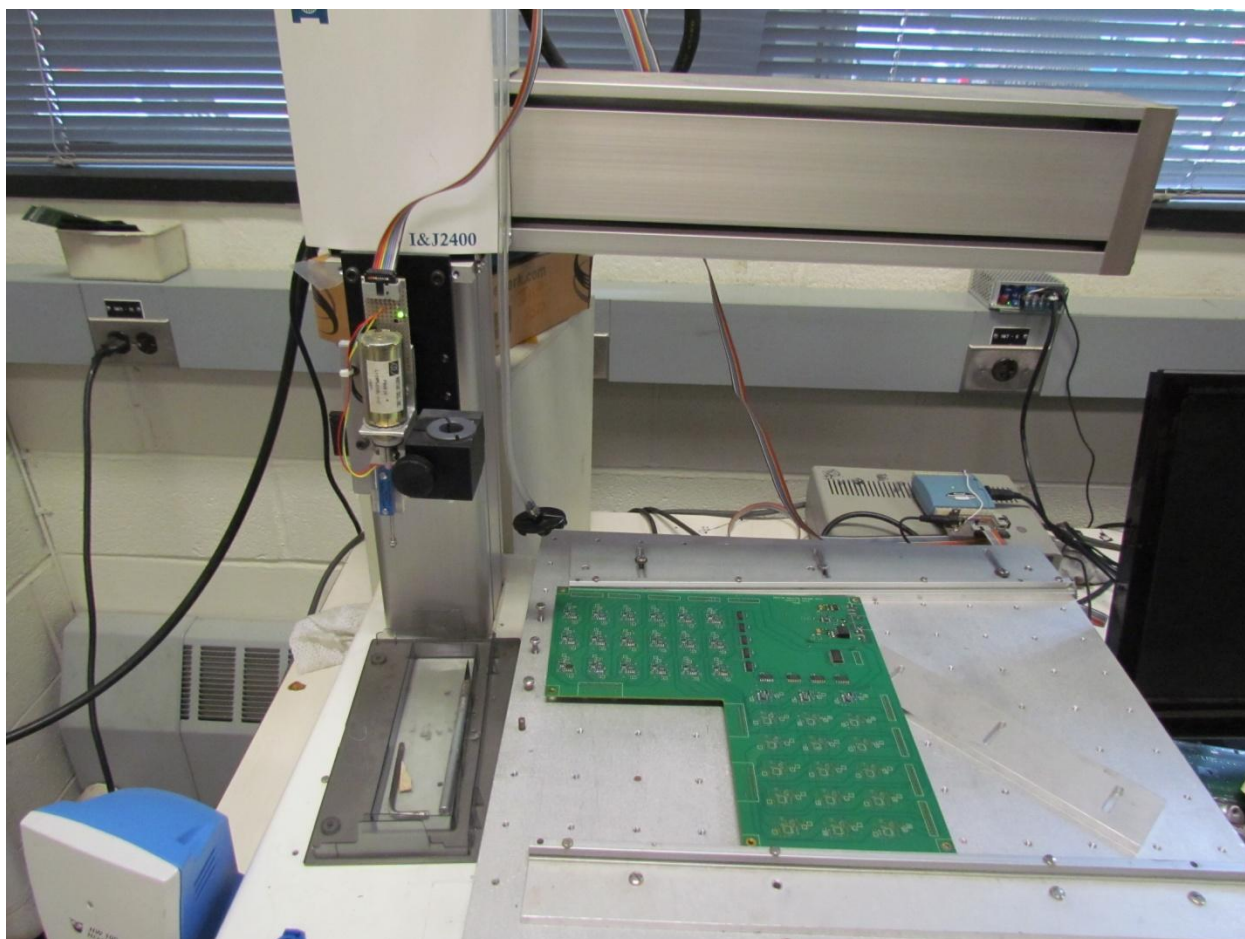
There are four amplifier boards for each chamber layer. Here one of the boards is on the automated machine which mounts the components. There are mounted amplifier circuits on both the front and back surfaces of this card.
The amplifier and ADC readout design is being revised by the electronics group at Penn. The current solution is expensive and it will be a challenge to support the large number of channels that need to be read. A 20 x 20 cm2 layer at 5 mm pixel spacing would have 1600 channels. With only 30 layers that would make almost 50,000 data channels.
One design option is shown below. Each pixel requires a pre-amplifier. Several pre-amplifiers are muxed together and passed into a single ADC. This saves on the cost of digitization electronics but imposes a limit on the per channel sample time. The frame rate limit is almost 300 kHz which is more than adequate even for a fast pencil beam scanning application.

AMP & ADC readout

Dual 4 chan Mux

Cell 1

ADC

9 - 8 Channel Cells

A0
A1

Dual 4 chan Mux

Cell 9

ADC

A0
A1

Gate

Gated CLK

SPI Data 1

clk1

40MHz
low jitter clock

clk2

**Connector To
FPGA Board**
•9 SPI inputs
•Ethernet Interface
•Sample Sync

Data 9

Convert

S0

S1

Gain
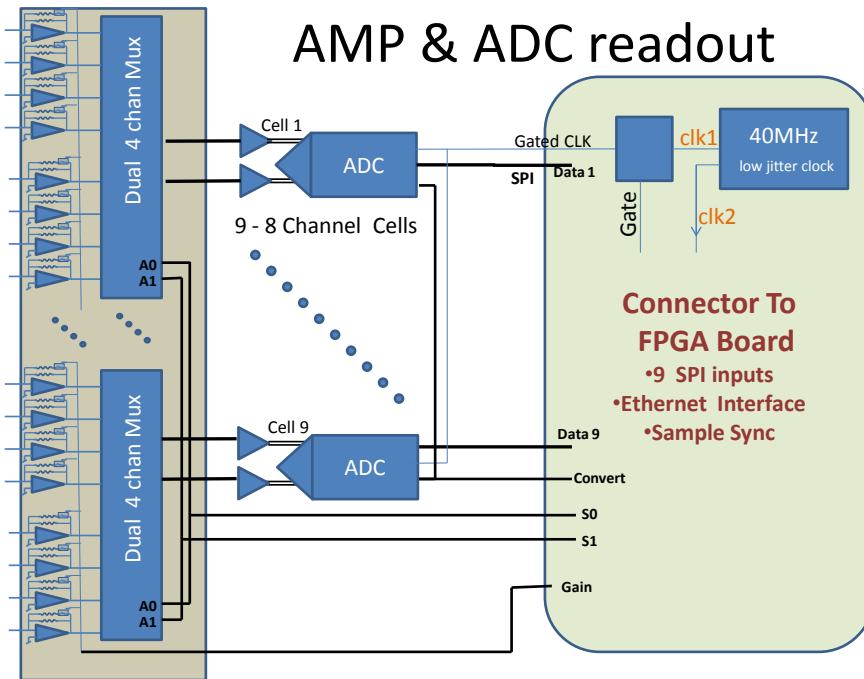
Data Rates

- Dual Channel ADC conversion time = 34 clock cycles 850ns.
- Readout Unit = Cell
    One Cell = 2 sets of 4 channels Multiplexed to one Dual ADC
- Cell Sample Cycle readout time (40MHz clock) = 3.4uS
    Frame Time = 1 read of all Cells = 3.4uS (4 sets of 34 clock cycles)
- Max Frame Rate = 1/3.4us = 294KHz

	Frame Rate	
Data Rates	50kHz	100KHz
Cell (ADC) →	6.4	12.8 Mbps
Quadrant →	57.6	115 Mbps
Half Plane →	115	330 Mbps
Detector →	3.7	7.4 Gbps

An FPGA is proposed to manage all of the ADCs. The FPGA would initialize the ADCs, but also support some signal processing such as pedestal subtraction, thresholding, and sparsification, in order to reduce the flow of raw data that must be passed upstream to a PC.

DAQ BOARD

DAQ MODULE #1

PWR

DATA AND USER INTERFACE

FPGA

ADC READOUT INTERFACE

3

1:6 CLK DVR

DAQ MODULE #2

DATA AND USER INTERFACE

FPGA

ADC READOUT INTERFACE

3
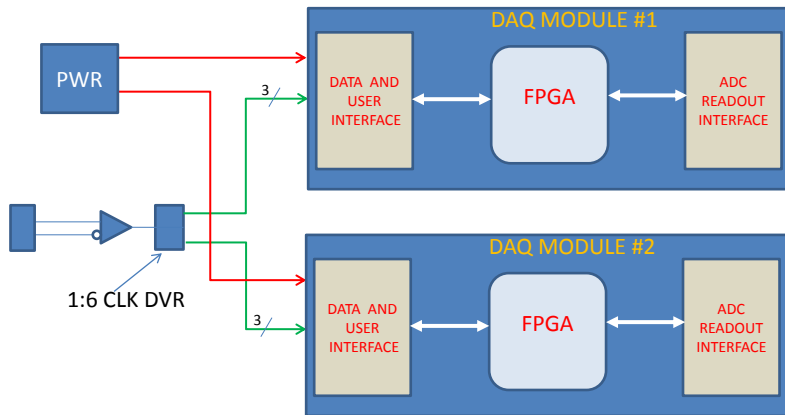
DAQ MODULE

CLK_EnX	ADC SCLK ENABLE
SD0_X <8..0>	ADC SERIAL DATA OUT
GSW_CTRLX<3..0>	GAIN SWITCH CONTROL
MUX_SELX<1..0>	ADC MUX SELECT
ADC_CONVT_X	ADC CONVERT
TEMP_MON_X	TEMP MONITOR READ

3 of 1:6 CLK DVR

CLK OSC SOCKET

¼ Plane 72 ch. ADC Board Connectors

GLOBAL CLK_IN

RS232 FOR DEBUGGING

RS232

2

2

GLOBAL TRIG

FPGA JTAG

4

USB FOR DEBUGGING

USB

4

8

14

GIGA EHTERNET

RJ45

PWR

CLK IN

GCLK_IN

RX/TX

GTRIG

JTAG

DIN<7..0>

GIGA ETHERNET

FPGA

CLK_ENA
SD0_A <8..0>
GSW_CTRLA<3..0>
MUX_SELA<1..0>
ADC_CONVT_A
TEMP_MON_A

CLK_ENB
SD0_B<8..0>
GSW_CTRLB<3..0>
MUX_SELB<1..0>
ADC_CONVT_B
TEMP_MON_B

40 PIN CONN

18

40 PIN CONN

18

40

AUX I/O
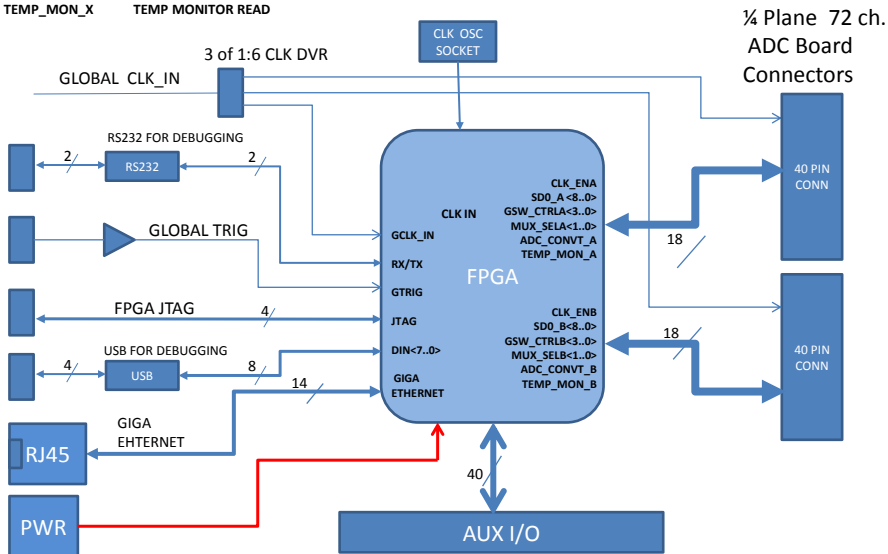
GLOBAL CLOCK DISTRIBUTION
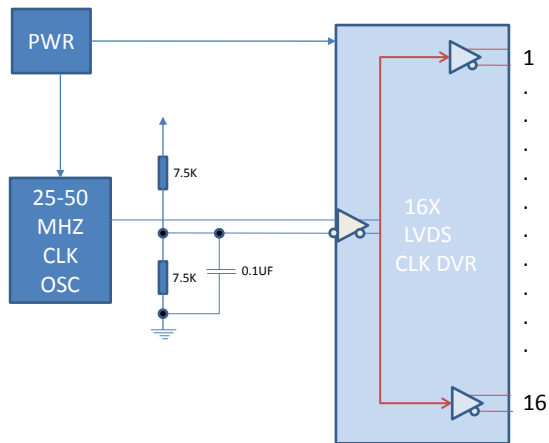
Amplifier to Data Acquisition connectors

Connections between the chamber and amplifier boards and between the amplifier boards and the data acquisition system require a number of small boards, connectors and cables. The figure shows the configuration for the connectors.

Automated channel index database

REFDES	PIN_NUMBER	Det pin	SYM_NAME	COMP_DEVICE_TYPE	PAD_STACK_NAME	PIN_X	PIN_Y	NET_NAME	PIN_X	PIN_Y	
C2	1	C2.1	C1210	CSMD1210-0.01UF		20%	1210	16V	SMD45_100	1210	16V	8486.229
C2	2	C2.2	C1210	CSMD1210-0.01UF		20%	1210	16V	SMD45_100	1210	16V	8486.229
C3	1	C3.1	C1210	CSMD1210-0.01UF		20%	1210	16V	SMD45_100	1210	16V	8486.229
C3	2	C3.2	C1210	CSMD1210-0.01UF		20%	1210	16V	SMD45_100	1210	16V	8486.229
R1	1	R1.1	R1206	RSMD1206-1K		5%	1206	SMD80_65	8825.025	1206	SMD80_65	9176.266 MESH_HV_II
R1	2	R1.2	R1206	RSMD1206-1K		5%	1206	SMD80_65	8689.025	1206	SMD80_65	9176.266 UNNAMED_
R2	1	R2.1	R1206	RSMD1206-1K		5%	1206	SMD80_65	8828.373	1206	SMD80_65	9980.057 MHV_GND
R2	2	R2.2	R1206	RSMD1206-1K		5%	1206	SMD80_65	8692.373	1206	SMD80_65	9980.057 UNNAMED_
R6	1	R6.1	R1206	RSMD1206-10K		5%	1206	SMD80_65	8318.002	1206	SMD80_65	9174.861 UNNAMED_
R6	2	R6.2	R1206	RSMD1206-10K		5%	1206	SMD80_65	8182.002	1206	SMD80_65	9174.861 MHV
R7	1	R7.1	R1206	RSMD1206-1K		5%	1206	SMD80_65	8305.362	1206	SMD80_65	9982.446 UNNAMED_
R7	2	R7.2	R1206	RSMD1206-1K		5%	1206	SMD80_65	8169.362	1206	SMD80_65	9982.446 GND
U2	1	U2.1	PATCH_PROBE	PATCH_PROBE-BASE	HOLE250	2606.322	7130.064		2606.322	7130.064	
U3	1	U3.1	PATCH_PROBE	PATCH_PROBE-BASE	HOLE250	3688.195	3056.939		3688.195	3056.939	
U4	1	U4.1	PATCH_PROBE	PATCH_PROBE-BASE	HOLE250	6679.447	3056.939		6679.447	3056.939	
U5	1	U5.1	PATCH_PROBE	PATCH_PROBE-BASE	HOLE250	2606.322	4138.812		2606.322	4138.812	
U6	1	U6.1	PATCH_PROBE	PATCH_PROBE-BASE	HOLE250	7761.32	7130.064		7761.32	7130.064	
U7	1	U7.1	PATCH_PROBE	PATCH_PROBE-BASE	HOLE250	6679.447	8211.937		6679.447	8211.937	
U8	1	U8.1	PATCH_PROBE	PATCH_PROBE-BASE	HOLE250	3688.195	8211.937		3688.195	8211.937	
U9	1	U9.1	PATCH_PROBE	PATCH_PROBE-BASE	HOLE250	7761.32	4138.812		7761.32	4138.812	
U10	1	U10.1	PATCH_PROBE	PATCH_PROBE-BASE	PAD100CIR84D	9396.07	9176.266	MESH_HV_IN	9396.07	9176.266	
U11	1	U11.1	PATCH_PROBE	PATCH_PROBE-BASE	PAD100CIR84D	9411.519	9981.041	MHV_GND	9411.519	9981.041	
U14	1	U14.1	PATCH_PROBE	PATCH_PROBE-BASE	ORING_POTENTIAL40X10HOLE	6137.642	7707.867	MHV	6137.642	7707.867	
U17	1	U17.1	PATCH_PROBE	PATCH_PROBE-BASE	PAD100CIR84D	8483.149	9605.693	GND	8483.149	9605.693	
U1_1	1	U1_1.1	CONN40_127MM	CONN40_127MM	PAD60CIR39_4D	8092.296	7961.318	GND	8092.296	7961.318	
U1_1	2	U1_1.2	CONN40_127MM	CONN40_127MM	PAD60CIR39_4D	8021.585	8032.029	GND	8021.585	8032.029	
U1_1	3	U1_1.3	CONN40_127MM	CONN40_127MM	PAD60CIR39_4D	7950.875	8102.739	PIX<50>_1	7950.875	8102.739	
U1_1	4	U1_1.4	CONN40_127MM	CONN40_127MM	PAD60CIR39_4D	7880.164	8173.45	PIX<46>_1	7880.164	8173.45	
U1_1	5	U1_1.5	CONN40_127MM	CONN40_127MM	PAD60CIR39_4D	7809.453	8244.161	PIX<43>_1	7809.453	8244.161	

The large number of signals in the system requires a database which can convert the design software quantities into tables for the analysis system. This is now complete. Routing tables, component lists, and connection diagrams are input directly from the electronic design software and produce the require channel index parameters. One small portion of this system is shown.

Two layer DataQ acquisition system

On the right side of the picture above is one of two completed layer acquisition systems consisting of 18 DataQ modules. The system is capable of reading 300 channels with synchronized clocks at rates up to 10kHz/channel.

Rolling cart

We have found that we need to arrange the entire apparatus on a movable cart in order to take maximum advantage of short periods of time available in the proton beams. We are constructing a rolling cart with an adjustable extension that projects into the proton beam area. It has space for all of the required electronics components, space

for the gas system, and a UPS (uninterruptable) power system. The prototype cart frame is shown below.

Four carts are being constructed. The cart will allow us to bring up the system including the computers, calibrate, disconnect without losing power and roll into the treatment area. Once there, we can reestablish wall power and take data. The entire process should take a few minutes.

Status of Milestones

This Micromegas proton monitor project began in 10/2011 and so was limited to4 quarters of research. This is was significantly shorter than the proposed 6 quarters and we have had to make adjustments to our goals.

All Q1 milestones were completed. Q2 milestones were completed except for the shielding design for the readout electronics and the study of stacking materials to give a tissue-equivalent assembly. Those studies will have to be done later. They will rely on the Geant4 simulations which we have shown to agree well with our measurements. As a compromise for the stacking material, we have purchased some solid water pieces that may not be ideal in terms of density or composition but will allow us to proceed with tests and demonstrate the 3D system. We can also use them to benchmark against some measurements the simulation geometry that will need to be developed to explore the choice of materials.

Q3 milestones involved assembly and testing of a 20x20 cm2 Micromegas layer. Due to time constraints we decided to make the first pixilated prototype design smaller than we had hoped. We ordered from CERN a 10 cm diameter prototype rather than the 20x20 cm2. This reduced the number of pads to readout, so that we would not need to assemble so many readout boards. Also it would be harder and take longer to design a Micromegas board to bring so many signals out to the edge of the board for readout. The 10 cm transverse size will still be useful to establish feasibility and maybe be used for small field measurements (some brain fields, for example). The first 10 cm Micromegas boards have just arrived and are being tested. We have not been able to complete any in-beam tests with those. Instead, we were able to obtain a limited 5-channel Micromegas board on a short timescale from CERN, and that was used to complete the milestones of Q3. The outcome of those tests essentially comprises the PRI manuscript.

Software has been written to control the data acquisition of two layers as described above. That uses a long chain of DATAQ modules. The software initializes all of the DATAQ modules and begins the data acquisition. At the end of the acquisition cycle, a file contains the digitized signal of all channels at rates up to 10 kHz. The signals (essentially dose rates on each pixel) can be displayed on screen or analyzed off-line.

In summary, we are about one quarter behind schedule, due to some problems with board designs that needed to be fixed, and also difficulty getting beam time due to downtime of the IBA system. Our intent is to continue work beyond the end of the award period. Derek is being supported by the Department of Radiation Oncology for two additional quarters. Bob will use some of his protected research time that is funded by the Department of Physics to continue. We will be able to purchase the Micromegas layers and the equipment that we need to assemble them and run the simulations before the end of the award.

Incorporation of beam scanning in treatment planning

Derek Dolney used Geant4 simulations to generate beam data libraries to enable us to use Varian's scanning algorithm in the Eclipse treatment planning system. This gives us the opportunity to evaluate patient plans from scanned beams prior to commissioning the system. Derek generated beam data for both of the IBA Dedicated and Universal Nozzles, based on the specifications of spot size near isocenter provided by the vendor. Derek has written a manuscript describing his method to generate beam data libraries from vendor specs. That manuscript is attached as an appendix. The manuscript was rejected by Physics in Medicine and Biology. We are considering submission to another journal at this time.

The beam data libraries allowed comparison of the quality of plans between the two IBA nozzles, for specific treatment sites. The Dedicated Nozzle has a smaller spot size but limited choice of beam angles since the only Dedicated Nozzle at Penn is in the fixed beam room.

One study used the generated PBS data library to compare PBS and double scattered proton therapy against IMRT for postoperative radiotherapy in completely resected stage IIIA non-small cell lung cancer. That study resulted in a manuscript (attached as an Appendix) that has been submitted for publication.

Another study considered proton DS vs. SFUD PBS vs IMPT vs IMRT for post-cystectomy irradiation of the pelvic nodes. That study appeared in a poster titled "Comparison of Treatment Techniques for Pelvic Node Irradiation: Intensity-modulated Photons Versus Protons " at the AAPM Annual Meeting in 2012.

Eclipse is commissioned and validated with data collected in Treatment Room #2. Treatment planning is working and we are treating about 12 patients per day with pencil beam scanning.

Measurement of dose distributions in static and moving phantoms

A major accomplishment of the Phase II research this past year is the development of software that, given a patient CT dataset and a treatment plan file from the Eclipse treatment planning system, performs the calculation of the 3D dose distribution in patient using the Geant4 Monte Carlo engine. We can perform the forward dose calculation using our in-house PBS simulation code based on the Geant4 Monte Carlo engine. We will use these simulations to validate the dose calc algorithms in Eclipse and to tune parameters in Eclipse that have an effect on fits of the commissioning data and parameters affecting the optimization engine. An example of the PBS forward calculation using Geant is shown in the figure below.
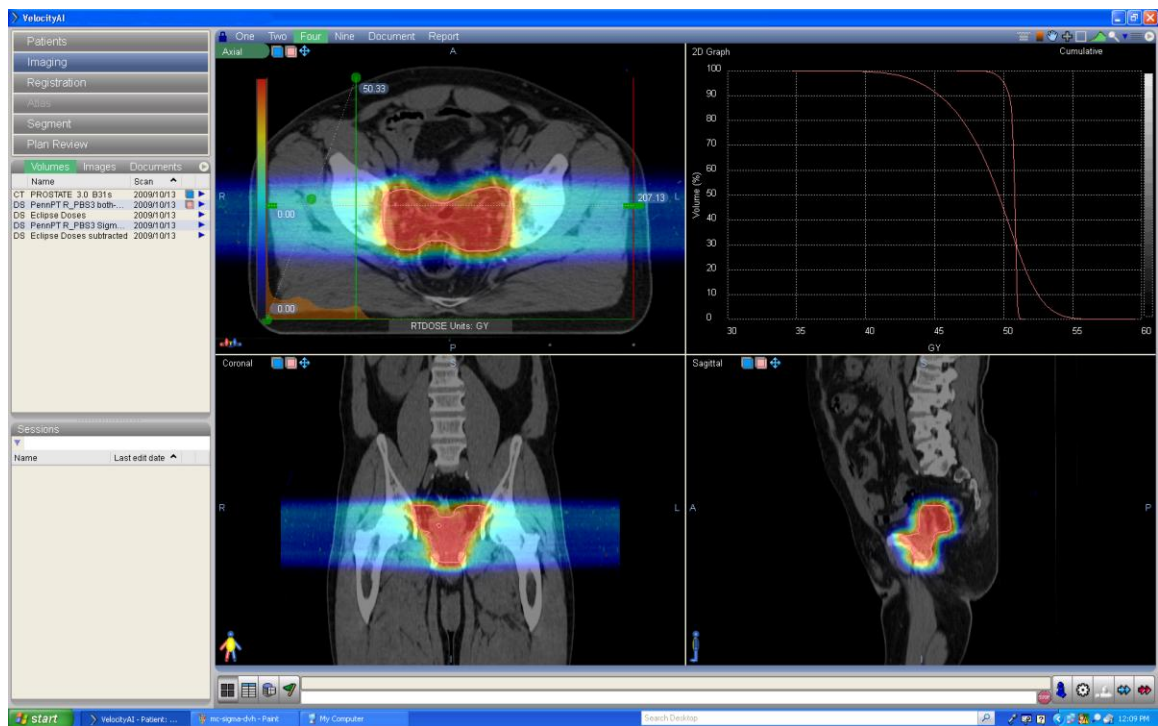
Figure. Dose distribution for a prostate case calculated with Geant4 Monte Carlo simulations. Note that the DVH line for target coverage is much worse for the Monte Carlo calc than for the Eclipse dose calc. This is due mostly to the sample variance contribution to the Monte Carlo dose uncertainty, which can be reduced by running longer simulations. The median dose for the Monte Carlo calc is only 49 Gy rather than the 51 Gy that Eclipse gives.

It is also possible to calculate the Monte Carlo sample variance as a 3D spatial distribution, as shown in the next figure.

Figure. Dose uncertainty distribution for the prostate case. This distribution essentially represents the error bars for the dose shown in the preceding figure. Note that the uncertainty shown here currently only includes the contribution of random sample variance inherent from the Monte Carlo method. No contribution is included for setup uncertainties, motion, target delineation, or other uncertainties. The white areas have uncertainty less than 4%. The top right panel is the analogue of DVH: an uncertainty volume histogram. It shows that the target dose is accurate to between 2 and 5%. The relative sample variance scales as 1/sqrt(dose), so the most uncertain points will be at the margin of the PTV, as can be seen top left where some of the PTV is not white, i.e. > 4% sigma.

Using Velocity, it is possible to compute the difference-of-dose between Monte Carlo and Eclipse. The two calculations mostly agree in the center of the PTV. Around the margin of the PTV, Monte Carlo is about 5% lower than Eclipse, and a little further outside the PTV Monte Carlo is 5% higher. This is consistent with the idea that some of the Gaussian peak has been scattered out to a longer tail that Eclipse is not modeling. Within Eclipse, it is possible to include a second Gaussian term in the model of the beam profile, but there is a parameter that must be tuned to adjust the relative weight of the two Gaussians.
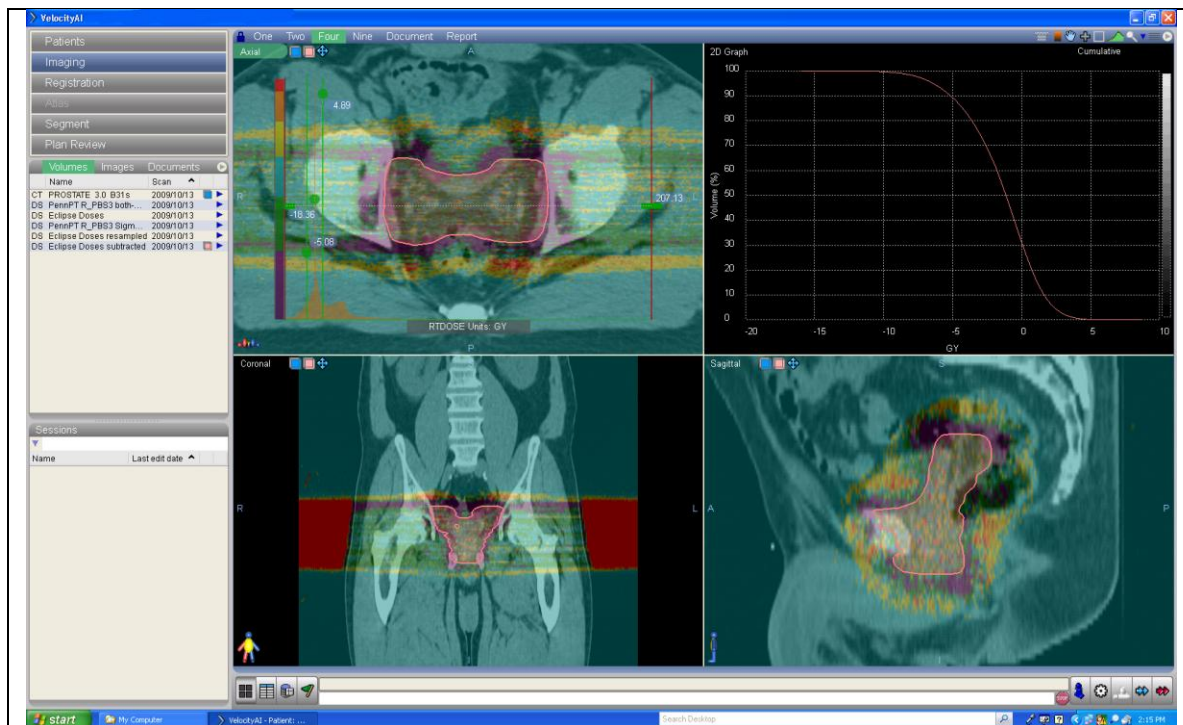
Figure. Distribution of the dose difference between Monte Carlo and Eclipse. A positive difference indicates that the dose from Monte Carlo simulation is larger than the dose from Eclipse. Red areas are where Monte Carlo is 5 Gy (10 % of prescription) higher than Eclipse, purple areas are where Monte Carlo is 5 Gy lower than Eclipse. Simulation is showing that near the margin of the PTV, the dose is generally about 10% lower than Eclipse (the purple border), and then about a centimeter beyond the margin it is 10% higher (the red/orange halo). We believe this is the effect of a dose halo that Monte Carlo is getting right, but Eclipse is failing to reproduce.

We continue to refine our implementation of the IBA nozzles in simulation to reach better agreement with data collected during commissioning of the proton treatment rooms.

Derek has also used the phase space data collected during room 2 commissioning to generate an initial phase space for simulations with starting point upstream in the treatment nozzle. That procedure has been described in previous reports: the beam spot profiles are corrected for multiple scattering in air by computing the scattering contribution to the spot size as calculated with Geant4, and a quadratic as a function of depth in air is fit to the resulting spot sigmas. This quadratic function thus represents the simple geometric beam optics that would determine the spot size were it to propagate in vacuum. The initial spot size and beam divergence are determined from the polynomial

coefficients. The difference in the case of fitting the commissioning data is that we have the spot size at 7 or 8 air depths to use to fit the quadratic. Previously we relied on IBA spec for spot size at isocenter, measurements of the beam emittance at another facility, and the idea that the beam would be focused at isocenter to determine the 3 parameters of the quadratic. It turns out that the beam is not focused exactly at isocenter, but it does not matter. The data is fit well by a quadratic function, which indicates that Geant4 is calculating the multiple scattering well enough in air, at least. The measured spot size in air is compared with Monte Carlo simulations in the next figure.
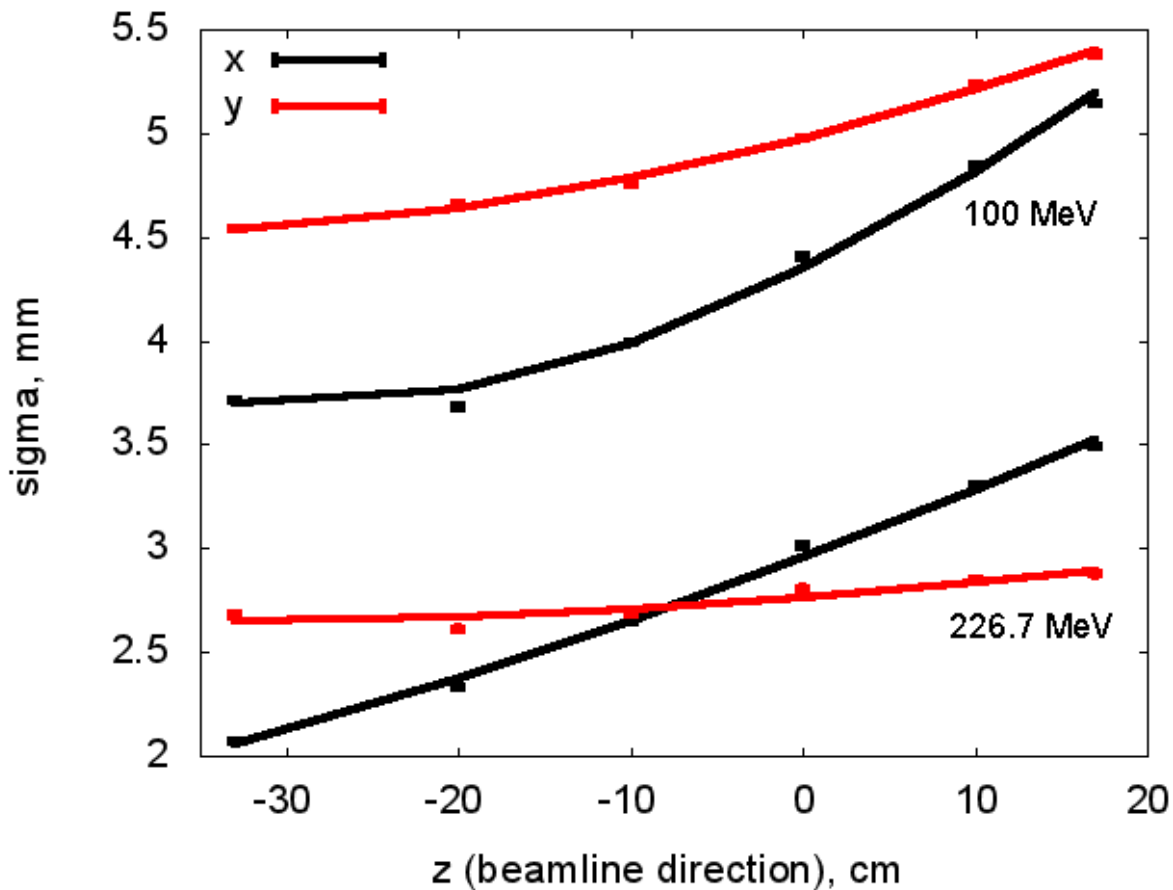
Figure. Comparison of Monte Carlo (lines) beam profile in air with data (points) measured during commissioning. Shown here are the maximum and minimum beam energies. The range shifter is not in the beam line.
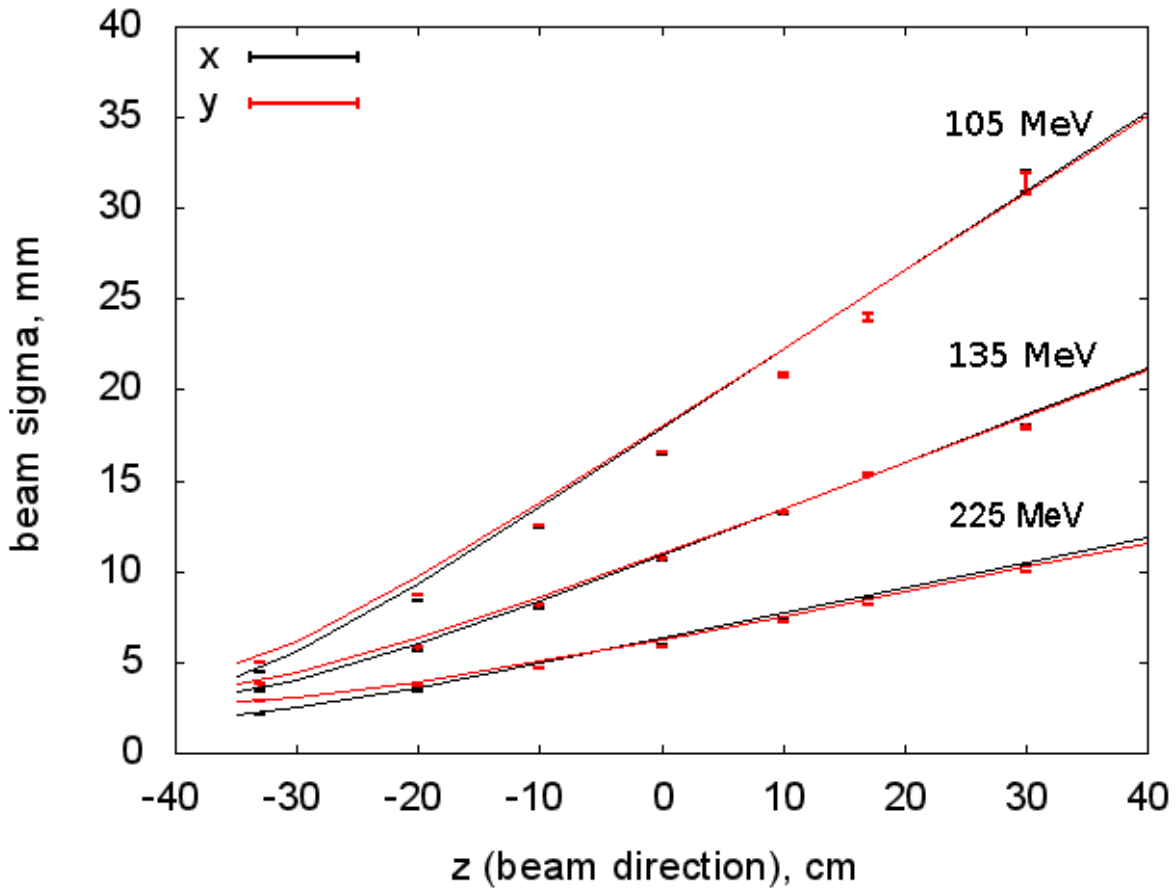
Figure. Comparison of Monte Carlo (lines) calculated beam profile with measured (points with error bars) data using the range shifter collected during Room 2 commissioning. The initial phase space for Monte Carlo was obtained from fit to the open beam commissioning data.

We have also verified that Geant simulations reproduce the spot size when the range shifter is used. The beam profiles measured with the range shifter were not used to produce new fitting functions. The same initial phase space that fits the open beam case also reproduces the spot size for the case of the range shifter, indicating that Geant is modeling the scatter in the range shifter well enough. The comparison of spot size measured and simulated for the range shifter case is shown in the figure above.

A comparison of depth dose curves is given in the next figure. There is some difference in the shape of the Bragg curve particularly the slope in the entrance region. We are investigating the origin of this difference at present. One possible effect contributing to the difference is that we are not collecting all of the charge deposited in the water phantom due to the finite size of the Bragg Peak chamber. A long dose tail is produced by multiple Coulomb scattering and nuclear interactions, and when many spots are summed to produce a uniform dose to s target, the tail accumulates to produce a so-called dose halo around the target. The dose tail can grow larger than the diameter of the chamber (8 cm). Some evidence for this can be seen in the commissioning measurements: the dose collected with a the beam scanning a large uniform field appears to be about 10% larger than that measured with a chamber attempting to integrate the full dose profile of an unscanned beam.
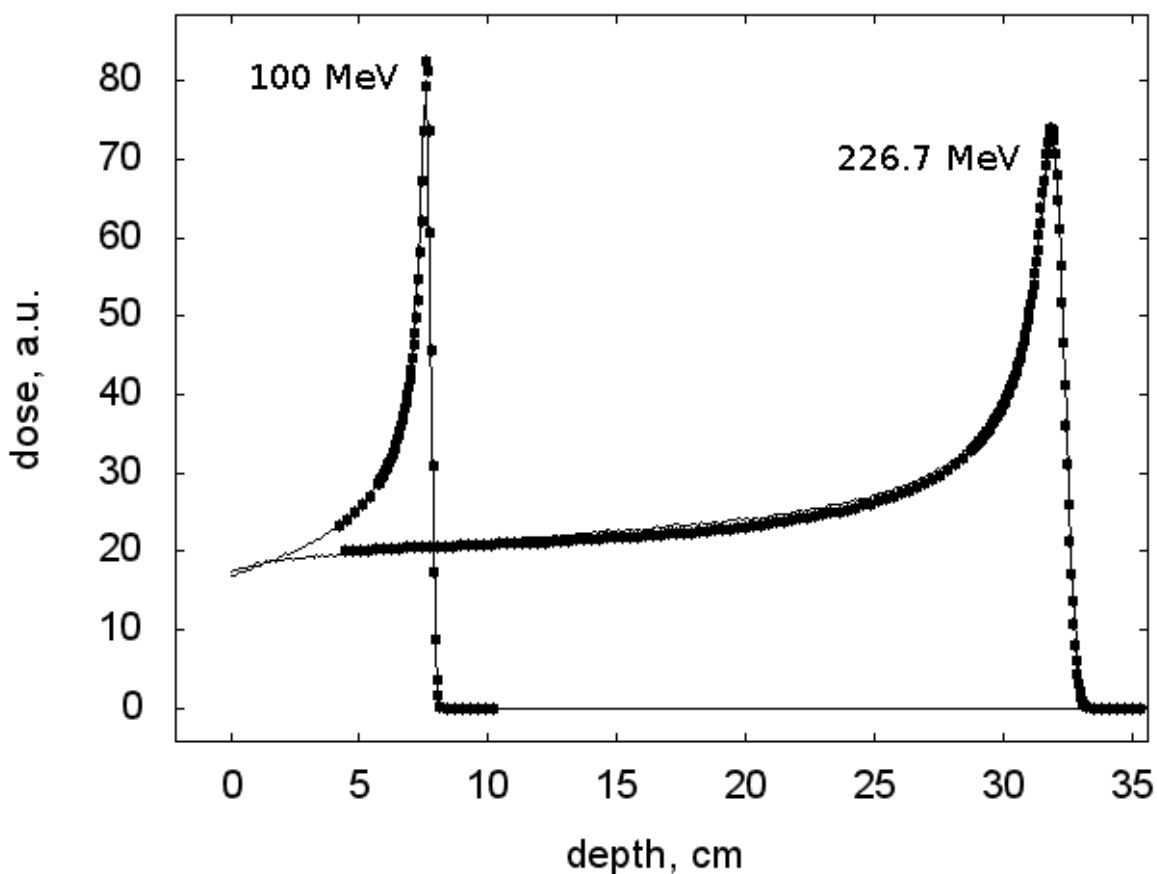
In the past quarter, Derek has implemented the scanning magnets in Geant4 simulation. Previously different targets were delivered by steering the beam geometrically, i.e. adjusting the mean proton direction for the phase space generation. Now magnetic fields are implemented based on specs from IBA. A constant magnetic field is implemented in simulation over the length of the magnet yokes. The field strength can be chosen in order to hit to desired target position by integrating the Lorentz force law, and this method hits the target within 0.5%. Derek has also implemented the thin vacuum windows and layers in the beam monitor ionization chambers, in an effort to reproduce the long tail ("halo") observed in the beam spot. Additionally, the energy deposit in the air in the monitor chambers can be used to achieve absolute dosimetry with simulation. The implementation of the nozzle is rendered in the next figure.
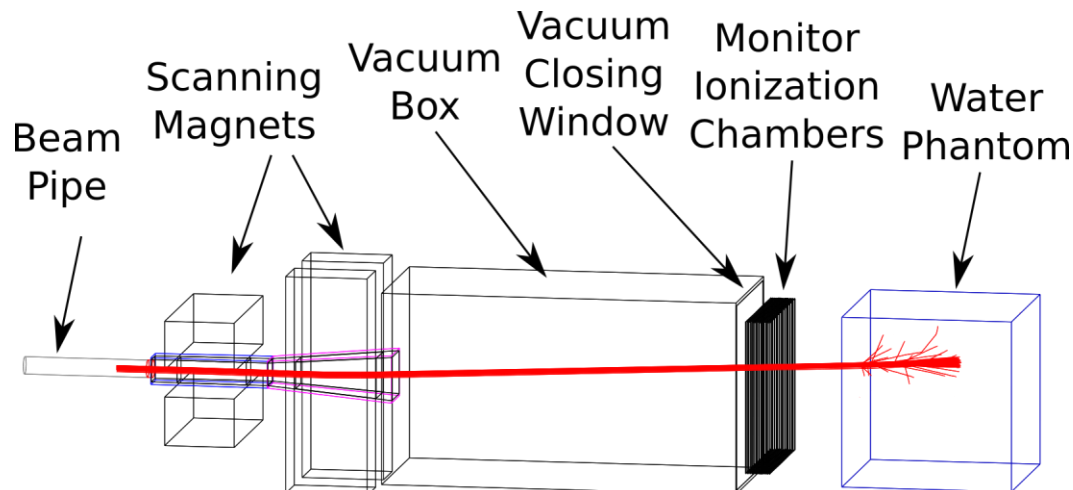
A prostate field was delivered to solid water with film placed within at different depths. The forward dose calculation was performed using the Geant4 Dedicated Nozzle implementation. A gamma analysis was performed to compare the dose distributions measured and calculated. Typical values were used for the gamma thresholds (3% dose/3mm). With these thresholds, we found that 99.8% of points pass the comparison, even in the distal falloff region, as shown in the next figure. A similar capability was demonstrated recently by (Grevillot et al. 2012) using GATE, though their simulations were started at nozzle exit and may not reproduce the beam halo accurately.
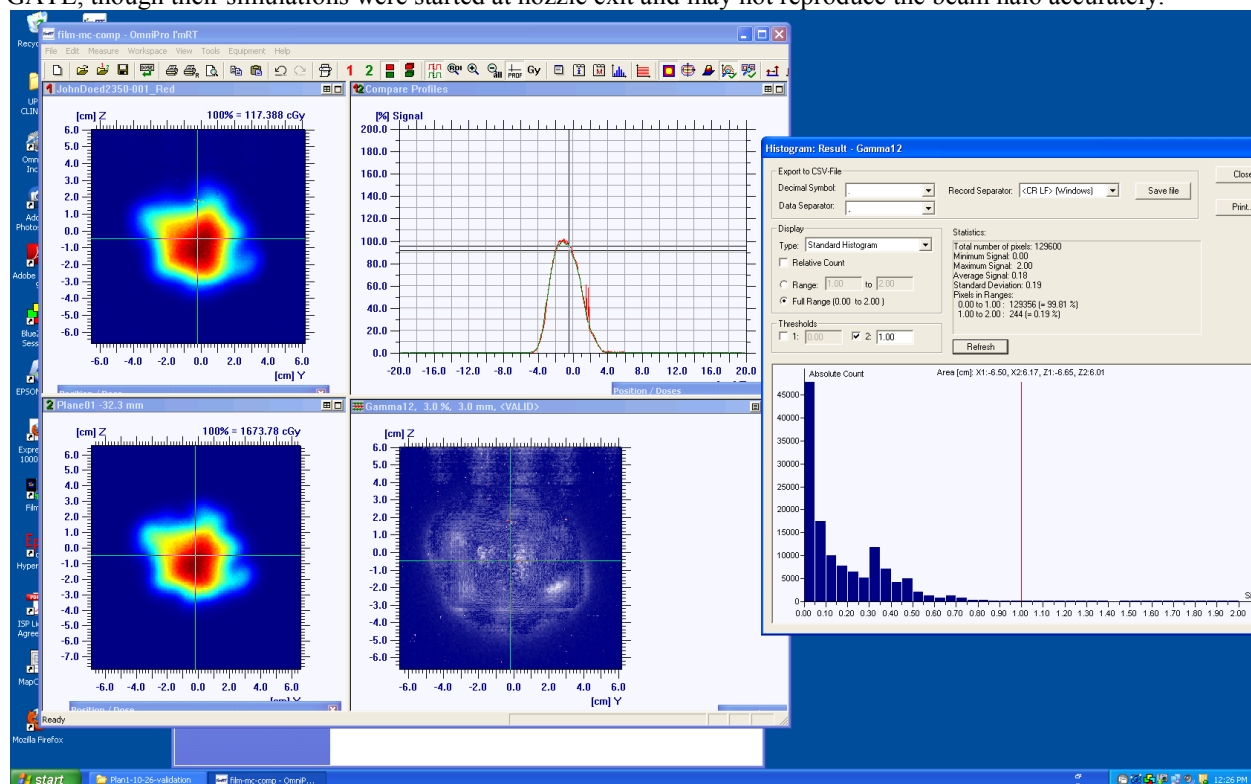
The prostate field was also measured with the IBA Matrixx and the results are consistent with the film measurements.

To examine the beam halo, ring patterns were delivered to film at Penn. The halo contribution is amplified at the center of the ring. The next figure shows a gamma comparison for one of the rings with an especially large halo (using the range shifter). At the center of the ring, the measured dose is 4.6% (of maximum) but the simulation onlygives 2.2%. At this level of agreement, 92% of points pass gamma analysis with 3% /3 mm thresholds.It is believed that there is an additional halo contribution generated in the focusing quadrupole magnets that can be even worse at shallower depths (see the next figure).

70
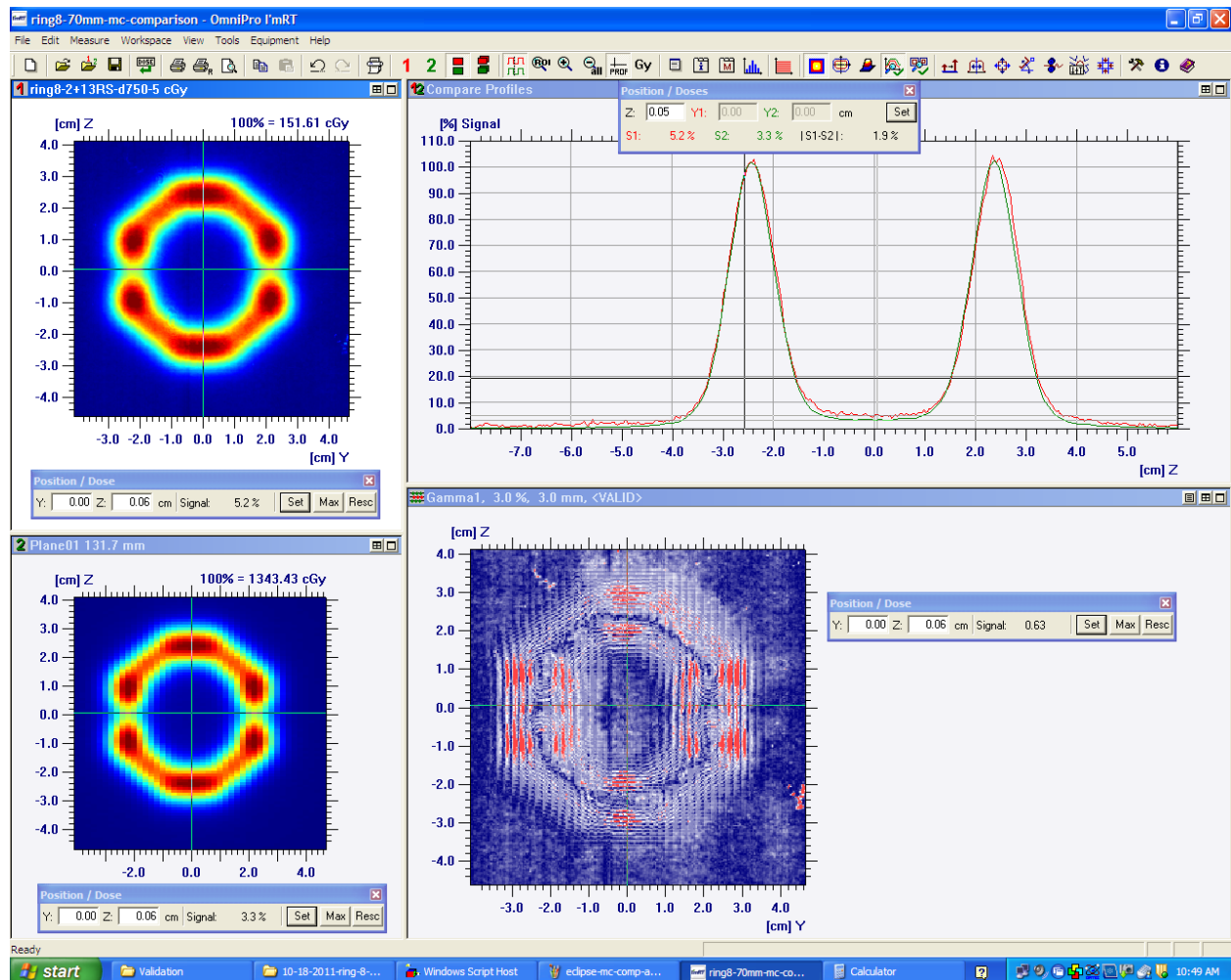
At shallower depths we have observed tails for the beam profile that appear to be quite long but in only one transverse dimension. In the next figure, at the 7.0 cm depth, the beam tails are quite long in the horizontal direction. This leads to as much as 8% of the prescription dose outside of the treatment target. We are still trying to understand the mechanism that is generating such a large beam halo in the one dimension.
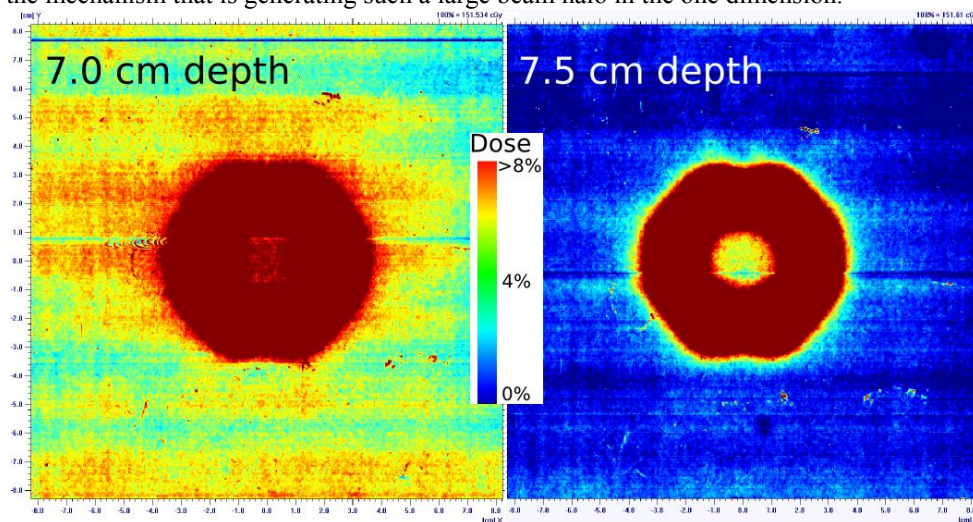
To get a better picture, we have measured spot profiles for a range of energies down to the 0.01% level. An example is shown in the next figure. This is time consuming, because it takes multiple deliveries of varying dose levels to different pieces of film. The film measurements are normalized and "stitched together" to produce a spot profile measured to very low dose levels.
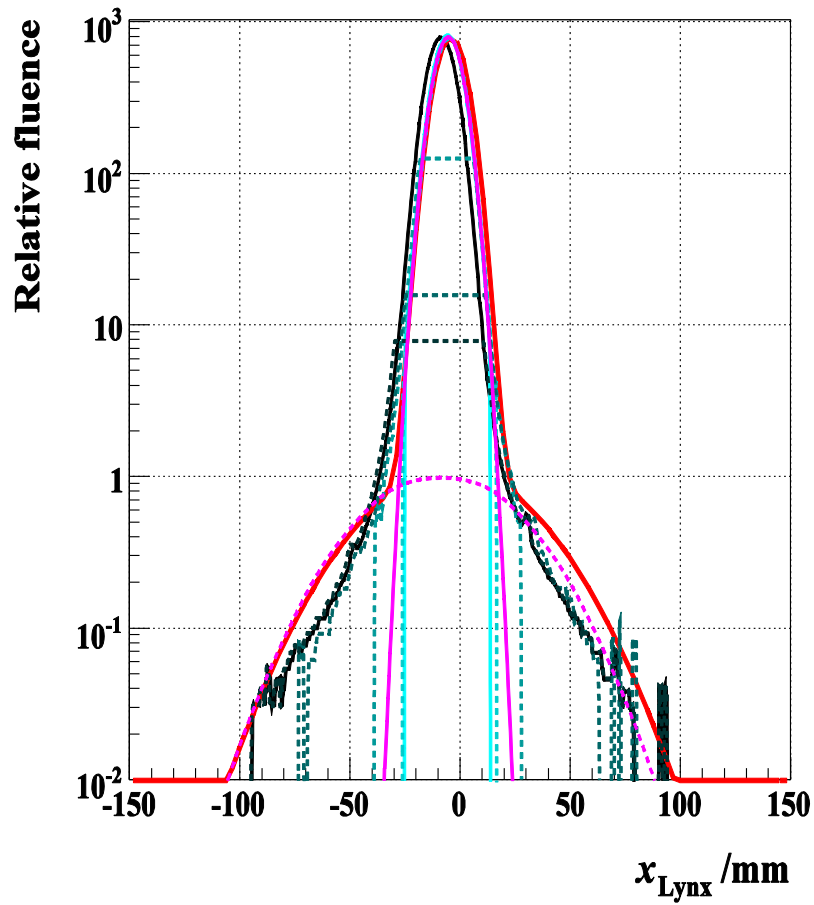
Phase III. Image Guided and Adaptive Proton Therapy

Cone Beam CT (CBCT) for proton Therapy

A major goal of phase III was the development of cone beam CT for proton therapy. Despite several years of intensive efforts to explore, alone or with several vendors, the feasibility of development of this device, we failed to find a solution that will have high likelihood of success until couple of years ago. At this point of time IBA introduced to us their idea to develop and install CBCT on a proton gantry which will use an upgraded version of the two orthogonal panels and X-Rays tubes that are currently installed on the gantry . We have reached an agreement with IBA regarding CBCT scanners and formalized a contract. The agreement is that IBA will install two CBCTs on the proton gantries in Room 1 and Room 3. They will use the two orthogonal imaging devices that we already have on the gantries and modify them with new flat panels; x-ray tubes, and an all-new control system to enable us to acquire CBCT images while rotating the gantries. The first installation is l projected to occur in early-2013, and we are starting to evaluate the planned workflow with these devices.

We had previously requested and were granted a no-cost extension with a new Scope-of-Work to perform the adaptive proton study. The protocol has not been modified and continues to enroll patients successfully, the data from whom we will continue to collect and analyze.

Telemedicine– Walter Reed

Introduction-Summary

An integral goal of cooperative agreement DAMD17-W81XWH-04-2-0022 focused on the development of remote proton treatment planning capabilities between the Walter Reed Army Medical Center and the University of Pennsylvania's Roberts Proton Therapy Center. To our knowledge, such a telemedicine platform had never been designed and successfully deployed in a clinical environment prior to this effort. Over the course of our research, several systems were designed and evaluated. It is our hope the robust system we eventually designed, tested and deployed, will not only serve our local DoD beneficiaries, but also be replicated at national Military Treatment Facilities, in partnership with their regional proton therapy centers.

Body

During phases 1 through 3 of this research, the Walter Reed Army Medical Center and the University of Pennsylvania designed and tested a series of solutions intended to meet the following deliverables (language taken from the original cooperative-agreement): 1) validation of the prototype-system (hardware/software), 2) development of communication protocols for electronic transfer of treatment plans, 3) comprehensive "operational" testing of the multi-source multi-zone telemedicine system, and 4) final evaluation, fine-tuning and implementation of solution. These goals were challenged by several operational and legal issues, such as integrating into existing clinical systems, meeting network security obligations at both sites, or addressing HIPAA-privacy concerns during the manipulation and transfer of patient data between sites.

Over the course of this research, several solutions were designed and tested, the two major ones resulting in publications (please see two references). The first solution consisted of a Polycom PVX-powered remote proton treatment system, 1) giving physicians the ability to remotely participate in refining and generating proton therapy plans via a secure and robust Internet2 VPN tunnel to the University of Pennsylvania's commercial proton treatment planning package, 2) allowing cancer-care providers sending patients to a proton treatment facility to participate in treatment planning decisions by

enabling referring or accepting providers to initiate ad-hoc, point-to-point communication with their counterparts to clarify and resolve issues arising before or during patient treatment, and thus 3) allowing stewards of an otherwise highly centralized resource the ability to encourage wider participation with and referrals to sparsely located proton treatment centers by adapting telemedicine techniques that allow sharing of proton therapy planning services.

When the DoD communicated its decision to no longer support the application-sharing portion of the Polycom PVX product, a much-needed functionality for remote treatment planning, our team was forced to pursue other avenues. Our second major initiative, one which led to the system currently in use at the Walter Reed National Military Medical Center, relied on a hybrid remote proton radiation therapy solution merging a CITRIX server (now Juniper) with a JITIC-certified desktop videoconferencing unit. This conduit, which met both HIPAA guidelines and the more stringent security restrictions imposed by the DoD, integrated both institutions' radiation oncology treatment planning infrastructures into a single entity for DoD patients' treatment planning and delivery. This system enabled DoD radiation oncologists and medical physicists the ability to 1) remotely access a proton therapy treatment planning platform, 2) transfer patient plans securely to the UPenn patient database, and 3) initiate ad-hoc point-to-point and multi-point video conferences to dynamically optimize and validate treatment plans.

Adaptive Radiation Treatment for Changes in Tumor Motion and Volume

OVERVIEW

In recent years, conformal techniques have been developed that allow for precise delivery of radiotherapy to the primary tumor and regional lymphatics while minimizing the dose to normal tissues. These approaches are predicated upon precise anatomic localization of the regions to be irradiated. Unfortunately, at present, most conformal treatment delivery approaches do not account for changes in tumor volume, tumor motion or changes in patient anatomy during the time course of definitive radiotherapy. Proton beam radiotherapy can potentially allow for ultra-precise delivery of treatment due to the physical characteristics of the proton beam. Therapeutic proton beam radiotherapy allows for the elimination of exit dose and a significant reduction in the entrance dose to the patient while maximizing dose delivered to the tumor (Figure 1). However, accurate treatment delivery with proton beam radiation is predicated upon precise definition of tumor volume and location. Tumor volume reduction during definitive proton beam radiotherapy has resulted in significant dosing errors, with dose deposition in unintended regions (MDACC PTCOG 47). The purpose of this protocol is to quantify the extent of tumor volume, motion, and anatomic changes that occur during the tumor course of definitive photon beam radiotherapy. As both proton beam and photon beam radiotherapy have nearly identical biological efficacy, the changes observed during photon beam radiotherapy should closely approximate that which would likely be observed during proton beam irradiation. The long-term goal is to use this data to develop an adaptive treatment approach for proton and photon beam radiation.
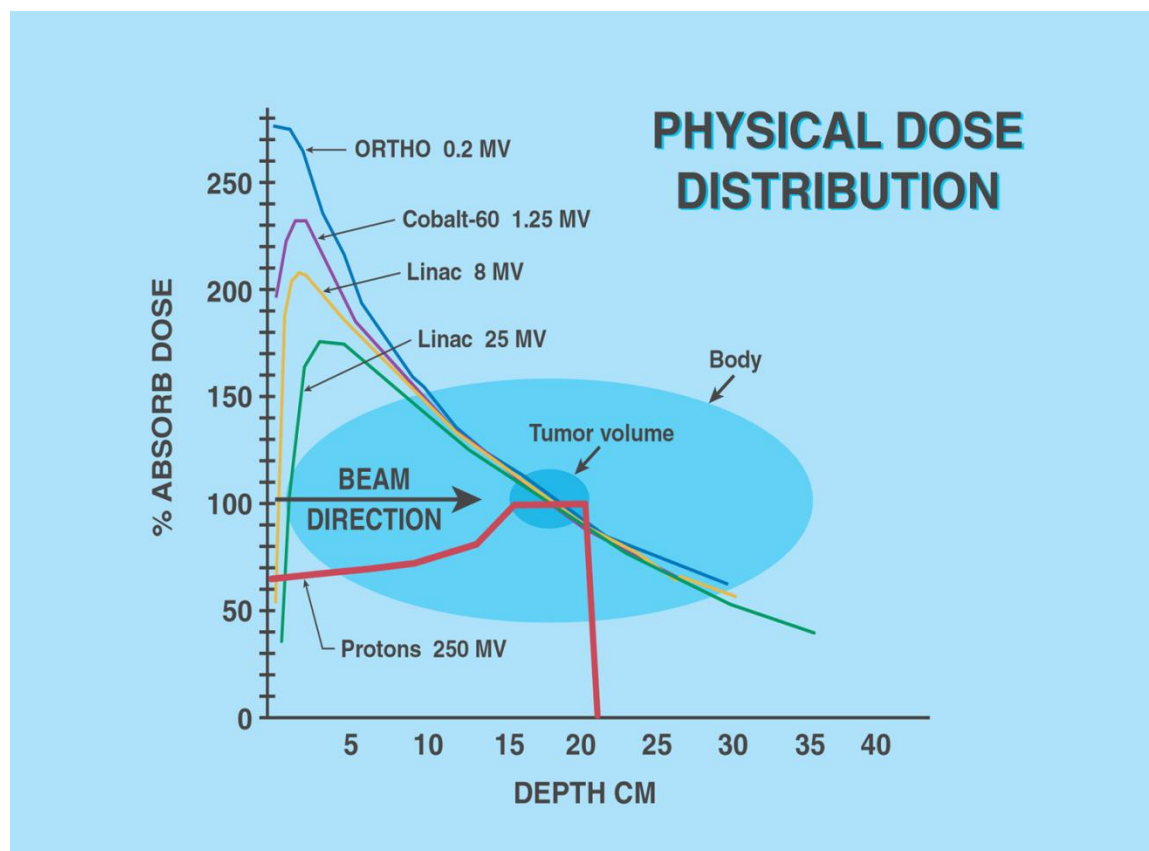
Figure 1: Comparison of Dose Deposition between Photon and Proton Beam Radiotherapy

SPECIFIC AIMS/OBJECTIVES

Overall Aim

To estimate the degree of tumor volume, tumor motion, and patient anatomy changes that occur during the time course of definitive photon and proton beam radiotherapy. To use the data obtained in this study to ultimately develop an adaptive radiotherapeutic approach that accounts in fast dose calculation engine to allow for adaptation to account for these changes

Primary Aim

To estimate the degree of tumor volume, tumor motion and patient anatomy change during treatment with photon beam radiotherapy using weekly 4D or 3D CT Scans and use this data to develop a fast dose calculation engine to allow for treatment adaptation.

Secondary Aims

To estimate the degree of tumor volume, tumor motion and patient anatomy change during treatment with proton beam radiotherapy using weekly 4D or 3D CT Scans

Progress

The protocol received Penn IRB approval to open for recruitment in November 2009 and is expected to complete accrual in November 2014. The protocol enrollment goal is 120 subjects with 30 patients per stratum (e.g. gynecologic cancers).

From 08/2010 until 10/1/2012, we screened 66 people and of the 66, enrolled 63 people on the Adaptive protocol. With 63 enrolled subjects, we met 52.5% of the protocol enrollment goal (N=120). Among the total 63 enrolled subjects, the breakdown per stratum is: 29 lung (SCLC and NSCLC), 9 GI, 22 GYN, and 3 head & neck. Demographic data shows: 23 male, 40 female, 44 white, 17 black, and 2 Asian.

Among the 63 enrolled subjects, 47 individuals completed the protocol while 16 were withdrawn. Among the 16 withdrawn cases: 10 lung, 1 head & neck, 4 GYN, and 1 GI.

Study Group	Current Count
Lung	29
GI	9
GYN	22
Head & Neck	3
TOTAL ENROLLMENT	63

	Current Count
Completed	47
Withdrawn	16
TOTAL ENROLLMENT	63

Sex	Current Count
Male	23
Female	40
TOTAL ENROLLMENT	63

Race	Current Count
White	44
White, Hispanic	0
Black	17
Asian	2
Other	0
TOTAL ENROLLMENT	63

Image quantification on the accrued data sets continues. Data analysis will examine the effect of tumor and patient anatomy changes on radiation treatment efficacy and will be initiated once contours are complete on current patients. To date, contouring has been completed for 9 GI, 22 gynecologic, 2 head and neck, and 10 lung patients. From a random sampling of patients, a GI patient involves contouring roughly 700 images, 40 images for a gynecologic patient, 50 for a head and neck patient, and 900 images for a lung patient. Contouring for the remaining patients will be completed within the next 1-2 months. Once contouring is complete, tumor volume and motion data will be tabulated and analyzed by Dr. Kevin Teo beginning in November 2012.

Preliminary data analysis may be completed in time for abstract submission to the American Society of Clinical Oncology in early 2013.

Report for the Proton Beam Allocation Project

Most of the work in this project is done in Phase IV of the award and is being reported with this award. The work is continuing.

We have made progress on three fronts: designing the real-time beam allocation application, building a simulation study focused on investigating the performance of beam allocation algorithms under stochastic durations of preparation and field times, and studying the influence of different patient sequencing schemes on throughput performance.

Key Research Accomplishments

Phase I

Multileaf collimator was successfully developed and constructed. The device got FDA approval and was installed on four proton gantries at UPENN, Roberts Proton Therapy Center .
The device is being used routinely for patients' treatment which is the ultimate success of this research goal.

Phase II

- rocured, installed, and upgraded a computing cluster (now 116 CPUs) that is shared by the research group at Penn.
- Developed a method to generate a PBS beam data library to commission a treatment planning system that fits vendor specifications for size of the primary Gaussian spot.
- Generated beam data libraries for the IBA Dedicated and Universal nozzles.
- Achieved a ridge filter design that reduces the number of energy layers required to treat shallow targets.
- Implemented several HU-to-Material calibration curves for simulations: tissue-based calibration, water-only calibration, prostate and brain site-specific calibrations.
- Developed the ability to perform fast spot weight optimization based on the Cimmino algorithm using Geant4 Monte Carlo calculated dose kernels.
- Developed DICOM I/O capabilities in support of simulations: CT datasets, RT Plan files (MLC leaf positions, compensator milling pattern, gantry and couch positions, etc), RT Structure files, writing out dose files and isotope maps.
- Implemented the IBA Pencil Beam Scanning delivery system for the Universal and Dedicated Nozzles in Geant4 simulation. Validated against measured data using gamma 3%/3mm criteria (>99% points pass).
- Developed a novel technology based on Micromegas providing good spatial resolution in two dimensions and fine time resolution for proton therapy dosimetry.

Phase III

Cone beam CT will be installed by IBA at UPENN proton therapy facility in 2013.

As indicated above, Walter Reed National Military Medical Center now has a fully functional remote proton treatment planning solution, one which has the potential to positively impact radiation oncology-care for our DoD beneficiairies.

We believe the four deliverables listed in the original language of the first cooperative-agreement have been met, as the remote proton treatment planning system was deployed shortly before the Walter Reed Army Medical Center and the National Naval Medical Center merged in September 2011. The system is now in-use at the Walter Reed National Military Medical Center, as both a research and clinical platform. Using telemedicine sytem that was developed as part of this research patients are being planned for proton therapy at Bethesda Maryland and their treatment is being delivered in Philadelphia.

Reportable outcomes

Phase I- MLC publications

Research articles (published)

[1]   E Diffenderfer, C Ainsley, M Kirk, J McDonough, R Maughan: Comparison of secondary neutron dose in proton therapy resulting from the use of a tungsten alloy MLC or a brass collimator system. Med. Phys. 38(11): 6248-6256, November 2011

[2]   E Diffenderfer, C Ainsley, M Kirk, J McDonough, R Maughan: Reply to Comment on "Comparison of secondary neutron dose in proton therapy resulting from the use of a tungsten alloy MLC or a brass collimator system" Med. Phys. 39(4): 2306-2309, April 2012

Research articles (in preparation)

[1]   C Ainsley *et al.*: Monte Carlo simulation and development of a multileaf collimator for proton therapy

[2]   C Ainsley *et al.*: Shielding tests of a multileaf collimator for proton therapy

[3]   C Ainsley *et al.*: Monte Carlo study of the dosimetric characteristics of a multileaf collimator for proton therapy

[4]   C Ainsley *et al.*: Practical consequences of the use of a multileaf collimator for proton therapy

[5]   C Ainsley *et al.*: Optimization of Monte Carlo model parameters for the simulation of a commercial proton therapy double scattering system

Scientific abstracts

[1]   AAPM 49th Annual Meeting, Minneapolis, MN, USA (July 2007)
      "Perturbation to dose distribution caused by utilizing an MLC instead of a brass aperture in passive scattering proton therapy"
      D Goulart, R Maughan, J McDonough, P Bloch, S Avery, C Ainsley

[Poster]

[2]   AAPM 49th Annual Meeting, Minneapolis, MN, USA (July 2007)

"Investigation of the impact of leaf design on the radiation leakage through a multileaf collimator for use in proton radiotherapy"

C Ainsley, S Avery, R Maughan, J McDonough, P Bloch, D Goulart, M Ingram

[Oral]

[3]   PTCOG 47, Jacksonville, FL, USA (May 2008)

"Designing a multileaf collimator for proton therapy"

C Ainsley, S Avery, R Maughan, J McDonough, J Metz, R Scheurermann, Z Tochner

[Poster]

[4]   AAPM 51st Annual Meeting, Anaheim, CA, USA (July 2009)

"Monte Carlo simulation and development of a multileaf collimator for proton therapy"

C Ainsley, R Scheuermann, S Avery, D Dolney, R Maughan, J McDonough

[Moderated poster]

[5]   AAPM 51st Annual Meeting, Anaheim, CA, USA (July 2009)

"Determination of neutron dose due to a therapeutic proton beam incident on a closed tungsten MLC using the dual hydrogenous/non-hydrogenous ionization chamber method"

E Diffenderfer, R Maughan, C Ainsley, S Avery, J McDonough

[Oral]

[6]   PTCOG 48, Heidelberg, Germany (September 2009)

"Design and performance of a multileaf collimator for proton therapy"

C Ainsley, S Avery, E Diffenderfer, D Dolney, L Lin, J McDonough, J Metz, R Scheuermann, Z Tochner

[Poster]

[7]   AAPM 52nd Annual Meeting, Philadelphia, PA, USA (July 2010)

"Comparison of proton MLC with non-divergent brass and tungsten apertures"

M Kirk, C Ainsley, J McDonough

[Poster]

[8]   PTCOG 50, Philadelphia, PA, USA (May 2011)

"Comparison of secondary neutron dose in proton therapy resulting from the use of a tungsten MLC or a brass aperture system"

E Diffenderfer, C Ainsley, J McDonough, R Maughan

[Poster]

[9]   PTCOG 50, Philadelphia, PA, USA (May 2011)

"Design, testing and characterization of a multileaf collimator for proton therapy"

C Ainsley, S Avery, E Diffenderfer, D Dolney, M Kirk, L Lin, R Maughan, J McDonough, J Metz, R Scheuermann, Z Tochner

[Oral]

[10] PTCOG 50, Philadelphia, PA, USA (May 2011)

"Optimizing Monte Carlo parameters to fit proton-beam measurements with a tungsten MLC"

M Kirk, C Ainsley, D Dolney, J McDonough

[Poster]

Phase II- publications (Research articles-in preparation)

[1]   A manuscript about the novel two-dimensional proton dosimetry technology has been submitted to a Special Issue titled "Detectors for Hadron Therapy: Operational Principles, Techniques, and Readout" of the journal Physics Research International. It is attached as an Appendix.

[2]   A manuscript about the generation of beam data libraries from vendor specs has been prepared for publication. It is resected stage IIIA non-small cell lung cancer was prepared and is being submitted for publication attached as an Appendix.

[3]   A manuscript comparing proton therapy modalities with IMRT for postoperative radiotherapy in completely

. It is attached as an Appendix.

Abstracts

- Oral Presentation (speaker: Derek Dolney): R. Hollebeek, M. Newcomer, G. Mayers, B. Delgado, G. Shukla, R. Maughan, D. Dolney, "A New Technology for Fast Two-Dimensional Detection of Proton Therapy Beams", IEEE Nuclear Science Symposium, Medical Imaging Conference (2012).
- Poster: K. Noa, J. Christodouleas, D. Dolney, A. Kassaee, Comparison of treatment plans with photons using intensity modulated radiation therapy and protons using pencil beam scanning for pelvic nodes, AAPM Annual Meeting (2012).
- Poster: J. Durgin, D. Dolney, J. McDonough, "Treatment Time Reduction for Proton Modulated Scanning Beams Using a Ridge Filter", AAPM 52nd Annual Meeting, Philadelphia, PA (2010).
- Poster: S. Both, T. Zhu, J. Finlay, X. Zhu, R. Slopsema, D. Dolney, J. McDonough, "An Independent Program for MU Check of Modulated Scanning Beam for IMPT", AAPM 51st Annual Meeting, Anaheim, CA (2009).
- Proposal: "A detector system for imaging radiotherapeutic dose distributions in 4D" submitted to Recovery Act Limited Competition: NIH Challenge Grants inHealth and Science Research (RC1) submitted to NIH, submitted 2009, not funded.
- Proposal: NIH R21 "An investigation on the use of Micromegas technology for proton therapy dosimetry", submitted 2009, not funded.
- Proposal: NIH R21 "Three-Dimensional Dosimetry for Proton Therapy using Micromegas Detectors", submitted 2010, not funded.
- Proton dosimetry with Micromegas ranked top 4 among ideas at the University of Pennsylvania competing for a Keck Foundation award.
- Proposal: NIH R01 "Three-Dimensional Dosimetry for Proton Therapy using Micromegas Detectors", submitted 2012.
- Derek Dolney invited to interview for the position of Research Physicist at St. Jude Children's Hospital (Nov 2012).

Phase III- publications (Research articles -published]

[1]   Development of a remote proton radiation therapy solution over internet2. Belard A., Tinnel B., Wilson S., Ferro R., O'Connell J., Telemed J E Health. 2009 Dec;15(10):998-1004.

[2]   Improving proton therapy accessibility through seamless electronic integration of remote treatment planning sites. Belard A, Dolney D, Zelig T, McDonough J, O'Connell J., Telemed J E Health. 2011 Jun;17(5):370-5.

Conclusion

We have successfully advanced an developed several key technologies to advance and move proton therapy to the next stage.
1.We built clinical MLC for proton therapy.

2. There are several very positive outcomes from Phase II of the award. Most notable is the development of a new detector technology for proton therapy dosimetry. This two-dimensional layer achieves better spatial and time resolution than was previously available. The investigators believe that this technology can be assembled into a system to provide full three-dimensional dosimetry, which is not currently available.
Additionally, a capability has been developed to compute dose distributions for patient treatment fields using Geant4 Monte Carlo (i.e., the forward dose calculation). The method requires some more validation against measurements (e.g., in heterogeneous media), but could be applied clinically.
The capability has been developed to do inverse treatment planning and spot-weight optimization using Monte Carlo calculated dose kernels. The kernel generation is still time-consuming, however the cost function is flexible and could incorporate LET/TCP/NTCP information, or be otherwise modified for robust treatment planning.

3.Our robust and secure remote treatment planning solution not only grants DoD patients access to a state-of-the-art treatment modality, it also allows participation in the treatment planning process by DoD radiation oncologists and medical physicists.

This telemedicine system, one which we hope to improve overtime, has the potential to lead to a greater integration of military treatment facilities and/or satellite clinics into regional proton therapy centers.

4. We are installing the first CBCT in proton therapy.

Appendices

| W81XWH-04-2-0022
Award Period: 05/17/2004 - 10/31/2012
List of personnel (not salaries) receiving pay from the research effort | |

Name	Role
AINSLEY,CHRISTOPHER	Postdoctoral Researcher
APPENZOLLER,LINDSEY	Summer Student
AVERY,STEPHEN	Co-Investigator
BALDYTCHEV,MAXIM	Graduate Student
BLOCH,PETER H	Co-Investigator
BOTH,STEFAN	Co-Investigator
BUI,STEPHANIE	Research Assistant
DELGADO,BRIAN M	Summer Student
DIIANNI,SAMUEL	Grants Administrator
DOLNEY,DEREK	Postdoctoral Researcher/Instructor
DURGIN,JAMES L	Graduate Student
EGAN,ALEXANDER JOSEPH	Summer Student
FERRO,RALPH J	Computer Technician
FOWLER,SUSAN J	Summer Student
GOULART,DICKSON C	Postdoctoral Researcher
HOLLEBEEK,ROBERT JOHN	Co-Investigator
INGRAM,MARK S	Graduate Student
JOZWIAK,MICHAEL	Computer Technician
KARASICK,TODD	Summer Student
KEENER,PAUL T	Systems Programmer

KIRK,MAURA L	Graduate Student
KLEIN,STUART L	Grants Administrator
MAUGHAN,RICHARD	Co-Investigator
MAYERS,GODWIN M.	Electrical Mechanical Designer
MCDONALD,CLIFFORD S.	Summer Student
MCDONOUGH,JAMES E.	Co-Investigator (former PI)
MCKENNA,W GILLIES	Former PI
METZ,JAMES M.	Co-Investigator
MICK,ROSEMARIE	Co-Investigator
NEWCOMER,F MITCHELL	Electronics Engineer
PATRICK,MARK S	Grants Administrator
PRENDERGAST,SUSAN	Research Nurse
REILLY,MICHAEL B	Electrical Mechanical Designer
RENGAN,RAMESH	Co-Investigator
REY,FELIPE	Medical Resident
ROSENFIELD,JONATHAN R	Graduate Student
SCHEUERMANN,JOSHUA S.	Graduate Student
SCHEUERMANN,RYAN M	Graduate Student
SHARKOSKI,TIFFANY E.	Clinical Research Coord.
SHUKLA,GAURAV	Summer Student
SMITH,DEBORAH	Research Nurse
STEIN,SARAH A	Summer Student
TOCHNER,ZELIG A.	PI
VAPIWALA,NEHA	Project Leader
WANG,YI WEI	Summer Student
XANTHOPOULOS,ERIC	Medical Resident

Phase I -journal publications – published

Comparison of secondary neutron dose in proton therapy resulting from the use of a tungsten alloy MLC or a brass collimator system

Eric S. Diffenderfer, Christopher G. Ainsley, Maura L. Kirk, James E. McDonough, and Richard L. Maughan
Department of Radiation Oncology, University of Pennsylvania, Philadelphia, Pennsylvania 19104

Purpose: To apply the dual ionization chamber method for mixed radiation fields to an accurate comparison of the secondary neutron dose arising from the use of a tungsten alloy multileaf collimator (MLC) as opposed to a brass collimator system for defining the shape of a therapeutic proton field.

Methods: Hydrogenous and nonhydrogenous ionization chambers were constructed with large volumes to enable measurements of absorbed doses below 10_{-4} Gy in mixed radiation fields using the dual ionization chamber method for mixed-field dosimetry. Neutron dose measurements were made with a nominal 230 MeV proton beam incident on a closed tungsten alloy MLC and a solid brass block. The chambers were cross-calibrated against a $_{60}$Co-calibrated Farmer chamber in water using a 6 MV x-ray beam and Monte Carlo simulations were performed to account for variations in ionization chamber response due to differences in secondary neutron energy spectra.

Results: The neutron and combined proton plus c-ray absorbed doses are shown to be nearly equivalent downstream from either a closed tungsten alloy MLC or a solid brass block. At 10 cm downstream from the distal edge of the collimating material the neutron dose from the closed MLC was $(5.3 \dot{6} 0.4)\_10\__5$ Gy/Gy. The neutron dose with brass was $(6.4 \dot{6} 0.7)\_10\__5$ Gy/Gy. Further from the secondary neutron source, at 50 cm, the neutron doses remain close for both the MLC and brass block at $(6.9 \dot{6} 0.6)\_10\__6$ Gy/Gy and $(6.3 \dot{6} 0.7)\_10\__6$ Gy/Gy, respectively.

Conclusions: The dual ionization chamber method is suitable for measuring secondary neutron doses resulting from proton irradiation. The results of measurements downstream from a closed tungsten alloy MLC and a brass block indicate that, even in an overly pessimistic worst-case scenario, secondary neutron production in a tungsten alloy MLC leads to absorbed doses that are nearly equivalent to those seen from brass collimators. Therefore, the choice of tungsten alloy in constructing the leaves of a proton MLC is appropriate, and does not lead to a substantial increase in the secondary neutron dose to the patient compared to that generated in a brass collimator.Vc 2011 American Association of Physicists in Medicine. [DOI: 10.1118/1.3656025]

I. INTRODUCTION

In recent years, most effort in measuring secondary neutron doses in proton therapy has focused on estimating the dose to the patient outside of the treatment field either laterally or beyond the spread out Bragg peak. Secondary neutrons produced by interactions of the proton field with beam modifying devices (e.g., double scattering system, beam shaping collimators, and range compensators) and the patient have been studied by many authors.[1–23] These secondary neutrons are responsible for whole body irradiation of high LET particles at low dose levels where the long term effects are not fully understood.[24–27] Consequently, there is some concern of radiation-induced secondary cancers in patients treated therapeutically with protons.[28]

These concerns are also important when using a multileaf collimator (MLC) in place of brass or Lipowitz's metal collimators because of the effect that the MLC may have on secondary neutron dose. Moyers et al.[10] found that most secondary neutrons are produced in the final collimator of a passive scattering proton system. Tayama et al.[8] measured secondary neutron dose from a passively scattered proton beam and determined that adjustment of the aperture diameter of a brass MLC precollimator can reduce the neutron dose equivalent outside of the treatment field. Taddei et al.[11] found a reduction in neutron equivalent dose through Monte Carlo simulations replacing the brass final collimator with a tungsten collimator of the same thickness. Brenner et al.[13] used Monte Carlo simulation to study changes in neutron dose as a function of collimator material and thickness. Daartz et al.[14] used a Bonner sphere to measure an increase of up to two-fold in neutron equivalent dose when using a tungsten MLC in place of a brass final collimator.

In the present paper, we are interested in comparing the secondary neutron dose arising from the use of a tungsten alloy MLC, which is in use on the double scattering and uniform scanning beam lines at the University of Pennsylvania Roberts Proton Therapy Center, to a brass collimator system for defining the lateral field shape. We have measured neutron absorbed dose due to a proton beam of the highest energy available from our cyclotron. Measurements were performed downstream from a closed tungsten alloy MLC or solid brass block. This is an extreme case which does not represent a realistic clinical situation, but offers the best

geometry for making a quantitative comparison of secondary neutron production for a tungsten alloy MLC and brass collimator system.

Based on nuclear cross-sections for proton–neutron interactions in tungsten or brass, one would expect tungsten to produce the greater neutron flux. However, when constructing the MLC it is necessary to use a thickness of tungsten alloy equivalent to slightly greater than twice the range of the highest energy protons, because the leaf design must incorporate side- and end-steps to prevent interleaf leakage. In a solid brass collimator, a thickness equivalent to just over one proton range is used and the thickness can be adjusted according to the energy of the incident protons. Although more neutrons are produced in a tungsten alloy MLC, due to increased thickness there is substantial self attenuation[13] of the neutron flux which is not present in the thinner brass collimator, the difference being particularly pronounced at the highest proton energies.

Previous efforts aimed at measuring the out-of-field neutron doses produced by a therapeutic proton beam have employed instruments that are traditionally used in a radiation protection setting such as Bonner spheres,[29] long counters,[30] scintillation counters,[30] superheated neutron bubble detectors,[31] or foil activation techniques.[32] Measurements with these instruments are reported in terms of dose equivalent (Sv), which is a product of the absorbed dose (Gy) and a

neutron energy-dependent radiation weighting factor. Often commercial devices are used for these measurements with vendor-supplied calibrations that give no specifics of the radiation weighting factors used. Bonner spheres employ a boron trifluoride (BF$_3$) or $_3$He filled counter to detect neutrons which have been thermalized by a thick polyethylene moderator. The size of the moderator, which must be increased to accommodate higher energy neutrons, therefore limits their spatial resolution. Although neutron bubble detectors can have good spatial resolution, their accuracy is statistically constrained by the maximum number of bubbles that can be reliably counted, a number that is on the order of 100 bubbles per exposure.[31,33] The energy response of these detectors is often limited and they are, therefore, expected to under-respond to the secondary neutron dose produced by high energy therapeutic proton beams (_230 MeV), since these beams contain large numbers of high energy neutrons. Typically Bonner spheres, long counters, and bubble detectors respond to neutrons with energies up to 10–20 MeV. Recently, survey instruments have been developed with extended energy response. Such instruments include a Bonner sphere[34] and a long counter[35] with modified moderator, and an instrument based on scintillation counters.[36] These devices have large volumes and therefore poor spatial resolution and the uncertainties in their calibration factors can be considerable.

The measurements of Binns *et al.*[1] used a tissueequivalent proportional counter (TEPC) to study the microdosimetric spectra resulting from proton interactions with the dose delivery system. Such measurements have the advantage of providing absorbed dose measurements as a function of lineal energy. This can then be used to assign appropriate radiation weighting factors or relative biological effectiveness (RBE) for calculating dose equivalent in Sv or Gy(RBE).[37] While a commercial instrument is available which incorporates a TEPC and multichannel analyzer in a single portable device (REM 500, Far West Technology, Inc., Goleta, CA), this instrument lacks the spectral dynamic range that is required for precision microdosimetric measurements. Precise measurements require careful control of gas pressure in the TEPC and the use of 2–4 amplification channels to acquire the entire signal dynamic range. It is likely due to the increased challenge these difficulties present that this method has not been widely pursued for measuring secondary dose in proton therapy fields.

Ionization chambers such as those that are routinely used in radiation therapy dosimetry and quality assurance would tend to alleviate these issues were it not for the large background of leakage protons passing through the interleaf gaps of the MLC and c-rays induced through (p,c) and (n,c) reactions. These chambers are typically constructed of tissueequivalent (TE) materials and respond to neutrons, protons, and c-rays with equivalent sensitivities. However, the neutrons display different LET and radiation weighting factors from the protons and c-rays, so their respective dose contributions must be separated in some way.

We determine the absorbed neutron and combined leakage proton plus c-ray (pþc) absorbed doses directly by means of a dual ionization chamber method originally developed as a mixed-field dosimetry technique used to separate the neutron dose from the background neutron-induced c-ray dose in fast neutron therapy beams.[38] An advantage of this technique is that it determines absorbed dose and allows the user to input appropriate radiation weighting factors or RBE to calculate dose equivalent or RBE-weighted dose, respectively. In this technique, two ionization chambers with different sensitivities to the two types of radiation are used to evaluate the separate absorbed doses of neutrons and c-rays. The contribution from interleaf leakage protons to the absorbed dose cannot be separated from that due to c-rays, but this has little impact because the RBE of protons and crays are relatively close and generally small compared to that of neutrons.[39] The chambers are constructed to have approximately the same sensitivity to protons and c-rays, while one of the two is designed to be relatively insensitive to neutrons compared to the other. This was accomplished by constructing one chamber using materials that closely mimic the dose response of tissue exposed to proton, c-ray, and neutron radiation; for neutrons, this ideally requires the chamber wall and gas to simulate the atomic composition of tissue exactly. In practice, this is not possible in a solid material and matching hydrogen content (i.e., using hydrogenous materials) is a good compromise since most of the neutron kerma originates from (n,p) elastic scattering interactions.[38] In contrast, the other chamber is constructed using materials with relatively low neutron interaction crosssections (i.e., using nonhydrogenous and higher atomic number (Z) materials).

The absorbed dose of secondary neutron or pþc radiation downstream of a closed collimator or outside of a

therapeutic proton beam is expected to be in the range 0.01%–0.5% of the primary open field proton dose,[1,2,7,32] depending on the delivery mode (e.g., scattering or scanning). Collection volumes of commercially available ionization chambers suitable for use in the dual ionization chamber method are on the order of 1 cm^3. The charge collected in a volume of this size for doses on the order of 0.2 mGy may therefore be as low as 5 pC. With a measured leakage charge of 2–4 pC over the elapsed time of dose delivery, the secondary radiation signal is easily lost in the noise due to current leakage. Therefore, we have designed and built a set of larger volume ionization chambers that increase the charge collection efficiency to an extent that exceeds the signal to noise ratio limits imposed by the leakage current. For instance, with a ten-fold increase in chamber volume over commercially available chambers and with reproducible charge leakage in the range of 2–4 pC, we estimate that doses as low as 0.2 mGy can be measured with an accuracy of approximately 6%.

II. METHODS AND MATERIALS

In the dual chamber method,[38] the two chambers are first calibrated in a reference photon field. When placed at the same point in a mixed field each exhibits an independent response according to its relative sensitivity to neutrons and pþc radiation. The dose responses of the chambers can be described as a simple sum of the products of their sensitivity to the separate types of radiation with the dose due to the respective radiation. In the following we will assign the subscript T to the chamber designed to have equal sensitivity to both neutrons, protons, and c-rays and we will assign U to the chamber designed to have lower relative neutron sensitivity. In the mixed field, the ratio of the dosimeter responses with their sensitivities to the photon field used for calibration, R^0_T and R^0_U, are given by

$$R^0_T = k_T D_n + h_T D_{p\flat c}; \quad (1)$$

and

$$R^0_U = k_U D_n + h_U D_{p\flat c}; \quad (2)$$

in units of absorbed dose. The parameters k and h are the respective sensitivities of the dosimeters to neutrons and pþc radiation relative to their sensitivities to the photon field used for calibration. Then, the absorbed dose to water from neutrons and pþc radiation, D_n and $D_{p\flat c}$, is obtained by solving Eqs. (1) and (2) simultaneously

$$D_n = \frac{(h_U R^0_T - h_T R^0_U)}{(h_U k_T - h_T k_U)}; \quad (3)$$

$$D_{p\flat c} = \frac{(k_T R^0_U - k_U R^0_T)}{(h_U k_T - h_T k_U)}: \quad (4)$$

The two components of dose as they are presented in Eqs. (3) and (4) depend on the relative sensitivities of the chambers to pþc and neutron radiation.

To implement the dual chamber method we have built a chamber using TE materials with nearly equal proton, c-ray, and neutron sensitivities and a second chamber constructed using higher Z material to obtain a lower sensitivity to neutron radiation. Both were based on a thimble-type ionization chamber design, providing an active volume of 9.14 cm^3. The walls of the ionization chambers are 0.318 cm thick with an inner diameter of 1.91 cm, Fig. 1. A Rexolite 1422 (C-Lec Plastics, Philadelphia, PA) polystyrene base supports the outer shell, the electrode, and the guard ring which reduces leakage current between the outer shell and inner electrode. The polystyrene base also provides an inlet and outlet port to the ionization chamber for gas flow through the

active volume. The gas flow is metered using an adjustablerate
flow-meter at a rate low enough to ensure that air is
completely flushed from the system without increasing the
chamber above atmospheric pressure. A thin-walled 1/4 00 diameter
aluminum stem attached to an aluminum base provides
a means of supporting the chamber in the radiation
field as well as routing the tri-axial cable and the 1/16 00 PVC
tubing that is used to provide gas flow. The TE chamber was
constructed with the outer shell, the inner electrode, and the
guard ring composed of A-150 TE plastic.[40] Methane-based
TE gas[38] flows through the chamber's active volume. For the
nonhydrogenous chamber, magnesium, and argon were the
wall material and gas of choice, respectively, due to their

FIG. 1. (a) Drawing of the large volume ionization chambers designed and built for use at the University of Pennsylvania's Roberts Proton Therapy Center. (b)
Image of the assembled Mg-Ar (top) and TE-TE (bottom) ionization chambers.

relatively low neutron interaction cross-sections. The construction
of this chamber is identical to the TE chamber
except that the magnesium components have been substituted
for the A-150 TE plastic components.

The chambers were cross-calibrated against a $_{60}$Co-calibrated
Exradin A12 (Standard Imaging, Middleton, WI)
Farmer-type ionization chamber (0.65 cm$_3$ active volume)
using the 6 MV x-ray beam of a Varian Clinac iX (Varian
Medical Systems, Palo Alto, CA) linear accelerator. The large
volume chambers were placed in 3.3 mm thick waterproof
PMMA sleeves within a 30_30_30 cm water phantom with
0.5 cm thick PMMA walls at an SSD of 100 cm, with the xray
beam delivered horizontally. Readings were taken at a
depth of 10 cm with stabilized gas flow through the large volume
chambers. The Exradin A12 readings were corrected
with the x-ray beam quality factor, k_Q¼0.994, which was
determined using the beam quality specification procedure of
Almond *et al.*[41] Additional corrections for leakage current,
temperature and pressure variations, polarity effects, ion collection
efficiency, and the electrometer calibration factor were
applied to all chamber readings. Table I shows active volumes
and calibration factors for the dosimeters.

Dual chamber measurements were made in air to compare
the secondary neutron dose for tungsten alloy and brass collimators.
All measurements of secondary radiation dose
from tungsten alloy were done with the MLC fully closed,
Fig. 2(a). Measurements with brass were completed by placing
a 12 cm diameter and 6.5 cm thick cylindrical brass
block directly downstream from the MLC with 20 open leaf
pairs of the MLC (each of physical width 4.35 mm and
roughly 9 cm thick) forming an 8.7 cm diameter circle, Fig.
2(b). An unmodulated proton beam with kinetic energy of
230 MeV was delivered in uniform scanning mode with no
lateral deflection and with all beam-line scatterers removed
so that the neutron production would be confined to the
MLC or brass collimator material. Readings were taken with
the chambers placed at isocenter 10 cm from the distal edge
of the closed MLC or brass block. To obtain a comparable
neutron source to detector distance and accounting for the

92

difference in collimator thickness, readings were also taken 50 cm downstream from the proximal edge of the closed MLC or brass block. Gas flow through the chambers was allowed to stabilize at the same flow rate used for calibration and chamber readings were corrected for all previously mentioned effects.

The proton beam used in this study was characterized with film and ionization chamber measurements. Lateral beam dose profiles with the MLC fully open were measured with film (Gafchromic EBT2, International Specialty Products, Wayne, NJ) placed at 0 and 32 cm depths in solid water plastic, where 32 cm depth is at isocenter. An 8.4 cm diameter plane parallel ionization chamber (Model 34070, PTW, Freiburg, Germany) was scanned in a water tank along the beam axis to measure the fractional depth dose profile. Implementation of the dual chamber method requires knowledge of the neutron energy spectrum for an accurate assessment of the dose response of the chambers. To this end, we have performed simulations of secondary radiation production from the proton beam at the University of Pennsylvania using the Geant4 simulation toolkit.[42] The simulations incorporate beam shaping components of the universal nozzle and tungsten alloy MLC and have been experimentally verified in separate measurements to be published later. Secondary neutron fluence spectra is recorded in a 1 cm diameter sphere at the measurement positions distal to the closed tungsten alloy (92.5% W, 5.2% Ni, and 2.3% Cu by weight) MLC or 6.5 cm brass block (62% Cu, 35% Zn, and 3% Pb by weight).

The relative neutron sensitivities, k_U and k_T, as a function of incident neutron energy up to 50 MeV have been computed iteratively by Waterman *et al.*[43] using tabulated tissue kerma factors and experimentally determined chamber responses in a number of neutron fields with known neutron energy spectra. However, since neutron sensitivities are also a function of chamber gas composition, wall material, and chamber size,[44–46] and in our case the secondary neutron energies are expected to approach the primary proton energy, we have developed Monte Carlo simulations to calculate the sensitivities of our large volume chambers. We modeled the magnesium-walled and argon gas-filled (Mg-Ar) chamber as well as the A150 TE plastic-walled and methane-based TE gas-filled (TE-TE) chamber using dimensions and material

TABLE I. The dose to water calibration factors, N_{DW}, for the chambers used in the measurements.

Chamber	Active volume (cm^3)	N_{DW} (Gy/C)
Exradin A12	0.65	5.040_10^7
TE-TE	9.14	3.44_10^6
Mg-Ar	9.14	2.33_10^6

FIG. 2. Experimental setup (not to scale) showing the measurement points 10 cm downstream from the distal side and 50 cm downstream of the proximal side of either the closed MLC (a) or a 6.5 cm thick brass block placed downstream of the MLC with leaves open to form an 8.7 cm diameter circle (b).

compositions based on the design drawings and measurements of the finished chambers. Each chamber was uniformly

irradiated with a simulated neutron beam having a circular diameter sufficient to fully encompass the entire chamber with the beam oriented perpendicular to the chamber's cylindrical axis. The dose deposited within the gas volume of the chamber was scored as a function of incident neutron energy which ranged 0–250 MeV. We are interested in the absorbed dose to water, so the sensitivities were calculated as the ratio of the dose deposited in the chamber gas volume to the dose deposited in the gas volume of an identical chamber composed of water. The water density of the wall and gas is adjusted such that the total areal density of each is equivalent to the areal densities of the Mg-Ar or TETE chambers. Relative sensitivities were calculated by taking the quotient of the neutron sensitivity with the sensitivity obtained through simulating exposure of the chamber to a photon field with an energy spectrum that approximates the 6 MV photon field used for calibration.

To test the reliability of the above method for calculating k_U and k_T, we have also calculated relative sensitivity functions for the chambers described in the Waterman study. In this case, dimensions of the Mg-Ar chamber were modeled after an Exradin model 2 Spokas thimble chamber with 0.54 cm^3 active volume and dimensions of the TE-TE chamber were modeled on the FWT IC-17 (Far West Technology, Inc.) chamber with 1.0 cm^3 active volume. Since the neutron sensitivities given by Waterman *et al.*[43] are relative to tissue, the Mg-Ar and TE-TE chamber sensitivities are calculated relative to a chamber composed of ICRU muscle[47] with the density of the wall and gas adjusted appropriately. The results fall within the errors (1–2 s.d.) and deviations from the measured values can be attributed to a lack of neutron cross-section data above 20 MeV (Ref. 47) and ambiguities in Waterman *et al.*[43] regarding the dimensions of the chambers, the material composition of the TE-TE chamber, and the elemental composition of tissue.

Since measurements are performed in a spectrum of neutron energies, the effective relative neutron sensitivity of an ionization chamber in any given neutron energy spectrum replaces the energy dependent neutron sensitivity in Eqs. (3) and (4). Effective sensitivity can be expressed as the dose-weighted average of relative neutron sensitivity[43]

$$k_i = \frac{\int k_i(E) D_w(E) dE}{\int D_w(E) dE}; \quad (5)$$

where i represents the chambers T or U, $D_w(E)$ is the dose to water as a function of neutron energy, and $k_i(E)$ is neutron sensitivity relative to the sensitivity to the photon field used for calibration.

The systematic errors in Monte Carlo calculated chamber sensitivities are difficult to estimate and a detailed analysis of dose measurement errors arising from these calculations is beyond the scope of this work. However, the overall measurement uncertainties (ΔD_n and ΔD_{p+c}) can be derived through error propagation of Eqs. (3) and (4) (Ref. 48) assuming the uncertainties are uncorrelated

94

$$\frac{DD_2}{n} = \frac{R_0}{\upsilon - k_\upsilon D_n}$$
$$h_{\upsilon k\tau} - h_{\tau k\upsilon}$$
$$\left[\ \right]^2$$
$$Dh_2$$
$$\tau \þ$$
$$R_0$$
$$\tau - k_\tau D_n$$
$$h_{\upsilon k\tau} - h_{\tau k\upsilon}$$
$$\left[\ \right]^2$$
$$Dh_2$$
$$\upsilon$$
$$\þ$$
$$h_\upsilon D_n$$
$$h_{\upsilon k\tau} - h_{\tau k\upsilon}$$
$$\left[\ \right]^2$$
$$Dk_2$$
$$\tau$$
$$\þ$$
$$h_\tau D_n$$
$$h_{\upsilon k\tau} - h_{\tau k\upsilon}$$
$$\left[\ \right]^2$$
$$Dk_2$$
$$\upsilon; \quad (6)$$
$$\frac{DD_2}{p\þc} = \frac{k_\upsilon D_{p\þc}}{h_{\upsilon k\tau} - h_{\tau k\upsilon}}$$
$$\left[\ \right]^2$$
$$Dh_2$$
$$\tau \þ$$
$$k_\tau D_{p\þc}$$
$$h_{\upsilon k\tau} - h_{\tau k\upsilon}$$
$$\left[\ \right]^2$$
$$Dh_2$$
$$\upsilon$$
$$\þ$$
$$R_0$$
$$\upsilon - h_\upsilon D_{p\þc}$$
$$h_{\upsilon k\tau} - h_{\tau k\upsilon}$$
$$\left[\ \right]^2$$
$$Dk_2$$
$$\tau$$
$$\þ$$
$$R_0$$
$$\tau - h_\tau D_{p\þc}$$
$$h_{\upsilon k\tau} - h_{\tau k\upsilon}$$
$$\left[\ \right]^2$$
$$Dk_2$$
$$\upsilon: \quad (7)$$

In the following, the component of the uncertainty in $p\þc$ sensitivity (Dh_τ and Dh_υ) arising from sensitivity to c-rays is ignored because the chambers are calibrated in a photon field. The sources of error inherent in calculating neutron sensitivity as a ratio of doses can be estimated by approximating neutron

dose as the product of the neutron kerma factor (K) with the neutron fluence (U). Then, the neutron sensitivity error is a function of the errors in the neutron kerma factor, neutron fluence, and the sensitivity to the photon field used for calibration. Systematic error in the fluence calculations is primarily dependent on neutron emission cross-section uncertainties which are estimated to be 20–40% for protons and neutrons.[47] As an approximation, we ignore this error because the neutron sensitivity is calculated as a ratio of doses which are each affected by fluence error in largely the same manner. Sensitivity to the calibration field is also calculated as a dose ratio, so the effects of systematic error in the estimation of photon fluence for the calibration field are also ignored. Then, with the uncertainty in the mass attenuation coefficient being 1%–2% in the energy range of the photons used for calibration,[49] an estimate of 2.5% uncertainty in the sensitivity of the dosimeters to the calibration field agrees with that of ICRU Report 78.[37] The remaining systematic errors in neutron sensitivity can be attributed to uncertainty in the neutron kerma factors which are directly related to uncertainty in neutron interaction cross-sections. Kerma factor uncertainty is estimated to be up to 2% for water and 5% for A-150 TE plastic or TE gas when uncertainty in elemental composition and the neutron spectra used to measure the kerma factors is considered.[50] Kerma factors for magnesium and argon are not well known and their uncertainties are estimated to be up to 20%.[47] Analogous to our approach with neutrons, the uncertainty in relative proton sensitivity can be estimated by taking a fluence based approach to calculate the doses that are used in the ratio for relative proton sensitivity. Then, the error depends on proton stopping power uncertainty, which has been estimated at less than 2% for elements and 4% for compounds.[51]

III. RESULTS AND DISCUSSION

Shown in Figs. 3(a) and 3(b) are Gafchromic EBT2 film absorbed dose profiles along the lateral x- and y-axis for 0

and 32 cm depth in solid water plastic, displayed in units of cGy per machine monitor unit (MU). Gaussian functions with a constant background were fit to the profiles to determine the beam width. At 0 cm depth (32 cm upstream from isocenter), $r_x \frac{1}{4} 1.66$ cm and $r_y \frac{1}{4} 1.84$ cm. The 32 cm depth measurement is at isocenter and the widths are $r_x \frac{1}{4} 2.04$ cm and $r_y \frac{1}{4} 2.17$ cm. During the neutron measurements the proximal face of the MLC is approximately 19 cm upstream from isocenter. When measurements are made with the brass block and the MLC open to form an 8.7 cm diameter circle, less than 4% of the proton dose is deposited in the MLC. Therefore, the effect on measurements with the brass block is negligible because the neutron and pþc doses are less than 0.01% of the dose delivered to isocenter with an open collimator, as shown below.

A fractional depth dose profile in water measured with the PTW plane parallel chamber is shown in Fig. 3(c). The peak absorbed dose at isocenter was determined to be 6.95 cGy/MU using the product of the surface dose (2.33 cGy/

MU), the peak to surface ratio obtained from Fig. 3(c), and the ratio of fractional profile areas measured by the 8.4 cm plane parallel chamber at the surface to the peak at 32 cm. Simulated neutron fluence spectra 10 cm from the distal edge of the closed tungsten alloy MLC or 6.5 cm brass block are shown in Fig. 4(a). The fluence spectra 50 cm from the proximal edge of the closed MLC and the brass block are shown in Fig. 4(b). In all cases, the spectra are heavily dominated by low energies with a long tail approaching the incident proton energy. The mean neutron energies from the MLC, which has a thickness equivalent to twice the proton range, are notably lower than the mean energies from the brass block, whose thickness is <10% greater than the proton range. The simulations also indicate that dose due to interleaf leakage protons greatly outweighs c-ray dose distal to the closed MLC while almost no protons pass completely through the brass block.

The sensitivity functions, k_T and k_U, calculated from Monte Carlo simulations of the large volume chambers are plotted as a function of neutron energy in Fig. 5. The Mg-Ar relative sensitivity, k_U, falls rapidly to zero with decreasing neutron energy so integration, in Eq. (5), of the sensitivity function with a dose distribution that is heavily weighted toward low energy neutrons will result in a small effective neutron sensitivity. Conversely, the TE-TE relative sensitivity, k_T, varies little with neutron energy and is found to be nearly unity after integration with the neutron dose distribution.

Given the chambers are calibrated in an x-ray field, then each chamber's c-ray sensitivity relative to the radiation used for calibration can be assumed to be unity because the Compton effect predominates in both the x-ray calibration and in the c-rays of the mixed field. Where interleaf leakage protons outnumber secondary c-rays, as is the case downstream of the closed MLC, the proton sensitivity was calculated using the same Monte Carlo model used to find the neutron sensitivities. The proton sensitivity was found to be approximately invariant with proton energy for both chambers. Furthermore, the TE-TE chamber is constructed of hydrogenous materials with proton stopping powers close to that of water and therefore exhibits a relative sensitivity to protons that is equivalent to its relative sensitivity to c-rays. The calculated sensitivities of the Mg-Ar and TE-TE chambers to pþc radiation are approximately 0.9 and 1.0,

FIG. 3. Lateral beam profiles, taken with radiochromic film, along the x- and y-axis for 0 cm (a) and 32 cm (b) depth in solid water plastic, where the 32 cm measurement is at isocenter. The fractional depth dose profile (c) in water measured with the PTW 8.4 cm diameter plane parallel chamber.

respectively, for the MLC measurements where the interleaf leakage protons dominate over c-rays. When measurements are performed downstream of the brass block, the c-rays dominate over protons and the sensitivities of both chambers are approximately 1.0.

Shown in Table II are effective sensitivities for each of

the measurements described above along with the absorbed dose responses of the dosimeters and calculated neutron and pþc doses in units of 10^{-5} Gy absorbed dose to water per Gy of absorbed dose to water delivered to isocenter at 32 cm depth by a pristine 230 MeV proton beam. Relative uncertainties were approximated at 5% for pþc sensitivities, 20% for k_U, 6% for k_T, and inserted into Eqs. (6) and (7) to estimate the relative uncertainty of the dose calculations. Approximate uncertainties in the MLC doses are 8% for neutrons and 9% for pþc radiation. A higher mean neutron energy of 29 MeV in the brass spectra compared to the tungsten MLC, Figs. 4(a) and 3(b), leads to a higher effective neutron sensitivity, k_U, which in turn leads to higher uncertainties. Consequently, the brass measurements exhibit uncertainties of approximately 11% in neutron dose and 20% in pþc dose.

The respective neutron and pþc doses due to protons are nearly equivalent for a closed tungsten alloy MLC or a brass block. This disagrees with the results of Daartz et al.[14] who used a 25.4 cm Bonner sphere to measure neutron doses at isocenter for a 185 MeV proton beam fully blocked by either a brass collimator or tungsten MLC. Neutron dose equivalents of 3×10^{-4} and 5×10^{-4} Sv/Gy for a 10 cm air-gap and 1.3×10^{-4} and 2.3×10^{-4} Sv/Gy with a 30 cm air-gap were reported for the brass collimator and tungsten MLC, respectively. These correspond to a nearly two-fold increase in neutron dose equivalent at isocenter when switching from a closed brass collimator to a tungsten MLC. In contrast, using their stated radiation weighting factor of 5.9, we measure 3.2×10^{-4} Sv/Gy and 3.8×10^{-4} Sv/Gy for an 8.7 cm airgap to the brass block and MLC, respectively. For 42.2 cm

FIG. 4. Simulated neutron fluence spectra through a 1 cm diameter sphere placed 10 cm from the distal edge of the closed MLC or the brass block (a), and 50 cm from the proximal edge of the MLC or the brass block (b).

FIG. 5. Relative chamber sensitivity as a function of incident neutron energy for the large volume Mg-Ar and TE-TE chamber. The sensitivities are calculated with the Geant4 (Ref. 42) Monte Carlo toolkit using detailed geometrical models of the chambers.

TABLE II. Relative pþc and neutron sensitivities of the Mg-Ar chamber (h_U and k_U) and the TE-TE chamber (h_T and k_T), dosimeter response (R'_U and R'_T), neutron (D_n) and pþc ($D_{pþc}$) absorbed doses to water per Gy of absorbed dose to water delivered at isocenter by a pristine 230 MeV proton beam. Relative uncertainties of approximately 5% for pþc sensitivities (h_U and h_T), 20% for k_U, and 6% for k_T are inserted into Eqs. (6) and (7) to determine the relative uncertainty of the absorbed dose calculations. The materials used in this experiment are an MLC with tungsten alloy leaves and a 6.5 cm thick brass block used for custom-milled proton collimators. Measurements are at isocenter 10 cm from the distal edge and 50 cm from the proximal edge of the collimating material.

Material	Position	h_U	h_T	k_U	k_T	$R'_U{}^a$	$R'_T{}^a$	$D_n{}^a$	$D_{pþc}{}^a$
Tungsten	10 cm distal	0.9	1.0	0.10	0.97	1.95	6.77	5.3±0.4	1.6±0.2
Brass	10 cm distal	1.0	1.0	0.25	0.98	3.89	8.57	6.4±0.7	2.3±0.5
Tungsten	50 cm proximal	0.9	1.0	0.11	0.97	0.369	1.00	0.69±0.06	0.33±0.03
Brass	50 cm proximal	1.0	1.0	0.26	0.98	0.393	0.846	0.63±0.07	0.23±0.05

[a]Dosimeter response and absorbed dose are in units of 10^{-5} Gy/Gy.

6254 Diffenderfer et al.: Neutron dose from tungsten MLC or brass aperture 6254

(brass) or 39.7 cm (MLC) air-gaps, we measure 0.41_10_4 and 0.37_10_4 Sv/Gy for the brass block and MLC, respectively. The discrepancy must also be considered in light of the differences in beam characteristics, materials, collimator design, and measurement techniques. The collimator leaf design is particularly important for reducing interleaf proton leakage. Unlike the proton MLC used here, the MLC used in the Daartz et al. experiment was intended for use in a clinical linear accelerator and may not incorporate the same design considerations, such as multiple steps on abutting leaves that went into the development of the MLC made specifically for proton therapy. In addition, our simulations indicate that the mean neutron energy increases with a brass collimator compared to the tungsten MLC, Figs. 4(a) and 4(b). We further expect the mean neutron energy to increase with primary proton energy, and this may lead to differences in the neutron spectra produced in this experiment with a 230 MeV beam versus the 185 MeV proton beam used in the study of Daartz et al. The Bonner sphere used in those measurements underresponds to neutrons greater than _15 MeV compared to the response of the dual ionization chambers which show better than 20% separation between hydrogenous and nonhydrogenous chambers up to 100 MeV, Fig. 5. Moreover, the large diameter of the Bonner sphere leads to much greater positional uncertainty over the ionization chambers described here, which makes comparison difficult.

The neutron absorbed dose is typically 3 times the pþc absorbed dose in the measurements observed here. Therefore, the impact of uncertainty in pþc absorbed dose on the total absorbed dose is minor. If the neutron dose is expressed in Gy(RBE)[37] or dose equivalent (Sv) then the impact of uncertainties in the pþc absorbed dose becomes negligible when considering the summed dose in Gy(RBE) or the total dose equivalent (Sv). While this is not important for the relative dose measurements required to make a comparison between tungsten alloy and brass as collimator materials, it will be an issue when the dual ionization chamber method is used to make quantitative measurements outside the treatment volume for realistic geometries (i.e., open fields) where RBE or dose weighting factors should be taken into consideration. Even though the production of secondary neutrons in tungsten alloy is higher than that of brass, in practice this effect is mitigated because a proton MLC must be designed to incorporate side- and end-steps into the leaves to prevent interleaf leakage of protons, resulting in a leaf thickness equivalent to at least twice the proton range in the collimating material. A custom-milled brass collimator is typically designed with a thickness of just over one proton range to reduce weight since the device must be manually exchanged for each new treatment field. The additional material in the tungsten alloy collimator compared to brass has a selfattenuating effect on the neutrons produced within the collimating material.

IV. CONCLUSION

Using the dual ionization chambers and Monte Carlo

simulations described above, dose measurements were performed in the mixed neutron and pþc field produced by the proton beam at The University of Pennsylvania Roberts Proton Therapy Center. Of particular interest is the production of secondary neutron radiation by the collimation of a proton beam with the newly developed tungsten alloy MLC in comparison to the conventional brass collimation system, and the potential for an increase in secondary neutron dose to the patient during treatment. Our results indicate that secondary neutron production in a tungsten alloy MLC leads to doses that even in an overly pessimistic clinical worst-case scenario are no greater than those seen from brass collimators. The doses measured here have been obtained in a nonclinical geometry, which was chosen to illustrate that the tungsten alloy MLC produces a secondary neutron dose comparable to that of a brass collimator system. This study also serves to demonstrate the value of the dual ionization chamber method of mixed-field dosimetry, which was developed for fast neutron beam dosimetry, in measuring the secondary neutron dose associated with therapeutic proton beams. The absolute values of the secondary neutron and pþc absorbed doses measured here should not be considered representative of the absorbed doses that will be seen outside a collimated therapeutic proton field, since these measurements have been made with a closed tungsten alloy MLC or a solid brass collimator to maximize neutron production. Furthermore, this study was limited to only two measurement positions along the proton beam axis in order to provide a timely comparison of the secondary neutron dose due to the newly implemented proton MLC at the University of Pennsylvania Roberts Proton Therapy Center. Additional measurements using the dual ionization chamber technique to map the neutron dose outside of an open proton field shaped with the tungsten alloy MLC are planned for the future.

ACKNOWLEDGMENTS

[1]P. J. Binns and J. H. Hough, "Secondary dose exposures during 200 MeV proton therapy," Radiat. Prot. Dosim. 70, 441–444 (1997).

[2]H. Paganetti, "Nuclear interactions in proton therapy: dose and relative biological effect distributions originating from primary and secondary particles," Phys. Med. Biol. 47, 747–64 (2002).

[3]U. Schneider, S. Agosteo, E. Pedroni, and J. Besserer, "Secondary neutron dose during proton therapy using spot scanning," Int. J. Radiat. Oncol., Biol., Phys. 53, 244–51 (2002).

[4]X. Yan, U. Titt, A. Koehler, and W. Newhauser, "Measurement of neutron dose equivalent to proton therapy patients outside of the proton radiation field," Nucl. Instrum. Methods Phys. Res. A 476, 429–434 (2002).

[5]H. Jiang, B. Wang, X. G. Xu, H. D. Suit, and H. Paganetti, "Simulation of organ-specific patient effective dose due to secondary neutrons in proton radiation treatment," Phys. Med. Biol. 50, 4337–4353 (2005).

6J. C. Polf and W. D. Newhauser, "Calculations of neutron dose equivalent exposures from range-modulated proton therapy beams," Phys. Med. Biol. 50, 3859–3873 (2005).

7G. Mesoloras, G. A. Sandison, R. D. Stewart, J. B. Farr, and W. C. Hsi, "Neutron scattered dose equivalent to a fetus from proton radiotherapy of the mother," Med. Phys. 33, 2479–2490 (2006).

8R. Tayama, Y. Fujita, M. Tadokoro, H. Fujimaki, T. Sakae, and T. Terunuma, "Measurement of neutron dose distribution for a passive scattering nozzle at the Proton Medical Research Center (PMRC)," Nucl. Instrum. Methods Phys. Res. A 564, 532–536 (2006).

9Y. Zheng, W. Newhauser, J. Fontenot, P. Taddei, and R. Mohan, "Monte Carlo study of neutron dose equivalent during passive scattering proton therapy," Phys. Med. Biol. 52, 4481–4496 (2007).

10M. F. Moyers, E. R. Benton, A. Ghebremedhin, and G. Coutrakon, "Leakage and scatter radiation from a double scattering based proton beamline," Med. Phys. 35, 128–144 (2008).

11P. J. Taddei, J. D. Fontenot, Y. Zheng, D. Mirkovic, A. K. Lee, U. Titt, and W. D. Newhauser, "Reducing stray radiation dose to patients receiving passively scattered proton radiotherapy for prostate cancer," Phys. Med. Biol. 53, 2131–2147 (2008).

12S. Yonai, N. Matsufuji, T. Kanai, Y. Matsui, K. Matsushita, H. Yamashita, M. Numano, T. Sakae, T. Terunuma, T. Nishio, R. Kohno, and T. Akagi, "Measurement of neutron ambient dose equivalent in passive carbon-ion and proton radiotherapies," Med. Phys. 35, 4782–4792 (2008).

13D. Brenner, C. Elliston, E. Hall, and H. Paganetti, "Reduction of the secondary neutron dose in passively scattered proton radiotherapy, using an optimized pre-collimator/collimator," Phys. Med. Biol. 54, 6065–6078 (2009).

14J. Daartz, M. Bangert, M. R. Bussiee`re, M. Engelsman, and H. M. Kooy, "Characterization of a mini-multileaf collimator in a proton beamline," Med. Phys. 36, 1886–1894 (2009).

15J. D. Fontenot, A. K. Lee, and W. D. Newhauser, "Risk of secondary malignant neoplasms from proton therapy and intensity-modulated x-ray therapy for early-stage prostate cancer," Int. J. Radiat. Oncol. Biol. Phys. 74, 616–622 (2009).

16A. Pe´rez-Andu´ jar, W. D. Newhauser, and P. M. Deluca, "Neutron production from beam-modifying devices in a modern double scattering proton therapy beam delivery system," Phys. Med. Biol. 54, 993–1008 (2009).

17D. Shin,M. Yoon, J. Kwak, J. Shin, S. B. Lee, S. Y. Park, S. Park, D. Y. Kim, and K. H. Cho, "Secondary neutron doses for several beam configurations for proton therapy," Int. J. Radiat.Oncol. Biol. Phys. 74, 260–265 (2009).

18A. Wroe, B. Clasie, H. Kooy, J. Flanz, R. Schulte, and A. Rosenfeld, "Out-of-field dose equivalents delivered by passively scattered therapeutic proton beams for clinically relevant field configurations," Int. J. Radiat. Oncol. Biol. Phys. 73, 306–313 (2009).

19B. Clasie, A. Wroe, H. Kooy, N. Depauw, J. Flanz, H. Paganetti, and A. Rosenfeld, "Assessment of out-of-field absorbed dose and equivalent dose in proton fields," Med. Phys. 37, 311–321 (2010).

20D. Hecksel, V. Anferov, M. Fitzek, and K. Shahnazi, "Influence of beam efficiency through the patient-specific collimator on secondary neutron dose equivalent in double scattering and uniform scanning modes of proton therapy," Med. Phys. 37, 2910–2917 (2010).

21X. Wang, N. Sahoo, R. X. Zhu, J. R. Zullo, and M. T. Gillin, "Measurement of neutron dose equivalent and its dependence on beam configuration for a passive scattering proton delivery system," Int. J. Radiat. Oncol., Biol., Phys. 76, 1563–1570 (2010).

22M. Yoon, S. H. Ahn, J. Kim, D. H. Shin, S. Y. Park, S. B. Lee, K. H. Shin, and K. H. Cho, "Radiation-Induced Cancers From Modern Radiotherapy Techniques: Intensity-Modulated Radiotherapy Versus Proton Therapy," Int. J. Radiat. Oncol. Biol. Phys. 77, 1477–1485 (2010).

23R. Zhang, A. Pe´rez-Andu´ jar, J. D. Fontenot, P. J. Taddei, and W. D. Newhauser, "An analytic model of neutron ambient dose equivalent and equivalent dose for proton radiotherapy," Phys. Med. Biol. 55, 6975–6985 (2010).

24E. J. Hall, "Intensity-modulated radiation therapy, protons, and the risk of second cancers," Int. J. Radiat. Oncol., Biol., Phys. 65, 1–7 (2006).

25D. J. Brenner and E. J. Hall, "Secondary neutrons in clinical proton radiotherapy: a charged issue," Radiother. Oncol. 86, 165–170 (2008).

26F. A. Cucinotta, R. Katz, J. W. Wilson, L. W. Townsend, J. Shinn, and F. Hajnal, "Biological effectiveness of high-energy protons: Target

fragmentation," Radiat. Res. 127, 130–137 (1991).

27A. M. Kellerer, "Risk estimates for radiation-induced cancer—The epidemiological evidence," Radiat. Environ. Biophys. 39, 17–24 (2000).

28X. G. Xu, B. Bednarz, and H. Paganetti, "A review of dosimetry studies on external-beam radiation treatment with respect to second cancer induction.," Phys. Med. Biol. 53, R193–R241 (2008).

29R. L. Bramblett, R. I. Ewing, and T. W. Bonner, "A new type of neutron spectrometer," Nucl. Instrum. Methods 9, 1–12 (1960).

30G. F. Knoll, Radiation detection and measurement, 3rd ed. (John Wiley & Sons, Inc., New York, 2000).

31L. Bourgois, D. Delacroix, and A. Ostrowsky, "Use of bubble detectors to measure neutron contamination of a medical accelerator photon beam," Radiat. Prot. Dosim. 74, 239–246 (1997).

32S. Agosteo, C. Birattari, M. Caravaggio, M. Silari, and G. Tosi, "Secondary neutron and photon dose in proton therapy," Radiother. Oncol. 48, 293–305 (1998).

33F. Vanhavere and F. d'Errico, "Standardisation of superheated drop and bubble detectors," Radiat. Prot. Dosim. 101, 283–287 (2002).

34R. M. Howell, E. A. Burgett, B. Wiegel, and N. E. Hertel, "Calibration of a Bonner sphere extension (BSE) for high-energy neutron spectrometry," Radiat. Meas. 45, 1233–1237 (2010).

35R. H. Olsher, H. Hsu, A. Beverding, J. H. Kleck, W. H. Casson, D. G. Vasilik, and R. T. Devine, "WENDI: an improved neutron rem meter," Health Phys. 79, 170–181 (2000).

36R. H. Olsher, D. T. Seagraves, S. L. Eisele, C. W. Bjork, W. A. Martinez, L. L. Romero, M. W. Mallett, M. A. Duran, and C. R. Hurlbut, "PRESCILA: A new, lightweight neutron rem meter," Health Phys. 86, 603–612 (2004).

37ICRU, "Prescribing, Recording, and Reporting Proton-Beam Therapy," Report No. 78, International Commision on Radiation Units and Measurements (Bethesda, MD, 2007).

38ICRU, Neutron Dosimetry for Biology and Medicine, Report No. 26, (International Commission on Radiation Units and Measurements, Bethesda, MD, 1977).

39E. J. Hall and A. J. Giaccia, Radiobiology for the Radiologist, (Lippincott Williams & Wilkins, Philadelphia, 2006).

40J. B. Smathers, V. A. Otte, A. R. Smith, P. R. Almond, F. H. Attix, J. J. Spokas, W. M. Quam, and L. J. Goodman, "Composition of A-150 tissueequivalent plastic," Med. Phys. 4, 74–77 (1977).

41P. R. Almond, P. J. Biggs, B. M. Coursey, W. F. Hanson, M. S. Huq, R. Nath, and D. W. O. Rogers, "AAPM's TG-51 protocol for clinical reference dosimetry of high-energy photon and electron beams," Med. Phys. 26, 1847–1870 (1999).

42S. Agostinelli et al., "Geant4—a simulation toolkit," Nucl. Instrum. Methods Phys. Res. A 506, 250–303 (2003).

43F. M. Waterman, F. T. Kuchnir, L. S. Skaggs, R. T. Kouzes, and W. H. Moore, "Energy dependence of the neutron sensitivity of C-CO2, Mg-Ar and TE-TE ionisation chambers," Phys. Med. Biol. 24, 721–733 (1979).

44A. Rubach and H. Bichsel, "Neutron dosimetry with spherical ionisation chambers I. Theory of the dose conversion factors r and W_n," Phys. Med. Biol. 27, 893–904 (1982).

45A. Rubach and H. Bichsel, "Neutron dosimetry with spherical ionisation chambers IV. Neutron sensitivities for C/CO2 and tissue-equivalent chambers," Phys. Med. Biol. 27, 1455–1463 (1982).

46A. Rubach, H. Bichsel, and A. Ito, "Neutron dosimetry with spherical ionisation chambers V. Experimental measurements and comparison with calculations of the cavity size dependence of the specific ionization," Phys. Med. Biol. 28, 913–924 (1983).

47ICRU, Nuclear Data for Neutron and Proton Radiotherapy and for Radiation Protection, Report No. 63 (International Commission on Radiation Units and Measurements, Bethesda, MD, 2000).

48A. Nohtomi, N. Sugiura, T. Itoh, T. Sakae, T. Terunuma, and T. Fujibuchi, "An alternative method of neutron–gamma mixed-field dosimetry by using paired ionization chambers," Nucl. Instrum. Methods Phys. Res. A 614, 159–161 (2010).

49J. H. Hubbell, "Review of photon interaction cross-section data in the medical and biological context," Phys. Med. Biol. 44, R1–R22 (1999).

50M. Awschalom, I. Rosenberg, and A. Mravca, "Kermas for various substances

averaged over the energy spectra of fast neutron therapy beams: A
study in uncertainties," Med. Phys. 10, 395–409 (1983).
51ICRU, Stopping Powers and Ranges for Protons and Alpha Particles,
Report No. 49 (International Commission on Radiation Units and Measurements,
Bethesda, MD, 1993).

Correspondence

Reply to "Comment on 'Comparison of secondary neutron dose in proton therapy resulting from the use of a tungsten alloy MLC or a brass collimator system'" [Med. Phys. 38(11), 6248–6256 (2011)]

To the Editor,

We thank Dr. Moskvin et al.[1] for their interest in our recent paper and we agree that tungsten may not be the optimal material to use in a proton MLC from a purely radiological point of view. However, many other practical considerations must be taken into account when undertaking the design and manufacturer of a practical MLC; primarily among them are cost and project risk. Our project was one of joint research development with two commercial vendors who kindly undertook to collaborate on the MLC design and manufacture: IBA as our primary proton therapy vendor, and Varian Medical Systems. A proton MLC leaf has a complex design, with multiple steps between adjacent and abutting leaves to prevent proton leakage. Such leaves must be manufactured with very high tolerances to minimize leaf gaps and the risk of mechanical interference as they move. Varian is among the most experienced MLC manufacturers for radiation oncology equipment. In order to reduce project cost and risk it was deemed expedient to produce an MLC which was designed based on the wealth of Varian's experience. Critical to this is selecting a leaf material, the mechanical properties of which need to be excellently understood. Although brass was considered as a possible leaf material, manufacturing brass leaves to the required tolerance was identified as a highly significant risk factor, and, therefore, the choice of tungsten as a leaf material was fixed early in the project. The primary objective of our manuscript[2] was not to determine the optimum proton MLC leaf material, but to validate tungsten as a viable alternative to brass as a collimating material, and in doing so to extend an established neutron dosimetry technique to proton therapy with the purpose of comparing the secondary neutron dose arising from the use of a tungsten leaf proton MLC to that of a brass collimator in a simple, nonclinical geometry. Moskvin et al.[1] present a number of criticisms of this work based on perceived discrepancies with Monte Carlo simulations that they have performed for similar, but fundamentally different, geometries.

103

The majority of these criticisms focus on differences in simulated neutron spectra or computations directly affected by same.

One of the main results of Moskvin et al.,[3] that, by their estimation, "has huge ramification for proton centers,"[1] is that in the unlikely scenario a patient undergoes proton therapy with a 6.5 cm thick closed tungsten MLC obstructing the beam, a Monte Carlo simulation predicts the patient would receive 50% more neutron ambient dose equivalent (measured in mSv/Gy) than if a 6.5 cm thick block of brass had been used in its place. In our recent manuscript[2] we have presented similar data in the form of measurements of absorbed neutron dose under somewhat different circumstances; most notable is the use of a real proton MLC with an actual leaf thickness of 9 cm. Our measurements indicate that the absorbed neutron dose decreases by 16% at 10 cm from the distal edge and increases by 10% at 50 cm from the proximal edge for proton irradiation of a closed tungsten MLC compared to a 6.5 cm brass block. We estimate dose measurement uncertainties to be 10% and conclude that the difference between brass and tungsten under these circumstances cannot be distinguished beyond the error (1–2 s.d).

Using the FLUKA Monte Carlo engine, Moskvin et al.[3] report dose differences favoring brass over tungsten by 15% at 10 cm and 19% at 30 cm when a more realistic 8.2 cm thick tungsten block is compared to the 6.5 cm brass block (Fig. 4 of Ref. 3). In response to our manuscript, Moskvin et al.[1] incorporated our measurement geometry[2] and a 9 cm thick tungsten block into their FLUKA simulation and determined ambient dose equivalent differences of 3.8% at 10 cm and 9.7% at 50 cm, attributing the reduction in difference to the less than 4% of proton dose deposited in the open MLC when brass measurements are made in our geometry. Recognizing their inability to simulate our treatment nozzle to the same level of precision and having no available estimates of their dose uncertainty, we interpret these calculations as providing a solid validation of our work within the uncertainties of our measurements and their calculations. Unfortunately, in the absence of clinically relevant field geometries, neither the measurements nor simulations discussed here can provide a reasonable estimate of the neutron dose to proton therapy patients. Indeed, these measurements will not even place an upper bound on neutron exposures as the role of proton energy, field size, spread out Bragg peak width, and range modulators cannot be ignored.[4]

Moskvin et al.[1] take issue with the bin size of the neutron energy histograms that we have used to calculate detector sensitivity, claiming that the summing of all low energy neutrons into the first bin neglects the structure of the neutron spectrum in this low energy regime. This is of course entirely true, but of little consequence in our measurements. As an integral part of the measurement technique, we calculate energy dependent neutron sensitivities for ionization chambers based on the energy spectrum of neutrons produced in Monte Carlo simulation. These sensitivity calculations have been validated in our

104

manuscript against the measurements and calculations of
Waterman et al.[5] The most important of these is the sensitivity
of the nonhydrogenous chamber since the hydrogenous chamber
sensitivity shows little variation with neutron energy. The
sensitivity of the nonhydrogenous chamber falls rapidly to
zero (less than _0.03 for neutron energies below 6 MeV) as
the neutron energy approaches zero. Consequently, the overall
chamber sensitivity to a specified neutron spectrum, calculated
as a dose weighted average of the energy dependent sensitivity,
shows very little dependence on low energy neutrons.
In fact, the approach of binning all neutrons below 6 MeV together
may be too conservative since all of them are accumulated
with the sensitivity of a 3 MeV neutron even though the
majority fall below 1 MeV.[1,3] This may lead to artificially
increased nonhydrogenous chamber neutron sensitivity and,
following the dose calculation formalism we have presented,[2]
larger neutron doses for both tungsten and brass.
Moskvin et al.[1] argue that GEANT4 (Ref. [6]) is unsuited to
simulation of neutron transport and offer two published
articles to support this argument. One of these pertains solely
to neutrons in the thermal energy range,[7] which we have discussed
above. The other demonstrates a global increase in
neutron production with GEANT4 over experiment for 190
GeV muons incident on graphite, copper, and lead.[8] This
does not imply inflated neutron production for 230 MeV protons
on brass (an alloy of copper) over tungsten. However,
Moskvin et al.[1] state "Indeed, GEANT4 tends to overestimate
the production of high energy neutrons in the brass." A simple
comparison of the relative difference in neutron fluence
as a function of energy reveals only minor differences for
the two Monte Carlo packages in question, FLUKA and
GEANT4. Shown in Fig. 1 is the percentage difference in neutron
fluence (neutron energies above 9 MeV) for brass and
tungsten relative to the brass fluence, DU_{B-W}/U_B, for neutron
spectra simulated with FLUKA and GEANT4. In fact, the mean
fluence difference in Fig. 1 is 40%6̶23% for FLUKA and
60%6̶21% for GEANT4, demonstrating the difficulty in trying
to extract a meaningful difference between two noisy
data sets.
In addition, the GEANT4 Monte Carlo package may offer
some advantages over FLUKA for practical Monte Carlo calculations.
In particular, the geometry module makes it easier
to model the treatment head in great detail. For instance, our
model includes features of the treatment head and the collimator
assembly at the level of bolt holes. In fact others have
made use of GEANT4 in modeling the intricacies of the IBA
treatment nozzle and have published widely on topics related
to the radiological properties of proton beams using this
model.[9–11] For the record, the simulations in our manuscript[2]
used GEANT4 version 4.9.2_p2 with the physics settings recommended
in Jarlskog and Paganetti.[12]
Given the difference in simulated neutron energy spectra,
Moskvin et al.[1] claim to have invalidated the accuracy of
our detector sensitivity calculation and, therefore, the accuracy
of our measurements. On the contrary, their data demonstrate
that the neutron energy spectra for brass and

tungsten display the same high energy neutron characteristics for both FLUKA and GEANT4 aside from a global normalization factor. Fortunately, our measurement method has no dependence on total number of neutrons produced per proton in simulation and only a second order dependence on the detailed structure of the neutron energy spectra. This is in contrast to Monte Carlo simulated dose deposition which is directly proportional to neutron fluence and energy. As a demonstration of the stability of this measurement technique, we recalculated neutron doses for both brass and tungsten MLC using the same neutron sensitivity factor, implying the same neutron energy spectrum, and the measured dose

FIG. 1. The percentage difference in neutron fluence (neutron energies above 9 MeV) for brass and tungsten relative to the brass fluence, DU_B-w/U_B, for neutron spectra simulated with FLUKA and GEANT4. The FLUKA spectra used in this calculation were extracted from Fig. 1 of Ref. 1 and data points above 150 MeV could not be distinguished due to energy scale compression of the log–log plot. Fig. 4 of Ref. 3 indicates that neutrons with energies approaching 200 MeV are produced in the FLUKA code for both brass and tungsten.

becomes equivalent at 10 cm and 34% higher for tungsten at 50 cm. This is of course an entirely unfair comparison because it is clear from both FLUKA and GEANT4 simulations that brass produces more high energy neutrons under these conditions.

Moskvin et al.[1] correctly point out that we did not use an energy dependent weighting factor when we calculated neutron dose equivalent for the sole purpose of comparing our measurements to other published data. This was by design. Most commercially available instruments that provide measurement readings in dose equivalent (Sv) do not use an energy dependent factor, as was the case for the measurements reported in Daartz et al.,[13] and a meaningful comparison necessitated the use of the same factor. However, we have investigated the implication of Moskvin et al.[1] that the dose equivalent weighting factor depends strongly on the detailed structure of the neutron energy spectrum and have found this to be an exaggeration at least for the neutron energy spectra discussed here. Moskvin et al.[3] use a FLUKA routine[14] to calculate ambient dose equivalent, H*(10), which itself uses a fluence-to-ambient dose conversion factor based on the ICRP (Ref. 15) 60 recommended neutron dose weighting factors. Using neutron energy spectral data extracted from Fig. 1 of Ref. 1 and spectral data from our publication[2] we have calculated the fluence-averaged ambient dose equivalent conversion factor for each spectrum. Using the FLUKA simulations of brass, tungsten, and brass with an open tungsten MLC in Ref. 1 we calculate 12.9, 12.4, and 12.5 pSv_cm2, respectively. For our GEANT4 simulation of a tungsten MLC and brass block, we calculate 12.3 and 11.5 pSv_cm2, respectively. This is a maximum difference of 11% and should not be a major area of concern given the 20%–40% measurement errors typical of neutron dosimetry with survey type instruments.

Moskvin et al.[1] further conclude, "Thus, there is practically no difference in the neutron flux as a function of distance from the neutron source between a 6.5 and a 9 cm

thick tungsten block," yet they calculate entirely different ambient dose equivalents for each scenario. Down from the, across-the-board, 50% increase in neutron dose for a 6.5 cm tungsten block over a 6.5 cm brass block reported in Ref. [3], they now show only a 2.3% and 22.5% increase on axis at 10 and 50 cm, respectively, for a 9 cm tungsten block over a 6.5 cm brass block. Off-axis calculations show a trend to higher neutron dose for tungsten over brass, but none approaching a factor of 1.5.

To reiterate what we have previously stated,[2] it is well known that the yield of neutrons from irradiation with protons at therapeutic energies is higher for tungsten than for brass. However, when constructing a proton MLC, in order to minimize interleaf leakage of protons it is necessary to incorporate multiple steps and use a leaf thickness that is at least twice the range of the highest energy proton in the chosen material. We believe that the dual chamber neutron dosimetry technique, which is based on protocols developed for fast neutron therapy, [16] offers considerable advantages over measurement techniques using survey type instruments (e.g., Bonner sphere, modified Bonner sphere, scintillation counters, and bubble counters) for the reasons stated in our original paper.[2] Further studies should apply this technique to measurements outside of the treatment field in more clinically relevant geometries: we are in the process of collecting such data.

[1]V. Moskvin, C.-W. Cheng, Q. Zhao, and I. J. Das, "Comment on 'Comparison of secondary neutron dose in proton therapy resulting from the use of a tungsten alloy MLC or a brass collimator system,'" Med. Phys. 39(4), 2303–2305 (2012).
[2]E. S. Diffenderfer, C. G. Ainsley, M. L. Kirk, J. E. McDonough, and R. L. Maughan, "Comparison of secondary neutron dose in proton therapy resulting from the use of a tungsten alloy MLC or a brass collimator system," Med. Phys. 38, 6248–6256 (2011).
[3]V. Moskvin, C.-W. Cheng, and I. J. Das, "Pitfalls of tungsten multileaf collimator in proton beam therapy," Med. Phys. 38, 6395–6406 (2011).
[4]Y. Zheng, W. Newhauser, J. Fontenot, P. Taddei, and R. Mohan, "Monte Carlo study of neutron dose equivalent during passive scattering proton therapy," Phys. Med. Biol. 52, 4481–4496 (2007).
[5]F. M. Waterman, F. T. Kuchnir, L. S. Skaggs, R. T. Kouzes, and W. H. Moore, "Energy dependence of the neutron sensitivity of C-CO2, Mg-Ar and TE-TE ionisation chambers," Phys. Med. Biol. 24, 721–733 (1979).
[6]S. Agostinelli et al., "GEANT4—A simulation toolkit," Nucl. Instrum. Methods A 506, 250–303 (2003).
[7]C. Guardiola, K. Amgarou, F. Garcia, C. Fleta, D. Quirion, and M. Lozano, "GEANT4 and MCNPX simulations of thermal neutron detection with planar silicon detectors," J. Inst. 6 T09001 (2011).
[8]M. G. Marino, J. A. Detwiler, R. Henning, R. A. Johnson, A. G. Schubert, and J. F.Wilkerson, "Validation of spallation neutron production and propagation within GEANT4," Nucl. Instrum. Methods A 582, 611–620 (2007).
[9]H. Paganetti, H. Jiang, S. Y. Yee, and H. M. Kooy, "Accurate Monte Carlo simulations for nozzle design, commissioning and quality assurance for a proton radiation therapy facility," Med. Phys. 31, 2107–2118 (2004).
[10]H. Paganetti, H. Jiang, K. Parodi, R. Slopsema, and M. Engelsman, "Clinical implementation of full Monte Carlo dose calculation in proton beam therapy.," Phys. Med. Biol. 53(17), 4825–4853 (2008).
[11]B. Clasie, A. Wroe, H. Kooy, N. Depauw, J. Flanz, H. Paganetti, and A. Rosenfeld, "Assessment of out-of-field absorbed dose and equivalent dose in proton fields," Med. Phys. 37, 311–321 (2010).
[12]C. Z. Jarlskog and H. Paganetti, "Physics settings for using the GEANT4 toolkit in proton therapy," IEEE Trans. Nucl. Sci. 55, 1018–1025 (2008).
[13]J. Daartz, M. Bangert, M. R. Bussiee`re, M. Engelsman, and H. M. Kooy, "Characterization of a mini-multileaf collimator in a proton beamline," Med. Phys. 36, 1886–1894 (2009).
[14]S. Roesler and G. R. Stevenson, "deq99.f—A FLUKA user-routine converting

fluence into effective dose and ambient dose equivalent," Technical
Note CERN-SC-2006-070-RP-TN EDMS No. 809389 (2006).
15ICRP, "Recommendations of the International Commission on Radiological
Protection," ICRP Publication No. 60 (Pergamon, Oxford, 1990).
16ICRU, "Clinical neutron dosimetry—Part I: Determination of absorbed
dose in a patient treated by external beams of fast neutrons," Report No.
45 (International Commission on Radiation Units and Measurements, Bethesda,
MD, 1989).

E. S. Diffenderfer
Department of Radiation Oncology,
University of Pennsylvania,
Philadelphia, Pennsylvania 19104
C. G. Ainsley
Department of Radiation Oncology,
University of Pennsylvania,
Philadelphia, Pennsylvania 19104
M. L. Kirk
Department of Radiation Oncology,
University of Pennsylvania,
Philadelphia, Pennsylvania 19104

J. E. McDonough
Department of Radiation Oncology,
University of Pennsylvania,
Philadelphia, Pennsylvania 19104
R. L. Maughan
Department of Radiation Oncology,
University of Pennsylvania,
Philadelphia, Pennsylvania 19104
Richard.Maughan@uphs.upenn.edu

Phase II- journal publications – submitted

Monte Carlo simulations to configure a treatment planning system for modulated-scanning proton delivery

Derek Dolney and James McDonough
Department of Radiation Oncology, University of Pennsylvania, Philadelphia, PA 19104.
E-mail: Derek.Dolney@uphs.upenn.edu

Abstract. We used the Geant4 Monte Carlo simulation tookit to generate modulated scanning data for our treatment planning system. A simpli_ed model of the treatment delivery nozzle was implemented as our simulation geometry. Primary protons were generated in the nozzle just downstream of the last pair of focusing quadrupole magnets. The phase space used for these primary protons was double Gaussian in both of the spatial and angular distributions. Given from the vendor the spot size speci_cation at isocenter, the beam emittance, and the speci_cation that the beam will be focused to a double waist at the treatment isocenter position, the initial phase space was derived by calculating the contribution from multiple Coulomb scattering

and using a geometric projection of the residual phase space moments. Simulations starting with the initial phase space are shown to produce beams with spot sizes within 1% of the vendor speci_cation and the beam double waist is within 8 mm of the isocenter position. A realistic set of commissioning data can be quickly generated and used to con_gure a treatment planning system for facility planning, sta_ training, and research purposes.

1. Purpose

Construction of the Roberts Proton Therapy Center at the University of Pennsylvania began in 2006 and patient treatments began in 2010. Given the high cost to construct and operate a proton therapy center it was expected that the treatment rooms be properly commissioned and that sta_ be fully trained so that patient treatments could begin as early as possible. However, it was di_cult for some tasks to procede before commissioning data was available, such as training sta_ in proton treatment planning. Were beam data available early, prior to commissioning, training and research could progress in parallel to the construction, acceptance, and commissioning of the Monte Carlo simulations for modulated-scanning proton delivery 2

facility. Research projects comparing modulated-scanning proton therapy with other treatment options made progress with a Monte Carlo generated set of beam data, and treatment protocols were designed and implemented before treatments began based on the outcomes of those studies. In addition, the Roberts Center has the capability to deliver modulated-scanning treatment _elds using two di_erent proton therapy nozzles with di_erent beam properties, and it was possible to compare the two nozzles for speci_c treatment sites using our treatment planning system, to assist with equipment selection and other facility planning decisions even before real beam data was available from the commissioning process.

Monte Carlo based simulation techniques have been used to generate commissioning data for treatment planning systems in the past for photons (Ding 2003), electrons (Antolak et al. 2002), stereotactic radiosurgery (Ding et al. 2006), and double-scattered proton systems (Newhauser et al. 2007). Some sections of a recently published AAPM task group are devoted to the subject (Das et al. 2008). This work describes how we used Monte Carlo simulations to generate a body of data that was used to con_gure a treatment planning system for the modulated-scanning delivery technique. We do not mean to imply that this data is a substitute for measured commissioning data. Rather, this data allows some research and veri_cation of the treatment planning system to take place before real measured data is available, as well as training of sta_ in how to commission and use the treatment planning system with a new modality.

The goal here was not to produce a complete model of the treatment nozzle. Though interesting, that process can take a long time and many iterations of improvements to the implementation of the nozzle and the physics models are often needed in order to _t well the measured data (see (Jarlskog & Paganetti 2008) regarding Geant4 or (Newhauser et al. 2005) regarding MCNPX), especially for example to reproduce the non-Gaussianity of the beam due to scattering in one or more items in the nozzle (see (Sawakuchi, Mirkovic, Perles, Sahoo, Zhu, Ciangaru, Suzuki, Gillin, Mohan & Titt 2010) and (Gillin et al. 2010)). The goal here was to rapidly produce an approximate set of relative beam uence data and relative depth dose data, so that the Varian Eclipse treatment planning system could be con_gured and used for training and research

projects. Accurate monitor unit calculations were not an objective.

2. Methods and Materials

The Geant4 Monte Carlo toolkit version 4.9.4, patch-01, (Agostinelli et al. 2003), was used to build a basic model of the PBS treatment nozzles. There are two di_erent nozzles

in use at the Roberts Center: the IBA Universal Nozzle is used for double-scattering and uniform-scanning delivery techniques in addition to modulated-scanning, and the IBA Dedicated Nozzle which is modulated-scanning only. For the IBA Universal Nozzle the beamline vacuum pipe extends to 1.7 meters upstream of isocenter where there is a tray that holds the second scatterers. A second scatterer is not used for modulated-scanning; the tray instead positions and seals a thin vacuum closing window to the Monte Carlo simulations for modulated-scanning proton delivery 3

Beam Direction, m

2

1.5

1

0.5

0

Transverse Direction, cm

30

20

10

0

10

20

30

Vacuum Air
Fluence Scored on
Planes in Air

Figure 1. Monte Carlo simulation to generate beam pro_les in air for the Universal Nozzle. The color indicates the relative proton uence for illustrative purposes only using a two-dimensional proton scoring mesh with 2 mm resolution, with redder colors indicating regions with larger proton uence.

Beam Direction, m

2

1.5

1

0.5

0

Transverse Direction, cm

30

20

10

0

10

20

30

Vacuum Air Dose Scored in
Water Phantom

Figure 2. Monte Carlo simulation to generate depth dose in water for the Dedicated treatment nozzle. The color indicates the relative proton uence for illustrative purposes only using a two-dimensional proton scoring mesh with 2 mm resolution, with redder colors indicating regions with larger proton uence.

end of the beam pipe. In the Dedicated Nozzle the vacuum extends all the way to the end of the nozzle which is 0.6 meters upstream of isocenter. Because of the greater thickness of air that the beam must pass through, the multiple Coulomb scattering

(MCS) contribution to the beam spot size at isocenter is larger by a factor of 6 or more for the Universal Nozzle, depending on the beam energy. See Figures 1 and 2 for the simulation geometries.

Primary protons were generated in the nozzle between the two scanning magnets, 2.1 m upstream of isocenter for the Universal Nozzle, and 2.0 m upstream for the Dedicated Nozzle. Since the goal was to generate beam profiles and depth dose data along the central axis, it was not necessary to simulate the beam scanning magnets. The location of primary generation was chosen downstream of the last pair of quadrupole magnets which are used to focus the beam to a double waist near isocenter. We model the spatial and angular probability density functions (PDFs) for the beam protons at this location as correlated Gaussian functions in the two directions transverse to the direction of beam propagation. Six parameters fully describe the PDF for primaries: Monte Carlo simulations for modulated-scanning proton delivery 4 in one transverse dimension there are the initial (i.e., at $z = 0$) spatial sigma, $\sigma_{x;0}$, the angular sigma, $\sigma_{\theta;0}$, and the correlation between the spatial and angular PDFs, $C_{x\theta;0}$. There is an analogous set of three for the other transverse dimension. Note that in our notation, $\sigma_x^2 = \langle x^2 \rangle$, $\sigma_\theta^2 = \langle \theta^2 \rangle$, and $C_{x\theta}^2 = \langle x\theta \rangle$. For a beam that is converging to a waist (having been focused by quadrupoles, for example), $C_{x\theta;0}$ is negative, meaning that protons that have positive spatial coordinate tend to have momentum with a negative angle with respect to the beam direction, i.e. having momentum directed back toward the central axis.

To determine the initial moments, we take the Fermi-Eyges approach (Rossi & Greisen 1941, Eyges 1948) and assume that the beam PDFs remain Gaussian as the beam propagates through materials. In the simplified model of the treatment nozzle studied here, the beam travels only through a layer of air that is thin with respect to its radiation length, so this approximation is a good one. The ionization chambers and vacuum windows in the nozzle are made of thin layers, typically only tens of microns, and were neglected for this study. The spatial sigma as a function of the propagation length, z, is given by:

$$\sigma_x^2(z) = \sigma_{\theta;0}^2 z^2 + 2C_{x\theta;0} z + \sigma_{x;0}^2 + \sigma_{x;MCS}^2(z) \quad (1)$$

The first three terms on the right hand side describe the simple geometric propagation of the beam spatial moments (the spatial mean does not change by choice of coordinates).

The last term represents the increase in beam sigma due to multiple Coulomb scattering (MCS) of the beam protons as they travel through materials. We discuss the

computation of σ_2

$x;MCS(z)$ below. Having done so, we are left with the determination of the coefficients of the remaining quadratic function. It was stipulated in the contract with the beamline vendor for Roberts, that the beam spot size at isocenter be less than specified values at particular energies. That is, in our notation, we were provided $\sigma_x(z_{iso};E)$. We were also given beam emittance data, $\epsilon(E)$, from a similar facility. The emittance is a measure of the phase space volume of the beam and is conserved in vacuum, even through magnetic fields, as a consequence of Liouville's Theorem. For Gaussian spatial and angular distributions, the emittance can be defined as

$$\epsilon = \sqrt{\sigma_{x}^2 \, \sigma_{x'}^2 - C^2_{x x'}} : \quad (2)$$

Note that some authors define the emittance with a factor of π or $\pi = 2$. In any case, the emittance is proportional to the area of a phase space ellipse. Since we are discussing PDFs, the ellipse corresponds to an iso-probability contour in phase space. Emittance is conserved after the beam of particles undergo multiple Coulomb scattering,

however, inelastic nuclear interactions are not described by a classical Hamiltonian and so Liouville's Theorem does not apply to them. Inelastic nuclear interactions can generate secondary particles with momenta directed at large angles to the incident, and their general effect is to increase the beam emittance. Because lower energies are produced by degrading the fixed output energy of the cyclotron by passing the beam through a graphite/beryllium degrader wheel, the emittance becomes larger for lower

Monte Carlo simulations for modulated-scanning proton delivery 5

beam energies. Downstream of the degrader, divergence limiting slits are used to remove

the large-angle scattered protons from the beam, but the total beam current is lowered as a result, and treatment times become long for shallow targets. Therefore, the slits are not controlled to maintain constant beam emittance, but rather a compromise between beam current, divergence near isocenter, and other beam properties is necessarily made.

The effect of multiple Coulomb scattering is described by the theory of Molière (Molière 1947) which provides the full angular distribution of particles after a step through material. The angular distribution is mostly Gaussian, at small angles, but has a larger tail arising from single large-angle scattering events. Fermi, Rossi, and Eyges (Rossi & Greisen 1941, Eyges 1948) developed an approximate theory for Gaussian beam transport, and various other fit formulae for the width of the central Gaussian can be found in the literature, for example, Highland (1975) and Highland (1979), and Lynch & Dahl (1991). The latter is shown by Lynch & Dahl to fit the central 98% of the angular distribution to better than 11%. The largest deviations occur for higher Z materials. For scattering in air, which is all we need here, the agreement is better than 2%. Note that the fitting functions, and even the rigorous Molière theory, only give the angular distribution of particles after MCS, but the spatial distribution is also

needed, not only for this work, but in general a Monte Carlo engine implementing a multiple scattering model must sample both spatial and angular PDFs after each tracking step. The theory of Lewis (1950) can provide the moments of the spatial distribution, but there is currently no theory that gives the spatial PDF itself. In Geant4, model functions for the spatial and angular PDFs were developed by Urban (2006) that reproduces the central Gaussian width calculated by Lynch & Dahl and _ts the Lewis theory calculation for the moments of the distributions. The Geant4 MCS implementation further attempts to minimize the e_ect of the simulation step size (see (Gottschalk 2010) and (Kanematsu 2008) for excellent reviews of the subject of accurate

di_erential scattering power formulae). We do not explicitly set a _xed step size limit in our simulations, but rely on the step limitation algorithm implemented in Geant4 that limits the step size to be a fraction of the range or mean free path of a particle (Geant4 Physics Reference Manual 2010). At any rate, the Geant4 MCS does have some

step size dependence, and so we opted to just obtain σ_2

$_{x;MCS}$ at the desired depth using

another Geant4 simulation, rather than attempting to evaluate the Urban function or one of the other _ts. This simulation is very simple: primaries are generated at a point with no angular distribution and momentum determined by the beam energy with no momentum dispersion. The protons propagate in air some distance and their lateral positions are recorded to obtain the lateral PDF (that is, the proton uence) at the given distance. We obtain the beam sigma at the given depth by _tting a Gaussian to the central 98% of the proton uence. We obtained the beam sigma in this way at 32 depths in air and _t a 4th-order polynomial. We evaluated the polynomial and its derivative at the isocenter position to obtain $_{x;MCS}(z_{iso})$. The process is repeated for 14 beam energies. We _t a function of the Fermi-Eyges form (Rossi & Greisen 1941), which makes the approximation of small deection angles and ignores energy loss in the Monte Carlo simulations for modulated-scanning proton delivery 6

air,

$_{x;MCS}(z) = S_1$

p

$z = Z_0$

p_

; (3)

where Z_0 is the radiation length of air (= 303.9 m), p the momentum of the particle, and _ its velocity.

Our vendor has speci_ed the spot size in air at isocenter as a function of energy (Figure 3) in the two transverse dimensions, the emittance in the evacuated beam pipe (Figure 4) in the two dimensions, and that the beam will be focused at isocenter in both dimensions (i.e, the double waist). The three constraints per dimension allow the three unknowns in Equation 1, the moments of the initial phase space, to be determined for any beam energy. We de_ne _ = $(d_2$

$_{x;MCS} = dz)j_{z_{iso}}$ and obtain the following solution for the beam phase space:

$_2$

$$\bar{\sigma}_{x';0} = (\bar{\sigma}_2 + \bar{\sigma}_{2=4})=$$

$$\bar{\sigma}_2$$

$$x \square \sigma_2$$

$$x;MCS(z_{iso})$$

$$\bar{\sigma}; (4)$$

$$C_{x\_;0} = \square (\sigma_2$$

$$\bar{\sigma}_{;0} + \sigma_{=2}); \text{ and } (5)$$

$$\sigma_2$$

$$x;0 = \sigma_2$$

$$x \square \sigma_2$$

$$x;MCS(z_{iso}) \square \sigma_2$$

$$\bar{\sigma}_{;0}z^2$$

$$iso \square 2C_{x;0}z_{iso}: (6)$$

The correlation is always negative, meaning the beam is focusing to a waist downstream
of z = 0. In general, a large MCS contribution is compensated by a large σ_2
$\bar{\sigma}_{;0}$. That
is, the defocusing e_ect of a large MCS tends to push the waist downstream, which is
o_set by a larger initial angle that works to focus the beam further upstream against
the MCS e_ect.

The momentum dispersion of the proton beam depends on the width setting for a
collimating slit downstream of the energy degrader and a bending magnet that acts
like a spectrometer. The slit width settings are de_ned, as a function of energy,
during acceptance of the treatment room. The vendor provided us with measurements
of the momentum dispersion for di_erent beam energies across the deliverable range
obtained from another facility. The dispersion is about 0.5% and is shown in Figure
5. We generated primaries with the momentum dispersion shown using the solution
given in Equations 4{6. The Geant4 engine tracked the particles to scoring planes
that record proton uence pro_les at various depths near isocenter to validate our
primary generation scheme. We then proceeded to generate the data necessary to
commission a treatment planning system: uence pro_les (Figure 1) and depth dose
curves (Figure 2) for a range of energies covering the full deliverable range at 10 MeV
spacing. We obtain uence pro_les at 5 depths in air by recording the positions of
protons as they cross planes at isocenter, 10 cm upstream and downstream, and 20
cm upstream and downstream, of isocenter, as in Figure 1. We obtained a depth dose
curve by recording the energy deposited in 2 _m thick slabs of water placed in a water
tank, as in Figure 2. The thickness of the slabs was chosen to be equal to the water-
equivalent thickness of standard plane-parallel chambers used to measure Bragg
peaks.

The threshold for production of secondaries was set to 1 _m. We used the physics
list of Jarlskog & Paganetti (2008). The multiple scattering model used for protons
Monte Carlo simulations for modulated-scanning proton delivery 7
Energy, MeV
100 120 140 160 180 200 220 240
Beam Sigma, mm

3
4
5
6
7
8
Universal Nozzle
Dedicated Nozzle

Figure 3. Spot size (1_) in air at isocenter. The line represents the target spot size at isocenter and the points are the results of simulation. The spot sizes from simulation are within 1% of the target for any energy in the deliverable range.

Energy, MeV
100 120 140 160 180 200 220
Emittance, mm mrad
4
5
6
7
8
9
10
11
12
13

Figure 4. Beam lateral emittance in the x (circles) and y (squares) directions of the IEC Beam Limiting Device Coordinate System measured and kindly provided to us by IBA. The line is a spline _t that was used to constrain the initial phase space (Equation 4).

is G4UrbanMscModel90 via the physics process class G4hMultipleScattering (Geant4 Physics Reference Manual 2010).

We generated 100 million primary proton events per energy to produce our pro_les in air. We take advantage of the axial symmetry of our geometry and primary PDF by tallying both the x- and y-distances from central axis as statistically independent samples for a modest signal-to-noise gain of
p
2. We generated 1 million primaries per
energy to produce our depth dose data. These choices are considered more carefully in the Discussion section.

3. Results

Rossi & Greisen derived Equation 3 with S_1 = 15.0 MeV by ignoring energy loss in the medium and making a small angle approximation on the total scattering angle. We treat S_1 as a _t parameter and obtain 9.5 MeV for the Universal Nozzle and 9.0 MeV for the Dedicated Nozzle. We compare our _t with the Geant4 results and the Lynch Monte Carlo simulations for modulated-scanning proton delivery 8

Energy, MeV
100 120 140 160 180 200 220
/ $p \cdot 100\%$ $_p$

σ
0.10
0.15
0.20
0.25
0.30
0.35
0.40
0.45

0.50
0.55
0.60
Figure 5. Momentum dispersion measured by IBA at a similar facility.
Depth in Air, m
0.0 0.5 1.0 1.5 2.0 2.5 3.0
, mm x
σ
0.0
0.5
1.0
1.5
2.0
2.5
3.0
3.5
4.0
4.5
Geant4 Single Scattering
Geant4 Multiple Scattering

Figure 6. Contribution to the spatial beam sigma from multiple Coulomb scattering
as a function of the depth of penetration in air for a 230 MeV beam. The lower
series of points and error bars were obtained from Geant4 simulation using the
G4hMultipleScattering model. The line _tting those points is our _t to those results
using the Fermi-Eyges functional form (Equation 3). The upper series of points were
obtained using the Geant4 G4IonCoulombScatteringModel, which is a single Coulomb
scattering physics implementation designed for protons and other ions. The upper line
is the _t of Lynch & Dahl (1991).

& Dahl (1991) _t in Figure 6. Equation 3 is also a function of energy, and we _x the
depth to be the isocenter depth for the Universal Nozzle and plot our _t as a function of
energy in Figure 7. The Lynch & Dahl formula says that the MCS contribution to the
spot size should be 15% larger than what the Geant4 MCS model gives for air depths
up
to 3 m. Our _t reproduces the Geant4 MCS result to within 3% over the depth range
we are considering.

Our primary PDF produces a beam focused at isocenter with the speci_ed spot
size using Monte Carlo. The focus is demonstrated in Figure 8 while the spot size at
isocenter was compared with the vendor speci_cation in Figure 3. In our simulations
using the phase space generated with Equations 4{6, and our _t Equation 3, the beam
waist is within 1{8 mm of isocenter, with better agreement at higher energies. The spot
size at isocenter is within 1% of the vendor speci_cations.

Our Monte Carlo generated pro_les in air at isocenter are plotted in Figure 9 for two
Monte Carlo simulations for modulated-scanning proton delivery 9
Energy, MeV
100 120 140 160 180 200 220
, mm x
σ
1.5
2.0
2.5
3.0
3.5
Geant4 Single Scattering
Geant4 Multiple Scattering

Figure 7. Contribution to the spatial beam sigma at isocenter from multiple Coulomb
scattering as a function of the beam energy. The air depth at isocenter is 1.7 m, which
is the speci_cation for Universal Nozzle. The lower series of points were generated

by Geant4 simulation using the G4hMultipleScattering model, and the upper series were generated using the G4IonCoulombScatteringModel, which is a single Coulomb scattering physics implementation designed for protons and other ions. The lower line is our _t to the multiple scattering simulation results using the Rossi & Greisen (1941) functional form. The upper line is the _t of Lynch & Dahl (1991).

Depth, cm

40

20

0 20 40

Beam Profile 1σ, mm

2.5

3

3.5

4

4.5

5

5.5

6

100 MeV
150 MeV
190 MeV
230 MeV

Figure 8. One sigma for beam uence pro_les in air near isocenter. Isocenter is at the origin. The lines were generated using Fermi-Eyges theory and the _t of Lynch & Dahl (1991). The data points were calculated using Monte Carlo, with the error bars indicating the sample variance for the Monte Carlo simulations.

di_erent beam energies. Also plotted is a Gaussian _t to the central 98% of the beam uence. The central Gaussian is the beam pro_le that a typical treatment planning system will use to model the beam pro_le. These are pro_les for the minimum and maximum energies for the Dedicated Nozzle. The Universal Nozzle produces similar pro_les (not shown, but see Figure 8) but with larger transverse size, and somewhat more large angle scattering, due to the extra thickness of air between the beam vacumm

window and isocenter.

Our Monte Carlo generated depth dose curves are given as Figure 10. The number of monitor units (MU) refers to an amount of charge collected by transmission ionization chambers mounted inside the nozzle. For modulated-scanning delivery, Eclipse computes

Monte Carlo simulations for modulated-scanning proton delivery 10

x, mm

150

100

50

0 50 100 150

2

Fluence, mm

5

10

4

10

3

10

2

10

1

10

1

100 MeV
230 MeV

Figure 9. Monte Carlo-generated uence pro_les for the Dedicated Nozzle minimum

and maximum beam energies. Energies lower than 100 MeV are obtained via a range shifter mounted on the end of the nozzle. The lines are the Gaussian _ts to the central 98% of the pro_les.

Depth, cm
0 5 10 15 20 25 30 35
) 2 Dose, Gy/(MU mm
0
10
20
30
40
50
60
70
80

Figure 10. Monte Carlo generated commissioning library of depth dose curves. Energies are from 100 MeV and 230 MeV spaced every 10 MeV.

the number of monitor units (MU) that should be delivered per spot given depth dose data speci_ed in units of measured-dose-to-water per MU per mm$_2$. For our simulations, since the transmission ionization chambers are air-_lled, we scaled the number of primary

protons per MU based on the stopping power of protons in air. Since the ratio of stopping

power in air to stopping power in water for protons is nearly constant between 100 MeV and 230 MeV, it can be seen that the curves in Figure 10 are e_ectively normalized at the entrance dose.

4. Discussion

Our simulation procedure quickly generates a data library for commissioning a treatment

planning system. Of course, the data is not a substitute for properly measuring the beam data once the treatment rooms are ready, but nevertheless we feel that the data is accurate enough for the purposes of facility planning, training, and research. We are able to _t the vendor speci_cations to within 1% for spot size. The beam waist is

Monte Carlo simulations for modulated-scanning proton delivery 11

also very close to isocenter: compared with the air depth to isocenter for the Dedicated Nozzle, the position of the waist is within about 1%. It is not exact because our _t function is not. As stated previously, if a larger MCS contribution is expected when the phase space generated with Equations 4{6, the mean angle will be larger and the waist will occur further upstream. This is exactly what happens if the Lynch & Dahl (1991) _t is used directly. We tried this _rst, and our Geant4 simulations produced a beam waist 10{20 cm upstream of isocenter, depending on the beam energy. Alternatively, one

could use the Lynch & Dahl _t for $_{x;MCS}(z_{iso})$ to generate the initial phase space and then use the single Coulomb scattering physics model G4IonCoulombScatteringModel implemented in Geant4 for protons and other ions. This would probably give good results in terms of spot size and waist at isocenter. Generating the depth dose data in water, however, would take a much longer time unless a multiple scattering physics model is used.

The fact that Geant4 simulations produce a smaller spot size after multiple Coulomb

scattering in air may be due to a step size dependence in the physics models. Gottschalk
(2010) reports a step size dependence for the multiple Coulomb scattering implemented in Geant4 of up to 11%. He discusses how a step size dependence arises from the type of
modi_ed Highland formula employed by Geant4 for its MCS calculation, and suggests that a corrected Rossi formula, or a new functional form that he calls \di_erential Moli_ere", may be accurate enough for radiotherapy purposes without having such a large
step size dependence. Although the di_erence in the multiple scattering contribution to the spot size between Lynch & Dahl (1991) and Geant4 is as large as 15% at the depth in air where the treatment isocenter is located, the spot size we obtain is accurate,
within 1%, at the isocenter depth because we have imposed the spot size there as one of the constraints for our primary PDF. Practically, a patient could be setup at most 50 cm upstream or downstream of isocenter. Looking at Figure 8, the largest di_erence between the Lynch & Dahl spot size and our simulations occurs at 50 cm upstream of isocenter, and is about 4% in the worst case.
The _t we obtain is speci_c to air, to the depth in air of isocenter, to protons, and to the Geant4 multiple scattering models and the step size used for our simulations. The intent here is not to produce a widely applicable _t like Lynch & Dahl (1991). Rather, we have devised a method that, given accurate beam quality spec_cations from the vendor, is able to produce commissioning data with spot size (and therefore beam penumbra) accuracy of 2% or better.
The energy selection system provides continuous energy modulation, so that the exact energy-range relationship is not so important. The treatment planning system interpolates between the Bragg peaks with which it was commissioned. Even a discrete system like the synchrotron-based Hitachi system provides _ne enough energy increments to construct a smooth SOBP layer-by-layer, so we do not feel that getting the energy-range relationship exactly right is necessary for the purposes that this data serve.
Although we have used 100 million primary events to generate beam pro_les, we

Monte Carlo simulations for modulated-scanning proton delivery 12

found that it is possible to get good results using far fewer numbers of primaries since what we ultimately needed was only the beam spatial sigma from a Gaussian _t to the pro_le. By simulating only 10,000 primary events, one obtains less than 1% error on the sigma _t to the central 98% of the uence pro_le. This number of events takes only 80 to 100 s per energy, depending on the energy and whether a range shifter is inserted into the beam. So the 14 energies that we used to commission Eclipse took only 20 minutes using a single CPU. Neither are large numbers of events needed to generate acceptable depth dose curves since the dose is integrated over large transverse
planes. We used 50 cm transverse planes to ensure that all of the dose was collected. We found that 50,000 events already gives a Bragg curve with less than 2% error bars, except beyond the peak where there is some small exit dose from mostly secondary neutrons. This number of events takes 1.9{3.8 CPU hrs per energy, or about 2 CPU

days to generate all 14 energies for the commissioning data. In summary, once the simulation code is setup, it is possible to generate a library of commissioning data using a single standard desktop CPU core in less than 3 days. A treatment planning system like Eclipse performs a Gaussian _t to the beam pro_le, so it is valid to only consider the accuracy of the extracted sigma for this purpose. Some treatment planning systems, including recent versions of Eclipse, will _t a second Gaussian to the beam pro_le to model the large dose envelope, also called the dose \halo", that arises from large-angle Coulomb scattering and nuclear interactions (Sawakuchi, Zhu, Poenisch, Suzuki, Ciangaru, Titt, Anand, Mohan, Gillin & Sahoo 2010, Sawakuchi, Mirkovic, Perles, Sahoo, Zhu, Ciangaru, Suzuki, Gillin, Mohan & Titt 2010). It is interesting to note from Figure 9 there is some halo produced even in 64 cm of air for the Dedicated Nozzle, though it is only at the 0.1% level. Certainly a larger number of events would be required to resolve well the relatively low particle uence in the beam halo, which is typically a few percent or less, of the peak uence. In that case, we recommend 100 million events per energy, which we have found to provide a relative uncertainty of 1% far in the tail of the pro_le where the uence is 1% of maximum. This large number of events took our computing cluster 8 CPU days per energy. For the depth dose data, to resolve the low exit dose beyond the Bragg peak, 1 million events requires 3 CPU days per energy and results in 0.4% error shallower than the proton range and 10% error beyond.

We assumed the beam is focused at isocenter in both transverse directions, producing the so-called \double waist" at isocenter. In fact, this is not a speci_cation of the beam tuning procedure, and we have found, after measurements to commission our _rst PBS room, that in practice the double waist ends up positioned 20{30 cm upstream of isocenter. Our formalism is not restrictive in this regard: just replace z_{iso} with the waist desired depth in air. One could in principle explore optimizing the position of the waist for speci_c treatment sites and patient setups. The gain in spot size is likely slight however, and we have not explored this further.

We have used a similar method to determine an initial phase space from our measured commissioning data. The commissioning data includes beam uence pro_les measured in air at several depths for many energies from which the spot sigmas are

Monte Carlo simulations for modulated-scanning proton delivery 13

extracted. The contribution to the spot sigma for the multiple scattering that occurs between the initial phase space position and the measurement depth needs to be subtracted from the spot sigmas so that what remains is only the geometric projection of the moments, as in Equation 1. Then a quadratic can be _t to obtain the moments at the chosen initial position. We will report elsewhere that this procedure _ts our commissioning data very well. Note that if the simulations will be used to investigate the beam halo, then the initial phase space position should of course be placed upstream of monitor chambers, vacuum windows, and other elements where the beam halo is generated. Finally, the initial phase space determination becomes more complicated if magnetic _elds are to be included, such as the _elds from focusing quadrupole magnets, and the e_ect of these elements on the beam moments would need to be included.

5. Conclusions

We have shown how, given speci_cations of the treatment nozzle geometry and beam tuning, accurate beam data can be generated for use by semiempirical dose calculation algorithms like those implemented in treatment planning systems. While this is certainly not a substitute for properly commissioning a treatment planning system with carefully measured data, it can allow planning and research to proceed in parallel with construction of the facility. Given a recipe for the primary PDF, as described here, one may additionally generate data using beamline modi_ers such as range shifters and ridge _lters, not only to commission the treatment planning system with those devices, but more importantly to investigate the e_ect of them on, for example, the beam

penumbrae and width of the Bragg peaks. Those data would ideally be used to develop appropriate, possibly site speci_c, treatment approaches that maxmize the potential of proton therapy with modulated, scanned beams. At the University of Pennsylvania, we commissioned our treatment planning system early, before data from our treatment rooms was ready, and were able to gain experience working with it while the rooms were being commissioned. We were able to use this data to complete planning studies, for several treatment sites, comparing treatment strategies including IMRT compared with proton double-scattering and or PBS, proton single-_eld uniform dose vs. IMPT optimizations, and Universal Nozzle vs. Dedicated Nozzle comparisons at the treatment plan and DVH level. Our facility does not have a Dedicated Nozzle on a gantry, though we researched the improvements that that capability would a_ord by commissioning a gantry beamline in Eclipse using the Dedicated Nozzle data from simulation. This should

underscore the value of realistic beam data even during the early stages of planning the construction of the facility.

Monte Carlo simulations for modulated-scanning proton delivery 14

Acknowledgments

Agostinelli S et al. 2003 Nucl. Instrum. Methods A 506, 250{303.

Antolak J A, Bieda M R & Hogstrom K R 2002 Med. Phys. 29, 771{786.

Das I J, Cheng C W, Watts R J, Ahnesj• o A, Gibbons J, Li X A, Lowenstein J, Mitra R K, Simon W E & Zhu T C 2008 Med. Phys. 35, 4186{4215.

Ding G X 2003 Phys. Med. Biol. 48, 3865{3874.

Ding G X, Duggan D M & Co_ey C W 2006 Phys. Med. Biol. 51, 2549{2566.

Eyges L 1948 Physical Review 74, 1534{1535.

Geant4 Physics Reference Manual 2010 Available for download from http://geant4.web.cern.ch/geant4/support/userdocuments.shtml. Version 9.4 (17 December 2010).

Gillin M T, Sahoo N, Bues M, Ciangaru G, Sawakuchi G, Poenisch F, Arjomandy B, Martin C, Titt U, Suzuki K, Smith A R & Zhu X R 2010 Med. Phys. 37(1), 154{163.

Gottschalk B 2010 Med. Phys. 37(1), 352{367.

Highland V L 1975 Nucl. Instrum. Methods 129, 497{499.

Highland V L 1979. Erratum.

Jarlskog C Z & Paganetti H 2008 IEEE Trans. Nucl. Sci. 55(3), 1018{1025.

Kanematsu N 2008 Nucl. Instrum. Methods B 266, 5056{5062.

Lewis H W 1950 Physical Review 78(5), 526{529.

Lynch G R & Dahl O I 1991 Nucl. Instrum. Methods B 58, 6{10.

Moli_ere G 1947 Z. Natur. A2, 133.

Newhauser W, Fontenot J, Zheng Y, Polf J, Titt U, Koch N, Zhang X & Mohan R 2007 Phys. Med. Biol. 52, 4569{4584.

Newhauser W, Koch N, Hummel S, Ziegler M & Titt U 2005 Phys. Med. Biol. 50, 5229{5249.

Rossi B & Greisen K 1941 Rev. Mod Phys. 13, 240{309.

Sawakuchi G O, Mirkovic D, Perles L A, Sahoo N, Zhu X R, Ciangaru G, Suzuki K, Gillin M T, Mohan R & Titt U 2010 Med. Phys. 37(9), 4960{4970.

Sawakuchi G O, Zhu X R, Poenisch F, Suzuki K, Ciangaru G, Titt U, Anand A, Mohan R, Gillin M T & Sahoo N 2010 Phys. Med. Biol. 55, 3467{3478.

Urban L 2006 A multiple scattering model. CERN-OPEN-2006-077.

A new technology for fast two-dimensional detection of proton therapy beams

Robert Hollebeek,[1] Mitch Newcomer,[1] Godwin Mayers,[1] Brian
Delgado,[1] Gaurav Shukla,[1] Richard Maughan,[2] and Derek Dolney[2]

[1]Department of Physics, University of Pennsylvania, Philadelphia, PA 19104.
[2]Department of Radiation Oncology, University of Pennsylvania, Philadelphia, PA 19104.
(Dated: July 20, 2012)

The Micromesh Gaseous Structure, or Micromegas, is a technology developed for high count-rate applications in high-energy physics experiments. Presented here are tests using a Micromegas chamber and specially designed ampli_ers and readout electronics adapted to the requirements of the proton therapy environment and providing both excellent time and high spatial resolution. The device was irradiated at the Roberts Proton Therapy Center at the University of Pennsylvania. The system was operated with ionization gains between 10 and 200 and in low and intermediate dose-rate beams and the digitized signal is found to be reproducible to 0.8%. Spatial resolution is determined to be 1.1 mm (1_) with a 1 ms time resolution. We resolve the range modulator wheel rotational frequency and the thicknesses of its segments and show that this information can be quickly measured owing to the high time resolution of the system. Systems of this type will be extremely useful in future treatment methods involving beams that change rapidly in time and spatial position. The Micromegas design resolves the high dose rate within a proton Bragg peak and measurements agree with Geant4 simulations to within 5%.

I. INTRODUCTION

At the time of this writing there are 40 hadron therapy facilities in operation worldwide treating cancer patients with hadrons. Nearly 100,000 patients have completed treatments [1]. The path of a hadron in tissue is essentially straight with relatively low energy loss until very near the end of the range where most energy is deposited

in a small region called the Bragg peak, with little exit dose relative to photons. The depth of the Bragg peak in the patient is controlled by the beam energy, and modern delivery systems allow fast and continuous modulation of beam energy during delivery. Collimation of treatment _elds achieves good lateral dose gradients, comparable to X-ray _elds, and systems of detectors exist to measure 2D planes of dose distributions. The steep longitudinal dose gradient that is the motivation behind proton therapy additionally allows for high dose conformity in a third dimension, but detector systems for characterizing 3D dose distributions do not exist. As an alternative to collimation, narrow proton pencil beams can be scanned magnetically, but such treatments have been relatively rare so far even though the technology does not require an aperture and o_ers the possibility of improved dose localization [2]. Due to the potential for interplay between the motion of the pencil beam and the respiratory motion of the patient, it is necessary to resolve the time structure of the dose delivery to fully realize the capabilities of hadron therapy, particularly for lung tumors. Direct detection of the high beam current used for hadron therapies requires a new generation of dosimetry devices capable of high spatial and time resolution accompanied by good linearity and little to no saturation in the Bragg peak. New dosimetry technology tailored to hadron therapy will:

_ Reduce the uncertainties in beam characteristics (position, energy/range, stability), partially addressing the range uncertainty problem and potentially allow for a reduction in treatment margins, thereby permitting additional disease sites to be treated with particle beams, improving the prospects for dose escalation and hypofractionation strategies, and generally lowering the integral dose to normal tissues across all disease sites,

_ Accelerate the development and optimization of the next generation of dose delivery technologies, including intensity-modulated scanned pencil beams, especially in conjunction with patient motion management and image-guided radiation therapy (IGRT) systems, by providing good spatial and time resolution for the dose delivery,

_ Assist in the development of new and more advanced therapy-supporting technologies, and become key components of those technologies, including proton radiography [3], proton computed tomography [4{6], range veri_cation [7], and range probes [8], where high spatial and time resolution are important requirements,

_ Facilitate more rapid delivery and commissioning of new particle therapy facilities, and

_ Allow more comprehensive Quality Assurance (QA) measurements of patient treatment plans to be performed [9, 10].

This paper describes the design and performance of a new device with millimeter and millisecond resolution and high dynamic range. We will be discussing proton therapy in particular, though our design could be adapted for other particle types. The requirements for

2

an ideal beam monitoring device used for the characterization of proton therapy beams are stringent: beam position should be resolved at the order of about 1 mm and dose measured with an accuracy of 2% or better. Ionization chambers represent the gold standard for dose accuracy since the gain depends only on ionization in the gas mixture used. Good spatial resolution however requires multiple chambers. The high ampli_er gain required to detect the small signals leads to limited bandwidth and therefore limited time resolution. If using a single chamber, it must be repositioned to obtain beam pro_les. This is very time consuming whether done manually or using stepping motors. Multiple devices can be placed in the beamline to obtain some spatial resolution from a single beam delivery, and one and two dimensional arrays of ionization chambers are now available commercially and useful for proton therapy measurements. Semiconductor detectors are also a possible choice for proton therapy dosimetry as they can be made small and thus provide good spatial resolution, and they can be read out fast for good time resolution, however they tend to be expensive for large volume arrays, su_er degradation from radiation exposure, and have a response depending on energy, temperature, and dose rate. Detector systems based on scintillating materials can be manufactured at relatively low cost and can provide good resolution in 2D using planes of scintillating material [11] and in 3D using a volume of scintillator [12]. Thus far however, scintillating devices used in proton therapy beams su_er from radiation damage and some saturation in the Bragg peak, though it appears that corrections can be made to obtain a reasonable calibration. Chemical dosimeters, including ferrous (Fricke) gels and polymer gels, can be poured into containers of di_erent sizes and shapes and irradiated, followed by readout by methods such as MRI or optical CT, but these, like _lm, are strictly integrative materials that o_er no time resolution.

A typical proton therapy irradiation will deliver 2 Gy to a 1 L volume in 1{2 minutes, mostly by direct ionization of tissue molecules, meaning that ion pairs are created in the volume at a rate of a few hundred _A. A small chamber with active volume 1 mm_3 would see only a few hundred pA. The dose pro_le at the edges of the treatment _eld falls o_ like an error function, and ideally one would like to resolve the dose in this penumbra at the level of 1% of the maximum dose. Therefore, the goal of a dosimeter for proton therapy is to resolve pA-scale currents. In the case of actively scanned beams, the beam may be swept across the chamber volume on millisecond timescales.

Compared to ionization chambers, proportional counters provide larger signals by operating at a su_ciently high _eld strength such that primary ions in the gas are accelerated enough to produce additional ionization. Counters operating in the proportional region achieve high enough gain for sensitivity to single ionizing particles. Multiwire proportional chambers, and drift chambers can be fabricated into devices that cover large volumes. While many traditional chambers of this type were constructed with small diameter wires, there are now competing technologies for this application, including GEM detectors where the small structures producing the high electric _elds are holes, and Micromesh Gaseous Structure, or so-called Micromegas where the structures are _ne meshes [13]. The Micromegas is a variation of an ionization chamber where a _ne mesh has been introduced to create a high-_eld region where large gas gains, up to factors of 10_6, can be realized [14{16]. Advantages of this approach include large dynamic range, high rate capability, good time resolution, and _ne segmentation. A manufacturing process to produce Micromegas chambers in bulk at relatively low cost has matured [17], and re_nements to the basic design continue to develop [18]. In this work, we present a novel adaptation of the Micromegas technology for the proton therapy environment, where the device is operated at low gain and is operated in current mode rather than pulse mode.

In this paper we describe the con_guration and testing of a multi-channel Micromegas detector that has been designed and assembled at the University of Pennsylvania and irradiated in the proton therapy beam at the Roberts Proton Therapy Center. We present measurements of spatial and time resolution and show that the chamber resolves a proton Bragg peak without saturation. To our knowledge, this is the _rst data obtained with this type of detector in a proton therapy beam.

II. METHODS AND MATERIALS

A prototype Micromegas chamber with a segmented anode plane was designed and assembled at the University of Pennsylvania. The mesh plus anode layer were fabricated at CERN following the bulk Micromegas process described elsewhere [17]. The chamber has a circular center channel and four peripheral quadrants (see Figure 1) etched on one side of a standard 2 oz double-sided copper clad G10 printed circuit board (PCB). The segments are electrically connected to readout channels by plate-through holes to the back of the PCB. The micromesh is a woven stainless steel mesh of 20 _m wires at 80 _m spacing. The micromesh is held above the anode planes with a uniform gap of 128 _m by photoetched stand-o_s. The micromesh is connected to a high voltage feed by a copper trace on the PCB. The drift gap region of 1.275 cm thickness is de_ned by a ring fabricated from polyether ether ketone (PEEK) insulator material that also has provisions for the gas inlet and outlet and gas seal o-rings. The drift cathode is another G10 PCB. The

chamber uses a 70% argon, 30% CO_2 gas mixture, selected to give lower gain but higher current capability. The Micromegas assembly contains an ^{55}Fe calibration source embedded in the drift region.

Typical operating potentials are -710 V on the drift electrode and between -400 and -600 V on the micromesh, depending on the gain desired. The choice of negative po-

3

FIG. 1: The Micromegas board. The _ve readout anodes can be seen in the center and are numbered. The woven micromesh is held above the readout anodes by photoetched Kapton stando_s (visible as small points covering the anode plane) that maintain a uniform 128 _m gap. The center channel is 5 cm in diameter. Also visible is the insulating ring, O-ring for gas seal, high voltage lead (lower right), and gas feed pipe (upper left).

larity for the mesh was guided by Poisson Super_sh [19] electromagnetic _eld simulations of the chamber geometry, as shown in Figure 2. In the case of the mesh held at negative potential relative to the collecting electrode, a high _eld region is created in the relatively narrow ampli_cation gap between the mesh and the anode where gas gain occurs. The shape of the _eld near the mesh is such that it tends to focus electrons between the wires of the mesh as they move from the drift gap into the ampli_cation region. Since the ampli_cation occurs in the small gap region, positive ions can be cleared out more quickly. Alternatively, the con_guration with the mesh held positive relative to the electrodes is more like a multiwire proportional counter, with the electrons being collected at the mesh. Ionization gain occurs near the mesh wires where the _eld strength is very high, proportional to $\log(r_{wire}=r)$. Some gain is also realized in the ampli_cation gap for primary ionization produced there, however primary electrons from the drift region do not generally cross the mesh plane and the number of primary ions produced is small. A drawback of this con_guration at high current is that slowly drifting positive ions produced near the mesh wires tend to build up in the low _eld regions that can be seen around the mesh wires in Figure 2. A buildup of positive ions near the mesh wires has the e_ect of increasing the e_ective wire diameter, r_{wire}, and so this type of chamber generally has less gain as beam current increases. We found by measurements in proton beams of the gain using the two polarities that the mesh held negative gives the ability

FIG. 2: Electromagnetic _eld simulations of the Micromegas geometry using Poisson Super_sh with the micromesh held positive (left) or negative (right) relative to the electrode at the bottom of the plots.

to produce higher gains and that the gain is more stable with respect to variations in the beam current. There are also low _eld regions in the con_guration with the mesh negative, but they tend to be located just above the mesh wires in the drift gap, where an accumulation of positive space charge may tend to defocus electrons drifting into the ampli_cation region, however the gain of the device

is observed to be more stable.

A preampli_er board was designed for the readout of ionization current on each of the _ve channels (Figures 3 and 4). Each preampli_er board has a total of ten channels. The power module derives stabilized _5 V from an external power supply and an additional -1 V reference voltage to which the current thru the input stage is compared. The current is fed into an operational ampli_er and each channel supports two di_erent gain settings individually selectable via an external digital I/O bit to achieve a wider dynamic range. The relative high/low gain settings were selected to accomodate the di_erent beam intensity produced by double-scattered and modulated-scanned delivery methods. The net gain of the overall system can be changed in several ways: there is a factor of 5 available in the digitizer gain, a factor of 40 in the high/low ampli_er setting, and a factor of 200 in the gas gain for the mesh voltage range that we have considered. Additional adjustments can be accomplished with di_erent gas choices which we will explore in a future study.

The analog outputs from the ampli_ers are connected to a DATAQ DI-720 which samples each channel at 1 kHz and digitizes and serializes the signals for transfer to a PC connected to the DATAQ by ethernet. Each channel is read at a 1 ms sampling interval for the experiments described here, though faster rates are possible with the DI-720.

The chamber assembly was irradiated with beams of protons at the Roberts Proton Therapy Center at the University of Pennsylvania. The cyclotron and beam-line were designed by and are operated by Ion Beam Applications (IBA). The facility was designed to deliver therapeutic beams of up to 230 MeV protons to

4

FIG. 3: Schematic showing the layout of the preampli_er board. The power module (top) is supplied with _6 V by ribbon cable and provides power to the 10 ampli_er modules. Ribbon connectors are used to connect the chamber channels (left) and the ADC data acquisition module (right). The preamp dimensions are indicated in inches.

FIG. 4: Photograph of the preampli_er module. Power is supplied by the ribbon cable shown. The chamber channels are connected at left and the data acquisition module interfaces with the ribbon connectors at right.

_ve treatment rooms using three di_erent delivery techniques. The _rst is a double-scattered beam and is the least intense in terms of instantaneous dose (ionization) rate. Beamline components spread the beam to the maximum treatment _eld size (_ 20 cm) and then collimate to a target-spec_c treatment area using a Varian Multi-leaf Collimator (MLC) comprised of 100 motorized tungsten leaves. The second type of beam is the uniform-scanned beam, which is also collimated with the MLC but the beam is magnetically scanned behind the collimator to generate larger _eld sizes. This delivery technique produces higher instantaneous dose rates at the

time the beam is swept across the measurement volume. Finally, modulated-scanned beams, which are magnetically scanned only and not collimated, are _nely focused with additional quadrupole magnets and are the most intense. We present here results obtained using the double-scattered and uniform-scanning delivery techniques. Experiments with modulated-scanned beams have also been successful but are ongoing and will be reported later.

The beam range, de_ned as the water-equivalent depth at which the dose is 90% of the peak, that was used for these experiments was 17.5 cm, corresponding to a mean kinetic proton energy of about 170 MeV. The beam current at cyclotron extraction was 3 nA. The transport e_-ciency to the treatment rooms is nominally of order 10% at this beam energy. For some experiments we have delivered spread-out Bragg peaks (SOBP) which are modulated using a range modulator wheel. We used SOBPs of 10 cm modulation (i.e, the length of the at, high-dose part of the SOBP in the depth direction) In other experiments, a single Bragg peak was delivered by stopping the modulator wheel on a particular segment. We used the MLC to collimate to small _elds by opening a single leaf pair. The e_ective leaf width is 4.5 mm and the leaf pair was opened between 1 and 5 mm as indicated for the experiment.

The entire chamber assembly was placed in a Faraday cage of 1/16 inch copper sheet for noise shielding and the Faraday cage was placed on top of the treatment couch near the isocenter position for the treatment room. An additional ionization chamber, composed of two sheets of copper clad G10, was located on top of the Faraday cage, upstream of the Micromegas chamber. The data from that ionization chamber was used for other experiments and is not discussed here. For the spread out and single Bragg peak measurements, an acrylic tank of dimensions 12 cm _ 12 cm transverse _ 30 cm depth was placed on top of the ionization chamber and _lled with water. A drain pipe was used to siphon water from the tank at a controlled rate and data was collected continuously with the proton beam while water owed out of the tank. The total water-equivalent depth of the acrylic tank bottom, the ionization chamber, the top copper sheet of the Faraday cage, and the cathode G10 board of the Micromegas chamber is calculated to be 2.2 cm using stopping power ratios to water from the NIST PSTAR database [20, 21] for 170 MeV protons.

5

We measured beam transverse pro_les with Gafchromic EBT2 _lm. A calibration curve was constructed for this batch of _lm by delivering uniform dose cubes of varying total number of MUs with the _lm located in the center of the delivered dose. The _lm was scanned and digitized with an Epson 10000XL atbed scanner. The red color channel was used for the optical density measurement.

We compare some of the Micromegas chamber mea-

surements to Monte Carlo results generated using simulation code developed at the University of Pennsylvania for the IBA proton therapy nozzles and Varian MLC using the Geant4 version 9.4 (Patch-01) toolkit [22]. Our physics list was originally provided by Harald Paganetti [23], though we had to modify it for the newer version of Geant4 by replacing G4MultipleScattering with G4eMultipleScattering for electrons and positrons and with G4hMultipleScattering for hadrons. We have implemented the modulator wheels based on IBA speci_cation and optimized the beam current modulation using least-squares _tting in order to reproduce commissioning measurements. Our simulations reproduce the beam range to within 2 mm and 1% dose accuracy everywhere for both the double-scattering and uniform-scanning modalities.

III. RESULTS

A. ^{55}Fe calibration

The chamber gas and gain calibration uses a readout connected to the mesh. Typical pulses from the source are shown in Figure 5. The pulse height spectrum of the ^{55}Fe calibration (Figure 6) can be used to correct for variations in the absolute gain due to changes in gas, voltage, temperature, or pressure since it measures the absolute gain. Figure 7 shows the peak height for -590 V mesh as a function of pressure and indicates that gain corrections for pressure and temperature are of the order of a few percent. The gas gain as a function of mesh voltage is given in Figure 8.

B. Precision and stability of chamber response

For proton therapy applications, one is typically interested in the total dose delivered to a spatial region. The integral response of the chamber should be very stable across a wide dynamic range. We measured the precision of the integrated Micromegas chamber signal by assuming a constant beam current and delivering the proton beam to the chamber for one second intervals. For each of 42 one second beam deliveries, the total charge collected by the center channel was determined by integrating the digitized signal. We plot in Figure 9 the results of those irradiations. The standard deviation from the mean for these 42 measurements is 0.8%. The data show a remarkable drift in time with a timescale of about one minute.

FIG. 5: Average of current pulses from a ^{55}Fe test source (green trace) and the calibration signal through a shaping ampli_er (purple trace).

0
50
100
150
200
250
0 50 100 150 200
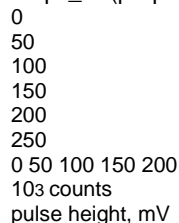10$_3$ counts
pulse height, mV

FIG. 6: An example calibration pulse height distribution from the ^{55}Fe calibration source embedded in the Micromegas chamber with mesh at -590 V. The pulse height is strongly dependent on the mesh potential, and somewhat dependent on the ambient temperature and pressure. The position of

129

the main peak is used as a daily gain calibration for the Micromegas. The smaller peak is the Argon escape peak.

We believe that it is the beam current that is uctuating and not the chamber response, and so consider this value to be an upper limit on the chamber precision.

C. Spatial resolution

We measured the spatial resolution of the Micromegas chamber by moving the chamber with the treatment couch across a uniform-scanned beam collimated with a 4 mm x 4.5 mm aperture positioned near the boundary between channels 2 and 5. That data is shown in Fig-

6
111
112
113
114
115
116
117
118
119
120
756 758 760 762 764 766
pulse height, mV
pressure, mmHg

FIG. 7: Pulse height versus pressure with ^{55}Fe calibration source for -590 V mesh.

10
100
500 520 540 560 580 600 620
pulse height, mV
mesh potential, V

FIG. 8: Gain calibration curve for the Micromegas chamber as a function of mesh potential.

ure 10. The pro_le of this beam was determined at the elevation of the center of the Micromegas drift gap by a placing a piece of Gafchromic EBT2 _lm downstream of the chamber PCBs and the Faraday cage top plate. The beam is su_ciently narrow (4.3 mm FWHM) in the direction transverse to the direction of couch travel that we collect all charge on channels 2 and 5. A ratio of the signal on channel 2 to the signal on channel 5 provides a position measurement for the beam. We measured _ = 1.1 mm for the beam position measurement using the Micromegas chamber.

0.98
0.99
1
1.01
1.02
0 5 10 15 20 25 30 35 40
% deviation from mean
time, s

FIG. 9: Reproducibility of the chamber response in the proton beam. The detector was irradiated in 1 second intervals. The integrated response of the chamber is constant across the 42 measurements to 0.8% (1_). The signal uctuates on about a one minute timescale and is likely due to a drift in the beam current.

0
10
20
30

40
50
60
-0.2 0 0.2 0.4 0.6 0.8 1
Q / Q
0 beam position, cm

FIG. 10: Spatial resolution measurement for the Micromegas chamber using a beam moving across the boundary between channels 2 and 5. The lines represent the fraction of the integrated beam pro_le that is delivered to channel 2 (dotted) and channel 5 (solid). The data points are the integrated charge Q measured on the given channel relative to the charge Q_0 measured with the transmission ionization chamber in the delivery nozzle. The ratio of the signal on the two channels can be used as a beam position measurement with _ = 1:1 mm.

D. Double-scattered proton beam

The double-scattered proton beam delivery technique uses a modulator wheel with segments of varying thicknesses of Lexan and Pb to produce a at spread-out Bragg peak (SOBP). The wheel rotates at a nominal 10

7

Hz and the beam is pulsed in phase with the wheel. The number of segments irradiated determines the length of the at part of the SOBP in the depth direction. The Micromegas signal in this type of beam is shown in Figure 11. The water level was lowered continuously with the beam on at a rate of 0.14 mm/s. The lower plots of Figure 11 show that the Micromegas chamber can resolve the time structure of this delivery technique. Each pulse corresponds to a rotation of the modulator wheel. Four segments of the wheel can be identi_ed in the lower right _gure, though the fourth gives a very low signal at the depth of the measurement (about 16.5 cm) and is in the beam for only a few ms before the next segment. In order to produce a at SOBP, the relative weight of Bragg peaks are set by the angular width of the corresponding segment on the modulator wheel and _ne-tuned by modulating the beam current in phase with the wheel rotation. We show in Figure 11 that the sum of the measurements over the wheel rotation indeed produces a at SOBP.

By smoothing individual pulses for ampli_er response and then averaging over the ten pulses contained in one second of data at a particular depth, it is possible to construct pro_les of the beam energy passing through the rotating wheel at di_erent depths yielding detailed information about the wheel structure. Examples of these pulses at six di_erent depths are shown in Figure 12. The leading and trailing edge of the distributions can be used to extract the size of the wheel angular segments and compare them to speci_cations from the manufacturer. Individual wheels may vary slightly and this technique is capable of measuring the di_erences between wheels in di_erent treatment rooms. The comparison for the room used in these tests is shown in Figure 13 and the agreement is excellent.

A Fourier transform of the signal collected with the double-scattering delivery is shown in Figure 14. This

131

provides a measurement of the wheel angular frequency, which we _nd to be 10.0046 _ 0.0032 Hz.

E. Uniform-scanned proton beam

A uniform-scanned beam of 17.5 cm water equivalent proton range was collimated to 5 mm x 4.5 mm using the MLC. The beam is scanned magnetically at nominal 3 Hz in the head to foot transverse direction and 30 Hz in the left right direction. Figure 15 shows a typical signal in the center channel of the Micromegas chamber for this kind of delivery. Each peak arises from the beam scanning at the high frequency across the collimation hole. The _rst four peaks correspond to the beam moving slowly in the head to foot direction. The pattern is reversed as the beam is scanned back in the opposite direction. The pattern of pulses observed is consistent with the nominal frequency values, but illustrates that much more accurate measurements are possible. In particular, we get from the Fourier transform of this data (Figure 16) a measurement of the scanning frequencies: 3.1146 Hz _ 0.2% in the slow direction, and 31.146 Hz _ 0.04% in the fast direction (using the fundamental peaks). However, Figure 15 is actually 65 consecutive pulse patterns plotted with a phase shift of 0.32112 s between pulses. The 65 pulses trains overlay extremely well indicating that the beam scan pattern is very well controlled and reproducible. Changing the phase shift by only 0.00001 s disrupts the overlay of the pulses, and so this is a measurement of one of the scan frequencies that is much more precise than from the FT: 3.1141 Hz _ 0.002%. At this level of precision one has to consider the accuracy of the data acquistion clock itself.

F. Bragg peak measurement

We delivered a pristine (unmodulated) Bragg peak to the detector by stopping the modulator wheel on the _rst (thinnest) segment. The beam was collimated with a 5 mm x 4.5 mm aperture. The beam was not scanned. The water level was lowered continuously with the beam on at a rate of 0.14 mm/s. The data collected with the Micromegas is compared with Geant4 simulations in Figure 17.

The measured detector signals indicate that the beam in this con_guration is synched to 60 Hz and is on for 10.00 microseconds and o_ for the following 6.67 microseconds. Averaging samples over as few as 10 pulses (1 second) can be used to detect pulse to pulse variations in delivered current to high accuracy as shown in Figure 12 which shows the result of averaging 5 pulses to the left and 5 to the right and the e_ect of smoothing the distribution. The result is a fraction of a percent accuracy every second.

IV. DISCUSSION

There are over two orders of magnitude di_erence in the instantaneous ionization rates encountered in proton therapy, from the relatively low rate double-scattered delivery to the high-rate modulated-scanning delivery, with uniform-scanning intermediate between the other two. The Micromegas chamber described in this paper

is designed to resolve typical treatment dose rates for all modalities and is capable of a very wide dynamic range. The digitization gain is adjustable, each channel of the preampli_er board has two gain settings switchable by external digital control and further _ne tuning of the gain is accomplished by adjusting the mesh potential using a calibration curve like that shown in Figure 8 and remeasuring the gain with the calibration channel.

The measurements indicate the Micromegas response is reproducible to better than 0.8% in a double-scattered proton therapy beam. The prospects for Micromegas for relative and absolute dosimetry appear promising. Indeed, while ionization chambers are currently the standard for absolute dosimetry in the _eld of external beam

8
-1
-0.8
-0.6
-0.4
-0.2
0
0.2
0.4
70 72 74 76 78 80
signal, V
time, s

(a)

-1
-0.5
0
0.5
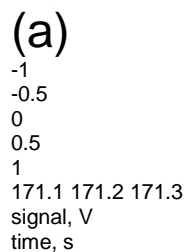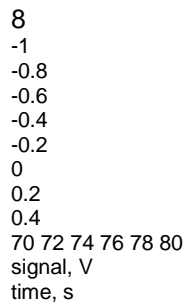1
171.1 171.2 171.3
signal, V
time, s

(b)

FIG. 11: Micromegas measurement (black points, upper chart) of a proton spread-out Bragg peak (SOBP) delivered using the
double-scattered technique. Five individual Bragg peaks can be seen corresponding to the _rst (most distal) _ve segments on
the modulator wheel. The _ve Bragg peaks combine to produce a at SOBP, as shown by the red line, which was obtained by
summing the Micromegas signal over three complete wheel rotations. Two regions are highlighted for closer examination: (a,
bottom left) showing the series of pulses generated by the modulator wheel increasing in amplitude as the water depth lowers,
e_ectively moving the detector into the distal fallo_ region; and (b, bottom right) showing three wheel rotations at a depth
where four Bragg peaks can be discerned both in the datapoints in the top chart and in the pulses in the bottom right.

therapy, the technique used here might achieve the same absolute level of accuracy with vastly improved spatial and time resolutions. The challenge for Micromegas will be to achieve stable gain, including a precise method to correct for ambient conditions. This is commonly achieved by a feedback voltage of order less than 1 volt applied to the preamp voltage reference and calibrated using the calibration source. We continue to optimize the chamber geometry, gas composition, and operation settings and the preampli_er design and look forward to

reporting in the future on its performance across the full dynamic range of proton therapy ionization rates.

The 1 mm spatial resolution that we demonstrate is encouraging and is in line with what is typically accepted as a clinically meaningful resolution. The commercially available 2D arrays of ion chambers or diodes are typically spaced at _7 mm. We have designed a Micromegas chamber with smaller pads and look forward to resolving modulated-scanning beams as they are steered magnetically. Current therapy-grade systems produce these
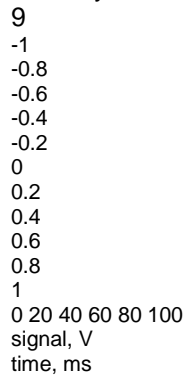
9
-1
-0.8
-0.6
-0.4
-0.2
0
0.2
0.4
0.6
0.8
1
0 20 40 60 80 100
signal, V
time, ms

FIG. 12: Pulses produced by the range modulator wheel at six di_erent depths in water averaged over one second intervals. In order of increasing width, the pulses were taken from the data in Figure 11 at time 0, 51, 130, 190, and 237 s, corresponding to water-equivalent depths of 17.9, 17.2, 16.2, 15.4, and 14.8 cm, respectively.

0
5
10
15
20
25
30
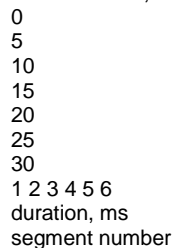1 2 3 4 5 6
duration, ms
segment number

FIG. 13: Duration (in ms) that segments of a modulator wheel cross the beam path measured with the Micromegas (points with error bars) compared to the manufacturer data (shaded columns). The measurements were extracted from the pulses at six di_erent depths in water averaged over one second shown in Figure 12.

beams with beam sigmas _3 mm, though that size could be driven smaller in the future as the technology improves.

It is interesting that the individual segments on the modulator wheel can be identi_ed in the data we have taken. Proton centers that are commissioning modalities that use modulator wheels may need to input the water-equivalent thicknesses of the track segments (the Varian Eclipse treatment planning system requires this

0
0.2
0.4
0.6
0.8
1
0 20 40 60 80 100 120 140
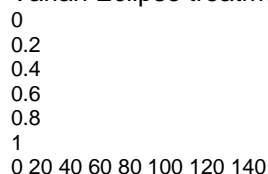
amplitude

frequency, Hz

FIG. 14: Fourier transform of ionization current collected using the double-scattered proton delivery technique. We measure the wheel rotational frequency to be 10.0046 _ 0.0032 Hz.

-1
-0.8
-0.6
-0.4
-0.2
0
0.05 0.1 0.15 0.2 0.25 0.3

signal, V

time, s

FIG. 15: Ionization signal from the Micromegas chamber using the uniform-scanned proton delivery technique in which a relatively large Gaussian spot is magnetically scanned to produce a large, uniform uence behind a collimating aperture. The aperture was 5 mm x 4.5 mm. The beam was on for 21 seconds and 65 pairs of pulse sets were collected in that time. All 65 sets are plotted here by shifting the phase of each set by 0.32112 s.

information). While the proton system vendor will typically provide tables of the segment materials and thicknesses, users may want to verify the data for themselves with measurements. We are excited by the possibility of accurately and rapidly characterizing modulator wheels without resorting to tedious delivery of beam on each individual segment of the nine wheel tracks that have been commissioned at Roberts. It would also be interesting to characterize any di_erences between the modulator

10
0
0.2
0.4
0.6
0.8
1
0 20 40 60 80 100 120 140

amplitude

frequency, Hz

FIG. 16: Fourier transform of uniform-scanning delivery data. We measured the fundamental frequencies to be 6.2291 and 62.29 Hz. The beam scanning frequencies are one-half these values, because the beam passes the collimator hole twice per scan cycle.

0
0.2
0.4
0.6
0.8
1
1.2
4 6 8 10 12 14 16 18 20

0
0.2
0.4
0.6
0.8
1
1.2

charge

energy deposit

water equivalent depth, cm

Micromegas measurement
Geant4 simulation

FIG. 17: A proton Bragg peak measurement using the Micromegas chamber compared with Geant4 simulation of the IBA Universal Nozzle, Varian MLC, and the Micromegas detector and water column. Agreement is within 5% across the water-equivalent depth range from 7.5{19.5 cm. The curves are normalized at the peaks. The error bars on the Micromegas measurement represent the 0.8% dose reproducibility (see Figure 9) and the error bars on the simulation represent the Monte Carlo sample variance.

wheels across the four treatment rooms that have wheels at Roberts. Based on the speci_cations of the modulator wheels provided by IBA, the _rst four wheel segments should cross the beam path in 26, 9, 7, and 5 ms respectively, and these values are consistent with what we have measured from Figure 11. Accurate knowledge of the shape of the beam pulses produced by the modulator wheel may be important information for a new range veri_cation method currently under development [24]. The Fourier transform of the ionization current shown in Figure 14 indicates some noise at the rate of a few Hz. We have identi_ed noise on the preampli_er circuit coming back from the DATAQ module. A new revision of the preampli_er board has been designed with a _lter to remove this noise. We have also increased the bandwidth of the operational ampli_er and improved the input compensation which should provide time resolution as low as as 50 microseconds in the next version. However, we also believe that the beam current actually uctuates at about 2 Hz at the few percent level. This can be seen in the treatment control rooms on the signals coming from the beam monitor ionization chambers in the nozzle. Such small uctuations are not important for patient treatments; the system is designed to deliver a precise integral dose over millisecond or longer timescales using beam turn o_ times of order a few microseconds. However in the case of rapidly scanned beams, this may no longer be negligible.

It is interesting to note that the data resolve the very stable uniform scanning pattern (Figure 15) and therefore provides a measurement of the unknown beam pro_le upstream of the collimator. The peak of each pulse in the Figure corresponds to a point on the (Gaussian) beam pro_le in the slow scanning direction, or more precisely, the beam pro_le convolved against the aperture window. Furthermore, the width of these pulses determines the scan velocity of the beam in the fast scan direction, given the size of the aperture in that dimension.

Other detectors tend to saturate in the high dose rate of the Bragg peak, but we have resolved the peak relative to the entrance (Figure 17). There is some disagreement between the simulations and the measurement especially around 12{13 cm depth. We are told by the vendor that the beam current can drift on timescales of about 10 minutes. Typically for commissioning measurements, depth dose pro_les are normalized to the signal from one of the

transmission ionization chambers in the nozzle to remove beam current uctuations. In the future we will follow that method. Alternatively, the small treatment _elds that we have prepared using the MLC for these experiments are much smaller than the _elds used to treat patients, and this is the _rst data that we have collected in order to verify the Geant4 simulations for small _elds. We also point out that there are features in the proton inelastic cross section data that the Geant4 physics models do not reproduce [25]. We intend to investigate this further.

V. CONCLUSIONS

Micromegas is a gas-_lled detector technology that can be manufactured in bulk at low cost. We have demonstrated a new use for Micromegas as a beam monitor for proton therapy, and the data presented here indi-

11

cates that Micromegas holds promise as a high spatial and time resolution measurement device for proton therapy. We believe the design could be adapted to heavier ion beams. We look forward to continuing to improve the designs and will publish additional _ndings in the future.

[1] M. Jermann (2012), http://ptcog.web.psi.ch/ptcentres.html.
[2] A. Smith, Med. Phys. 36, 556 (2009).
[3] U. Schneider, J. Besserer, P. Pemler, M. Dellert, M. Moosburger, E. Pedroni, and B. Kaser-Hotz, Med. Phys. 31, 1046 (2004).
[4] R. W. Schulte, V. Bashkirov, T. Li, Z. Liang, K. Mueller, J. Heimann, L. R. Johnson, B. Keeney, H. F.-W. Sadrozinski, A. Seiden, et al., IEEE Trans. Nucl. Sci. 51, 866 (2004).
[5] L. Johnson, B. Keeney, G. Ross, H.-W. Sadrozinski, A. Seiden, D. C. Williams, L. Zhang, V. Bashkirov, R. Schulte, and K. Shahnazi, Nucl. Instrum. Methods A 514, 215 (2003).
[6] S. N. Penfold, A. B. Rosenfeld, R. W. Schulte, and H.-F. W. Sadrozinksi, Radiat. Meas. 46, 2069 (2011).
[7] H.-M. Lu, Phys. Med. Biol. 53, N415 (2008).
[8] M. Mumot, C. Algranati, M. Hartmann, J. M. Schippers,

E. Hug, and A. J. Lomax, Phys. Med. Biol. 55, 4771 (2010).

[9] B. Arjomandy, N. Sahoo, X. Ding, and M. Gillin, Med. Phys. 35, 3889 (2008).

[10] B. Hartmann, J. Telsemeyer, L. Huber, B. Ackermann, O. Jkel, and M. Martikov, Phys. Med. Biol. 57, 51 (2012).

[11] S. N. Boon, P. van Luijk, T. Bohringer, A. Coray, A. Lomax, E. Pedroni, B. Scha_ner, and J. M. Schippers, Med. Phys. 27, 2198 (2000).

[12] S. Beddar, L. Archambault, N. Sahoo, F. Poenisch, G. T. Chen, M. T. Gillin, and R. Mohan, Med. Phys. 36, 1736 (2009).

[13] M. Titov, Nucl. Instrum. Methods A 581, 25 (2007).

[14] Y. Giomataris, P. Rebourgeard, J. Robert, and G. Charpak, Nucl. Instrum. Methods A 376, 29 (1996).

[15] Y. Giomataris, Nucl. Instrum. Methods A 419, 239 (1998).

[16] I. Giomataris, in Proceedings of the International Symposium On Detector Development For Particle, Astroparticle And Synchrotron Radiation Experiments (SNIC 2006) (2006).

[17] Y. Giomataris, R. D. Oliveira, S. Andriamonje, S. Aune, G. Chapak, P. Colas, et al., Nucl. Instrum. Methods A 560, 405 (2006).

[18] R. Oliveira, V. Peskov, F. Pietropaolo, and P. Picchi, IEEE Trans. Nucl. Sci. 57, 3744 (2010).

[19] K. Halbach and R. F. Holsinger, Particle Accelerators 7, 213 (1976).

[20] http://physics.nist.gov/PhysRefData/Star/Text/PSTAR.html.

[21] ICRU report 49: Stopping powers and ranges for protons and alpha particles (1993).

[22] S. Agostinelli et al., Nucl. Instrum. Methods A 506, 250 (2003).

[23] C. Z. Jarlskog and H. Paganetti, IEEE Trans. Nucl. Sci. 55, 1018 (2008).

[24] B. Gottschalk, S. Tang, E. H. Bentefour, E. W. Cascio, D. Prieels, and H.-M. Lu, Med. Phys. 38, 2282 (2011).

[25] http://geant4.web.cern.ch/geant4/results/validation_plots/cross_sections/hadronic/inelastic/test1/inelastic.shtml.

Phase III -journal publications – published
ORIGINAL RESEARCH

Development of a Remote Proton Radiation
Therapy Solution over Internet2

Arnaud Belard, M.B.A.,[1,2] Brent Tinnel, M.D.,[2] Steve Wilson, M.D.,[3] Ralph Ferro, M.S.C.E.,[4] and John O'Connell, M.D.[2]

[1]Henry M. Jackson Foundation for the Advancement of Military Medicine and [2]Radiation Oncology Service, Department of Radiology, Walter Reed Army Medical Center, Washington, DC.

[3]Department of Radiation Oncology, University of Pittsburgh Medical Center, Pittsburgh, Pennsylvania.

[4]Department of Radiation Oncology, University of Pennsylvania, Philadelphia, Pennsylvania.

Abstract

Through our existing partnership, our research program has leveraged the benefits of proton radiation therapy through the development a robust telemedicine solution for remote proton therapy planning. Our proof-of-concept system provides a cost-effective and functional videoconferencing desktop platform for both ad-hoc and scheduled communication, as well as a robust interface for data collaboration (application-sharing of a commercial radiation treatment planning package). Over a 2-year period, our evaluation of this model has highlighted the inherent benefits of this affordable remote treatment planning solution, i.e., (1) giving physicians the ability to remotely participate in refining and generating proton therapy plans via a secure and robust Internet2 VPN tunnel to the University of Pennsylvania's commercial proton treatment planning package; (2) allowing cancer-care providers sending patients to a proton treatment facility to participate in treatment planning decisions by enabling referring or accepting providers to initiate ad-hoc, point-topoint communication with their counterparts to clarify and resolve issues arising before or during patient treatment; and thus (3) allowing stewards of an otherwise highly centralized resource the ability to encourage wider participation with and referrals to sparsely located proton treatment centers by adapting telemedicine techniques that allow sharing of proton therapy planning services. We believe that our elegant and very affordable approach to remote proton treatment planning opens the door to greater worldwide referrals to the scarce resource of proton treatment units and wideranging scientific collaboration, both nationally and internationally.

Key words: business administration=economics, distance learning, remote treatment planning

Introduction

Malignant neoplasm, or cancer, is the second leading cause of death in the United States, behind diseases of the heart.[1] Excluding carcinoma in situ, basal cell and squamous cell cancers of the skin, 1.4 million new cancer cases are expected in 2008.[2] As life expectancy and healthcare expenditures rise, the question of balancing innovative treatment delivery and cost-effectiveness becomes increasingly relevant.[3] The implementation of a robust telemedicine solution linking strategically placed remote treatment planning centers to highly centralized proton radiation therapy facilities may be part of the solution. Recently added to the external beam radiation therapy arsenal, proton beams have gained in popularity and acceptance in the cancer-care community.

The physical properties of high-energy proton beams include the distinct ability to control the range of the beam, depositing the majority of the dose deep in tissue at a controlled depth and with no exit

139

dose (Bragg peak). This intrinsic physical property lends proton beam therapy potential clinical benefits. These benefits have already been demonstrated clinically in improved local control of tumors located

in difficult locations, such as skull base tumors, that limit complete surgical resection and limit high-dose irradiation with conventional techniques.[4] The physical advantages also are being used to decrease the dose delivered to normal and healthy tissue[5] and potentially lower toxicity and morbidity from the radiation treatments.[6] The improvements in local control and decreased irradiation to normal tissues have clear potential to improve survival rates.[7–10]

Recognizing the demonstrated physical and potential clinical benefits of proton radiation therapy, the U.S. government funded, through public law, a research program designed to (1) increase the quality of care provided to proton therapy patients (design of a multileaf collimator, tissue inhomogeneity correction, and issues relating to organ motion); and (2) implement a telemedicine solution for the remote treatment planning of patients affiliated with the Department of Defense (DOD).

This article shares our design and subsequent evaluation of a remote proton radiation therapy prototype linking the Walter Reed Army Medical Center (WRAMC) in Washington, DC, with the Roberts Proton Therapy Center at the University of Pennsylvania (Penn), PA. We hope to demonstrate that our solution has the potential to not only facilitate point-to-point communication between radiation oncology centers (physicians conducting ad-hoc calls fromtheir desks), but also bring convenience to WRAMC cancer patients (staged and planned locally, thus reducing the time a patient is away from work, home, and family). Another perceived, inherent benefit of this telemedicine research program was the potential greater acceptance and use of proton ra-

Fig. 1. Sample evaluation of existing video teleconferencing solutions.

REMOTE PROTON RADIATION THERAPY SOLUTION OVER INTERNET2

diation therapy in cancer care (i.e., offering a sense of ''ownership'' to physicians involved in the remote treatment of their patients when local expertise and=or infrastructure is unavailable locally).[11,12] Such enhanced connections between care providers can only benefit patients, who would be the recipients of more appropriate and customized care for their particular case of cancer.

Materials and Methods

Our investigation of existing solutions led us to several products (Fig. 1). While the appeal of Web-based applications was evident (hosted server, hence cost-savings), their limitations quickly disqualified them (inability to separate the video teleconferencing window from the data-collaboration window, video automatically minimized when application-sharing is enabled, lack of multipoint capabilities, inability to integrate seamlessly with existing technology and share applications remotely). In addition, a number of these products seemed geared toward ''planned events'' rather than ''ad-hoc calls.''[13,14] Others still were designed around the transfer of still images.[15–17] While relevant for their specialties (pathology, ophthalmology, radiology, and so on), these approaches focused on ''remote reading'' rather than ''dynamic remote planning.''[18]

Among the solutions tested and demonstrated, only one met several critical requirements of our program. As a simple software coder–decoder (CODEC) that could be installed on existing clinical machines, Polycom_ (Pleasantown, CA) PVX allowed seamless integration into our existing infrastructure (clinical workstations and dual-monitor setup), as well as the ability to collaborate remotely (i.e., applicationsharing). As an Internet Protocol-based (IP-H323) solution, PVXwould

also integrate nicely into a newly deployed gigabit network at WRAMC. An Integrated Service Digital Network-based (ISDN-H320) approach, while potentially more robust and secure,[19] would have brought on additional costs (leasing of Primary Rate Interface (PRI) or Basic Rate Interface (BRI) circuits and costly, dedicated phone line). This last variable wasmade all themore relevant to us in the context of trying to get other Regional Army Medical Centers and Proton Therapy Centers to emulate our efforts, while keeping within their budgetary constraints.[20–22] The cost, at $120 to $150 per license, was an additional, quantifiable benefit.

Further evidence of the product's attractiveness was the userfriendliness of its interface. Once demonstrated, we were convinced that physicians would require little to no training to start using the application in an operational setting.

Embedded in its code, this IP-based desktop solution also allowed its users to share applications remotely (T120 protocol) and separate the ''VTC window'' from the ''application-sharing'' window (Fig. 2). While the product did not allow users to participate in multipoint conferencing right out of the box, it did offer compatibility with existing bridging equipment. (An internal three-way test, using our own Tandberg (Reston, VA) 6000 Multi-Point Control Unit (MCU), confirmed that capability).

Although residency training falls outside the scope of this article, we did welcome PVX's ability to integrate with existing MCUs to accommodate desktop-driven conferences for more than 2 participants. Indeed, in the context of continuing medical education and graduate medical education, this product provided a cost-effective platform to conduct both virtual tumor boards, didactic lectures for the residency training program, and dosimetry teaching conferences with participating institutions (Penn, National Naval Medical Center, National Institute of Health=National Cancer Institute, and other Regional Army Medical Centers).[23–25] Bringing the cumulative expertise of all oncology specialties (gynecological, medical, pediatric, surgical, and radiation) to extend collaboration and education among the cancer-care community sounded like a very attractive proposition.[26]

Our initial tests on the WRAMC network, using existing workstations, yielded subpar results, with CPU use fluctuating between 40% for a dual-core PC to 100% for a single-core PC. While the video did show acceptable frame rates (15), the quality of the image was relatively poor (320 · 240 pixels, or Quarter Video Graphics Array (QVGA), actual versus 640 · 480, or Video Graphics Array (VGA),

Fig. 2. Single monitor with a three-window setup showing the application being shared (top) and the two near-end and far-end video transmissions (bottom left, Walter Reed Army Medical Center; bottom right, University of Pennsylvania).

BELARD ET AL.

expected). The application-sharing portion of the test also yielded disappointing results, with frame rates ranging from four to eight. Given those results, it was suggested by the WRAMC Directorate of Information Management that we acquire new dual-core computers as well as migrate our solution over Internet2 (whose utilization was estimated to be between 10% and 15%). One of the appeals of this hybrid optical-packet network rested in its ability to eventually offer 100 megabits per second of connectivity between every Internet2 Network connected desktop. Limited to the spheres of academia and research, it was also immune from the Defense Information Systems Agency rules governing access DOD-managed networks. Finally, while WRAMC had access to this resource via the MANVT project, Penn was also connected via a Mid-Atlantic Point of Presence. Given the graphic-intensive nature of our telemedicine program, bandwidth was viewed as a critical factor for success.[27]

In order to comply with the Healthcare Information Portability and Accountability Act, a Virtual Private Network (VPN) tunnel was configured between two SSG-5 Juniper routers to create a secured pipe between WRAMC and Penn (Juniper Networks' products meet a wide range of ISO 17799 guidelines).

The PC units purchased to conduct these tests were dual-core Dell (Round Rock, TX) Precision 380 workstations (3.2 GHz ·2), with 2GB of RAM. These computers were equipped with NVidia (Santa Clara, CA) Quadro FX3450 video cards (256 MB) and ran on Windows XP SP2 (Microsoft, Redmond, WA). The decision to settle on these units was derived from our previous experiences running PVX on our fastest clinical machine, whose specifications closely matched those listed above.

While the Polycom PVX install was minimal (44 MB), we did encounter a problem with the application-sharing function being disabled when patched to version 8.0.2. Reverting back to version 8.0.1 did solve the problem, with no loss and=or degradation of other capabilities. The PVX platform was also paired with a Logitech (Fremont, CA) QuickCam_ Pro 5000.

So as to maximize the efficiency of the processor=memory, no other applications were installed on these machines. In addition, for security reasons, the machines located at WRAMC connected to Internet2 were isolated from those on the WRAMC LAN, with the ''tennis shoe network'' (thumb drives) used to transfer needed image files (Fig. 3).

Results

Our initial point-to-point tests with the Penn Radiation Therapy department were conducted at a call rate of 1,920 kilobits per second (Kbps). A single 21-inch monitor was used. The CPU charge fluctuated between 35% and 40% (with 300MB of memory use). The quality of the video remained stable at 15 frames per second (FPS) (VGA quality), although greater movement on camera would have an adverse impact on the fluidity of the video transmission.[28,29]

When subsequent calls were made at 384 Kbps, the CPU load dipped to around 30% with no decrease in audio=video quality. We have yet to find an explanation for the call rate needing to be higher than 384 Kbps. Desktop sharing and application sharing worked as expected: quality of far-end video dropped to QVGA (30 FPS) while content was being shared at a reasonable 7 FPS (XVGA). These initial tests confirmed that the VPN connection over Internet2 was a solid networking platform for our telemedicine link.

Further optimization of the CODEC was subsequently performed: (1) alteration of the PVX configuration file (forcing the recognition of dual-core processors), and (2) tweaking of the audio=video=network settings to account for greater processing power (enabling peopleþcontent, H239, H264, VGA encoding, and allocation of maximum processing power to Polycom when running).

Several tests by staff radiation oncologists at Walter Reed and Penn ensued. The video was consistently broadcasted at 15 FPS over a 384 Kbps link, and control of the commercial radiation treatment

Fig. 3. Diagram of proposed solution (over Internet2).

REMOTE PROTON RADIATION THERAPY SOLUTION OVER INTERNET2

planning package Eclipse (Varian Medical Systems, Palo Alto, CA) was seamlessly shared back and forth. The application being shared was accessed through the ''remote desktop'' function embedded in the Windows XP SP2 Operating System (accessible via the Accessories folder under All Programs). Because our prototype was registered on the University of Pennsylvania's health network, we were able to subsequently take control of and manipulate Penn's commercial treatment planning system.

Running PVX on a dual-monitor setup (21-inch for applicationsharing and 17-inch for VTC) further improved the solution by optimizing work management (maximized window for Eclipse) while providing uninterrupted visual communication. Our tests did point out that users had to adopt the screen resolution of the ''host'' PC (the one on which the application resides) for optimal screen viewing. This presented a minor challenge, which ultimately required very little tweaking (both sites simply needed to agree on a common resolution for all PCs used in the test).

To prepare for an actual test of the solution (live optimization of a treatment plan via VTC), DICOM-RT imaging sets were uploaded to a shared folder residing on the Penn Radiation Oncology server (DICOM-RT refers to a Radiation Therapy specific format used for the storage and transfer of Digital Imaging and Communications in Medicine [DICOM] files). Several series of tests were subsequently conducted to ascertain the user-friendliness and limitations of the point-to-point solution.

Two plans were opened to test the robustness of the system (one phantom and one actual, ''sanitized'' plan, i.e., with patientidentifiable data stripped from the image set). Users were asked to rate the user-friendliness of the solution as either poor (extreme delay; nondynamic), fair (some delay but still usable), or excellent (near real-time feedback). While not as crucial as in telesurgery,[30] the fluidity of video transmission needed to be monitored.

The frame rate for the application-sharing portion of the call was rated from ''fair'' for the real-time 3-D rendered setup of the radiation field on the virtually reconstructed patient, to ''excellent'' for computerized tomography (CT) viewing and CT contouring. We concluded that the lower frame rates recorded in the graphics-intensive FIELDS section result from bandwidth limitations, a parameter over which we have no control. However, in the context of fiberoptic being deployed at an increasing rate, we are hopeful that the efficiency of the solution can only improve over time.

Additional tests were conducted by our department's medical physicists, during which a dummy treatment plan was used for the purpose of evaluating the user friendliness of the interface. The absence of a calculation engine on this version of the Eclipse package did limit the scope of the evaluation, but all participants came out pleased with the solution, going so far as to use the term ''deployable.''

Discussion

Our research grant has put us in the unique position to design a prototype for a functional, point-to-point, remote proton therapy planning tool. Our research program believes that Polycom PVX, coupled with a Logitech QuickCam Pro 5000 or equivalent, provides a cost-effective solution to allow for both audio–video communication and data collaboration.

In the context of remote care being administered by satellite clinics,[31] this inexpensive yet potent solution brings about new opportunities for not only remote treatment, but also virtual desktopto-desktop collaboration in other clinical areas of interest (virtual tumor boards in cancer care, for example, to view diagnostic images of potential referrals for treatment before the treatment planning begins, as well as didactic opportunities for the teaching of medical residents), provided the hardware fielded by each user can accommodate the somewhat demanding requirements of the PVX package.

Although not compulsory, the dual-monitor setup does provide better workspace management by dividing the two portions of calls (VTC and data collaboration). Considering that most physicians in our radiation oncology department already use two monitors, our proposed setup works well within the existing framework (singlemonitor setups may also work, at the expense of screen resolution used for application-sharing). We further believe that by not having

the audio=video window minimized, there is a continuity of communication,
of which visual cues are an integral part (as one example,
the recognition of when the other party is ''tuning out'' when
interrupted and on mute, and not really engaged in the current topic
of the VTC).

This prototype solution does have its limitations, however, which
is why it has yet to be deployed. First and foremost, this low-cost
approach limits itself to point-to-point calls; beyond two users, a
MCU would have to be purchased to manage the technical complexities
intrinsic to multipoint video teleconferencing. With a
maintenance contract and a server, a low-end bridge (Radvision_
(Fair Lawn, NJ) Scopia_ 12, Polycom MGC-25) can cost anywhere
from $30,000 to $40,000, a figure that dwarfs in size the aggregate
cost of a few PVX licenses.

The question of using either IP or ISDN systems was also examined
and while both have their own sets of advantages,[32] the additional
cost associated with the latter (leasing of a line, purchase of a

BELARD ET AL.

gateway to allow for data collaboration) tilted the balance in favor of
a network-based approach.

As corporations move toward large-scale boardroom systems
(RealPresenceTM, Polycom) and=or monitor-size hardware-based
VSX700 or HDX4000 CODECs, we do wonder if maintenance releases
for PVX will keep up with the requirements of programs like ours.
This concern stems from the release of the latest patch (version 8.0.4,
released June 2007), which brought compatibility with Windows
Vista and dual-core processors, but removed support for the T120
application-sharing protocol altogether.

Using a VPN has several advantages, such as transferring provider
notes, radiology reports, DICOM, or other graphic formats depicting
patient imaging data (which can be viewed through the treatment
planning application or other viewing packages). This approach
further ensures that any contextual data exchanged between the two
institutions (which are using the same treatment planning application)
would completely safeguard patients' personal health information.
Virtual tumor boards are also useful, as a separate event, to
actually make the decision about treatment and share related data,
usually in advance of the treatment planning process.

Following comprehensive testing over a period of 2 years, we still
view PVX as a cost-effective solution whose strengths lie in its wideranging
applications, from virtual tumor boards to patient–doctor
consults. Its user-friendly interface and robust image-processing
CODEC make it ideal for small-scale telemedicine programs focused
on point-to-point communications.

Due to PVX version 8.0.1's use of the T120 protocol to accomplish
application-sharing, it is not supported by the United States Army
Medical Information Technology Centers, and therefore, not a viable
option for DOD medical centers. With the emergence of sophisticated
cooperative-Web solutions, it is very likely that they could be used in
the place of PVX without the security vulnerabilities of using a T120
protocol. However, based on the cooperative-Web solutions we have
tested to date and their relatively poor video and audio quality, we are
pursuing a hybrid solution combining a traditional VTC hardware
CODEC paired with a cooperative-Web enabled application. For
networks that allow T120 sharing, we are convinced that the desktop
software CODEC solution we have tested and presented is an outstanding
solution for remote radiation treatment planning; nevertheless,
because security vulnerabilities are an increasing concern
across all networks, further investigation is required.

Conclusions

Our experience with Polycom PVX demonstrates that a simple

desktop VTC CODEC can provide a powerful and cost-effective solution for clinicians seeking to offer remote treatment capabilities for their satellite institution.

Acknowledgment

Disclosure Statement

No competing financial interests exist.

REF E RENCE S

1. Billingsley K, Schwartz D, Lentz S, Vallie`res E, Montgomery B, Schubach W, Penson D, Yueh B, Chansky H, Zink C, Parayno D, Stakerbaum G. Development of a telemedical cancer center within the Veterans Affairs Health Care System. Telemed J 2002;8:123.
2. Jemal A, Siegel R, Ward E, Hao Y, Xu J, Murray T, Thun M. Cancer statistics. CA Cancer J Clin 2008;58:71–96.
3. Kung H-C, Hoyert D, Xu J, Murphy S. Deaths: Final data for 2005. National Vital Data Statistics. Atlanta, GA: Centers for Disease Control and Prevention, 2008:56.
4. Rosenburg AE, Nielsen GP, Lebsch NJ, et al. Chondrosarcoma of the base of the skull: A clinicopathologic study of 200 cases with emphasis on its distinction from chordoma. Am J Surg Pathol 1999;23:1370–1378.
5. Vargas C, Fryer A, Keole S, et al. Dose-volume comparison of proton therapy and intensity-modulated radiotherapy for prostate cancer. Int J Radiat Oncol Biol Phys 2008;70:744–751.
6. Merchant TE, Hua C, Oelfke U, et al. Proton versus photon radiotherapy for common pediatric brain tumors: Comparison of models of dose characteristics and their relationship to cognitive function. Pediatr Blood Center 2008;51:110–117.
7. Michaelson D, Cotter S, Gargollo P, Zietman A, Dahl D, Smith M. Management of complications of prostate cancer treatment. CA Cancer J Clin 2008;58:196–213.
8. Yuh G, Loredo L, Yonemoto L, Bush D, Shahnazi K, Preston W, Slater J, Slater J. Reducing toxicity from craniospinal irradiation: Using proton beams to treat medulloblastoma in young children. Cancer J 2004;10:386–390.
9. Bush D, Slater J, Garberoglio C, Yuh G, Hocko J, Slater J. A technique of partial breast irradiation utilizing proton beam radiotherapy: Comparison with conformal x-ray therapy. Cancer J 2007;13:114–118.
10. Zytkovicz A, Daftari I, Petti PL, et al. Peripheral dose in ocular treatments with cyberKnife and gamma knife radiosurgery compared to proton radiotherapy. Phys Med Biol 2007;52:5957–5971.

REMOTE PROTON RADIATION THERAPY SOLUTION OVER INTERNET2

11. Sudhamony S, Nandakumar K, Binu PJ, Niwas SI. Telemedicine and tele-health services for cancer-care delivery in India. Communications IET 2008; 2:231–236.
12. Kunkler I, Rafferty P, Hill D, Henry M, Foreman D. A pilot study of tele-oncology in Scotland. J Telemed Telecare 1998;4:113–119.
13. Stitt JA. A system of tele-oncology at the University of Wisconsin Hospital and Clinics and regional oncology affiliate institutions. Wisc Med J 1998; 97:38–42.
14. Lugg D. Telemedicine: Have technological advances improved healthcare to remote Antarctic populations? Int J Circumpolar Health 1998;57(suppl 1): 682–685.
15. Malone F, Athanassiou A, Craigo S, Simpson L, D'Alton M. Cost issues surrounding the use of computerized telemedicine for obstetric ultrasonography. Ultrasound Obstet Gynecol 1998;12:120–124.
16. Norum J, Bergmo T, Holdo B, Johansen M, Vold I, Sjaaeng E, Jacobsen H. A tele-obstetric broadband service including ultrasound, videoconferencing and cardiotocogram: A high cost and a low volume of patients. J Telemed Telecare 2007;13:180–184.
17. Ricur G, Batiz M, Romano A, Grandin JC, Arrieta J, Valdivia A. Clinical grand

rounds and corporate training trials across borders. American Telemedicine Association Meeting, Seattle, Washington, April 6–8, 2008.

18. Tucker JH, Busch C, Spatz A, Wells C, Brugal G. An experimental interexpert telepathology network using static imaging. J Clin Pathol 2001; 54:752–757.

19. Nagata H, Mizushima H. A remote collaboration system for telemedicine using the Internet. J Telemed Telecare 1998;4:89–94.

20. Bar-Sela S, Glovinsky Y. A feasibility study of an Internet-based telemedicine system for consultation in an ophthalmic emergency room. J Telemed Telecare 2007;13:119–124.

21. Takada A, Kasahara T, Kinosada Y, Hosoba M, Nishimura T. Economic impact of real-time teleradiology in thoracic CT examinations. Euro Radiol 2003;13:1566–1570.

22. Gortzis L, Karnabatidis D, Siablis D, Nikiforidis G. Clinical-oriented collaboration over the Web during interventional radiology procedures. Telemed J 2006; 12:448–456.

23. Glinkowski W, Makoca K, Pawlica S, Marasek K, Go´recki A. Interactive teleeducation in orthopedics and orthopedic trauma using Internet based videoconferencing. 12th Mednet World Conference, Leipzig, Germany, October 2007.

24. Rossaro L, Tran T, Ransibrahmanakul K, Rainwater J, Csik G, Cole S, Prosser C, Nesbitt T. Hepatitis C videoconferencing: The impact on continuing medical education for rural healthcare providers. Telemed J 2007;13:269–278.

25. Allen M, Sargeant J, MacDougall E, O'Brien B. Evaluation of videoconferenced grand rounds. J Telemed Telecare 2002;8:210–216.

26. Atlas I, Granai CO, Gajewski W, Steinhoff M, Steller M, Falkenberry S, Legare R, Szalb S, Prober A, Zafrir H, Farbstein J. Videoconferencing for gynaecological cancer care: An international tumour board. J Telemed Telecare 2000; 6:242–244.

27. Kaidu M, Toyabe S, Oda J, Okamoto K, Ozaki T, Shiina M, Sasai K, Akazawa K. Development and evaluation of a teleradiology and videoconferencing system. J Telemed Telecare 2004;10:214–218.

28. Huang K-J, Qiu Z-J, Fu C-Y, Shimizu S, Okamura K. Uncompressed video image transmission of laparoscopic or endoscopic surgery for telemedicine. Telemed J 2008;14:479–485.

29. Miyazaki M, Stuart M, Liu L, Tell S, Stewart M. Use of ISDN video-phones for clients receiving palliative and antenatal home care. J Telemed Telecare 2003;9:72–77.

30. Fabrizio MD, Lee BR, Chan DY, Stoianovici D, Jarrett TW, Yang C, Kavoussi LR. Effect of time delay on surgical performance during telesurgical manipulation. J Endourol 2000;14:133–138.

31. Norym J, Bruland O, Spanne O, Trine B, Green T, Olsen D, Olsen J, Sjaeng E, Burkow T. Telemedicine in radiotherapy: A study exploring remote treatment planning, supervision and economics. J Telemed Telecare 2005;11:245–250.

32. Hunter D, Brustrom J, Goldsmith B, Davis L, Carlos M, Ashley E, Gardner G, Gaal I. Teleoncology in the Department of Defense: A tale of two systems. Telemed J 1999;5:273–282.

Address correspondence to:
Arnaud Belard, M.B.A.
Henry M. Jackson Foundation for the Advancement
of Military Medicine
Radiology–Radiation Oncology
Walter Reed Army Medical Center
6900 Georgia Avenue NW
Building 2, Room 1H46A
Washington, DC 20307
E-mail: arnaud.belard@amedd.army.mil

BELARD ET AL.

Original Research

Improving Proton Therapy Accessibility Through Seamless Electronic Integration of Remote Treatment Planning Sites

Arnaud Belard, M.B.A.,[1,2] Derek Dolney, Ph.D.,[3]
Tochner Zelig, M.D.,[3] James McDonough, Ph.D.,[3]
and John O'Connell, M.D.[2]

[1]Henry M. Jackson Foundation for the Advancement of Military Medicine, Rockville, Maryland.

[2]Radiation Oncology Service, Department of Radiology, Walter Reed Army Medical Center, Washington, District of Columbia.

[3]Department of Radiation Oncology, University of Pennsylvania, Philadelphia, Pennsylvania.

Abstract

Objectives: Proton radiotherapy is a relatively scarce treatment modality in radiation oncology, with only nine centers currently operating in the United States. Funded by Public Law 107-248, the University of Pennsylvania and the Walter Reed Army Medical Center have developed a remote proton radiation therapy solution with the goals of improving access to proton radiation therapy for Department of Defense (DoD) beneficiaries while minimizing treatment delays and time spent away from home/work (time savings of up to 3 weeks per patient). Materials and Methods: To meet both Health Insurance Portability and Accountability Act guidelines and the more stringent security restrictions imposed by the DoD, our program developed a hybrid remote proton radiation therapy solution merging a CITRIX server with a JITIC-certified (Joint Interoperability Test Command) desktop videoconferencing unit. This conduit, thoroughly tested over a period of 6 months, integrates both institutions' radiation oncology treatment planning infrastructures into a single entity for DoD patients' treatment planning and delivery. Results: This telemedicine solution enables DoD radiation oncologists and medical physicists the ability to (1) remotely access a proton therapy treatment planning platform, (2) transfer patient plans securely to the University of Pennsylvania patient database, and (3) initiate ad-hoc point-to-point and multipoint videoconferences to dynamically optimize and validate treatment plans. Conclusions: Our robust and secure remote treatment planning solution grants DoD patients not only access to a state-ofthe-art treatment modality, but also participation in the treatment planning process by Walter Reed Army Medical Center radiation oncologists and medical physicists. This telemedicine system has the potential to lead to a greater integration of military treatment facilities and/or satellite clinics into regional proton therapy centers.

Key words: Cancer, radiation therapy, virtual medical simulation, remote treatment planning

Introduction

According to the National Center for Health Statistics, one in four deaths in the United States is due to cancer.[1] In the arsenal of treatment modalities used to manage the disease, proton radiation therapy is a relatively new weapon. Because the technology involved in producing and delivering protons is quite complex, the cost of developing multiroom

proton therapy centers is significant (anywhere between $150 and $250 million dollars depending on the number of gantries deployed). At the time of writing this article, there were only nine centers in the United States offering comprehensive proton radiotherapy.

Through public law, a partnership was established in 2004 between the hospital at the University of Pennsylvania (UPenn) (Roberts Proton Therapy Center) and the Walter Reed Army Medical Center (WRAMC) (Department of Radiology–Radiation Oncology Service) to engage in several areas of research as it pertains to the delivery of proton radiation therapy. One of the goals of this grant was the development of a robust remote proton radiotherapy treatment planning system to (1) facilitate the determination of protocol eligibility and enrollment at the local level, (2) eliminate duplicate consultations by different radiation oncologists, duplicate tumor board reviews, and duplicate image staging, and (3) significantly reduce the patient's time away from work and family by performing the entire treatment planning process remotely (i.e., simulation, fabrication of immobilization devices, contouring, plan creation, dose calculation, and plan approval and prescription). Although the field of radiation oncology has used telemedicine in the recent past,[2–6,34] and more specifically, as it applies to both Department of Defense (DoD) and Veterans Affairs beneficiaries,[7,8] we believe our solution pushes a new frontier.

Materials and Methods

Building upon our experience with the ''Remote Proton Radiation Therapy over Internet2'' prototype,[9] our research program has developed a hybrid telemedicine solution that offers the following functionalities to the remote cancer-care provider: (1) ability to conduct both planned or ad-hoc high-definition audio-videoconferences with one or more sites, (2) ability to upload treatment plans to a shared folder via a secure VPN connection, (3) sharing of treatment planning applications with authorized users for the purpose of optimizing/validating prescriptions, and (4) seamless integration of the hybrid design with existing multipoint control units (MCU) for calls involving more than two sites.

This hybrid solution merges a high-definition video teleconferencing (VTC) unit configured over an integrated services digital network (ISDN),[10,11] with an internet protocol (IP)[12] CITRIX client. Before selecting a desktop VTC unit, our research program looked at all available models from both Polycom and Tandberg. Demonstrations at the American Telemedicine Association Annual Meeting (Nashville, 2007 and Seattle, 2008) and in-house (Directorate of Information Management) confirmed that all units would meet our requirements in terms of connectivity (IP) and quality (minimum of 640 by 480 pixels). Our engineers seemed to have a slight preference for the Tandberg models, for both their JITIC (Joint Interoperability Test Command) certification and their substantial use within the DoD network. Once confronted with the option of going either SD (standard definition or 480i max resolution) or HD (high definition or 1080i/720p max resolution), we opted for the latter, anticipating that future improvements in network capabilities would result in improved visual content for the users.

Our choice was the Tandberg 1700 MXP, a 20-inch widescreen LCD with a high-definition audio-videoconferencing unit equipped

with a built-in HD camera. Of the four units we initially purchased, two had the embedded multisite functionality, thus turning them into a portable MCU for up to four sites. The Tandberg further gave the ability to place calls up to 2 megabits-per-second with H.235 encryption. With true CD-quality audio, protection against network interruptions for point-to-point calls, and superior video quality (H.264 standard), the 1700MXP seemed like a very robust desktop HD VTC solution. Finally, the 1700 could also serve as a PC monitor, thus doubling the virtual workspace of physicians.

Three of these hardware codecs were initially purchased for evaluation, at a cost of $8,000 per unit. Two were placed at the WRAMC (Radiation Oncology Service) and one at the UPenn (Department of Radiation Oncology). The three units were configured over their respective networks (MEDNET and UPHS).

For the two Walter Reed units, connectivity was achieved via an IP connection from the endpoint itself to a Tandberg Codian gateway. Both were assigned phone numbers by the United States Army Medical Information Technology Center (USAMITC); calls placed from these units are therefore IP pre-gateway and ISDN post-gateway. UPenn is using a similar setup at their end, having their endpoint connected via IP to their Polycom RMX 2000 bridge and also registered with their gatekeeper/gateway for ISDN calls.

Our current setup (Figs. 1 and 2) pairs a Tandberg 1700MXP with a standard 21-inch flat-screen liquid crystal display linked to a clinical computer. For its application-sharing function, our research program initially selected Defense Connect Online (DCO), an Adobe Connect product developed for the DoD. We tested both the DoD version and the commercial version of the core product. Both of those allowed us to evaluate window management (note, chat, attendee list, camera, share), as well as application sharing. DCO, based on the professional version of Adobe Connect, also offered additional functionalities, but those were of no particular benefit to our program (meeting recordings, administration and reporting, large events and polling, etc.).

Although free, DCO came with several drawbacks: (1) only individuals affiliated with the DoD can create an account and therefore open a room for data collaboration and (2) calls have the potential to be recorded and subsequently reviewed by staff who did not receive Health Insurance Portability and Accountability Act (HIPAA) certification. Because the risk of compromising a patient's protected health information was very real, our program decided to abandon this platform to focus instead on a CITRIX client for both the secure transfer of patient files and the sharing of the treatment planning application.

CITRIX is a powerful application granting users not only the ability to transfer files securely from their local workstation to a remote site, but also take control of an application remotely. In addition, the ''shadowing'' function allows the far user to also take part in any remote session, thus offering the ability to collaborate dynamically in real time. CITRIX is not only endorsed by the DoD, but also certified to meet all current HIPAA requirements. The application being accessed via CITRIX is an Eclipse treatment planning platform (Varian Medical Systems), enabled for both photon and proton calculations.

A CITRIX server was purchased by the research program and subsequently configured on the UPHS network; 20 licenses were also acquired for our users. The evaluation itself was performed on a UPenn system temporarily dedicated for DoD use (ultimately, a Walter Reed Eclipse workstation has to be transferred to the UPenn as part of this comprehensive solution).

Fig. 1. Schematics of the hybrid solution (part 1).

BELARD ET AL.

Results

As the solution was being designed, our program developed a standard operating procedure (SOP) to account for the inclusion of telemedicine equipment for both communication and treatment planning purposes. Tests were conducted over a period of a year and a half to ascertain the robustness of the solution. Although the SOP offers two alternative ways of conducting proton treatment planning, our evaluation focused on ''remote planning on Penn server from DoD MTF'' (Fig. 3), which we feel provides the greatest benefit to the telemedicine community.

The testing of the VTC link itself took about 12 months, as connectivity problems persisted despite numerous software refreshes and reconfigurations. Although both Tandberg and Polycom equipments are intended to follow industry standards, compatibility issues prevented us from achieving full bilateral connectivity (failure by UPenn to receive video) until the Tandberg development team was able to replicate and test our setup in their own laboratory. Once the issue had been identified and corrected, a patch was applied to the Codian gateway, the Tandberg device that integrates ISDN and IP networks. Since then, our two sites have been able to enjoy full bilateral connectivity (audio and video).

The feedback from users has been overwhelmingly positive. Time delay, a limit of both hardware and bandwidth,[13,14] is a problem often reported by users of telemedicine systems. Our solution offers not only real-time feedback,[15,16] but also fluidity of motion and optimal resolution[17] for treatment planning.

Patient selection and enrollment occurs either on-site (weekly rotation of DoD radiation oncologists to UPenn) or remotely (telemedicine solution). Once enrolled into a proton radiotherapy course of treatment, the DoD patient is scanned at Walter Reed and the CT sets acquired are subsequently transferred from the servers to the local drive of the user's treatment planning workstation.

The CITRIX application itself is launched through a small ''executable'' (CITRIX Secure Access Client). Once the connection is established, users can then access the UPenn Intranet (UPHSNET) and, subsequently, the treatment planning application. The CITRIX encryption technology (AES 256-bit) guarantees the integrity of any protected health information being transmitted over the Internet, as required by HIPAA. The UPenn Health System created a specific ''user group'' with rights to access the treatment planning package. Each user within that group (radiation oncologists, medical physicists, and dosimetrists) was assigned a specific login and password combination for both CITRIX and Eclipse access, further strengthening security.

Once the user has taken control of the workstation located at the UPenn (used to contour normal structures/ targets and design treatment plans), the mapped ''C:'' drive allows the user to seamlessly import these files into the Eclipse software; the treatment plan subsequently generated is automatically saved on the UPenn patient server (i.e., no manual transfer of files required). Any issues arising during the planning process, or the treatment itself, give rise to an ad-hoc call using the Tandberg 1700MXP audio-videoconferencing units to examine and troubleshoot the issue dynamically.

This hybrid solution not only ensures the involvement of a DoD radiation oncologist in the proton planning of his or her patients, but also prevents a certain degree of redundancy, such as rescanning of

patients (a time saving of up to several weeks) or restaging (identical immobilization devices at both sites).

Although our tests relied on three units (two of which had the multisite functionality), this SOP assumes that all caregivers involved in remote proton planning will be equipped with both a high-definition desktop VTC unit (Tandberg 1700MXP or Polycom 4000 HDX) and a CITRIX client on their treatment planning workstation.

Discussion

As network and computing capabilities improve, telemedicine is increasingly moving away from the now relatively trivial transfer of static images[18-20] to more complex clinical activities, such as telesurgery [21] or, in our case, dynamic treatment planning.

As reported in our previous publication, our initial prototype did not move past the testing phase, but we hope that satellite institutions will still view the Polycom PVX software solution as a costeffective and worthwhile solution to conduct point-to-point (and multipoint, should a bridge be available as a resource) VGA-quality audio-videoconferences. In addition, its data collaboration features, whether those take the form of sharing a desktop (still images) or an application (dynamic collaboration), can greatly enhance the

Fig. 2. Schematics of the hybrid solution (part 2).

REMOTE PROTON RADIOTHERAPY TREATMENT PLANNING

experience of far-site physicians seeking increased ''involvement'' in the treatment of their patients. In particular, we did welcome the capabilities of PVX to integrate with existing MCUs to accommodate desktop-driven conferences for more than two participants.

For the field of radiation oncology, this product could provide main hospitals and their satellite institutions with a cost-effective platform to conduct both virtual tumor boards and dosimetry conferences with participating institutions.[22-25] Although this prototype solution was not adopted by our program, the lessons learned enabled us to develop the vastly superior system we have now (Fig. 4).

The choice to go with a hybrid system, one relying on ISDN and IP rather than IP alone, was guided by the fact that a DoD-run network exists to run audio-videoconferencing (MEDNET VLAN). We were further assured by the Walter Reed Directorate of Information Management that conducting VTCs over an ISDN line was a much more robust and secure approach.[26] Respecting patient privacy, and data security as a whole, we went by the guidelines offered to us and therefore went for an ISDN videoconferencing solution.

Our hybrid remote proton therapy treatment planning solution not only improves access to a scarce treatment modality[27,28] for both patient and provider, as a telemedicine solution, but also has the potential to bring the cumulative expertise of all oncology specialties (gynecological, medical, pediatric, surgical, and radiation) to extend collaboration and education among the cancercare community.[29-32]

Although the cost of the hardware may present a budgetary challenge for smaller clinics,[33] the approach we propose will naturally scale upward as network capacities are expanding, giving users the ability to see and hear in high definition, while engaging in the real-time remote manipulation of complex treatment plans. The solution also gives users the ability to seamlessly interact, as if working side by side. The benefit to our patient community is also very real and quantifiable, as their time relocating to Philadelphia for treatment will be minimized because of the existence

151

of this telemedicine solution (needlessness of repeating scans, simulations, and planning of treatment); in routine cases, the net time savings associated with this solution is estimated to be between 1 and 3 weeks per patient.

Conclusions

Our robust remote treatment planning telemedicine solution offers a path toward greater integration of military treatment facilities, or satellite clinics, into regional proton therapy centers.

Fig. 3. Standard operation procedure (SOP) flowchart for the use of this solution in radiation therapy.

Fig. 4. Strengths and weaknesses of both solutions.

BELARD ET AL.

Acknowledgments

Disclaimer

The opinions, interpretations, conclusions, and recommendations in this article are those of the authors and are not necessarily endorsed by the US Army.

Disclosure Statement

No competing financial interests exist.

REF ERENC E S

1. Jemal A, Siegel R, Ward E, Hao Y, Xu J, Murray T, Thun MJ. Cancer statistics. CA Cancer J Clin 2008;58:71–96.
2. Sudhamony S, Nandakumar K, Binu PJ, Niwas SI. Telemedicine and tele-health services for cancer-care delivery in India. Commun IET 2008;2:231–236.
3. Norym J, Bruland O, Spanne O, Trine B, Green T, Olsen D, Olsen J, Sjaeng E, Burkow T. Telemedicine in radiotherapy: A study exploring remote treatment planning, supervision and economics. J Telemed Telecare 2005;11:245–250.
4. Kunkler I, Rafferty P, Hill D, Henry M, Foreman D. A pilot study of tele-oncology in Scotland. J Telemed Telecare 1998;4:113–119.
5. Stitt JA. A system of tele-oncology at the University of Wisconsin Hospital and Clinics and regional oncology affiliate institutions. Wisc Med J 1998;97:38–42.
6. Pare´ G, Sicotte C, Chekli M, Jaana M, De Blois C, Bouchard M. A pre-post evaluation of a telehomecare progam in oncology and palliative care. Telemed JE Health 2009;15:154–159.
7. Billingsley K, Schwartz D, Lentz S, Vallie`res E, Montgomery B, Schubach W, Penson D, Yueh B, Chansky H, Zink C, Parayno D, Stakerbaum G. Development of a telemedical cancer center within the veterans affairs health care system. Telemed J 2002;8:123.
8. Hunter D, Brustrom J, Goldsmith B, Davis L, Carlos M, Ashley E, Gardner G, Gaal I. Teleoncology in the department of defense: A tale of two systems. Telemed J 1999;5:273–282.
9. Belard A, Tinnel B, Wilson S, Ferro R, O'Connell J. Development of a remote proton radiation therapy solution over Internet2. Telemed J 2009;15:998–1004.
10. Norum J, Bergmo T, Holdo B, Johansen M, Vold I, Sjaaeng E, Jacobsen H. A teleobstetric broadband service including ultrasound, videoconferencing and cardiotocogram. A high cost and a low volume of patients. J Telemed Telecare 2007;13:180–184.
11. Miyazaki M, Stuart M, Liu L, Tell S, Stewart M. Use of ISDN video-phones for clients receiving palliative and antenatal home care. J Telemed Telecare 2003;9:72–77.
12. Bar-Sela S, Glovinsky Y. A feasibility study of an Internet-based telemedicine

system for consultation in an ophtalmic emergency room. J Telemed Telecare 2007;13:119–124.

13. Fabrizio MD, Lee BR, Chan DY, Stoianovici D, Jarrett TW, Yang C, Kavoussi LR. Effect of time delay on surgical performance during telesurgical manipulation. J Endourol 2000;14:133–138.

14. Malone F, Athanassiou A, Craigo S, Simpson L, D'Alton M. Cost issues surrounding the use of computerized telemedicine for obstetric ultrasonography. Ultrasound Obstet Gynecol 1998;12:120–124.

15. Huang K-J, Qiu Z-J, Fu C-Y, Shimizu S, Okamura K. Uncompressed video image transmission of laparoscopic or endoscopic surgery for telemedicine. Telemed J 2008;14:479–485.

16. Gortzis L, Karnabatidis D, Siablis D, Nikiforidis G. Clinical-oriented collaboration over the web during interventional radiology procedures. Telemed J 2006;12:448–456.

17. Patricoski C, Ferguson S. Selecting a digital camera for telemedicine. Telemed J 2009;15:465–475.

18. Tucker JH, Busch C, Spatz A, Wells C, Brugal G. An experimental interexpert telepathology network using static imaging. J Clin Pathol 2001;54: 752–757.

19. Kaidu M, Toyabe S, Oda J, Okamoto K, Ozaki T, Shiina M, Sasai K, Akazawa K. Development and evaluation of a teleradiology and videoconferencing system. J Telemed Telecare 2004;10:214–218.

20. Stong A, Nichols T, Rogers W, Fisk A. Systematic human factors evaluation of a teledermatology system within the U.S. Military. Telemed J 2008;14: 25–34.

21. Ereso A, Garcia P, Tseng E, Dua M, Victorino G, Guy T. Usability of robotic platforms for remote surgical teleproctoring. Telemed J 2009;15: 445–453.

22. Glinkowski W, Makoca K, Pawlica S, Marasek K, Go´ recki A. Interactive teleeducation in Orthopedics and Orthopedic Trauma using Internet based videoconferencing. 12th Mednet World Conference. Leipzig, Germany: s.n., October 2007.

23. Rossaro L, Tran T, Ransibrahmanakul K, Rainwater J, Csik G, Cole S, Prosser C, Nesbitt T. Hepatitis C videoconferencing: The impact on continuing medical education for rural healthcare providers. Telemed J 2007;13:269–278.

24. Allen M, Sargeant J, MacDougall E, O'Brien B. Evaluation of videoconferenced grand rounds. J Telemed Telecare 2002;8:210–216.

25. Ricur G, Batiz M, Romano A, Grandin JC, Arrieta J, Valdivia A. Clinical grand rounds and corporate training trials across borders. American Telemedicine Association Meeting. Seattle, Washington: s.n., April, 2008.

26. Nagata H, Mizushima H. A remote collaboration system for telemedicine using the Internet. J Telemed Telecare 1998;4:89–94.

27. Lugg D. Telemedicine: Have technological advances improved health care to remote Antarctic populations? Int J Circumpolar Health 1998;57(suppl 1): 682–685.

28. Khasanshina E, Wolfe W, Emerson E, Stachura M. Counseling center-based tele-mental heatlh for students at a rural university. Telemed J 2008;14: 35–41.

29. Atlas I, Granai CO, Gajewski W, Steinhoff M, Steller M, Falkenberry S, Legare R, Szalb S, Prober A, Zafrir H, Farbstein J. Videoconferencing for gynaecological cancer care: An international tumour board. J Telemed Telecare 2000;6: 242–244.

30. Erickson D, Greer L, Belard A, Tinnel B, O'Connell J. A hybrid integrated services digital network-internet protocol solution for resid education. Telemed J 2010;16:454–460.

REMOTE PROTON RADIOTHERAPY TREATMENT PLANNING

31. Paixao M, Miot H, Wen C. Tele-education on leprosy: Evaluation of an educational strategy. Telemed J 2009;15:552–559.

32. Conde J, De S, Hall R, Johansen E, Meglan D, Peng G. Telehealth innovations in health education and training. Telemed J 2010;16:103–106.

33. Takada A, Kasahara T, Kinosada Y, Hosoba M, Nishimura T. Economic impact of real-time teleradiology in thoracic CT examinations. Euro Radiol 2003;13:1566–1570.

34. Head B, Studts J, Bumpous J, Gregg J, Wilson L, Keeney C, Sharfenberger J, Pfeifer M. Development of a telehealth intervention for head and neck cancer patients. Telemed J 2009;15:44–52.

Address correspondence to:
Arnaud Belard, M.B.A.
Henry M. Jackson Foundation for the Advancement
of Military Medicine
6900 Georgia Ave.
NW Building 2, Room 1H46A
Washington, DC 20307
E-mail: arnaud.belard@amedd.army.mil